



University
of Glasgow

Krishnan, Anand (2008) *Laser and optical based methods for detecting and characterising microorganisms*.
PhD thesis.

<http://theses.gla.ac.uk/436/>

Copyright and moral rights for this thesis are retained by the author

A copy can be downloaded for personal non-commercial research or study, without prior permission or charge

This thesis cannot be reproduced or quoted extensively from without first obtaining permission in writing from the Author

The content must not be changed in any way or sold commercially in any format or medium without the formal permission of the Author

When referring to this work, full bibliographic details including the author, title, awarding institution and date of the thesis must be given

**Laser and optical based methods for
detecting and characterising microorganisms**

Anand Krishnan

**Submitted for the Degree of Ph.D. in the Department of
Mechanical Engineering at the University of Glasgow**

September 2008

©Anand Krishnan 2008

Acknowledgements

I would like to thank a number of people for helping me through the experimental work and writing that went into producing this thesis. I especially thank Dr Ian Watson and Dr Roger Parton for all of their technical advice, encouragement and time they gave in reading my thesis drafts.

My special thanks to Mr. Ian Peden, Technician, Department of Mechanical Engineering for imparting his practical knowledge on optics, microscopy and software programming. Thanks also go to Dr Rob Aitken, Director IBLS Undergraduate School and Mrs Susan M Baillie, Technician, IBLS, Division of Infection and Immunity for providing the microbiological support and basic knowledge for my experiments.

Thanks too to Mrs. Dorothy Armstrong, IBLS, Division of Infection and Immunity for the support rendered in culturing and providing protists at the right time.

A very special thanks go to my family and friends who gave me their encouragement and support throughout my Ph.D.

Abstract

Abstract

This work investigated novel optical methods of characterizing the activity of microorganisms. Two different systems are studied in detail in this work. The possibility of using line scan speckle systems and imaging systems to understand the microbial behaviour, growth and motility was investigated. Conventionally, the growth and viability of microorganisms are determined by swabbing, plating and incubation, typically at 37°C for at least 24 hrs. The proposed system allows real-time quantification of morphology and population changes of the microorganisms.

An important aspect of the line scan system is the dynamic biospeckle. Dynamic speckle can be obtained from the movement of particles suspended in liquids. The speckle patterns show fluctuations in space and time which may be correlated with the activity of the constituents in the suspension. Initially the speckle parameters were standardized to non-motile and inert specimens such as polystyrene microspheres and suspensions of *Staphylococcus aureus*. The same optical systems and parameters were later tested on motile, active and live organisms of *Escherichia coli*.

The experimental results that are presented describe the time history of the dynamic speckle pattern. A number of algorithms were used to analyse the intensity data. A 2D-FFT algorithm was used to evaluate the space and time-varying autocorrelation. Analysis of the speckle data in the Fourier domain provided insight into the motility of the organisms in broth. The mathematical analysis also gave further insight into the culture broth evaporation and its particle sedimentation characteristics at 37°C. These features correlated with the periodic motions associated with the organism and may therefore provide a signature for the organism and a means of monitoring. These results aided the development of imaging bacterial detection systems which were discussed in the second half of the work.

The second experimental system focuses on quantifying the morphology and population dynamics of *Euglena gracilis* under ambient conditions through image processing. Unlike many other cell systems, *Euglena* cells change from round to long to round cell shape and these different cell shapes were analyzed over time. In the morphological studies of single *Euglena* cells, image processing tools and filtering techniques were used and different

parameters identified and their efficiency at determining cell shape compared. The best parameter for processing the images and its effectiveness in detecting even the interior motions of constituents within a dead cell was found. The efficiency of the measurement parameters in following sequences of shape changes of the *Euglena* cell was compared with the visual assessment tests from 12 volunteers and other simple measurement methods including parameters relating to the cells eccentricity, and image processing in the space and frequency domains. One of the major advantages of this system is that living cells can be examined in their natural state without being killed, fixed, and stained. As a result, the dynamics of ongoing biological processes in live cells can be observed and recorded in high contrast and sharp clarity.

The population statistics of *Euglena gracilis* was done in liquid culture. A custom built microscopy system was employed and the laser beam was coupled with a dark field illumination system to enhance the contrast of the images. Different image filters were employed for extracting useful information on the population statistics. Similarly as with the shape study of the *Euglena* cell, different parameters were identified and the best parameter was selected. The population study of the *Euglena* cells provided a detection system that indicated the activity of the population.

List of Figures and Tables

List of Figures and Tables	Page
Figure 2.1 The schematic view of the hardware setup and optics for the experiments involving polystyrene microspheres.	24
Figure 2.2 The schematic view of the hardware setup and optics for the experiments involving <i>Staphylococcus aureus</i> suspension; cuvette is placed at position 2.	25
Figure 2.3 Universal bottles containing 10 fold dilutions of the <i>Staphylococcus aureus</i> suspension.	26
Figure 2.4 Comparison of average time-varying autocorrelation width ($T_{c_{avg}}$) parameter for 1 μm and 10 μm spheres under different conditions.	26
Figure 2.5 Comparison of spatially-varying autocorrelation function between the neat suspension of 10 μm spheres (counts = $10^6/\text{ml}$) spheres and diluted suspension of the same (counts= $8.33 \times 10^5/\text{ml}$) spheres.	27
Figure 2.6 Comparison of average time-varying autocorrelation width ($T_{c_{avg}}$) for <i>S. aureus</i> suspension kept under different dilutions (neat to 10^{-6}).	28
Table 2.1 The dilution of <i>S. aureus</i> suspension and its corresponding optical density	28
Figure 2.7 Comparison of the effect of different dilutions (from neat to 10^{-6}) on T_c plotted over a period of 25 min.	29
Figure 2.8 Absolute value of the differential standard deviation of T_c over a period of 25 min for different dilutions of <i>S. aureus</i> suspension.	30
Figure 2.9 Variation of autocorrelation width (T_c) over 25 min for <i>S. aureus</i> suspension (neat sample).	31
Figure 2.10 Variation of autocorrelation width (T_c) over 25 min for <i>S. aureus</i> suspension (10^{-1} dilution sample).	32
Figure 2.11 Variation of autocorrelation width (T_c) over 25 min for <i>S. aureus</i> suspension (10^{-2} dilution sample).	33
Figure 2.12 Variation of autocorrelation width (T_c) over 25 min for <i>S. aureus</i> suspension (10^{-3} dilution sample).	34
Figure 2.13 Variation of autocorrelation width (T_c) over 25 min for <i>S. aureus</i> suspension (10^{-4} dilution sample).	35
Figure 2.14 Variation of autocorrelation width (T_c) over 25 min for <i>S. aureus</i> suspension (10^{-5} dilution sample).	36

Figure 2.15 Variation of autocorrelation width (T_c) over 25 min for <i>S. aureus</i> suspension (10^{-6} dilution sample).	37
Figure 2.16 Variation of autocorrelation width (T_c) over 36 min for <i>S. aureus</i> suspension (10^{-1} sample) under vigorous stirring for 3 min ($t = 4$ to 7 min).	38
Figure 2.17 Comparing spatially varying autocorrelation function of <i>S. aureus</i> suspension at 10^{-1} dilution (8.88×10^7 cfu/ml) and 10^{-2} dilution (8.88×10^6 cfu/ml)	39
Figure 2.18 Comparing spatially-varying autocorrelation function of <i>S. aureus</i> suspension at 10^{-1} dilution (8.88×10^7 cfu/ml) before and after 40 min sedimentation.	40
Figure 3.1 The typical work scheme for <i>E. coli</i> for the first experiment (horizontal transmission) and second experiment (vertical transmission).	54
Figure 3.2 Schematic view of the hardware setup and optics; the cuvette is placed either at position 2 (horizontal transmission, first experiment) or position 1 (vertical transmission, second experiment).	55
Figure 3.3 Incubator setup and the optics.	56
Figure 3.4 Cuvettes employed in the actual experiment	56
Figure 3.5 Growth of <i>E. coli</i> for the first (horizontal transmission) and second (vertical transmission) experiments.	57
Figure 3.6 Growth of <i>E. coli</i> drawn on a log scale for the first (horizontal transmission) and second (vertical transmission) experiments.	58
Figure 3.7 Effect of different cuvettes on growth of <i>E. coli</i> in the second experiment.	59
Figure 3.8 Volume drop in LB broth in the second experiment, for different cuvettes.	60
Figure 3.9 Variation of $T_{c_{avg}}$ for the first (horizontal transmission) and second (vertical transmission) experiments.	61
Figure 3.10 Variation of $T_{c_{avg}}$ for the second experiment (vertical transmission).	62
Figure 3.11 Change in $\frac{T_{c_{avg}}}{CFU}$ (log scale) in the <i>E. coli</i> culture for both the first and second experiments.	63
Figure 3.12 Variation of $T_{c_{avg}}$ through serial dilution for the third experiment (where 100% was 15×10^{10} CFU/ml).	64
Figure 3.13 Variation of the normalised $T_{c_{avg}}$ through different serial dilutions	65

for the third experiment (vertical transmission), using <i>E. coli</i> in broth.	
Figure 3.14 Absolute value of the differential between the standard deviation of the Tcavg for back dilutions shown in Figure 3.12.	66
Figure 3.15 Variation of spatial autocorrelation through serial dilution of the <i>E. coli</i> culture for the third experiment.	67
Figure 3.16 Changes in the optical density of the <i>E. coli</i> culture over period of 36 h of sampling for two different samples.	68
Figure 4.1 Bright-field microscopy and image capture system optimized for high contrast to capture the movements of a single <i>Euglena gracilis</i> cell.	84
Figure 4.2 The random sequences of the images given to volunteers and the corresponding identification numbers.	85
Figure 4.3 <i>Euglena gracilis</i> and its intensity distribution before and after high pass filtering.	86
Figure 4.4 Schematic of the image processing workflow. Comparison of background subtracted and PSD images for unfiltered, filtered and edge-enhanced images of a <i>Euglena</i> cell.	87
Figure 4.5 The sequences of the images as arranged by volunteers.	88 -90
Table 4.1 Visual assessment sequence from volunteers.	91
Table 4.2 Number of volunteers agreed to place the particular picture at the particular position.	91
Table 4.3 Area calculated for different shapes of <i>Euglena</i> .	92
Figure 4.6 The sequences of the images as arranged by the measurement methods.	93-94
Table 4.4 Comparison of the results between the measurement method and the visual assessment method	95
Figure 4.7 Images of <i>Euglena</i> from bright field microscopy (on left) and corresponding in PSD (right) for different cell morphologies and no filtering.	96-97
Figure 4.8 Variation of average pixel intensity of the PSD converted images over different shapes of the <i>Euglena</i> taken from bright-field microscopy	98
Figure 4.9 Variation of intensity standard deviation of a PSD image over different shapes of the <i>Euglena</i> taken from bright field microscopy.	99
Figure 4.10 Variation of Gaussian standard deviation of a PSD image over different shapes of the <i>Euglena</i> taken from bright field microscopy	100

Figure 4.11 Crosscorrelation coefficient of every <i>Euglena</i> (unfiltered) image with respect to the broadest shape of the <i>Euglena</i> cell.	101
Figure 4.12 Exploded view of Figure 4.11 to unfold details within low crosscorrelation coefficients	101
Figure 4.13 Crosscorrelation coefficient of every unfiltered PSD image of <i>Euglena</i> with respect to the broadest shape of the <i>Euglena</i> cell.	102
Figure 4.14 Exploded view of Figure 4.13 to unfold details within low crosscorrelation coefficients.	102
Figure 4.15 The sequences of the images as arranged by the image processing parameters before filtering.	103-104
Table 4.5 Comparison of the results between the image processing before filtering and the visual assessment methods.	105
Figure 4.16 Variation of average pixel intensity of PSD images before filtering over the ratio of major axis to summation of minor axes.	106
Figure 4.17 Variation of intensity standard deviation of PSD images before filtering over the ratio of major axis to summation of minor axes.	107
Figure 4.18 Variation of Gaussian standard deviation of PSD images before filtering over the ratio of major axis to summation of minor axes.	108
Figure 4.19 Variation of crosscorrelation coefficient of the <i>Euglena</i> images before filtering over the ratio of major axis to summation of minor axes.	109
Figure 4.20 Variation of crosscorrelation coefficient of the PSD converted <i>Euglena</i> images before filtering over the ratio of major axis to summation of minor axes.	110
Figure 4.21 Actual (1) and PSD (2) image of the noise-filtered edge-enhanced image with A-F showing live cells and G showing the images derived from a dead cell.	111-112
Figure 4.22 Variation of average pixel intensity of the PSD image after noise filtering	113
Figure 4.23 Variation of intensity standard deviation of the PSD image after noise filtering	114
Figure 4.24 Variation of Gaussian standard deviation of the PSD image after noise filtering	115
Figure 4.25 Temporal variation of Intensity standard deviation from the PSD	116

image and comparison of values in live and dead *Euglena* cells

Figure 4.26 COLUMNS: A) Filtered image, B) Cross-correlation of filtered image, C) PSD of the filtered image, D)Cross-correlation of the PSD of filtered image. Figures arranged from broadest to elongated shape (A1, B1, C1, D1A6, B6, C6, D6).	117-120
Figure 4.27 Crosscorrelation coefficient of every <i>Euglena</i> (filtered) image with respect to the broadest shape of the <i>Euglena</i> cell.	121
Figure 4.28 Crosscorrelation coefficient of every PSD <i>Euglena</i> (filtered) images with respect to the broadest shape of the <i>Euglena</i> cell.	122
Figure 4.29 Exploded view of Figure 4.23 to unfold details within low crosscorrelation coefficients.	122
Figure 4.30 The sequences of the images as arranged by the image processing parameters after filtering.	123-124
Table 4.6 Comparison of the results between the image processing after filtering and the visual assessment methods.	125
Figure 4.31 Variation of average pixel intensity of PSD images after filtering over the ratio of major axis to summation of minor axes.	126
Figure 4.32 Variation of intensity standard deviation of a PSD images after filtering over the ratio of major axis to summation of minor axes.	127
Figure 4.33 Variation of Gaussian standard deviation of a PSD images after filtering over the ratio of major axis to summation of minor axes.	128
Figure 4.34 Variation of crosscorrelation coefficient of the <i>Euglena</i> images after filtering over the ratio of major axis to summation of minor axes.	129
Figure 4.35 Variation of crosscorrelation coefficient of the PSD converted <i>Euglena</i> images after filtering over the ratio of major axis to summation of minor axes.	130
Table 4.7 Comparison of the results from different analysis method and the visual assessment methods.	131
Table 4.8 Comparison of the results from image processing method with the ratio of major axis to summation of minor axes.	132
Figure 5.1 Ringing table for the specimen preparation.	151
Figure 5.2 Preliminary experiment under phase contrast microscopy system.	152
Figure 5.3 Schematic of the laser illuminated dark field microscopy system.	153

Figure 5.4 Custom built laser illuminated dark field microscopy system with beam expanders (middle).	154
Figure 5.5 Image processing flowchart.	155
Figure 5.6 Log magnitude and phase of the Laplacian image filter.	156
Figure 5.7 Log magnitude and phase of the Gaussian image filter.	156
Figure 5.8 Log magnitude and phase of the Low Pass image filter using <i>fsamp2</i> .	156
Figure 5.9 Log magnitude and phase of the low pass image filter using <i>fwind1</i> .	157
Figure 5.10 Log magnitude and phase of the low pass image filter using <i>fwind2</i> .	157
Figure 5.11 Log magnitude and phase of the high pass image filter using <i>fsamp2</i> .	157
Figure 5.12 Log magnitude and phase of the high pass image filter using <i>fwind1</i> .	158
Figure 5.13 Log magnitude and phase of the high pass image filter using <i>fwind2</i> .	158
Figure 5.14 Log magnitude and phase of the band pass image filter using <i>fsamp2</i> .	158
Figure 5.15 Log magnitude and phase of the band pass image filter using <i>fwind1</i> .	159
Figure 5.16 Log magnitude and phase of the band pass image filter using <i>fwind2</i> .	159
Figure 5.17 Point Spread Function intensity values of the portion to be deconvolved.	160
Figure 5.18 3-d plot of the point spread function intensity values of the portion (Figure 5.17) to be deconvolved.	161
Figure 5.19 Images of <i>Euglena gracilis</i> from a phase contrast microscopy system at different times (t = 40 to 65 s).	162
Figure 5.20 Images of <i>Euglena gracilis</i> under laser dark field microscopy system before filtering (t = 1 to 11 s).	163
Figure 5.21 Power Spectral densities of the <i>Euglena gracilis</i> images (Figure 5.20) under laser dark field microscopy over time (t = 1 to 7 s) before filtering.	164
Figure 5.22 Polar PSD of the <i>Euglena gracilis</i> images under laser dark field over time (t = 1 to 7 s) before filtering.	165
Figure 5.23 2-D representation of the polar PSD image of the <i>Euglena gracilis</i> under laser dark field microscopy (image at t = 1s).	166
Figure 5.24 Comparison of all the parameters of the PSD images before filtering.	167
Figure 5.25 Spatial domain analysis to perform counting without filtering.	168
Figure 5.26 The number of connected objects performed before any filtering.	169
Figure 5.27 Image convolution using standard Laplacian and Gaussian filters.	170
Figure 5.28 Image convolution for high pass filtering using MATLAB's special	171

functions.

Figure 5.29 Image convolution for low pass filtering using MATLAB's special functions.	172
Figure 5.30 Image convolution for band pass filtering using MATLAB's special functions.	173
Figure 5.31 Surface plots showing the effect of standard filters.	174
Figure 5.32 Comparison of the original image and the resultant images of convolution filters (from figures 5.28 to 5.31).	175
Figure 5.33 Comparison of the original (A series) and spatial domain filtered images (B series) over $t = 1, 2, 4, 7, 9, 11$ s respectively.	176
Figure 5.34 PSD images of <i>Euglena gracilis</i> after deconvolution filtering at different times ($t = 1$ to 11 s).	177
Figure 5.35 Comparison of polar PSD images before and after spatial filtering.	178
Figure 5.36 Comparison of all the parameters of the PSD images (Figure 5.24) after frequency domain filtering.	179
Figure 5.37 The number of connected objects (Figure 5.26) after spatial domain filtering.	180
Figure 5.38 Comparison of number of connected objects (spatial domain) and polar standard deviation of the PSD images (frequency domain) after filtering.	181
Figure 5.39 Magnified view of Figure 5.38 showing the comparison between number of connected objects and polar standard deviation of the PSD images.	182

List of abbreviations

List of abbreviations

Abbreviation	Expansion of abbreviation
<i>A. acidoterrestris</i>	<i>Alicyclobacillus acidoterrestris</i>
AVI	audio video interleave
B/W	black/white
BAW	bulk acoustic wave
BMP	bitmap
Ca	Calcium
CCD	charge coupled device
cfu	colony forming units
Cm	centimetre
CMOS	Complementary metal–oxide–semiconductor
dp	Decimal point
DNA	deoxyribonucleic acid
<i>E. coli</i>	<i>Escherichia coli</i>
<i>E. gracilis</i>	<i>Euglena gracilis</i>
ELISA	enzyme linked immunosorbent assay
FFC	Fountain flow™ cytometry
FIR	finite impulse response
FITS	flexible image transport system
FOBS	fiber optic biosensors
FOCS	fiber optic chemical sensors
FPS	frames per second
g	gram
GBRC	Glasgow biomedical research centre
h	hours
He-Ne Laser	helium – neon laser
Hz	Hertz
IBLS	Institute of biomedical and life sciences
IMS	immunomagnetic separation
LB	luria bertani
LTRS	Laser tweezers raman spectroscopy
Mg	Magnesium
µg	microgram
µl	microlitre
µm	micrometre

min	minutes
ml	millilitre
mW	milliwatts
NA	numerical aperture
NASA	National aeronautics and space administration
ND	neutral density
NIST	National institute of standards and technology
Nm	nanometre
NOST	NASA / science office of standards and technology
OD	optical density
PC	personal computer
PCR	polymerase chain reaction
PSD	power spectral density
PSF	point spread function
RGB	red green blue coding
s	seconds
<i>S. aureus</i>	<i>Staphylococcus aureus</i>
SAW	surface acoustic wave
SPR	surface Plasmon resonance
t	time
TV	television

List of symbols

List of symbols

Symbol	Meaning
$A(x1, t1),$ $A(x2, t2)$	Complex amplitudes of the speckle intensities detected at different position and time.
$\Gamma(x1, x2; t1, t2)$	Space-time varying autocorrelation function of the complex amplitude
ΔI	Intensity fluctuation
$X = x1 - x2$	Difference in position
$\tau = t1 - t2$	Difference in time
$\gamma_{\Delta}(X, \tau)$	Normalised space-time varying autocorrelation function of the intensity fluctuation while operating on Fresnel diffraction region under the Gaussian illumination (laser)
v	Velocity of the scattering particles
ω	Waist width of the beam
R	Distance between the diffusion plate and the observation plane
ρ	Wavefront curvature radius
λ	Wavelength of the laser beam
Tc	Time-varying autocorrelation width
Tc_{avg}	Average of the time-varying autocorrelation width (Tc) over a period of time
r	Average radius of the speckle grains
$J_1(r)$	Bessel function of the first order
$X_{(r,c)}$	Pixel value at r^{th} row and c^{th} column
N	Number of pixels in the image
\bar{X}	Average pixel intensity
σ	Standard deviation of the pixel intensity
σ_g	Gaussian standard deviation of the pixel intensity
r_g	Radius of the assumed cylindrical portion of the 3D Gaussian curve
$W(z)$	Multivalued function of a complex number z
R^2	Correlation coefficient to measure the reliability of the linear relationship between x and y values in the graph.
$y[r, c]$	The output of the convolved image with r rows and c columns
M	Width and height of the square image

Contents

Contents	Page
Acknowledgements	I
Abstract	II
List of Figures and Tables	V
List of abbreviations	XIII
List of symbols	XVI
Contents	XVIII

CHAPTER ONE: INTRODUCTION	1
1.1 Biological Techniques	4
1.1.1 Plate count	4
1.1.2 Enzyme linked immunosorbent assay (ELISA)	4
1.1.3 Polymerase chain reaction	5
1.2 Sensor Based Detection Techniques	5
1.2.1 Surface plasmon resonance (SPR)	5
1.2.2 Bulk acoustic wave (BAW) sensors	6
1.2.3 Surface acoustic wave (SAW) - love wave sensors	6
1.2.4 Fiber optic chemical sensors (FOCS), Fiber optic biosensors (FOBS)	6
1.2.5 Biosensing and monitoring of cell populations using the hydrogel bacterial microchip.	7
1.2.6 Porous silicon-based biosensor for bacterial detection	7
1.3 Light Scattering Techniques	7
1.3.1 Space-time varying correlation function	8
1.4. Aim of the Project	10

CHAPTER TWO: CALIBRATION TESTS FOR LINE SCAN SYSTEMS USING POLYSTYRENE MICROSPHERES AND STAPHYLOCCUS AUREUS SUSPENSION	13
2.1 Introduction	13
2.2 Materials and methods	13
2.2.1 Microscope slides and polystyrene microspheres	13
2.2.1.1 Microscope slide and cover slips	13

2.2.1.2 Polystyrene microspheres	13
2.2.1.3 Small dilution and inducing movements on microspheres	13
2.2.2 <i>Staphylococcus aureus</i> suspension	15
2.2.2.1 Quartz cuvette	15
2.2.2.2 <i>S. aureus</i> suspension for the speckle experiment	15
- LB broth preparation	15
- Preparation of overnight <i>S. aureus</i> culture	15
- Preparation of culture broth	15
- Centrifuging	16
- Washing	16
- Weighing the samples	16
2.2.2.3 Create different concentration by dilution	16
2.2.2.4 Optical density measurement	17
2.2.3 Hardware and optical setup	17
2.2.3.1 Setting up the laser beam and ND filters	17
2.2.3.2 Setting up the reflecting mirror	17
2.2.3.3 Setting up the Camera	17
2.2.3.4 Setting up the Incubator (only for the second experiment)	17
2.2.4 Speckle experiment setup	18
2.2.4.1 Control experiment for choosing the bandpass frequency	18
2.2.4.2 Experiment with microspheres and <i>S. aureus</i> suspension	18
2.3 Results and discussion	19
2.3.1 Data analysis and inference for 1 μm and 10 μm spheres	19
2.3.2 Data analysis and inference for <i>Staphylococcus aureus</i> suspension	20
2.4 Conclusion	23
CHAPTER THREE: LASER SPECKLE CHANGES DURING GROWTH OF <i>ESCHERICHIA COLI</i>	41
3.1 Introduction	41

3.2 Materials and methods	43
3.2.1 Sample preparation	45
3.2.1.1 LB broth preparation	45
3.2.1.2 <i>E. coli</i> culture preparation	45
3.2.1.3 Nutrient agar preparation	45
3.2.2 Hardware and optical setup	45
3.2.2.1 Setting up the laser beam and ND filters	45
3.2.2.2 Setting up the incubator	46
3.2.2.3 Setting up the reflecting mirror	46
3.2.2.4 Setting up the cuvettes	46
3.2.2.5 Setting up the camera	47
3.2.3. Software setup	47
3.2.4. Experimental setup	47
3.2.4.1 Trial experiment and choosing the band pass frequency range	47
3.2.4.2 Adding broth control specimen into the cuvette	47
3.2.4.3 Adding fresh <i>E. coli</i> culture to the cuvette	48
3.2.4.4 Sampling from reference cuvette	48
3.2.5 Speckle sampling	48
3.2.6 Third experiment	48
3.3 Results and discussions	49
3.4 Conclusions	53
CHAPTER 4 QUANTIFYING MORPHOLOGY DYNAMICS OF <i>EUGLENA GRACILIS</i>	69
4.1 Introduction	69
4.2 Materials and methods	70
4.2.1 <i>Euglena</i> and sample preparation	70
4.2.2 Microscopy and image capturing system	70
4.2.3 Visual assessment method	71
4.2.4 Measurement method	71
4.2.5 Image analysis method	71
4.2.5.1 Image conversion to bitmap format and RGB coding	72

4.2.5.2 Image adaptive high pass filtering	72
4.2.5.3 Image edge-detection filtering	73
4.2.6 Algorithm development	74
4.2.6.1 Average pixel intensity	75
4.2.6.2 Standard deviation of the pixel intensity	75
4.2.6.3 Gaussian standard deviation	75
4.2.6.4 Correlation analysis	76
4.3 Results and discussions	76
4.4 Conclusions and future scope	82
CHAPTER 5 POPULATION STATISTICS OF <i>EUGLENA GRACILIS</i>	133
5.1 Introduction	133
5.2 Materials and methods	135
5.2.1 <i>Euglena</i> culture preparation	135
5.2.2 Specimen slide preparation	136
5.2.3 Microscopy and image capturing system	136
5.2.4 Image analysis methods	137
5.2.5 Image convolution filtering	138
5.2.5.1 Standard convolution filters	139
<i>Laplacian filter</i>	139
<i>Gaussian filter</i>	140
5.2.5.2 Tailored convolution filters	140
<i>Lowpass filter</i>	141
<i>Highpass filter</i>	141
<i>Bandpass filter</i>	141
5.2.5.3 Deconvolution filters	141
<i>Normalize background intensity</i>	141
<i>Background subtraction</i>	142
<i>Choosing the point spread function</i>	142
<i>Deconvolution filtering</i>	142
<i>Full scale adaptive lowpass filter</i>	143
5.2.6 Algorithm development	143
5.2.6.1 Frequency domain analysis	143
<i>Average intensity</i>	144

<i>Intensity standard deviation</i>	144
<i>Gaussian standard deviation</i>	144
<i>Polar Standard deviation</i>	144
5.2.6.2 Spatial domain analysis	144
<i>Morphological opening operation</i>	144
<i>Contrast enhancement operation</i>	144
<i>Counting the number of connected objects</i>	145
5.3 Results and Discussions	145
5.3.1 Microscopy images	145
5.3.2 Image analysis without filtering	145
5.3.2.1 Frequency domain analysis	146
5.3.2.2 Spatial domain analysis	146
5.3.3 Image filtering	147
5.3.3.1 Convolution filters	147
5.3.3.2 Deconvolution filters	148
5.3.4 Image analysis after filtering	149
5.3.4.1 Frequency & spatial domain analysis	149
5.3.4.2 Spatial domain analysis	149
5.3.5 Selection of parameters	149
5.3.6 Inference	149
5.4 Conclusions	150
CHAPTER 6 CONCLUSIONS AND FUTURE WORK	183
REFERENCES	188
APPENDICES	201
APPENDIX A – Preparation methods for LB Broth medium to grow <i>E. coli</i> .	201
APPENDIX B – Preparation methods for Jaworski medium to grow <i>E. gracilis</i> .	202
APPENDIX C – Program to perform crosscorrelation between images using convolution	203
APPENDIX D – Program to perform convolution filtering with standard and special function filters.	204
APPENDIX E – Program to perform morphology opening operations, contrast enhancement and counting the number of connected objects.	211

CHAPTER 1 INTRODUCTION

Optical and microscopy based detection systems for analysing microorganism have been a subject of interest since Louis Pasteur and Robert Koch engaged in microscopy and the study of bacteria in 1880 (Clay and Court, 1975). Applications of microscopy detection systems include monitoring the quality of indoor air and potable water, detecting spoilage in the food industry, controlling contamination in fossil fuel and nuclear power plants, wastewater treatment plants and the detection of biological warfare agents, both on the battlefield and as a result of terrorist attacks (Zourob *et al.*, 2005).

Conventional methods for determining cell counts of bacteria and other microorganisms employ selective cultures and biochemical and serological characterization. Although these methods achieve sensitive and selective bacterial detection, the time required typically ranges from days to weeks to yield a result. There have been many advances in bacterial detection in recent years. Key developments in detection systems are collated in an excellent review by Hobson *et al.* (1997) and Deisingh and Thompson (2002). Reviews on electrophoresis (Suehiro *et al.*, 2003), acoustic (Howe and Harding, 2000) and optical methods of bacterial detection (Ivnitski *et al.*, 1999) are discussed at length by the researchers. But these sensors are expensive and require complicated deposition techniques. To replace the technology currently used, a cost effective, easily manufactured, and disposable technology is needed (Zourob *et al.*, 2005). Regardless of the area of application, there is an immediate need for the real-time detection of microorganisms. Increasing the rapidity of identification or characterising the behaviour of microorganisms will prove useful in identifying contaminants, which globally is an increasing problem.

Some specific examples of common bacterial hazards are as follows: *Escherichia coli* contamination of surfaces used for food preparation, urological catheters and industrial equipment; *Pseudomonas aeruginosa* contamination both in public water supplies and manufacturing applications and *Legionella* species in air conditioning units. (Malins *et al.*, 2004)

According to The Public Health Laboratory Service in the United Kingdom, there was a 600% increase in food poisoning notifications from 1982 to 2001 (Deisingh, 2003). It was

found that in the United States of America alone, 67 million cases of food-borne illnesses per year were associated with bacterial contamination of meat, poultry and eggs, and led to 4500 deaths. The economic impact of such food-borne illness was estimated as high as \$14 billion per year in the U.S. (Zourob *et al.*, 2005). US food laws do not require mandatory testing for all pathogenic bacteria and their toxins in food, and hence testing for these contaminants are not routinely performed on food products (Mathew and Alocilja, 2005). An epidemic surge of *E. coli* infections, due to either beef or water contamination, was observed in Australia, Africa, Canada, Japan, United States and in various European countries. In 1996, a significant epidemic of pathogenic *E.coli* was notified. *E.coli* infections affected about 6300 school children in Japan causing two deaths (Moll *et al.*, 2007).

In Ireland, an outbreak of *E. coli* O26 was reported in 1999 (McMaster *et al.*, 2001). Routine surveillance to detect *E. coli* in food, animals and the environment need to be introduced so that public health control measures can be implemented. Development of rapid diagnostics capable of detecting a wide range of *E. coli* serogroups associated with disease in humans is a priority (Moll *et al.*, 2007).

Perishable fruits and vegetables are two of the most important of all food categories in combating malnutrition diseases in the developing world. Losses occur at all levels of the post-harvest system, during pre-processing, transportation, storage, processing, packaging and marketing. There is an immediate need for monitoring these losses (Pajuelo *et al.*, 2003) and identifying sources of contamination.

The presence of viable *E. coli* in foodstuffs indicates unsanitary handling procedures, a process failure, post-process contamination, or cross-contamination with another product. Thus, rapid detection of *E. coli* or faecal contamination is important to the food industry to ensure the safety of the food supply (Mathew and Alocilja, 2005).

A survey by the National Food Processors Association (NFPA) in 1998 showed that large scale fruit juice spoilage was associated with a spore-forming microorganism. Results of the survey indicated that 35% of the fruit juice manufacturers could not visibly identify the spoilage but the tests confirmed the growth of acidophilic spore-formers (Bahceci and Acar, 2007).

In the 1980s, an acidophilic *Bacillus* species was isolated from apple juice and identified as a new type of spoilage bacterium. *Alicyclobacillus acidoterrestris* is a spore-forming organism that resists high temperatures and acidic environments. It has become an important potential spoilage concern for fresh fruit and vegetable juices (Bahceci and Acar, 2007). A small number of viable organisms have the potential to contaminate large volumes of juice resulting in severe financial losses for the producers. It was found that either fresh or pasteurized drinks were the most susceptible to these spoilages. Research shows that spoilage by *A. acidoterrestris* is difficult to detect (Bahceci and Acar, 2007).

The need for rapid detection of microorganisms is not restricted to the food industry, identifying potential pathogens is the subject of research in wide range of areas such as: bioterrorism, dental carries and varied human diseases.

Deliberate exposure of the public to anthrax spores at various sites in the USA has increased international concern regarding bioterrorism. The development of effective and efficient devices capable of rapid, accurate, sensitive, cost-effective and specific detection of biological agents is needed in response to these threats (Zourob *et al.*, 2005).

The bacterial content in human saliva is estimated to approach 10^9 bacteria per millilitre. Although saliva can act as a selective medium for bacterial growth, repeated swallowing results in clearing of bacteria (Bowen, 1996). Dental caries is a bacterial disease which is characterized by the demineralization of the inorganic portion and the destruction of the organic substance of the tooth (Tanzer, 1992). An investigation conducted on 235 children, aged 11/12 years with zero or moderate caries suggests that salivary tests can reduce the risk (Kneist *et al.*, 1998) as early identification of this disease enables dental professionals to formulate and incorporate preventive treatment plans for such patients. Earlier studies had shown that bacteria such as *Streptococcus mutans* and *Lactobacilli* at 10^5 Colony Forming Units (CFU) per ml are predictors of caries risk (Kneist *et al.*, 1998). It was found that *Streptococcus mutans* exists in saliva (Duchin and van Houte, 1978; Bowen, 1996; Gronroos, 2000). Earlier experiments with gnotobiotic animals have revealed that *streptococci* are the main microorganisms in dental caries (Fitzgerald and Keyes, 1960). A quantitative measure of *Streptococcus* is said to be a reliable measure to predict true caries activity (Alaluusua *et al.*, 1984, 1987; Kohler *et al.*, 1984, 1988) (Kishen *et al.*, 2003).

E. coli O157 was initially implicated in human disease in 1982 (Riley *et al.*, 1983) and since then the reported incidence of verocytotoxigenic *E. coli* (VTEC) related illness has increased worldwide (Tarr and Neill, 1996). This strain rapidly causes diarrhoeas, renal insufficiency, and sometimes death (Moll *et al.*, 2007).

From the above examples, it can be seen that it is imperative to detect pathogens at very low concentrations according to the latest European and worldwide standards, in multiple fields such as the environment, food safety or even the military sector. There have been many advances in microbial detection in recent years, towards more accurate and simpler processes. Some of these techniques are now reviewed before explaining the detection system researched in this thesis. The difficulties in developing real time detection systems come, in part, from strict requirements for sensitivity, specificity and response time.

1.1 BIOLOGICAL TECHNIQUES FOR DETECTION OF MICROORGANISMS

1.1.1 Plate count

The procedure involves the serial dilution of the liquid sample or suspensions of the test material e.g. with sterile water, to give a range of concentrations typically from 10^{-4} to 10^{-8} . The dilutions are mixed thoroughly before each dilution to ensure that microbial clumps are dispersed. Different pipettes are used for each dilution to avoid contamination. Typically 100 μ L samples of each dilution are then transferred to an empty sterile petri dish and agar, cooled to 50°C, is added. The plates are swirled to mix the inoculum and the agar, they are then incubated for 24-48 hours. Plates containing between 30 and 300 colony forming units (CFU) are selected and the CFU are counted. From this count the viable population of the original sample can be calculated (Miles and Misra, 1938).

1.1.2 Enzyme linked immunosorbent assay (ELISA)

The ELISA has been used as a diagnostic tool in medicine and plant pathology, as well as a quality control check in various industries (Lequin, 2005). In ELISA, an unknown amount of a substance that stimulates an immune response in the body (termed as antigen e.g. a microorganism contains many antigens) is fixed to a surface. This surface is then washed over by an antibody specific to that antigen which is linked to an enzyme. In the final step, the enzyme substrate is added to this surface, which the enzyme can convert to a detectable signal. In the case of a fluorescence ELISA, when light is shone upon this sample, any

antigen/antibody complexes will show fluorescence from which the amount of antigen in the sample can be measured (Lequin, 2005).

1.1.3 Polymerase chain reaction

The genetic material of each living organism possesses sequences of nucleotide building blocks that are unique and specific to that particular species. These unique variations create the possibility to trace genetic material back to its origin or identifying with accuracy the species of organism it came from, and often the particular strain of that species. Polymerases are enzymes that are present in all living things, and their job is to copy genetic material, to proof read and correct the copies if required. Polymerase Chain Reaction (PCR) is sometimes referred to as "molecular photocopying". It can work on extremely complex mixtures by characterizing, duplicating and analysing even a particular bit of genetic material from blood, hair, or tissue specimens, from microbes, animals, or plants that can possibly be thousands or even millions of years old. Thus PCR can be a useful tool for identifying the species of microorganism (Powledge, 2004).

Though plate counting, ELISA and PCR are very useful in certain situations, they usually also require enrichment, isolation, morphological examination, biochemical and serological testing to positively identify microorganisms. These techniques may take a long time to obtain reliable information.

1.2 SENSOR-BASED DETECTION TECHNIQUES

Many research efforts have been directed towards the development of effective instrumental methods for the detection of microorganisms. A few sensor-based detection techniques are described briefly below. Several alternative techniques have been employed for the detection of bacterial pathogens including, for instance, surface plasmon resonance (SPR) or bulk acoustic wave (BAW) sensors.

1.2.1 Surface plasmon resonance (SPR)

Microbiologists use SPR techniques to detect organisms by identifying the DNA or protein sequences in the molecules. This is done by adsorption of the target molecule or microorganism to a particular metal surface and then measuring the variations in the local refractive index. However, recent studies by Taylor *et al.* (2005) and Subramanian *et al.*

(2006) have highlighted a limit of detection of 10^6 untreated *E. coli* bacteria/ml using antibody based bacterial immobilisation with SPR biosensors

1.2.2 Bulk acoustic wave (BAW) sensors

BAW sensors are used to detect the changes in the physical properties of the species (membrane) that are wrapped around a piezoelectric resonator by monitoring the frequency shift of an oscillator. The adsorption or absorption of chemical species from either the gas or liquid phase affects the resonance frequency of the BAW structure, which helps to detect the changes in the physical properties. However, it was found that there is a limit of detection of 10^2 *E. coli* bacteria/ml with an extended sampling time of 15 h using the BAW technique (Moll *et al.*, 2007).

1.2.3 Surface acoustic wave (SAW) - Love wave sensors

Surface acoustic waves propagate in three directions and can be classified as longitudinal wave motion, normal waves or shear horizontal waves. A class of shear horizontal [SH] waves are called Love waves (Zimmermann *et al.*, 2001) which are propagated in layered devices that concentrate the wave energy in a highly confined region near to the surface. Research studies on Love acoustic wave sensors focus on techniques involving several antibodies to detect biological species by permitting bacterial immobilisation on the sensor surface (Moll *et al.*, 2007). Tamarin *et al.* (2003) managed to detect bacteriophages using antibody/antigen interactions on a Love wave sensor.

1.2.4 Fiber optic chemical sensors (FOCS), Fiber optic biosensors (FOBS)

The recent availability of high quality and inexpensive optical fibers has led to the development of chemical sensors called fiber optic chemical sensors (FOCS) (Lewis and Griffiths, 1996). A chemical sensor is a device that is used to measure the concentration or the activity of a chemical species in a sample of interest. The optical method of detecting transferred genetic material from one cell to another by bacteriophage allows a wide variety of chemical detection schemes that were not previously possible (John *et al.*, 1999). The fiber optic biosensor (FOBS) is a modified fiber optic chemical sensor (FOCS). The biosensor utilizes the fiber optic evanescent wave spectroscopy to monitor a bacterial mediated biochemical reaction. Fiber optic biosensors (FOBS) have been developed to monitor *Streptococcus* mutants' activity in human saliva, allowing rapid and quantitative measurement (Kishen *et al.*, 2003).

1.2.5 Biosensing and monitoring of cell populations using the hydrogel bacterial microchip.

A hydrogel microchip containing live bacteria was developed which enables monitoring of bacterial metabolism using a fluorescent stain and to exploit biosensing abilities of the cells. This technique has a limitation in that it cannot be applied to any specific bacterial strain (Fesenko *et al.*, 2005).

1.2.6 Porous silicon-based biosensor for bacterial detection

Porous silicon has recently been investigated as a potential platform for biosensor applications. *E. coli* produces an enzyme called β -D-galactosidase as a part of its metabolic process. A chemiluminescent reaction was reported between the dioxetane substrate and the β -D-galactosidase enzyme produced by *E. coli* during its growth (Schaap *et al.*, 1991). Using porous silicon platform during the chemiluminescent reaction would yield higher light emission than a planar silicon platform. This process has resulted in porous silicon sensors capable of detecting penicillin, alkali metal ions, humidity, and hydrocarbons. Here silicon was anodized electrochemically in Teflon containing ethanoic hydrofluoric acid solution to produce porous layer of silicon. The use of porous silicon as a biosensor platform has been reported for detecting only a few pathogens (Mathew and Alocilja., 2005).

1.3 LIGHT SCATTERING TECHNIQUES

Coherent (laser) light scattered from moving objects or particles produces intensity fluctuations that can be used to provide meaningful results about the sample constituents (Briers, 1996). Laser speckle is an optical interference effect that can be observed when objects are illuminated with laser light. It has a grainy appearance, “light” speckle is caused by constructive interference and “dark” speckle caused by destructive interference of scattered laser light. This is also due to movement in the scattering centres, changes in optical path length due to variations in the refractive index, changes in the configuration, or a combination of these factors. The speckle phenomenon has been extensively used in many applications in non-destructive testing. In other words, the phenomenon of dynamic speckle is observed when the sample illuminated with coherent light changes its properties. These situations usually occur in samples with biological activity but are also present in

some non-biological situations such as drying of coatings and paints, vibration, etc. (Arizaga *et al.*., 2002).

Biospeckle laser technology has been proposed as a powerful tool to obtain information from biological material by Briers (1975, 1993), Asakura and Takai (1981), Oulamara *et al.* (1989), Xu *et al.* (1995) and Ross *et al.* (1983). The name biospeckle is a derivation of the term ‘dynamic speckle’, in accordance with Asakura and Takai (1981), which is also referred to as ‘speckle fluctuations’ by Briers (1993) and Ross *et al.* (1983). It results from rapid changes in the laser interference pattern caused by microscopic changes due to cell activity in living material. Inert material will show no speckle changes. Biospeckle therefore offers a relatively easy method of measuring the level of biological activity in samples.

The dynamic speckle phenomenon has been used extensively in both medical and engineering applications. It is importantly used for measuring blood flow in the retina and other tissues (Cheng *et al.*, 2003), (Kalchenko *et al.*, 2007) blood platelet measurements (Piederriere *et al.*, 2004), clinical assessment and diagnosis (Briers, 2001). It has also been used to understand motion of particles within botanical samples like tomatoes, oranges and apples (Zhao *et al.*, 1997, (Briers, 2001), Braga Jr *et al.*, 2007) to model the impact on fruits (Pajuelo *et al.*, 2003), to relate to the theory of sound propagation in fluids (Mountain, 1966), in speckle shearography to provide surface strain data from non-planar surfaces (Francis *et al.*, 2007) and the deformation field of strains and displacements (Cheng *et al.*, 2002), to determine the surface roughness of dielectric or metallic surfaces (Gale *et al.*, 2004) and to design an optical computer mouse (Popov *et al.*, 2004).

Because of its varied application on different biological or non-biological surfaces, a complete theoretical analysis of a laser speckle system is very difficult. The experiments have been developed based on the fundamental derivation from the space-time varying correlation function described below.

1.3.1 Space-time varying correlation function

A space-time autocorrelation function of the complex amplitude can be expressed by the equation

$$\Gamma(x1, x2; t1, t2) = (A(x1, t1) * A(x2, t2)) \quad (1.1)$$

Where $A(x1, t1)$ and $A(x2, t2)$ are the complex amplitudes of the speckle intensities detected at a different position and time, respectively. According to optical diffraction theory (Zheng *et al.*, 1994), while using a Gaussian illumination (laser) and operating on Fresnel diffraction region, the autocorrelation function can be represented as

$$\gamma_{\Delta}(X, \tau) = \exp\left(-\frac{|v^2|\tau^2}{|\omega^2|}\right) \exp\left(\frac{-\pi^2 \omega^2}{\lambda^2 R^2} |X - \sigma v \tau|^2\right) \quad (1.2)$$

where $X = x1 - x2$, $\tau = t1 - t2$, ω is the waist width of the laser beam, v is velocity, λ is wavelength, and $\sigma = (R/\rho) + 1$, which is related to the ratio between the distance R from the specimen surface to the wavefront observation plane where the camera setup was made and ρ being the wavefront radius of curvature. Thus, Eq. (1.2) can be easily separated into two functions. By setting $\tau = 0$, the first function, a normalized space-varying autocorrelation function is obtained

$$\gamma_{\Delta}(X, 0) = \exp\left(\frac{-|X|^2}{\Delta x^2}\right) \quad (1.3)$$

$$\text{Where } \Delta x = \frac{\lambda R}{\pi \omega} \quad (1.4)$$

Similarly, setting $X = 0$, the second function, a normalized time-varying autocorrelation function is obtained.

$$\gamma_{\Delta}(0, \tau) = \exp\left(\frac{-\tau^2}{T_c^2}\right) \quad (1.5)$$

From Eq. (1.2) the time-varying autocorrelation width T_c , is defined as

$$T_c = \frac{1}{|v|} \left(\frac{1}{w^2} + \frac{\sigma^2}{\Delta x^2}\right)^{-\frac{1}{2}} \quad (1.6)$$

Finally, as seen from Eq. (1.6), T_c is inversely proportional to the absolute value of the velocity of the moving speckle grains (moving microorganisms or polystyrene microspheres) and the proportionality constant is also related to the average size of the speckle grains, λx . If T_c is high then the correlation between samples is large and therefore little motility is observed. On the other hand, if T_c is low then there exists vigorous motion in the scattering centres.

1.4. AIM OF THE PROJECT

It is seen that from the previous discussions that there is an immediate need for detection of microorganism that can find application in varied industries. This Chapter briefly reviewed the needs of the food industry, bioterrorism and medicine and gave a brief introduction to microbial detection techniques based on biological based methods, sensors and light scattering methods (see section 1.1, 1.2 and 1.3). In general, biological methods have a slow responsivity, possibly requiring minutes to many hours for reliable identification of the microorganisms. Often, they require some form of amplification of the sample such as with PCR. The sensor methods generally require development of sophisticated microelectronics and detectors for operation. Light based methods, however, are relatively simple to fabricate, are non-destructive and possibly have a rapid response time, even yielding information in real time, they therefore offer significant advantage over these other methods and are worthy of detailed study. The purpose of this research was to investigate the potential of using laser speckle based optical systems and image processing to detect and characterise microorganisms both at the individual cell level and for larger populations of microorganisms. The systems generally comprise the delivery of the light to the sample under investigation and a detection system of the scattered light after it has passed through the sample. The data was collected and subsequently processed using image processing techniques in the time and space domains.

The first part of the thesis (Chapters 2 and 3) are based on line scan systems and the second part (Chapters 4 and 5) are based on imaging systems. Laser based microscopy systems were also developed to characterise individual microorganisms. This project focuses mainly on extracting meaningful information from large volumes of data collected under these scanning or imaging systems.

In Chapter 2 an attempt was made to establish proper controls for the speckle experiments that principally involve the space-time varying correlation function. An inert medium of polystyrene micro-spheres and non-vegetative *Staphylococcus aureus* bacterial suspension were used as controls and the correlation function was successfully calculated using a line scan imaging system. Effects of dilution, mechanical stirring and sedimentation were investigated. This Chapter provided some basis for assessing the effects of motile microorganisms on the space-time varying correlation function, as described in Chapter 3.

Normally, faecal coliforms, particularly *Escherichia coli*, are often used as indicator organism to satisfy the microbiological criteria for food safety to indicate the possibility of a microbial infection (Mathew and Alocilja, 2005). Consequently, *E. coli* was chosen as one of the organisms for testing because of its motility and its indicator status. A calibration experiment was also performed. A line scan system was used, identical to that described Chapter 2. The effect of motility of *E. coli* on the space-time varying autocorrelation function was investigated along with cell concentration. Two transmission modes were used where the laser beam was either passed either vertically or horizontally through the sample.

In Chapter 4 a bright field microscopy system and image processing techniques were used to assess the morphological changes of single *Euglena gracilis* cells, using a high objective lens. This organism is relatively large and provided a useful model to develop and assess the performance of different processing methodologies under these microscopy conditions. Video was taken of the cell and individual frames were analysed to extract information on the external shape and internal structure of the cell as a function of time. Data was collected during the life cycle of the cell and methods were developed to identify its death phase.

Chapter 5 extends the morphological analysis of single cellular studies from Chapter 4 to population studies, where a low objective lens was used on a laser based dark field microscopy system. Images were also captured under phase contrast microscopy for visual assessment of the cells. Population statistics were gathered over time, and analysed using image processing techniques. The images were analysed in the Fourier and spatial domain. Different filters available from Matlab were used and specific filters were developed. This included background subtraction, deconvolution and adaptive low pass filtration. Four parameters were calculated in the Fourier plane to assess intensity information in the

images over time in an attempt to identify changes in the population numbers. These included: polar, Cartesian, Gaussian and the average intensity standard deviations. A Matlab program was written to count the number of connected cells in the spatial plane to estimate the cell concentration as a function of time. These two methods were compared.

Chapter 6 concludes the results from all of the experiments and suggests future work. Following the References, Matlab programs are included in the Appendices along with recipes for making LB broth for growing *E. coli* and *S. aureus* and Jaworski's medium for growing *Euglena gracilis*.

CHAPTER 2 CALIBRATION TESTS FOR LINE SCAN SYSTEMS

2.1 INTRODUCTION

Before performing experiments with live *E. coli* cells, it was important to establish proper controls using inert particles like polystyrene microspheres and suspension of pellets derived from less motile organisms such as *Staphylococcus aureus*. This chapter describes the calibration of the system, and the results from investigating the effects of dilution, concentration, ability to detect motility, Brownian motion and sedimentation through the system. The first experiment was a speckle study done on inert microspheres and the second experiment was also a speckle study done on a *S. aureus* suspension. The objective of the first experiment was to establish the controls and speckle measurement parameters and the second experiment was done to test and verify these established parameters inside an incubator under different dilutions and further to determine the sensitivity of the system with mechanical stirring and sedimentation over a period of time. Both the experiments in this chapter prove to be a useful calibration method for experimenting with motile organisms such as *E. coli* (See Chapter 3).

In the first experiment the spatially and temporally varying autocorrelation function of diluted and undiluted samples was studied. In the second experiment in addition to dilution, the effect of mechanical stirring and sedimentation was also studied. Also in the second experiment a concentrated *S. aureus* culture (around 400 ml) that was centrifuged into pellets (Section 2.2.2.2) was used. In order to study the effect of mechanical stirring, a sterile stirrer was used to mix the solution in the cuvette for about 3 min and its effect on the pellet suspension for another 29 min was studied using the time-varying autocorrelation parameter (T_c). In order to study the effect of sedimentation, the specimen was allowed to sediment for a period of 40 min and the difference before and after sedimentation was pictorially estimated by monitoring the spread of the spatially-varying autocorrelation curve from the X-axis.

2.2 MATERIALS AND METHODS

2.2.1 Microscope slides and polystyrene microspheres

2.2.1.1 Microscope slide and cover slips

The experiments relating to the polystyrene microspheres were performed on low iron microscope slides (BDH, Poole, UK). The plain micro slides of standard dimension 76 x 26 x 0.8 and 1.0 mm thick were used. The microscopic slide must be clean before use. It was first washed with diluted ethyl alcohol, wiped and dried using a tissue paper. For some of the specimens, an 18 mm² borosilicate coverglass or coverslip (BDH, Poole, UK) was used.

2.2.1.2 Polystyrene microspheres

Two different polystyrene microspheres (Duke Scientific Corporation, California, and USA) with nominal diameters of 1.0 μm and 10.0 μm were used. The NIST (National Institute of Standards and Technology) traceable diameter for 1.0 μm spheres was found to be $0.993 \pm 0.021 \mu\text{m}$ and that for 10.0 μm was $10.03 \pm 0.05 \mu\text{m}$. There were approximately 10^9 counts per ml for the 1.0 μm spheres and 10^6 counts per ml for the 10.0 μm spheres.

2.2.1.3 Small dilution and inducing movements on microspheres

The 1.0 μm and 10.0 μm microspheres in this system were used to understand its sensitivity for small changes in dilution and the influence of transient conditions. Therefore, a very small volume (10 μL) of the spheres was used and only 2 μL of distilled water was used for dilution studies. In order to induce varying transient conditions among the microspheres, a coverslip was simply placed over them. To start with about 10 μL of 1 μm spheres (10^9 counts per ml) were applied onto the microscopic slide using a micropipette. This was the specimen for the speckle experiment to be explained later in this chapter (section 2.2.4.2). At the end of this experiment, 2 μL of sterile distilled water was added to the microspheres and the speckle experiment was repeated again. After this, a cover slip was applied over the specimen and again the speckle data was collected for the same length of time. The same procedure was repeated for 10 μm polystyrene microspheres.

2.2.2 *Staphylococcus aureus* suspension

2.2.2.1 Quartz cuvette

In spectroscopic studies, quartz cuvettes are often used because of their high degree of well known parallelism and optical properties. They also eliminate radiation pathlength error when absorbance measurements are performed (Mavrodineanu and Lazar, 1973). A Quartz cuvette with the dimension 6 cm x 2 cm x 8 cm was therefore employed in this system.

2.2.2.2 *S. aureus* suspension for the speckle experiment

- LB broth preparation

LB (Luria Bertani) broth has been a widely used rich medium among bacteriologists because it permits fast growth and good growth yields for many species such as *Staphylococcus aureus* (Hoffman *et al.*, 2006) and *Escherichia coli* (Sezonov *et al.*, 2007). It is prepared by adding a few ingredients like tryptone, yeast extract, sodium chloride and distilled water. In the following work, LB broth was used in large volume (400 ml) to provide a concentrated culture of *S. aureus*.

- Preparation of overnight *S. aureus* culture

Staphylococcus aureus was kindly supplied by Dr. Roger Parton, Division of Infection and Immunity, IBLS, University of Glasgow. On the first day, a fresh streak of *Staphylococcus aureus* culture was maintained on a nutrient agar slope in a universal bottle and incubated overnight at 37° C. On the second day, 1 ml of LB broth was added to the overnight slope culture. This was mixed thoroughly and transferred into another universal bottle containing 4 ml of LB broth, and incubated overnight at 37° C.

- Preparation of culture broth

On the third day, 5 ml of the overnight culture was added to a baffled conical flask (2L) containing 400 ml of LB broth. The broth was shaken and incubated for 24 hours at 37°C. The plates were counted for their colonies the next day and were found to provide 6×10^7 cfu per ml.

- Centrifuging

It is important to separate the *S. aureus* culture from LB broth to provide a non-growing suspension. Therefore the large volume culture was placed in a centrifuge (Sorvall RC-5B refrigerated superspeed machine). Two centrifuge bottles (500 ml capacity) were used, one for *S. aureus* culture broth (400 ml) and other filled with distilled water (400 ml) for balancing. Centrifuging was done at 10,000 rpm for 20 min at a maximum temperature of 10°C and a minimum temperature of 4°C. After 20 min, a pellet had accumulated at the corner of the flask.

- Washing

The LB broth after centrifuging was transferred carefully removed without disturbing the pellet sediment. Around 5 ml of distilled water was added to the pellet, mixed thoroughly and transferred to a 20 ml centrifuge tubes. 5 ml of distilled water was filled into another centrifuge flask for balancing. The flasks were again centrifuged for 20 min at 10,000 rpm. This procedure was repeated again by centrifuging the pellet with 5 ml distilled water to ensure a thorough wash.

- Weighing the samples

The excess water after centrifuging was poured out and the bottle was weighed as W1. A micropipette was used to mix and transfer the pellets to a 5 ml universal bottle. The weight of this empty bottle was W2. The quantity of pellets = W1-W2. For this experiment, W1 = 18.3 g; W2 = 16.3 g; Thus the culture prepared from 400 ml of LB broth incubated at 37°C for 24 hrs after spinning three times gave 2.0 gram of *staphylococcus* pellets. 2.0 g of pellets is approximately the same as the weight provided by 2.4×10^{10} counts for 400 ml culture (as the initial concentration was found to be 6×10^7 cfu per ml).

2.2.2.3 Create different concentration by dilution

25 ml of sterile distilled water was added to flask 1 containing 2.0 grams of the pellet. This was considered to be a neat solution and would contain 2.4×10^{10} colonies for the total amount of solution in the flask (25 ml + 2.0 g of pellets). Thus the neat solution would contain 8.88×10^8 cfu per ml. Around 2.5 ml of this solution was added to a flask containing 22.5ml of distilled water (flask 2). This is now a dilution of 1 in 10. 2.5 ml of this diluted solution was added to a flask containing 22.5ml of water (flask 3). This is now a dilution of 1 in 100. This procedure was followed until a 1 in 10^6 dilution was achieved.

2.2.2.4 Optical density measurement

Optical density (OD) in this context is a measure of the amount of light absorbed by a suspension of bacterial cells or a solution of organic molecules. It is used to determine the concentration of bacteria in suspension and to gauge the purity and concentration of molecules (Davies, 2005). Colourimeters or spectrophotometers can be used to determine the optical density. A spectrophotometer was employed in this application and was aimed to compare the sensitivity of speckle methods compared to OD photometers.

2.2.3 Hardware and optical setup

2.2.3.1 Setting up the laser beam and ND filters

The beam from a low power (632.8nm, 2.45 mW) He-Ne laser (Spectra Physics Inc, California,USA) was passed through neutral density (ND) filters to reduce the incident power and avoid saturation of the camera.

2.2.3.2 Setting up the reflecting mirror

A reflecting mirror was kept at 45° so that the vertical beam was reflected into the horizontal plane and directed towards the specimen, see **Figures 2.1 and 2.2**

2.2.3.3 Setting up the Camera

A CCD camera (YD 66, 2.3 mega pixels, B/W surveillance camera, Taiwan) was positioned to capture the beam reflected by the reflecting mirror. The camera was placed right in front of glass door of the incubator and is shown in Figures 2.1 and 2.2. A line-scan from the camera was captured via an oscilloscope (Lecroy, Switzerland) and transferred to a PC for analysis. In the experiments with microspheres, the beam travelled the depth of the microscopic slide or cuvette and the data collected contained information relating to the integrated profile of the microspheres. In the experiments with *Staphylococcus aureus*, the collected data provided information relating to the integrated profile of the bacterial suspension (inert organism) in the cuvette.

2.2.3.4 Setting up the incubator (only for the second experiment)

It was important to conduct the control experiments and experiments in later chapters under the same ambient temperature. For the experiments in chapter 3, an incubator was used for the growth of the culture. In the preliminary control experiments on *S. aureus* suspension

discussed in this chapter, the same incubator and temperature was used. A hole (30 mm diameter) was drilled into the top of the incubator allowing the laser beam to enter into the incubator beneath which was placed the sample. Once the setup was complete, the incubator was maintained at 37°C through the duration of the experiments.

2.2.4 Speckle experiment setup

2.2.4.1 Control experiment for choosing the bandpass frequency

Around 25 ml of distilled water was added to a cuvette and the trial experiment was run for 30 min. The optimum band-pass frequency range that gave the best results was chosen. From various experiments it was found that a frequency range about 0-10 Hz was associated with a Gaussian frequency and 4000-5500 Hz was associated with the electrical noise and optical aberrations. Thus it was found experimentally that a band pass frequency range of 10-4000 Hz gave the optimal signal output.

2.2.4.2 Experiment with microspheres and *S. aureus* suspension

A 2.45 mW low power He-Ne laser was allowed to pass into the sample (See Figure 2.1 and 2.2) through the reflecting mirror. The beam traversed directly through the microscope slide containing the microsphere specimen during the first experiment and traversed through the incubator into the cuvette containing *S. aureus* suspension during the second experiment. The resultant beam was captured using a CCD TV camera (as mentioned in section 2.2.3.3) which was connected to the oscilloscope. Proprietary software was written to capture the data from the oscilloscope and write the data to an excel file. The data found included the mean voltage, standard deviation, integral of the power density and auto correlation. The proprietary software was written in Borland C⁺⁺. In addition, various Fourier functions, the autocorrelation and frequency spectrum were plotted.

To determine the instantaneous speckle changes between each pixel, a large number of samples were taken for analysis from 1 to 30 min intervals. The line scan was performed at a rate of 25 samples per min and with each sample 1024 pixels available from the single TV line was investigated. 1024 pixels were investigated to identify the relationship between the specimen properties with the autocorrelation and power spectral density, whilst at the same time reducing the data set. The software delay between each sample was

normally set to 40 μsec to enable the computer processor to multiplex between data capturing and the file saving.

2.3 RESULTS AND DISCUSSION

2.3.1 Data analysis and inference for 1 μm and 10 μm spheres

From equation (1.6) in section 1.3.1, it is clear that if the motility is high for the scatterers, the time-varying autocorrelation width (T_c) value would be less and vice versa. $T_{c_{\text{avg}}}$ represents the average of the time-varying autocorrelation width (T_c) over a period of 15 min and equation (1.6) also holds good for $T_{c_{\text{avg}}}$ values. **Figure 2.4** shows the results from four different specimens that were prepared from 1 μm and 10 μm spheres. The first set of histograms represent the plain slide, second the undiluted spheres (pure); third the diluted spheres (1 in 10) and the final one with a cover slip over the diluted sphere sample. The microspheres are basically inert and it is expected that such samples have a higher value of $T_{c_{\text{avg}}}$ than the diluted sample, where the spheres are able to move more freely because of the less dense suspending medium. A cover slip was placed over the fourth sample. It was observed that the velocity of scattering centres increased. It was assumed that this was due to lateral forces induced in the medium by the weight of the cover slip. From Figure 2.4, the neat suspension of 10 μm spheres show higher $T_{c_{\text{avg}}}$ values than the neat 1 μm spheres. As mentioned in section 2.2.4.2 around 25 samples were collected over a minute and the $T_{c_{\text{avg}}}$ of these values shown below are accurate to 3 dp. $T_{c_{\text{avg}}}$ went up to a maximum of 71.333 units for 10 μm spheres, whereas a value of 45.670 units was observed for the 1 μm spheres. This is because the heavier the sphere, the slower the motility because of viscosity, gravity and Brownian movement. The effect of dilution on 1 μm spheres was to reduce $T_{c_{\text{avg}}}$ value to 42.316 ± 0.276 from 45.667 ± 0.271 . By applying a cover slip, the velocity of the microspheres within the diluted medium increased and thus as indicated in equation (1.6), it reduced the $T_{c_{\text{avg}}}$ value from 42.316 ± 0.276 to 12.500. The effect of dilution on the 10 μm spheres produced a great variation in $T_{c_{\text{avg}}}$ than that of the 1 μm spheres. The value of $T_{c_{\text{avg}}}$ dropped from 71.333 to 46.220 showing the effect of water as the suspending medium facilitating their movement. Further, the value reduced to 30.230 after applying the cover slip. This demonstrates the effect of $T_{c_{\text{avg}}}$ on motility variation in the case of inert microspheres influenced only by concentration and size.

Figure 2.5 shows the comparison of the spatially-varying autocorrelation on undiluted and diluted 10 μm spheres over a single TV line consisting of 1024 pixels. The neat suspension of microspheres is supposed to have a higher concentration than the diluted one. From optical diffraction theory, one small particle (or microorganism) illuminated by a laser beam produces a diffraction pattern with an approximate intensity distribution of $\{[2J_1(r)/r]\}^2$, where $J_1(r)$ is the Bessel function of the first order. When more particles (or microorganisms) distribute inside the illuminating volume randomly, more coherent diffraction patterns are created. In general, the original diffraction pattern of $\{[2J_1(r)/r]\}^2$ breaks into more sections and creates a complicated structure consisting of many small and irregular spots. The bright area is then reduced. In this case, the bright spots in the undiluted sample are less and so its intensity amplitude is also lower than the diluted ones. Figure 2.5 shows that the higher the concentration of the culture, the smaller the bright speckles and the sharper the autocorrelation peak. Moreover the spatial curve tendency towards the X-axis indicates the presence of many small and irregular spots and higher concentration of the sample and vice versa. It is to be noted that dilution involved here is very small and the spatial curves are still sufficiently sensitive to determine the change in concentration. This technique may provide an auxiliary method for detection of the growth of microorganisms.

2.3.2 Data analysis and inference for *Staphylococcus aureus* suspension

Figure 2.6 shows the variation of $T_{c_{avg}}$ for serial dilutions of *Staphylococcus aureus* suspension. The autocorrelation width values dropped from 40 ± 4 to 30 ± 4 for the 10^{-1} dilution and reduced to 10 ± 4 for 10^{-4} dilution. $T_{c_{avg}}$ increased above this value for further dilutions, possibly indicating a limit to the resolution of the system. Interestingly **Table 2.1** shows the values from the optical density measurements for the same samples. It is seen the spectrophotometer cannot determine the concentration for a neat and 10^{-1} diluted suspension. The photometer also did not register any measurement for dilutions $\geq 10^{-4}$. This indicates that the sensitivity of the speckle system in this application may be better than that of the spectrophotometer.

Figure 2.7 shows the effect of different dilutions (from neat down to 10^{-6}) on Tc plotted over a period of 25 min. There was no correlation observed between Tc and concentration, probably because the sample was a non-motile organism. The value of Tc was most likely

dominated by sedimentation and Brownian movement of the cells. Further more, each sample measurement involved the replacement or reuse of the same cuvette, thereby adding indeterminate variables to the experiment. Interestingly, the absolute value of the differential between the standard deviations for each dilution is relatively linear ($R^2=0.90251$) with increasing dilution, see **Figure 2.8**. It would be interesting therefore to study the relationship of Tc over the different dilutions with the same cuvette. The graph that follows the same data for the neat solution and each dilution, plotted over different scales. This was done in an attempt to determine possible relationships between Tc and the concentration over time.

Figure 2.9 shows the variation of autocorrelation width over a time period of 25 min for the neat sample (2.4×10^{10} cfu/ml) of *S. aureus* suspension. It was found that the autocorrelation width maintained a relatively constant value all the time (14 ± 1), indicating that the motility of the sample is small with an error of 7.143 % with occasional increase or decrease. The reason being the *Staphylococcus aureus* strain is itself non-motile and does not swim like some other organisms. Also, the strain has been preserved in distilled water which is not a nutrient to facilitate growth. Variation in Tc is likely to be due to variation in ambient conditions, such as temperature or vibration, which may induce changes in the sample.

Figure 2.10 shows the variation of Tc over 25 min for a sample with 10^1 dilution. There was an occasional shift initially due to Brownian motion and the graph is somewhat comparable to **Figure 2.9**. It is found that the autocorrelation width maintained a relatively constant value all the time (15 ± 2) indicating that the motility of the sample was small with an error of 13.3 % with occasional increase or decrease.

Figure 2.11 shows the variation of Tc for a sample diluted to 10^2 . It is found that the autocorrelation width maintained a relatively constant value all the time, 28 with occasional increase to 29.

Figure 2.12 shows the variation of Tc for a dilution over 25 min with a sample diluted to 10^3 . The parameter value shows the relatively vigorous movement of the suspension during the initial 3 min of the experiment accompanied by Brownian motion and maintained a relatively constant value of (18 ± 1) thereafter.

Figure 2.13 shows the variation of Tc for a sample of 10^{-4} dilutions. There was a mild movement of the suspension throughout. The parameter Tc maintains a value of 11 ± 1 .

Figure 2.14 shows the variation of Tc for a dilution 10^{-5} . There was less motility of the suspension. After 15 min, the Tc values dropped and maintained a steady state value possibly due to sedimentation, although increases in Tc were observed at 14 and 22 min.

Figure 2.15 shows the Tc values of the 10^{-6} dilution and there was a reduced motility of the suspension being observed. The parameter maintained a constant value of 15 to 16. It may be the system is incapable of detecting these low concentrations.

The effect of stirring was investigated. **Figure 2.16** shows the results from a vigorous stirring of the *Staphylococcus aureus* suspension at 10^{-1} dilutions. Initially the sample was set up on the lens and mirror table and a small mechanical disturbance was induced in the sample while setting up the specimen. Over this period, the value of Tc increased for few min and reached a maximum value of 51. After it was stable, the sample was stirred vigorously for three min ($t= 4$ to 7 min) and the autocorrelation parameter value reduced to 15 showing the increase in speed of the scatterers. The value of Tc increased again for a few min and reached a maximum value of 37 and reduced to 12.5 showing the increase in speed of the scatterers. After which, Tc increased showing the decrease in the velocity for a period of 15 min then reaching a steady state maintaining a value of 37.5. Interestingly, after 26 min of the experiment, Tc dropped to 27.5 showing an apparent increase in velocity. However, this appeared to be a significant change with no apparent change in the system, and it was thought sedimentation may be play in a role in the reduction of Tc. With the specimen under study being a non-motile organism and having been supplied with a non-nutrient medium (distilled water), there is no vigorous movement inferred, as with previous experiments.

Figure 2.17 shows a comparison of the average spatially-varying autocorrelation values of *S. aureus* suspension with 10^{-1} (8.88×10^7 counts per ml) and 10^{-2} dilutions (8.88×10^6 cfu/ml). Comparing the distribution of the spatial curves with reference to the X-axis from either dilution indicates that the bright spots on the path of the laser beam must be more for high are the 10^{-2} dilution than that of the 10^{-1} dilution as mentioned earlier in Figure 2.5.

Figure 2.18 show the sedimentation effect as observed with diluted *S. aureus* suspension. The spatial autocorrelation data collected over the samples was found useful in determining the effect of sedimentation on the liquid samples. The spatial autocorrelation data of the suspension (10^{-1} dilution) in the cuvette was taken at first. Then the data collected over the sample after 40 min was also taken. It was found that the number of bright spots or concentration of the sample appears less over the path of the laser beam after sedimentation. As mentioned in Figure 2.17, if there is a dilution, then the spatial autocorrelation value should increase implying the increase in bright spots and subsequent increase in intensity data. Figure 2.18 shows the similar effect due to sedimentation of the sample. As the cuvette is placed in position 2 (Figure 2.2), at the beginning of the experiment, the sample will be turbid but after 40 min, the cells would have begun to settle out. For this reason, it was found that the initial turbid specimen appears to have a high concentration and, after sedimentation, the specimen shows a lower concentration.

2.4 CONCLUSION

The experiments were designed to be controls for the speckle system discussed in the next chapter. Inert particles like polystyrene micro-spheres were chosen for performing the study on the effect of microdilutions and the non-motile organism *Staphylococcus aureus* was chosen for higher-order dilution study (10^{-6}). In order to minimize the motility of the organism, it was cultured and diluted in water as suspensions. The same could have been achieved through microspheres (1 μm spheres and 100 μm spheres) but they are very expensive and they dehydrate quickly and cannot be used in large quantities. The optical density spectrophotometer was used to measure the concentration of the suspension. The main drawback with this is that it cannot detect suspensions which are highly turbid or those with very high dilution. The experiments were aimed to test the sensitivity of the autocorrelation width (T_c) and spatial autocorrelation curves in detecting the motility and concentration of the system, respectively. The system was also been helpful in comparing the sensitivity of speckle methods and OD photometers.

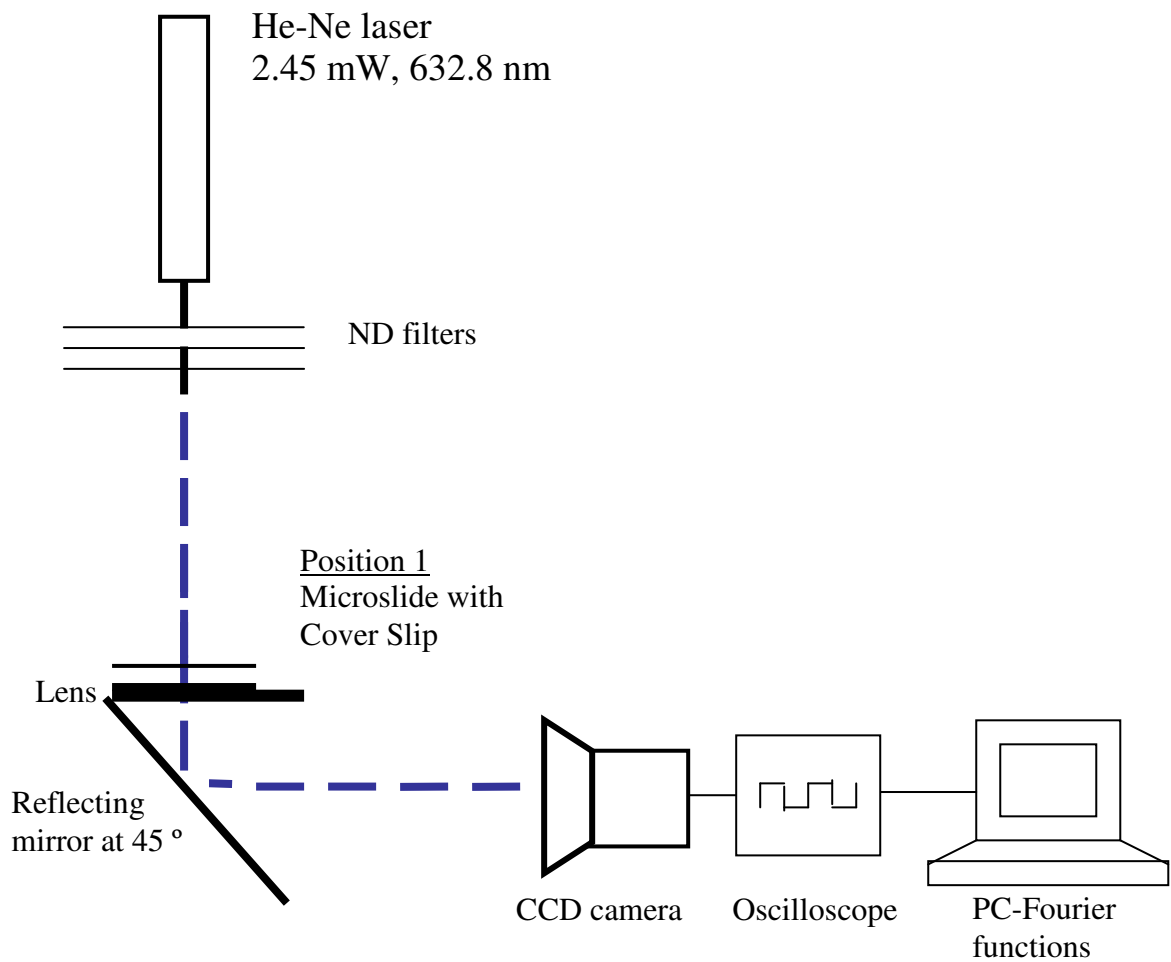


Figure 2.1 The schematic view of the hardware setup and optics for the experiments involving polystyrene microspheres; microslide is placed at position 1.

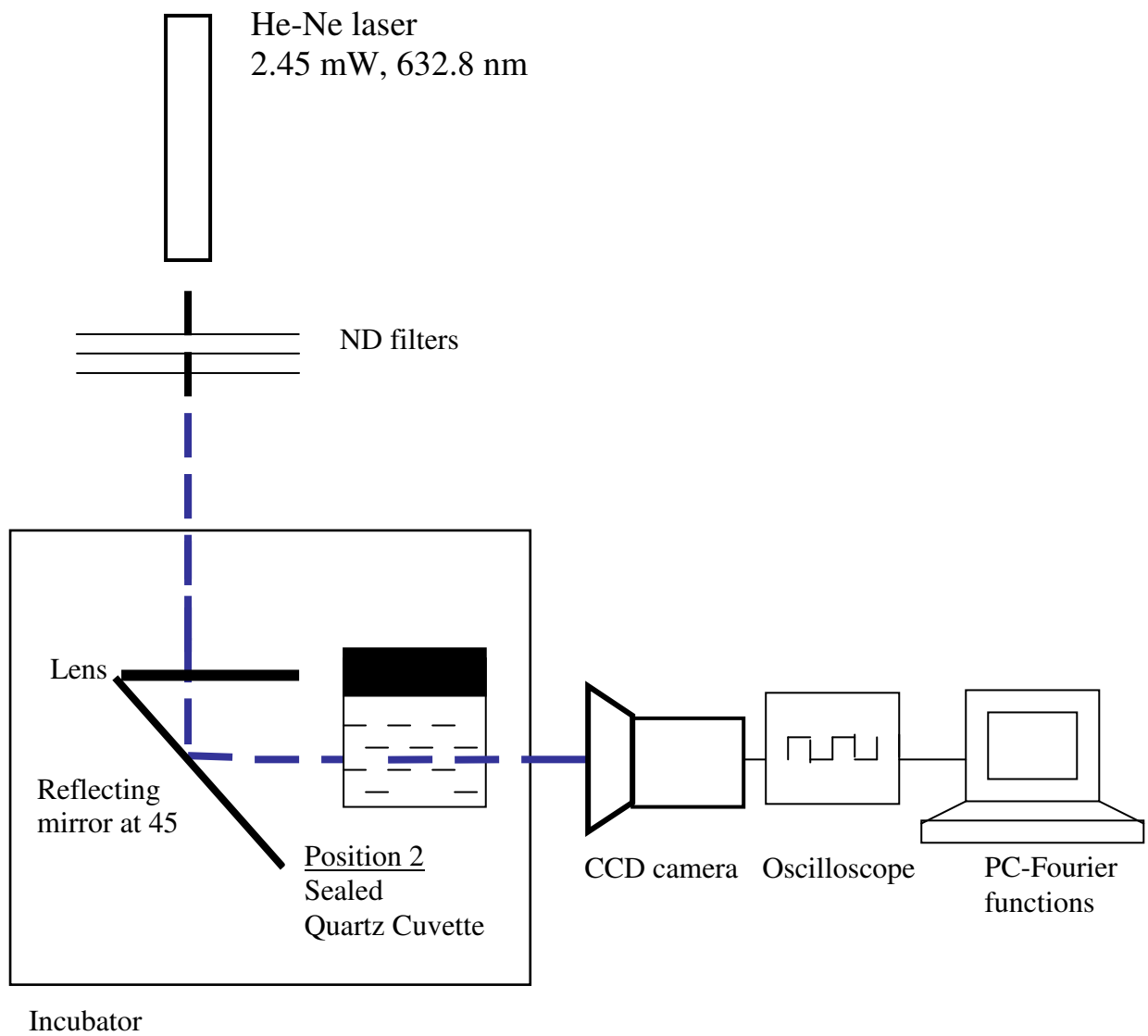


Figure 2.2 The schematic view of the hardware setup and optics for the experiments involving *Staphylococcus aureus* suspension; cuvette is placed at position 2.

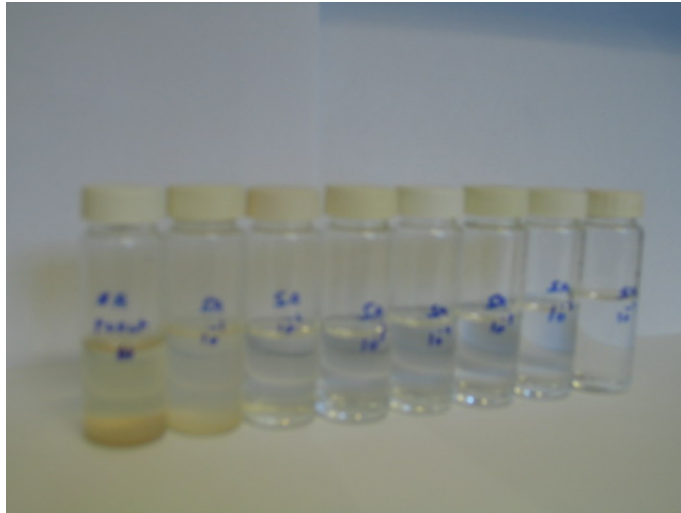


Figure 2.3 Universal bottles containing 10 fold dilutions of the *Staphylococcus aureus* suspension.

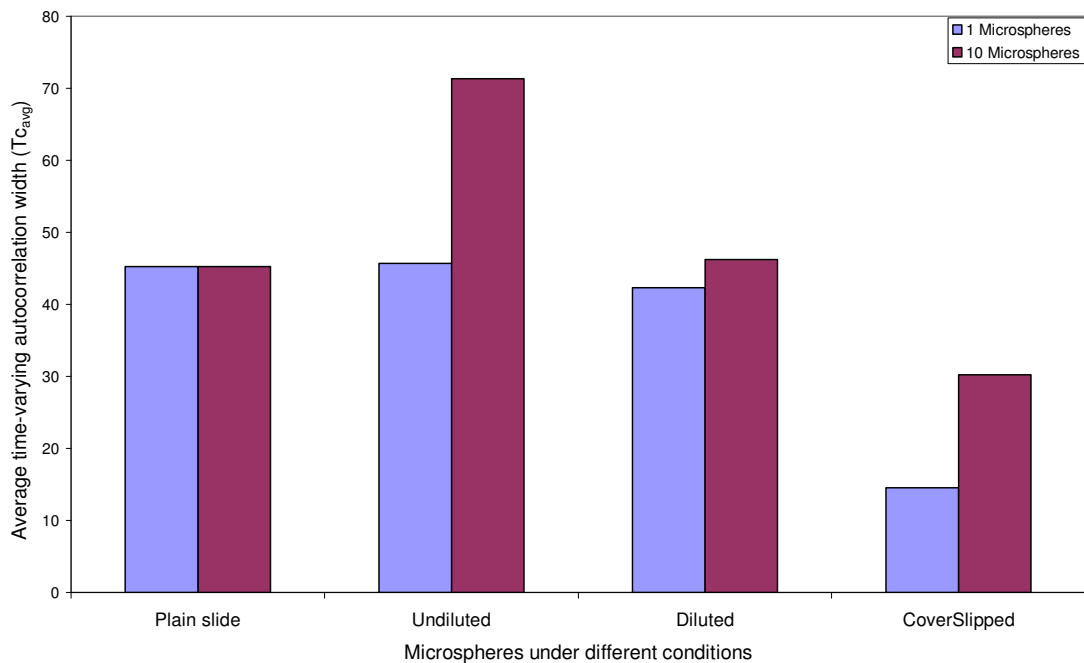


Figure 2.4 Comparison of average time-varying autocorrelation width ($T_{c_{avg}}$) parameter for 1 μm and 10 μm spheres under different conditions. There are four different classifications on the X-axis. Plain slide refers to the glass slide upon which the microspheres were studied. Undiluted refers to the addition of 10 μL volume of either of the microspheres on the plain slide. Diluted refers to the addition of 2 μL distilled water to the undiluted spheres. Coverslipped refers to the gentle placement of an 18 mm^2 cover glass over the diluted mixture.

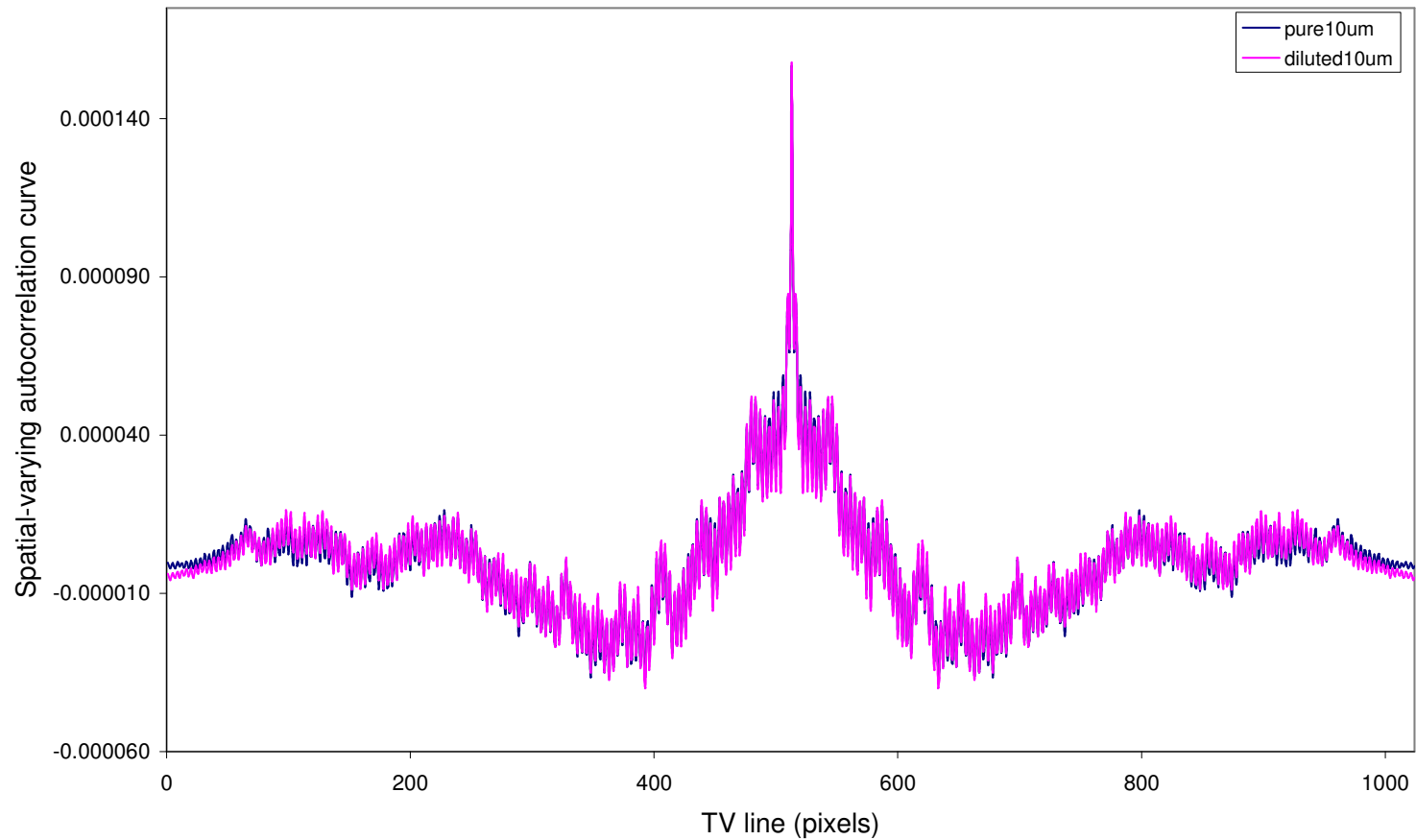


Figure 2.5 Comparison of spatially-varying autocorrelation function between the neat suspension of 10µm spheres (counts = 10^6 /ml) spheres and diluted suspension of the same (counts= 8.33×10^5 /ml) spheres.

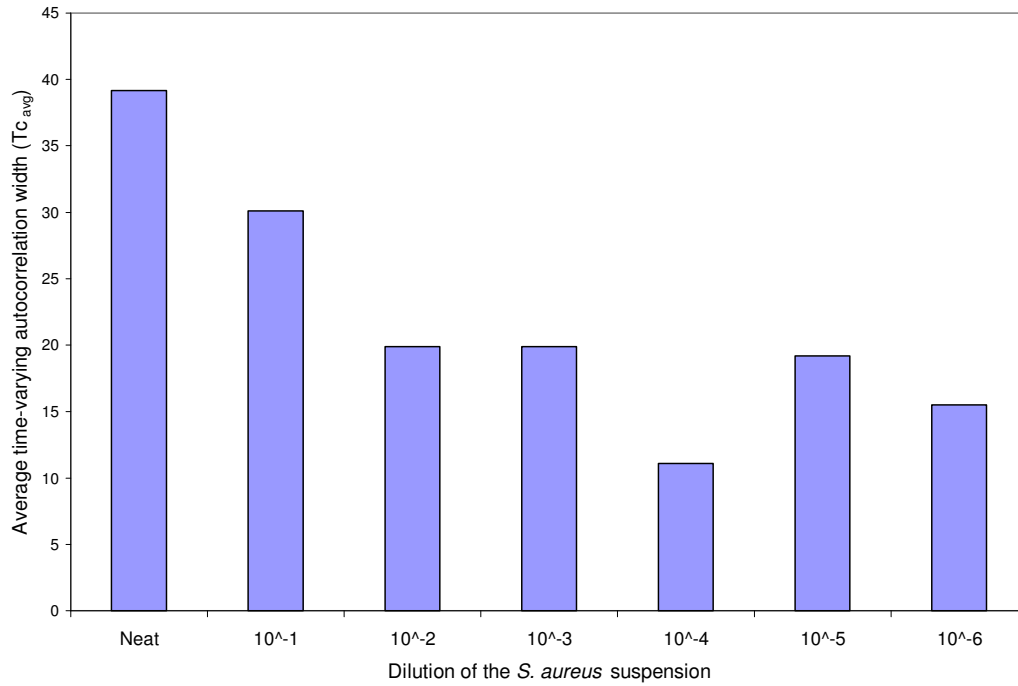


Figure 2.6 Comparison of average time-varying autocorrelation width ($T_{c_{avg}}$) for *S. aureus* suspension kept under different dilutions (neat to 10^{-6}).

Dilution	OD
Neat	2.00>>
10^{-1}	2.00>>
10^{-2}	0.33
10^{-3}	0.03
10^{-4}	0.00
10^{-5}	0.00
10^{-6}	0.00

Table 2.1 The dilution of the *S. aureus* suspension and its corresponding optical density.

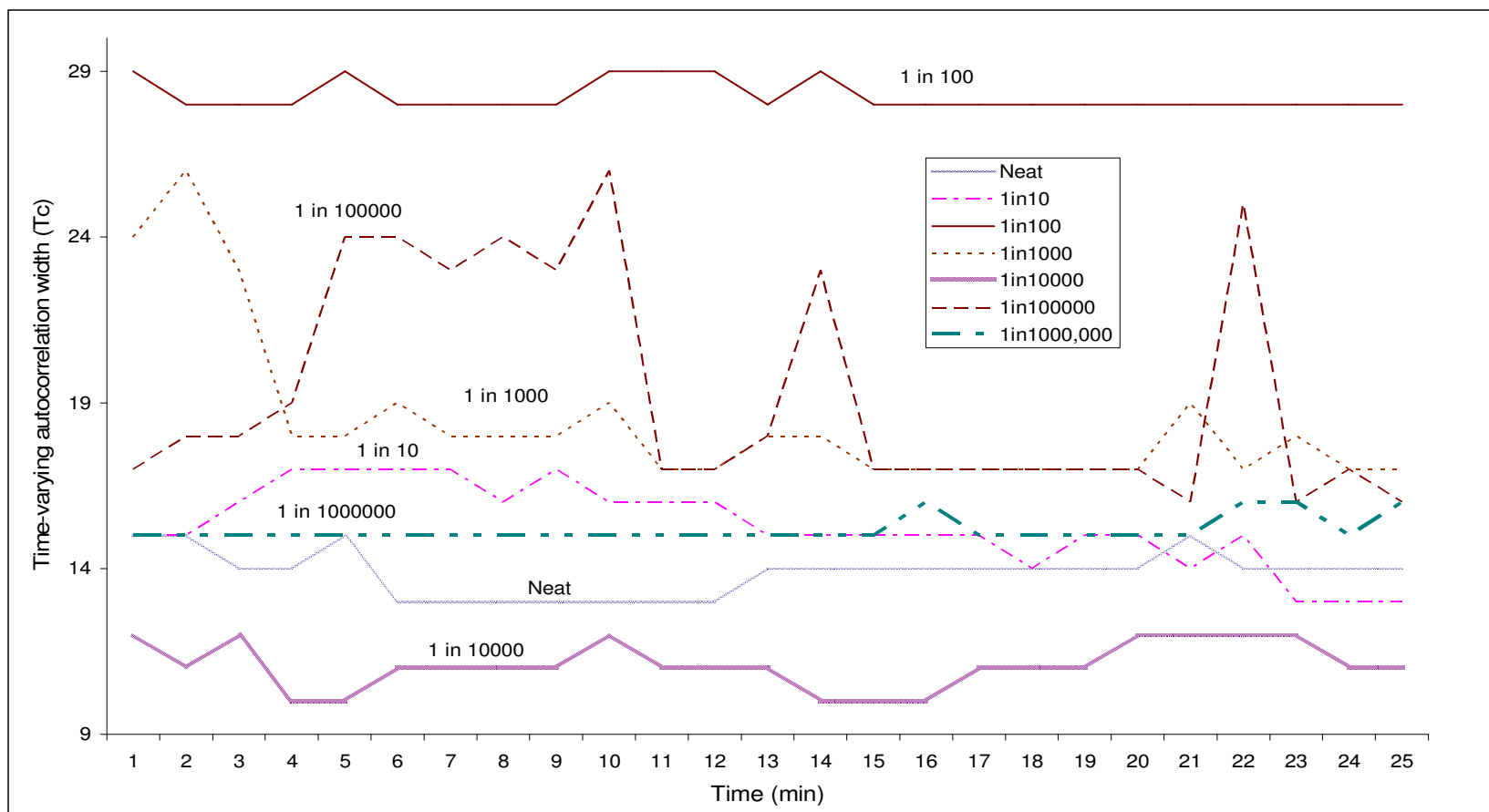


Figure 2.7 Comparison of the effect of different dilutions (from neat to 10^{-6}) on T_c plotted over a period of 25 min

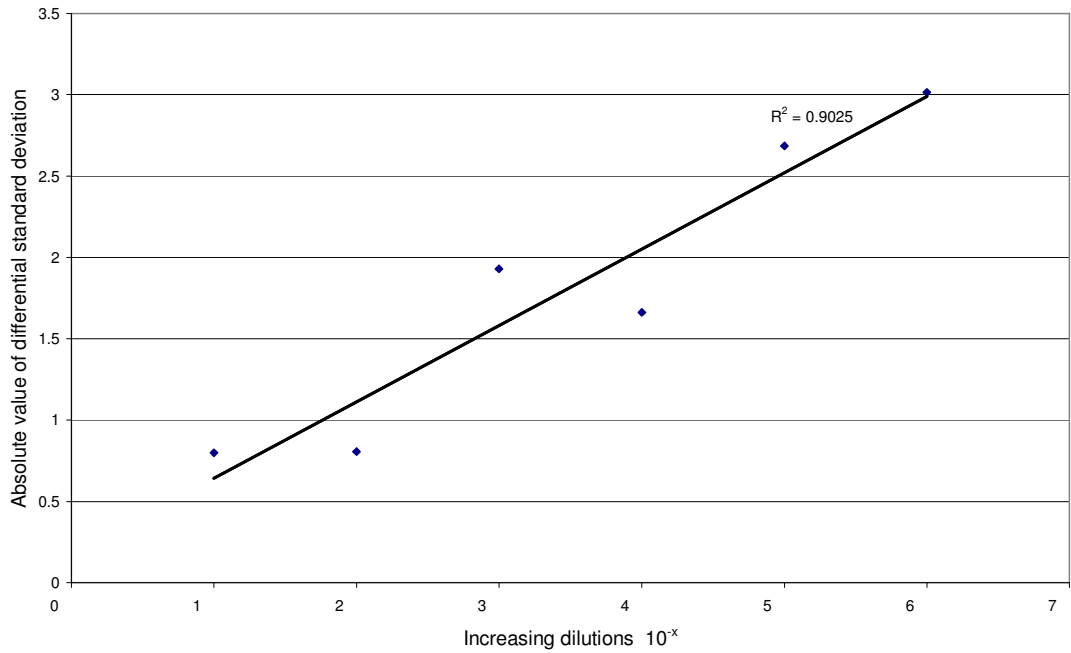


Figure 2.8 Absolute value of the differential standard deviation of Tc over a period of 25 min for different dilutions of *S. aureus* suspension. X-axis represents the order of increasing dilutions in steps 10^{-x}. Thus the first value on the X-axis is for 10⁻¹ dilution and the second value is for 10⁻² and so on.

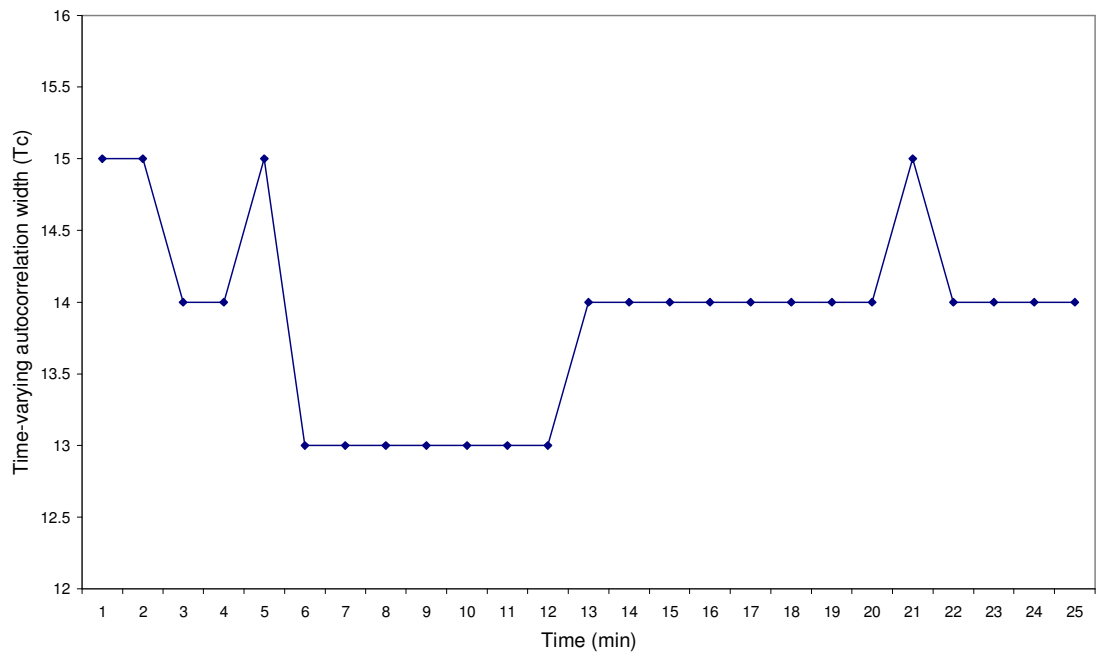


Figure 2.9 Variation of autocorrelation width (Tc) over 25 min for *S. aureus* suspension (neat sample).

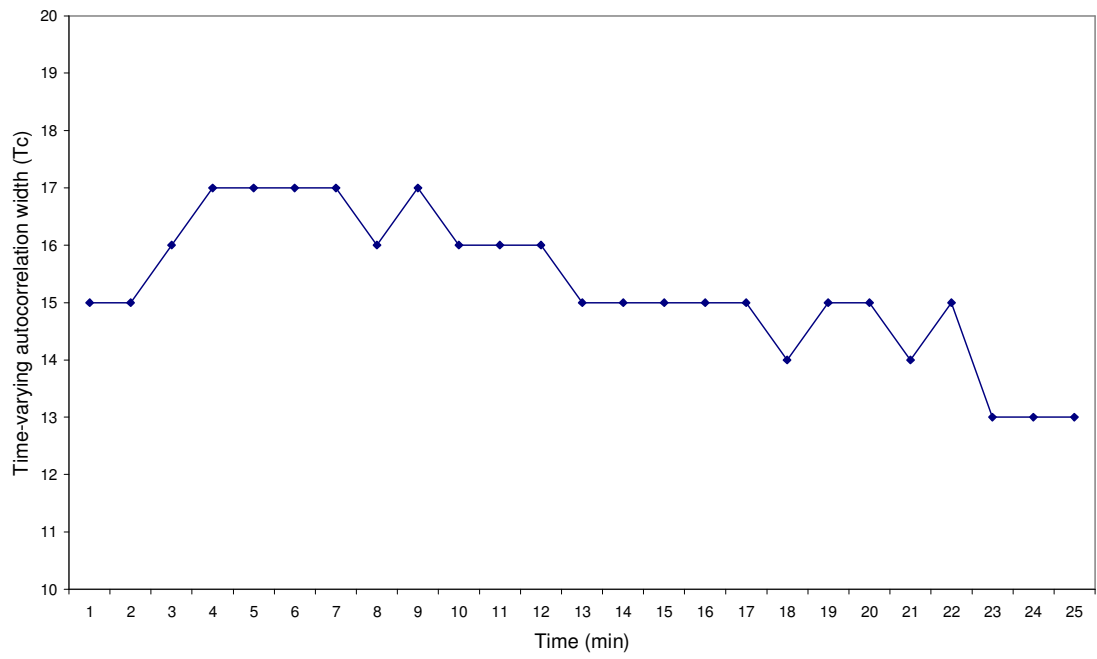


Figure 2.10 Variation of autocorrelation width (Tc) over 25 min for *S. aureus* suspension (10^{-1} dilution sample).

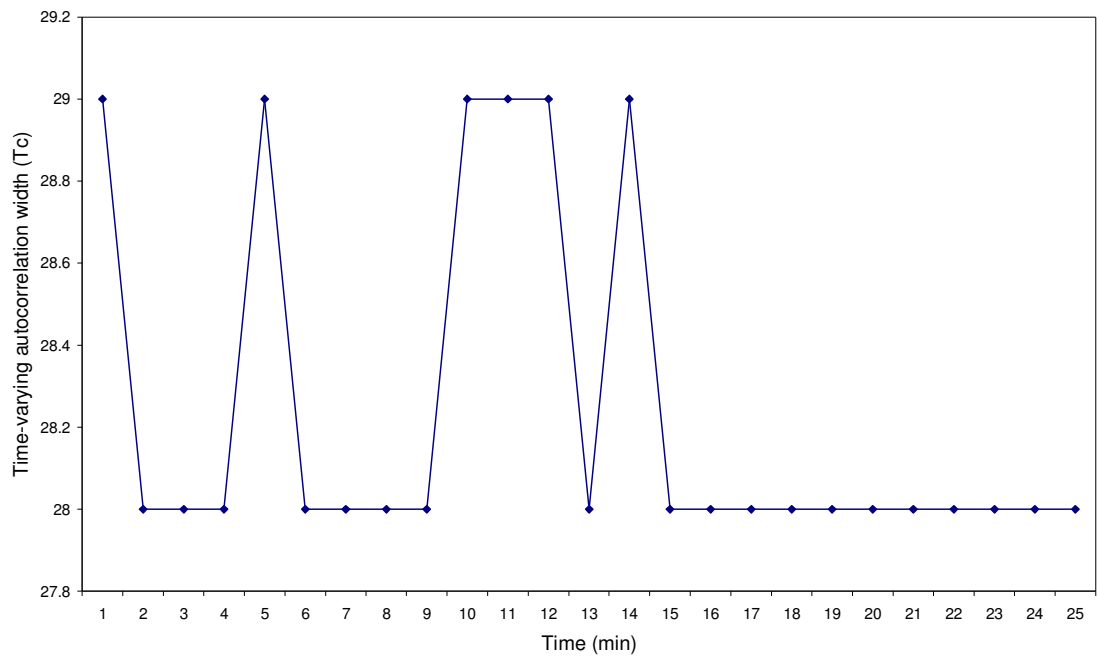


Figure 2.11 Variation of autocorrelation width (Tc) over 25 min for *S. aureus* suspension (10^{-2} dilution sample).

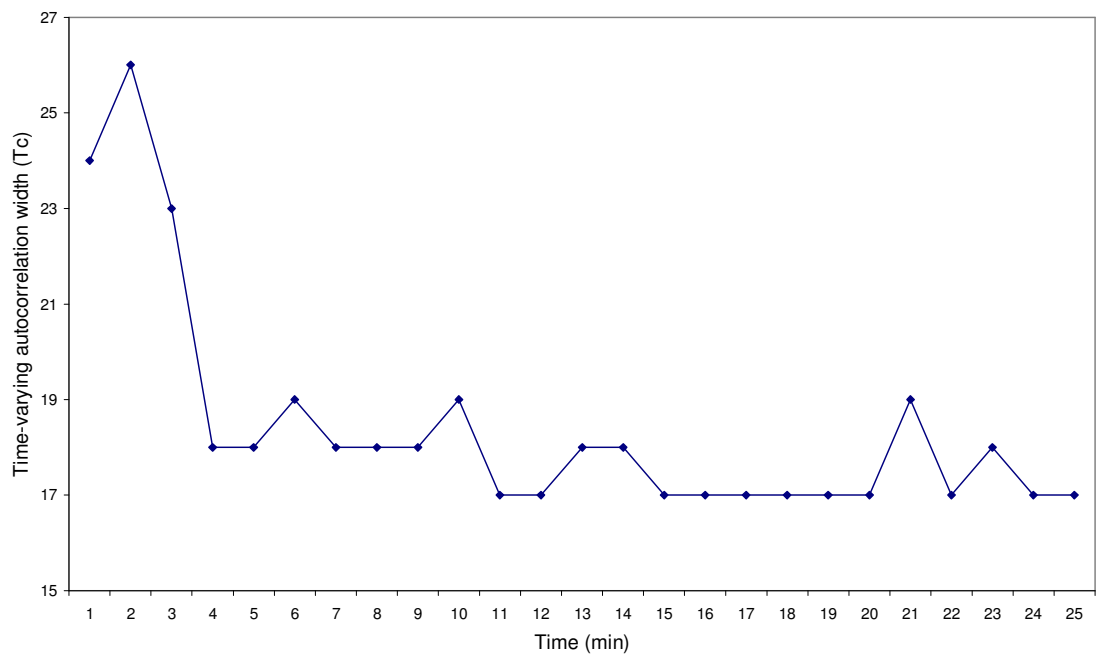


Figure 2.12 Variation of autocorrelation width (Tc) over 25 min for *S. aureus* suspension (10⁻³ dilution sample).

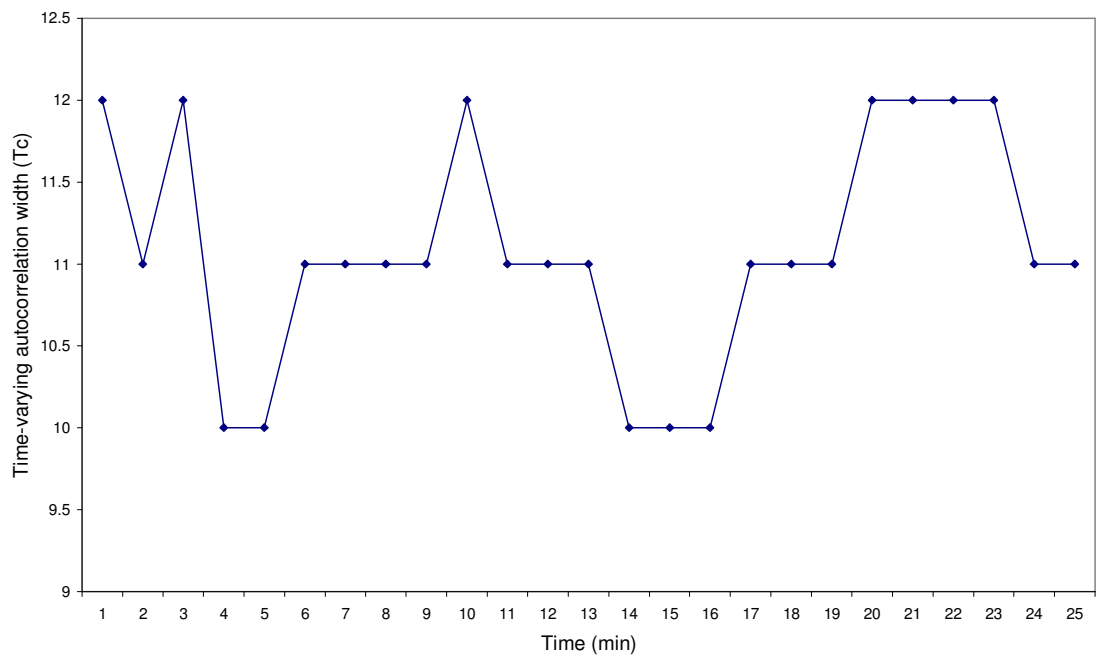


Figure 2.13 Variation of autocorrelation width (Tc) over 25 min for *S. aureus* suspension (10^{-4} dilution sample).

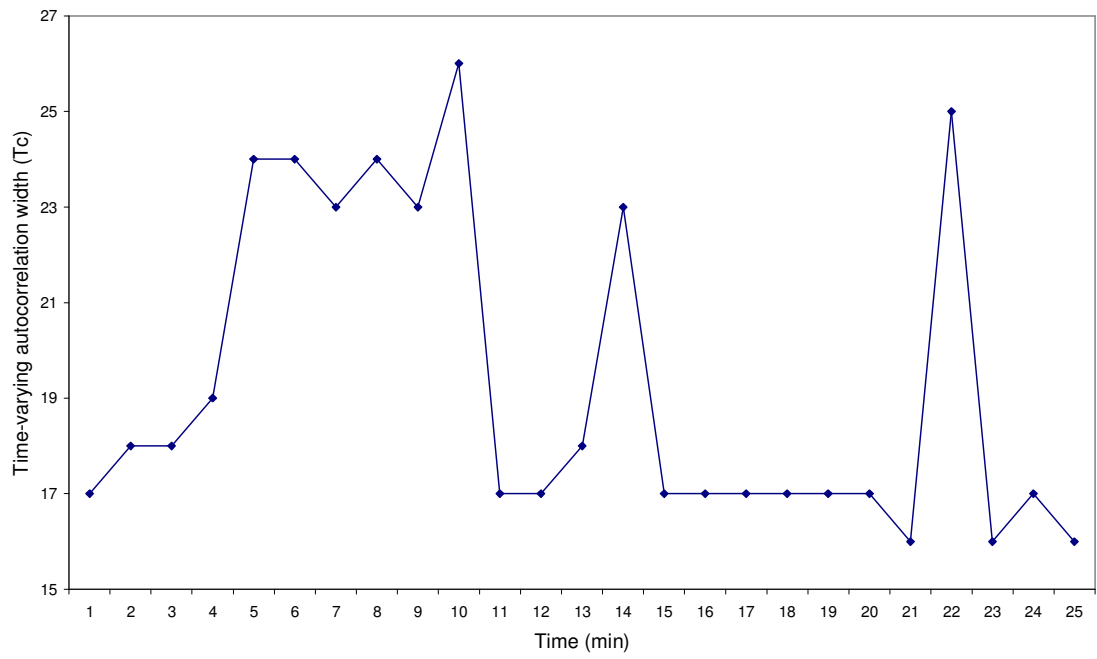


Figure 2.14 Variation of autocorrelation width (Tc) over 25 min for *S. aureus* suspension (10^{-5} dilution sample).

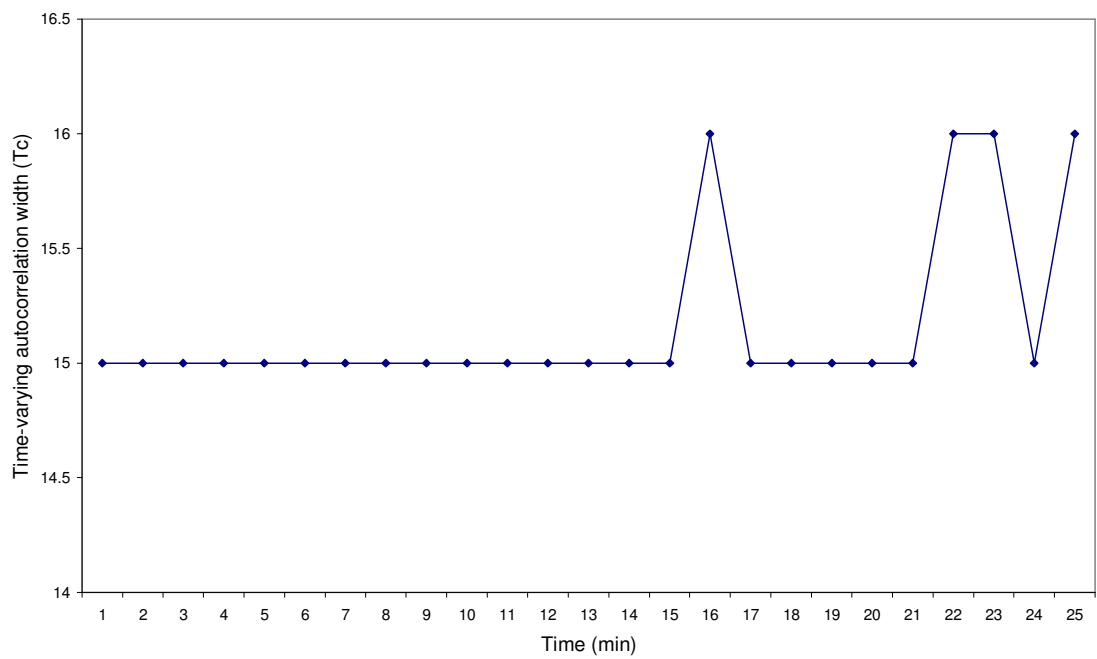


Figure 2.15 Variation of autocorrelation width (Tc) over 25 min for *S. aureus* suspension (10^{-6} dilution sample).

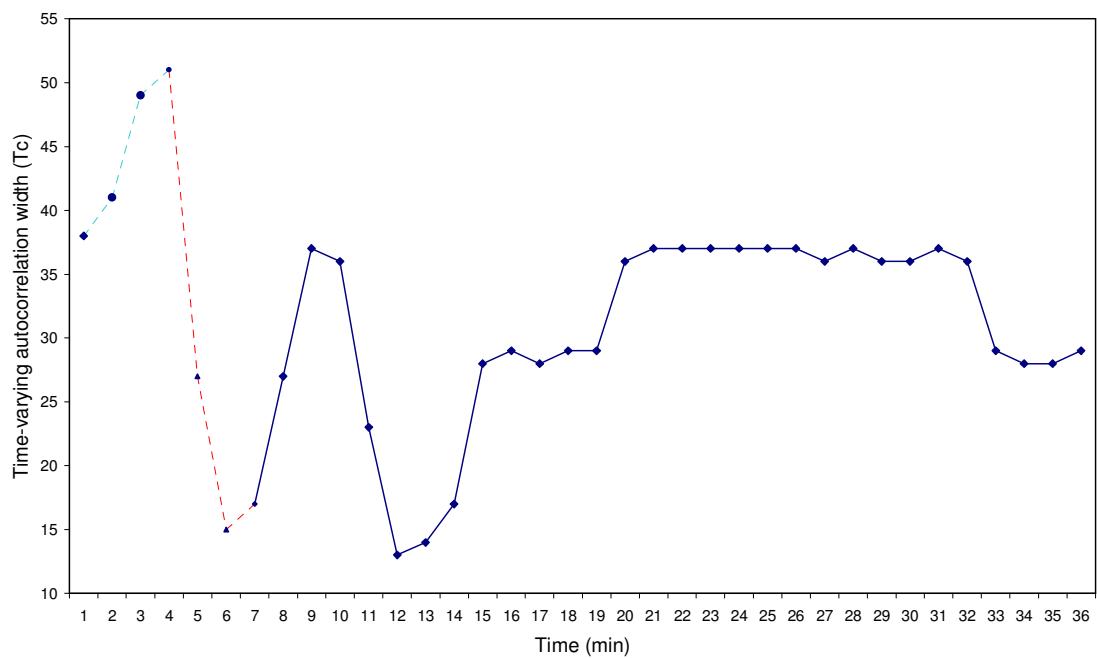


Figure 2.16 Variation of autocorrelation width (Tc) over 36 min for *S. aureus* suspension (10^{-1} sample) under vigorous stirring for 3 min (t = 4 to 7 min). The setting up time for the specimen took the initial 3 min (t = 1 to 3 min).

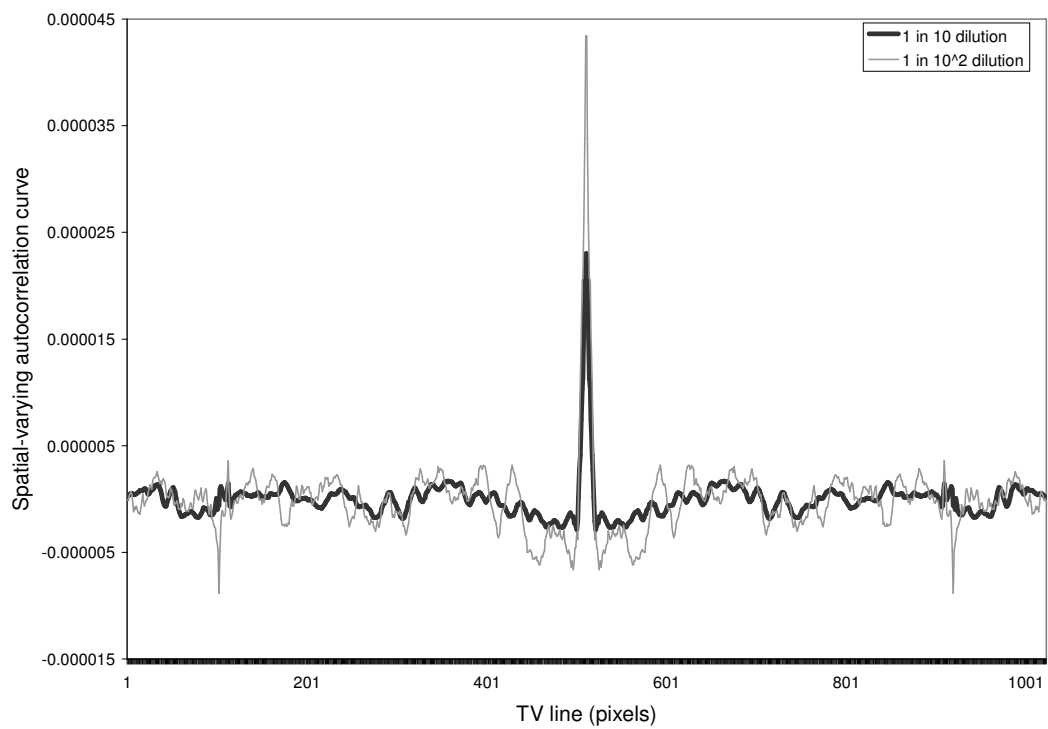


Figure 2.17 Comparing spatially-varying autocorrelation function of *S. aureus* suspension at 10^{-1} dilution (8.88×10^7 cfu/ml) and 10^{-2} dilution (8.88×10^6 cfu/ml).

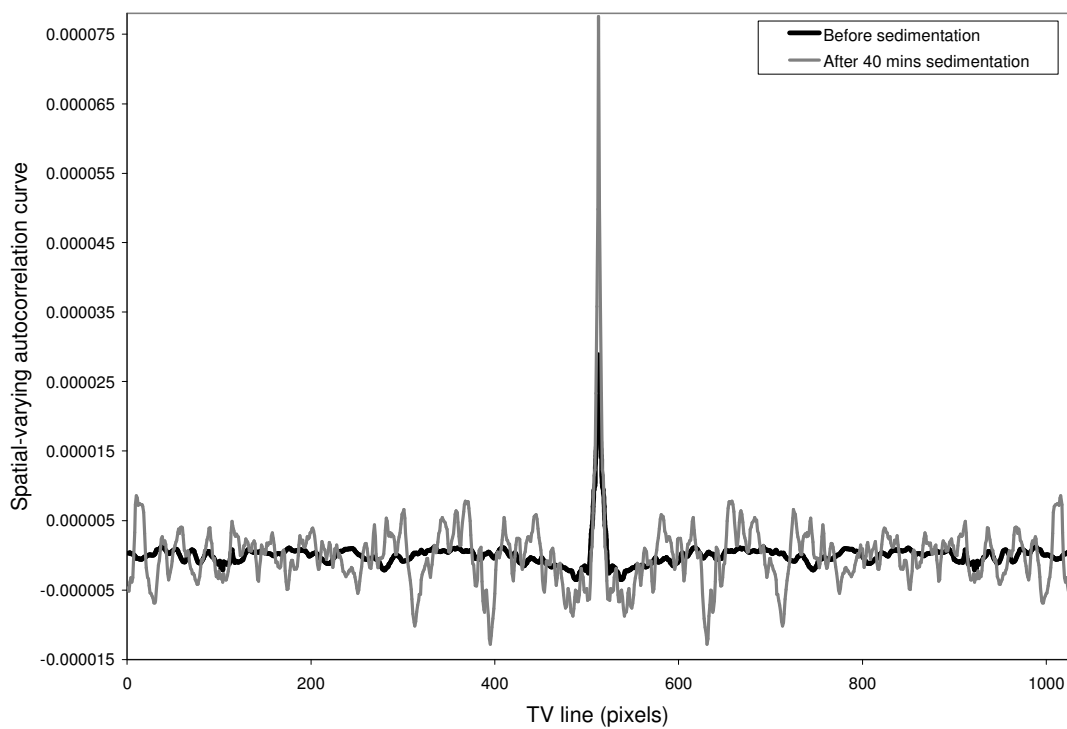


Figure 2.18 Comparing spatially-varying autocorrelation function of *S. aureus* suspension at 10^{-1} dilution (8.88×10^7 counts per ml) before and after 40 mins of sedimentation.

CHAPTER 3 LASER SPECKLE CHANGES DURING THE GROWTH OF *ESCHERICHIA COLI* CULTURE

3.1 INTRODUCTION

The previous chapter aimed to establish standard methods and protocols with inert polystyrene microspheres and a non-growing suspension of *Staphylococcus aureus* to determine the effects of the parameters that are investigated as described in this chapter. Here a motile, actively-growing organism, *Escherichia coli* would be used for all the different experiments described in Chapter 2. *E. coli* is a bacterium that is commonly found in the lower intestine of warm-blooded animals. Most *E. coli* strains are harmless as they normally live inside the human intestines and help the system break down and digest the food consumed, but some strains such as serotype O157:H7 can cause serious food poisoning in humans (Vogt and Dippold, 2005). The harmless strains of *E. coli* are a part of the normal flora of the gut and it can benefit their hosts in two different ways either by producing vitamin K or by preventing the establishment of pathogenic bacteria within the intestine. (Hudault *et al.*, 2001). *E. coli* is not always confined to the intestine. Their ability to survive for short periods of time outside the body makes them an ideal indicator organism to test environmental samples for fecal contamination. Its genetics are comparatively simple and easily-manipulated. Culturing them is also done easily and thus making them one of the best-studied prokaryotic model organisms, and an important species in biotechnology (Feng *et al.*, 2002). Researchers and scientists working in life sciences and applied optics commonly use *E. coli* as their model organism. Recent applications include Laser Tweezers Raman Spectroscopy (LTRS), Fountain Flow™ Cytometry (FFC), Surface Plasmon Resonance (SPR) and nanoshells.

The benefit of combining optical trapping (i.e. laser tweezers) with confocal Raman spectroscopies has been demonstrated for the analysis of micron-sized particles in solution (Chan *et al.*, 2004). A single laser beam (30 mW, 633 nm) when tightly focused can function as an optical trap to suspend micron-sized transparent particles near the laser focus. The beam also acts as the efficient source of excitation to obtain their Raman spectra. This approach when applied to living cells like *E. coli* can be used to rapidly analyze the biochemical composition of individual cells in suspension. LTRS was used to

quantitatively measure changes in cellular activity of single cells by monitoring protein expression in living *E. coli* (Chan *et al.*, 2007).

Fountain flowTM cytometry (FFC) methods are based on laser-induced fluorescence of the labelled cells. Here the suspended microorganisms are at first stained with dye to enable easy detection. The resulting aqueous sample is passed as a stream of river in front of a laser beam which excites the fluorescent labels. As the measured sample flows toward the imager along the optical axis, the resulting fluorescence is captured with a CCD or CMOS imager. The images are thus used to make photometric measurements of target particles throughout the focal plane.

The feasibility of fountain flow cytometry (FFC) for the rapid and sensitive detection method for individual organisms in aqueous samples was demonstrated by the detection of *E. coli* cultures labeled with ChemChrome CV6 and SYBR Gold in buffer and streamed with the natural river water in front of a laser beam, thereby exciting the labelled organisms (Johnson *et al.*, 2006). Batch and continuous cultures of a recombinant *E. coli* were experimented on to perform flow cytometry studies on its macromolecular compounds and light-scattering parameters (Fouchet *et al.*, 1994).

Based on surface plasmon resonance (SPR), immunosensors were developed for the detection of microorganism in real water samples. Surface plasmon resonance (SPR) is based on optical transduction and is one of the rapid detection techniques for antigens. SPR is a basically charge density oscillation that may exist at the interface of two media like a metal and dielectric (Homola *et al.*, 1999). When incident light is coupled with the metal interface, there exists a transfer of resonance energy from the incident light to the surface plasmon (Boozer *et al.*, 2006). The incident angle at which the resonance occurs is dependent on the refractive index near the sensor surface and so the adsorption of molecules on the metal surface can be detected accurately. This approach allowed the detection of *E. coli* in water samples in a rapid and selective manner (Dudak and Boyacl, 2007).

The efficiency of a monomolecular film of (3-glycidoxypropyl) trimethoxysilane (GPTS) on a shear horizontal guided acoustic wave immunosensor to detect microorganism was demonstrated with *E. coli* (Moll *et al.*, 2007).

Researchers have developed molecular-based detection methods with low limits of detection. One such method of detecting *E. coli* in food involves nutrient enrichment followed by concentration using immunomagnetic separation (IMS) with subsequent plating onto selective MacConkey agar (Murphy *et al.*, 2007). *E. coli* was used by researchers while proposing a bacteria detection scheme that measures the optical scattering from aligned asymmetric bacteria in the presence of an applied alternating electric field. This work also exploits the fact that most bacteria aggregate (Choi *et al.*, 2006).

Some scientists favoured the use of *E. coli* for the study of nanoshells. Antibody-conjugated silver nanoshells were used for the rapid detection of *E. coli* (Kalele *et al.*, 2006). Also the method of culturing *E. coli* in high concentration was proposed using nanoshells. It was suggested that building up a micro-fabricated wall of funnel shaped openings allows more concentration of organisms and prevents random motion (Galajda *et al.*, 2007).

In this chapter, the effect of scattering light from a growing liquid culture of *E. coli* organisms was investigated and algorithms were developed to test the effectiveness of the autocorrelation parameters (as explained in Chapter 2) to detect bacterial motility and concentration changes in the liquid culture. When the laser beam passes through a cuvette, containing a suspension of microorganisms, the scattered light falling on a screen shows interference patterns. If the organisms move, then so does the interference pattern. The spatial super positioning of the laser irradiation produces interference maxima and minima, which appear as bright or dark spots of light respectively. The statistical dynamics of this bio-speckle can be associated directly with a particular species. Furthermore, this system may provide a real-time non-destructive testing process to identify microbial population kinetics.

3.2 MATERIALS AND METHODS

Three different experiments were performed with the laser speckle system using growing *E. coli* cells. All these experiments involved repetition of the speckle experiments and measurement of speckle parameters explained in the previous chapter. **Figure 3.1** shows the typical work scheme that was common to the first and second experiments.

The first experiment aimed to monitor the motility of the *E. coli* cells from the initial stage of adding the overnight culture to LB broth until the point when there was a high concentration of cells and the nutrients in the broth were used up almost completely by growing cells and growth was slowing down. *E. coli* is a facultatively-anaerobic bacterium and will grow well under these conditions. The experiment examined the effect on the autocorrelation parameter $T_{c_{avg}}$ of live *E. coli* cells growing in a sealed cuvette kept inside an incubator. The experiments were done over a period of 38 h with a sealed cuvette placed at position 2 to ensure a horizontal transmission of the laser beam through the specimen. **Figure 3.2** shows the schematic view of the hardware set-up with the cuvettes at position 1 or 2 inside an incubator.

The second experiment consisted of two different phases. The initial 13 h of the second experiment was a broth pre-warming phase and facilitated a rapid growth when *E. coli* was added to the broth. This phase was also utilized to study two other characteristics. The first one was to study the effect on $T_{c_{avg}}$ of evaporation and volume reduction of the LB broth when an unsealed cuvette was kept inside an incubator. Secondly this phase was to understand the growth of the bacterium for different dimensions of the cuvette (See section 3.2.4.4 later in this chapter).

The remaining 25 h (13 to 38 h) of the second experiment was investigating *E. coli* motility phase. This aimed to verify the motility results of the second experiment when an unsealed cuvette containing a culture in LB broth was kept at position 1 and with a vertical transmission of the laser beam.

The third experiment was again done at position 1 of the cuvette (vertical transmission) and the concentrated culture that was remaining at the end of the first experiment (after 38 h) was used for this experiment. Like the second experiment, this experiment was also used to verify the motility results from the first experiment but through an alternative method of serial dilution on a prewarmed LB broth. The effect on $T_{c_{avg}}$ of the serial dilution of this concentrated culture was compared with the motility results with the other two experiments to understand the consistency of the autocorrelation parameter variation.

3.2.1 Sample preparation

3.2.1.1 LB broth preparation

As mentioned in section 2.2.2.2, LB broth is a rich nutrient medium that feeds the microorganisms such that they can grow quickly, if incubated at 37°C. Around 10 ml of LB broth was used individually for the first and second experiments but for the third experiment, a 20 ml of LB broth was preserved in a universal bottle and incubated separately for performing dilution during the third experiment.

3.2.1.2 *E. coli* culture preparation

A loopful of fresh *E. coli* culture from a nutrient slope was transferred into 10 ml LB broth in a universal bottle. It was incubated at 37° C overnight for around 20 h. After this 1 ml of this mixture was added and mixed into a universal bottle containing 4 ml of LB broth and incubated again at 37° C overnight. This was done to ensure the *E. coli* used in this experiment were completely fresh and prepared under sterile conditions.

3.2.1.3 Nutrient agar preparation

Nutrient agar was prepared by suspending agar powder (Oxoid) in distilled water, it was brought to the boil until completely dissolved and then sterilized by autoclaving at 121°C for 15 min. The agar was then poured into the agar plates. A sample of the *E. coli* culture growing in the cuvette was streaked onto these plates at different time periods as the experiment progressed. After incubation for 24 h, the number of colony forming units (cfu) was counted. The cfu information was related to the results from the laser speckle experiments for analysis.

3.2.2 Hardware and optical setup

The schematic view of the hardware setup and optics is shown in **Figure 3.2**

3.2.2.1 Setting up the laser beam and ND filters

The beam from a low power (632.8nm, 2.45 mW) He-Ne laser was passed through three neutral density (ND) filters to reduce the incident power and avoid camera saturation. This setup is same as mentioned in section 2.2.3.1.

3.2.2.2 Setting up the incubator

A 30 mm hole was drilled into the top of the incubator to allow the entry of the laser beam. If the cuvette is kept in position 1 (Figure 3.2), the beam passes through the cuvette and penetrates the specimen before being reflected by the mirror. If the cuvette is in position 2, the beam penetrates the specimen after being reflected. Once the hardware setup was complete, the incubator was adjusted to 37°C. The photographs of the incubator setup are shown in **Figure 3.3**.

3.2.2.3 Setting up the reflecting mirror

The reflecting mirror was kept at 45° so that if the cuvette is in position 1 (first experiment), the beam travels through the depth of sample and reflected to the camera. If the cuvette is in position 2 (second and third experiment), the beam will be reflected by the mirror and transmitted through the cuvette along its width. The reflecting mirror setup is shown in Figure 3.2.

3.2.2.4 Setting up the cuvettes

For the first experiment only one quartz cuvette of cuboidal shape (96 cm³, Thermo Fisher Scientific, Inc. USA) was used for the speckle study and was placed into the laser beam at position 2. For the second experiment, three sterile cuvettes were chosen, shown in **Figure 3.4**. Two quartz cuvettes of cuboid shape (96 cm³, Thermo Fisher scientific, Inc. USA) and one universal bottle (49.5 cm³ ~ 25 ml, Institute of biomedical life sciences, Glasgow, UK) were used. All three of them are marked with a measuring scale to allow easy monitoring of the reduction in volume of the nutrient broth level as the experiment progressed. Two different shaped cuvettes were used in an attempt to understand the effect of bacterial growth and volume reduction of the nutrient with cuvettes of different dimensions. Out of the three cuvettes, only one quartz cuvette was placed into the laser beam at position 1 and was named as speckle cuvette. The other two of them named as reference cuvettes (one cuboid and one universal) were used for culture sampling and to study bacterial growth and volume reduction of the broth. For the third experiment, the same quartz speckle cuvette from the second experiment was used at position 1.

3.2.2.5 Setting up the Camera

A CCD camera (YD 66, 2.3 mega pixels, Professional's choice B/W surveillance camera, Taiwan) was positioned to capture the beam after transmission through the optical system. The camera is placed in front of glass door of the incubator, as shown in Figure 3.3. As mentioned in section 2.2.3.3, a line-scan from the camera was captured via an oscilloscope (Lecroy, Switzerland) and transferred to a PC for analysis. If the culture was located at position 1, then the beam travelled the depth of the sample and the data collected contained information relating to the integrated profile of the microorganisms through the sample's depth. If the sample was located at position 2, the data is related to a certain depth only.

3.2.3. Software setup

Proprietary software was written and used to capture the data from the oscilloscope which was exported to a computer, where the data was saved into an excel file for analysis. The data included the mean voltage, standard deviation, power integral density and autocorrelation. The proprietary software was created using Borland C⁺⁺. The oscilloscope gathers the irradiance values from the camera and this was used as an input to the software which calculated the mean, standard deviation and variance of the signal. In addition the Fourier analysis of this signal was done and the autocorrelation and frequency spectrum can be plotted.

3.2.4. Experimental setup

3.2.4.1 Trial experiment and choosing the bandpass frequency range

25 ml of distilled water was added to a cuvette and a trial experiment was run for 30 min as mentioned in section 2.2.4.1. From various experiments it was found that a bandpass frequency range of 10-4000 Hz gave the optimal signal output.

3.2.4.2 Adding broth control specimen into the cuvette

The position where the distilled water (control specimen) was kept was now replaced with LB broth. A quartz cuvette was filled with 10 ml of broth and a test run was made and the bandpass frequency was set to 10-4000 Hz.

3.2.4.3 Adding fresh *E. coli* culture to the cuvette

For a 10 ml broth sample, 100 μ L of overnight *E. coli* culture was added. As mentioned previously, *E. coli* culture was added at the initial stage for the first experiment (without prewarming) but for the second experiment the culture was added only after 13 h of broth pre-warming. The third experiment does not need any fresh culture at the beginning as the well-grown culture at the end of the second experiment was directly used for the third experiment.

3.2.4.4 Sampling from reference cuvette (for second experiment)

At the beginning of the pre-warming phase, 10 ml samples of fresh broth were taken individually in both the reference cuvettes. At the end of this phase (13 h), around 10 μ L of the *E. coli* overnight culture was added separately to the fresh broth in all the three cuvettes and number of cfu was determined by inoculating 100 μ L samples from reference cuvettes at regular intervals onto nutrient agar plate and incubating overnight at 37°C. The 100 μ L samples are only taken from reference cuvettes, not from speckle cuvette. This was done so that the liquid was not disturbed in the speckle cuvette where the laser beam was pulsed, as this would obviously affect the speckle pattern. Moreover, the reference cuvette and speckle cuvette were of the same dimensions and the cfu values shown by the reference cuvette would be equivalent to that of the speckle cuvette. By comparing the determined with the bacterial counts shown by the universal bottle, the effect of colony growth on different dimensions of the cuvettes can understood.

3.2.5. Speckle sampling

As mentioned in section 2.2.4.2, a line scan was performed to determine the instantaneous speckle changes between each pixel and a large number of samples were taken for analysis at intervals between 1 to 30 min. The software delay between each sample was normally set to 40 μ secs to enable the computer processor to multiplex between data capturing and the file saving.

3.2.6. Third experiment

The third experiment was also considered to be the calibration for the first experiment but done in a different way. At the end of the second experiment, the *E. coli* culture will have reached its maximum growth with the available nutrients. The third experiment was started at this maximum growth stage and the *E. coli* culture in the cuvette is now supplied with

freshly prewarmed LB broth, thereby feeding the starving culture and allowing it to grow once again. In other words, the well-grown *E. coli* culture is diluted with a pre-warmed broth to obtain the desired concentration. This was done to check whether the average autocorrelation width, ($T_{c_{avg}}$) was dependant on bacterial concentration. The culture concentration at the end of the first experiment (38 h) was considered to be 100% (neat). Around 5 ml of the neat suspension was added to the cuvette and the speckle experiments were performed for 30 min. In order to obtain a 50% dilution, 2.5ml of neat culture was mixed thoroughly with 2.5 ml of prewarmed broth in a cuvette and speckle study was performed for another 30 min. Likewise, a neat culture 1.25 ml was added to 3.75ml of prewarmed broth to give a 25% dilution. Finally, 0.5 ml was added to 4.5ml of prewarmed broth in a cuvette to produce a 10 % dilution and experiments performed as mentioned before.

3.3 RESULTS AND DISCUSSION

Figure 3.5 shows the comparison of growth curves (cfu/ml) of *E. coli* for both experiments (See Figure 3.2). **Figure 3.6** shows the same data plotted on a logarithmic scale. As would be expected, the cfu/ml increased over time. As the fresh stock of *E. coli* is added to the nutrient broth (LB) after 13 h, in the second experiment, the cfu/ml (see Figure 3.5) increased only thereafter but until then it remained constant because the broth was sterile. For the first experiment *E. coli* was added at time 0 and rapid increase in the cfu/ml was observed. Otherwise the growth curves for the two experiments were very similar.

Figure 3.7 shows a considerable difference in the colony growth among two different dimensions of the reference cuvettes over a period of 38 h. This may be because the greater surface area of the culture provided by the quartz cuvette allowed a better aeration, leading to more rapid growth of the microorganisms than in the universal bottle.

Figure 3.8 shows results from the second experiment showing the reduction in volume (cm^3) and rate of volume drop ($\mu\text{L}/\text{min}$) over the period of 38 h for both cuvettes. It was found that about a 14 % volume reduction was observed with the universal bottle whereas for the quartz cuvette there was a 70% volume reduction. This explains the advantage of using a lid to close the cuvette while doing the first experiment.

Figure 3.9 shows the values of Tc_{avg} plotted as a function of time for both the first and second experiments. Another separate graph was plotted to explode the details of the second experiment (vertical transmission) see **Figure 3.10**. Tc_{avg} is a parameter derived from the time varying autocorrelation width (Tc), calculated from the e^{-1} values of the autocorrelation function from the line scan signal. The nutrient broth alone did not contribute significantly to the speckle pattern. Consequently, there was little variation in Tc_{avg} for the second experiment until the bacterial sample was added at 13 h. From this point the Tc_{avg} graph decreased until 30.5 h and then there was a slight increase. A similar shaped graph was observed for the first experiment (horizontal transmission) as shown in Figure 3.9. It should be noted that for the second experiment, the graph after 13 h followed the same shape as that of first experiment from the beginning. As the bacteria started growing at the nascent stage itself in case of the first experiment, the Tc_{avg} values showed greater sensitivity (i.e. greater variation) than for the second experiment.

In an attempt to decouple information relating to motility and concentration, the data in Figures 3.9 and 3.10 was normalized to the bacterial concentration and can be seen in **Figure 3.11**. It is seen that overall there was a downward trend in Tc_{avg} with time; a possible indication of reduced motility or change in some other characteristic of the organism with increasing age. Interestingly for the first experiment, there was essentially no change in Tc_{avg} for 4 h; then a sudden change was observed after another 7.5 h. Tc_{avg} then plateaued for about 13.5 h with only a small decrease observed. This was followed by a slightly sharper decrease in Tc_{avg} for the remainder of the experiment. The above results suggest that Tc_{avg} normalized to the bacterial concentration possibly be a function of motility or some of the characteristic of the microorganisms. Consequently to verify the dependency of the Tc_{avg} parameter on motility, a calibration experiment was performed with various dilutions of *E. coli* samples during the second phase of the second experiment.

Figure 3.12 shows Tc_{avg} plotted as a function of the seeded bacterial concentration, where 100% was 1.5×10^{10} cfu/ml. As mentioned in section 3.2.6, the *E. coli* culture was diluted to the desired concentrations. Tc_{avg} reduced from a maximum value of 10.8 at 10 % concentration to a minimum at 25 %. From this point the value increased slightly. Comparing this graph with Figures 3.9 and 3.10, it is seen that curves follow similar shapes as that of the first experiment (0-38 h) and second experiment (13-38 h). Thus Figure 3.12

suggests that an increase in Tc_{avg} may be related to the changes in motility of the bacteria. The same fact was implied theoretically by Figure 3.11.

In an attempt to identify the effects of motility and concentration on the speckle patterns, the value of Tc_{avg} was normalized to the bacterial concentration. **Figure 3.13** shows the data plotted as a function of bacterial concentration. It is seen that the normalized value of Tc_{avg} is much greater at 10% (low concentration) than at 100% (neat). This suggests overall that the scattering centers are moving much more rapidly for the lower concentration than the higher. Additionally, for the neat solution (100%), most of the nutrients would have been used and the organisms would be seeking nutrients and hence less motile because of starvation. With dilution with a prewarmed broth, the organisms would become refreshed and more motile.

It would be interesting to compare the absolute value of the differential between the standard deviations of a motile, vegetative *E. coli* cell and immotile non-vegetative *S. aureus*. **Figure 3.14** shows a relatively linear progression ($R^2 = 0.7841$) for a dilution series 50%, 75% and 100%, as done identical to Figure 2.8 which showed a linear progression ($R^2 = 0.9025$) for increasing dilutions in series of 10^{-x} .

The volume of the broth evaporated during the initial 13 h of the first experiment was measured from the cuvette scales shown in Figure 3.4. The calculation revealed that the volume of the nutrient broth was reduced from 10.000 ml to 7.727 ml (22.73% loss) over 13 h. It was interesting to identify the effect of this volume drop on Tc_{avg} . As mentioned earlier in this section, Tc_{avg} is dependent on the motility of the constituents in the medium and Figure 3.10 clearly shows that Tc_{avg} showed little changes during the first 13 h as the medium contained only broth without any *E. coli*. This parameter, therefore, does not vary even during evaporation showing that any movements in the broth constituents do not contribute to change in Tc value during that time.

Figures 3.9 and 3.10 also shows considerable differences in the Tc_{avg} values in the first and second experiments, with the parameter values showing huge variation between successive values in each experiment. With the second experiment, the cuvette was not kept open within the incubator, with prewarmed culture added later allowing evaporation to happen rapidly at the rate of 175 microlitre /hour. Though prewarming allowed the organism to

grow, evaporation at this rate would reduce its effect. This is reflected in $T_{c_{avg}}$ values with less variation among the successive values in this second experiment. The first experiment consists of sealing the cuvette and with no prewarming of the culture. Thus, the growth was not encouraged by prewarming yet the bacteria grew rapidly and growth continued for the whole duration of the experiment. Thus, the first experiment with the lid closed gave good results and $T_{c_{avg}}$ was sensitive. The other reason for the sensitivity of the first experiment is that the beam here is allowed to traverse through the cuvette for only a certain depth which is independent of the level of the medium in the cuvette. But under the second experiment, the beam passes through the whole depth of the sample which will eventually have a reduced volume due to evaporation. Thus it was interesting to note that $T_{c_{avg}}$ has been able to identify the process under both transmission experiments though there was a volume reduction. Yet for maximum accuracy and stability of the results, it proved useful to close the lid of the cuvette and adopt a first transmission experiment.

Figure 3.15 shows the variation of the autocorrelation function in the spatial domain for 10% and 100% (100% concentration is 1.5×10^{10} cfu/ml) concentration. It is implied that for the concentration where $T_{c_{avg}}$ values are less, the spatial autocorrelation graph shows fewer peak values. Thus the curve with less concentration appears with higher values than that with the higher concentration. Since a space-varying autocorrelation function of a static biospeckle is directly related to the number and the average size of speckle grains, this function is directly related to the concentration of the organisms.

As mentioned in section 2.3.1, Figure 2.5, any small particle (or microorganism) illuminated by a laser beam produces a diffraction pattern with an approximate intensity distribution of $\{[2J_1(r)/r]\}^2$, where $J_1(r)$ is the Bessel function of the first order. When more particles (or microorganisms) distribute inside the illuminating volume randomly, more coherent diffraction patterns are created. In general, the original diffraction pattern of $\{[2J_1(r)/r]\}^2$ breaks into more sections and creates a complicated structure, consisting of many small and irregular spots. The bright area is then reduced. Figure 3.15 shows that the higher the concentration of the culture, the smaller the bright speckles and the sharper the autocorrelation pulse. This technique may prove to be an auxiliary method for detection of the rate at which the bacterial growth changes with time (growth ratio).

3.4 CONCLUSIONS AND FUTURE SCOPE

These experiments show that the laser speckle system employed in this application was useful in determining the presence of microorganisms, their growth and motility. In this system, it was found that the correlation parameter ($T_{c_{avg}}$) derived from analysing the speckle-data in the spatial and Fourier domain provided details about the motility of the bacterial culture. Additionally, the gradient of $T_{c_{avg}}$ plotted against time was at its highest value for low concentration, indicating that the system has a high sensitivity to low bacterial concentration.

Figure 3.16 shows the results from the optical photometer measuring the optical density of the growing *E. coli* culture under the same conditions. It is interesting to see that the photometer was quite efficient in detecting changes in the concentration of the samples for only certain peak concentrations of the medium. When the sample was during its nascent stage of its growth, the optical density values were below 0. It began to increase as the culture grew, capable of detecting the changes in the concentration until a threshold was reached with an optical density of 2.0. When there was a large population, the photometer was not able to ascertain the optical density accurately due to poor transmission and internal reflections inside the photometer. Thus it is evident that the proposed laser speckle system employed in this application could be utilized for detecting the motility of organisms where there is a concentration that cannot be ascertained using a standard optical density photometer.

Extending the one dimensional study to three dimensional studies:

Instead of considering a single TV line, if all the lines were considered, this would provide better results from the analysis. This requires high end computers for capturing the images, storing and rapid analysis. An idea to determine the velocity of a scattering centre was formed from the equation described in Chapter 2.

$$Tc = \frac{1}{|v|} \left(\frac{1}{w^2} + \frac{\sigma^2}{\Delta x^2} \right)^{-\frac{1}{2}} \quad (3.1)$$

From this theoretical equation, the velocity of the scatterers can be ascertained. This is achieved by convolution. The point spread function (PSF) can be calculated from a single frame from the speckle pattern. When this function is convolved with the velocity function,

it gives the PSF of the moving blurred image. By deconvolving the point spread function of the actual image from the PSF of moving image, the velocity function or the motion function could be found.

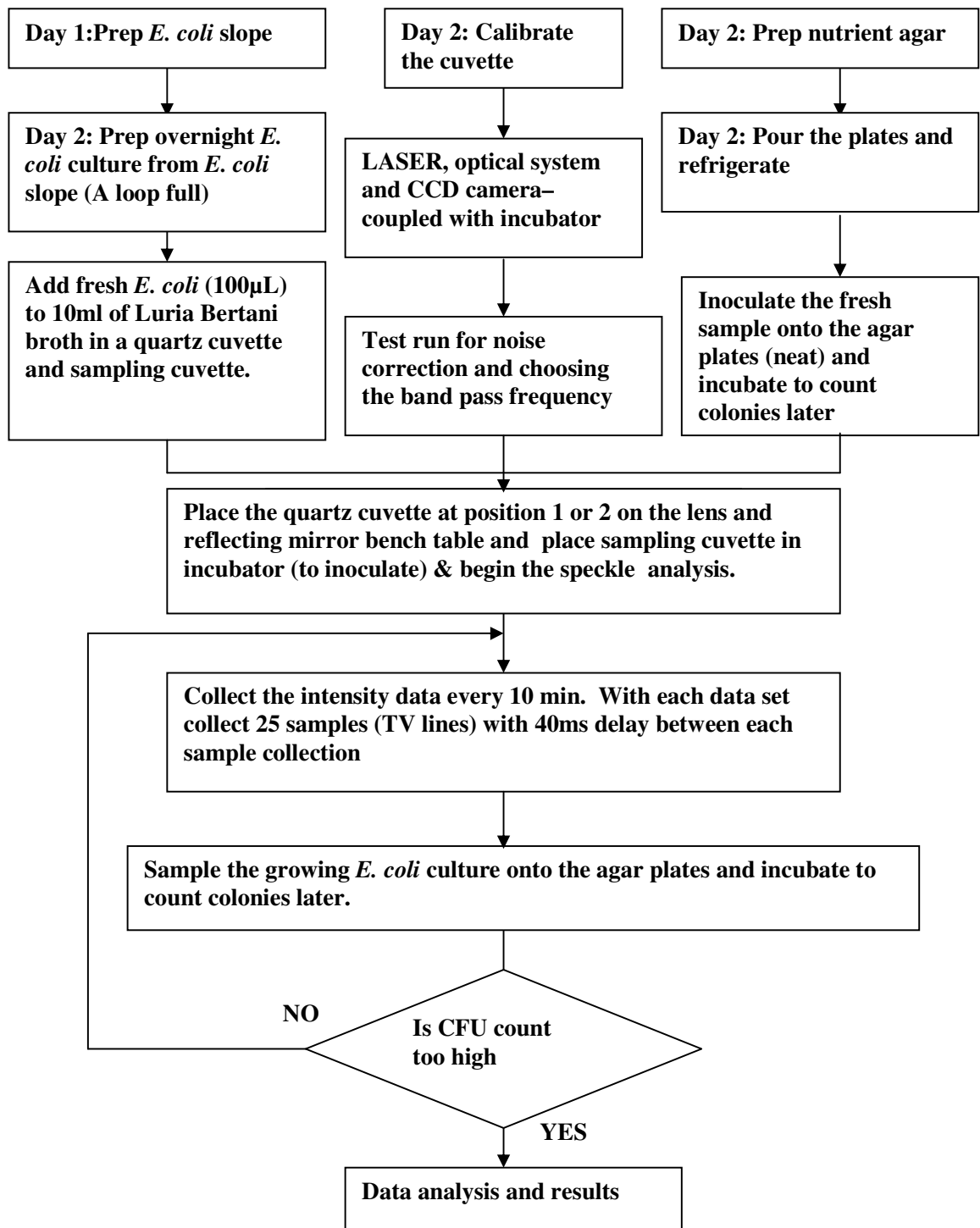


Figure 3.1 The typical work scheme for *E. coli* for the first experiment (horizontal transmission) and second experiment (vertical transmission).

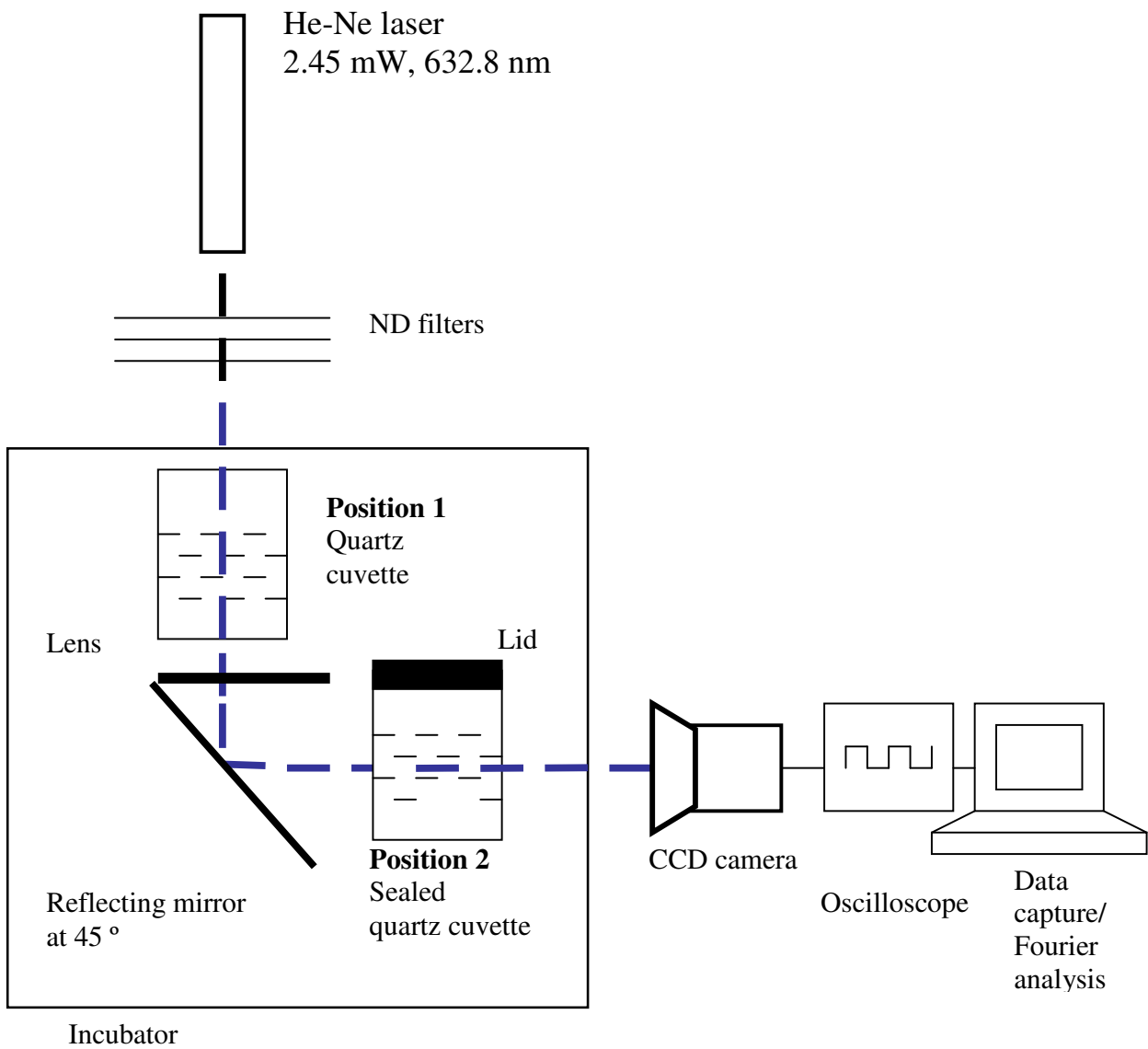


Figure 3.2 Schematic view of the hardware setup and optics; the cuvette is placed either at position 2 (horizontal transmission, first experiment) or position 1 (vertical transmission, second experiment).



Figure 3.3 Incubator setup and the optics.

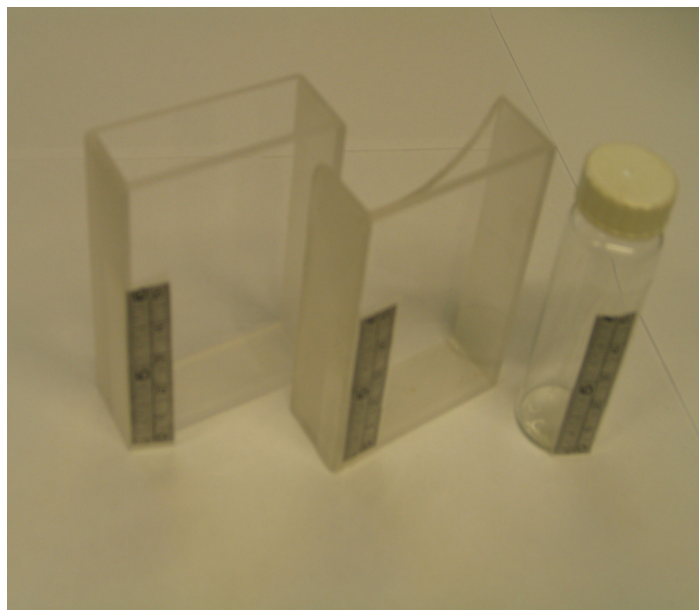


Figure 3.4 Cuvettes employed in the actual experiment.

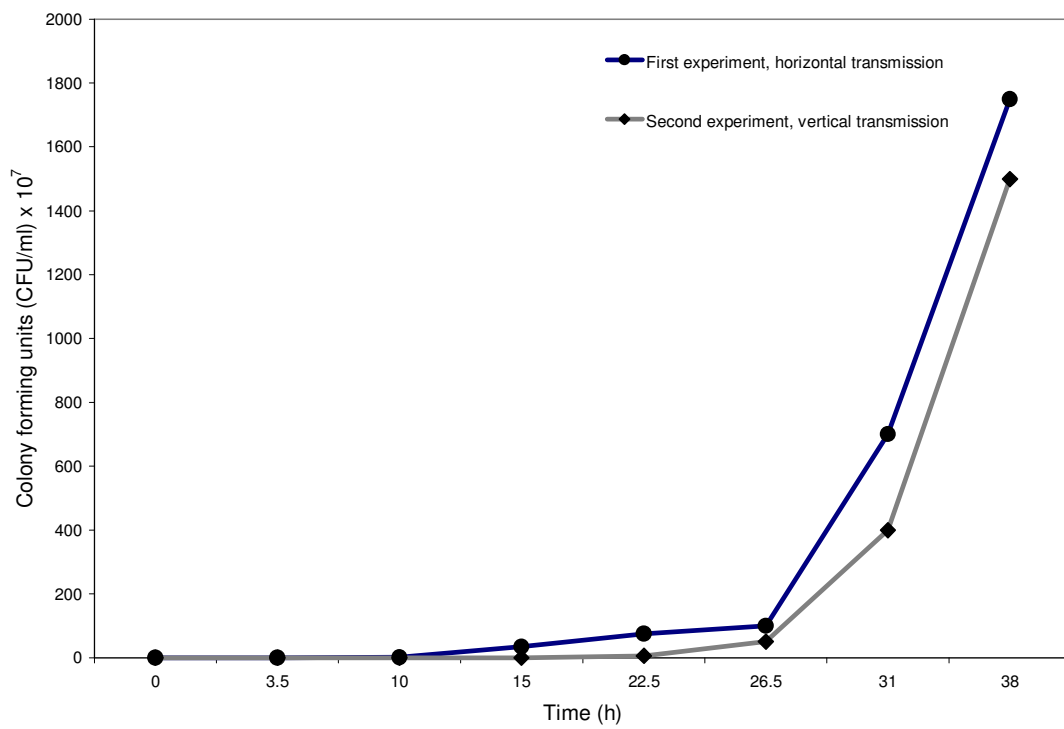


Figure 3.5 Growth of *E. coli* for the first (horizontal transmission) and second (vertical transmission) experiments.

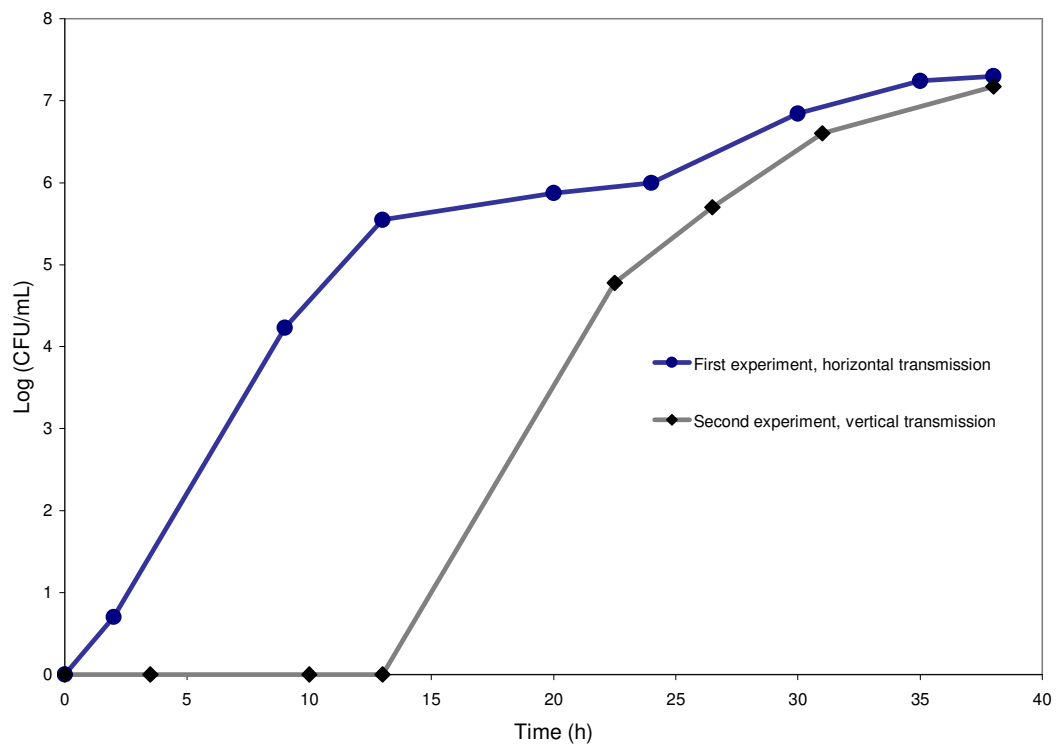


Figure 3.6 Growth of *E. coli* drawn on a log scale for the first (horizontal transmission) and second (vertical transmission) experiments.

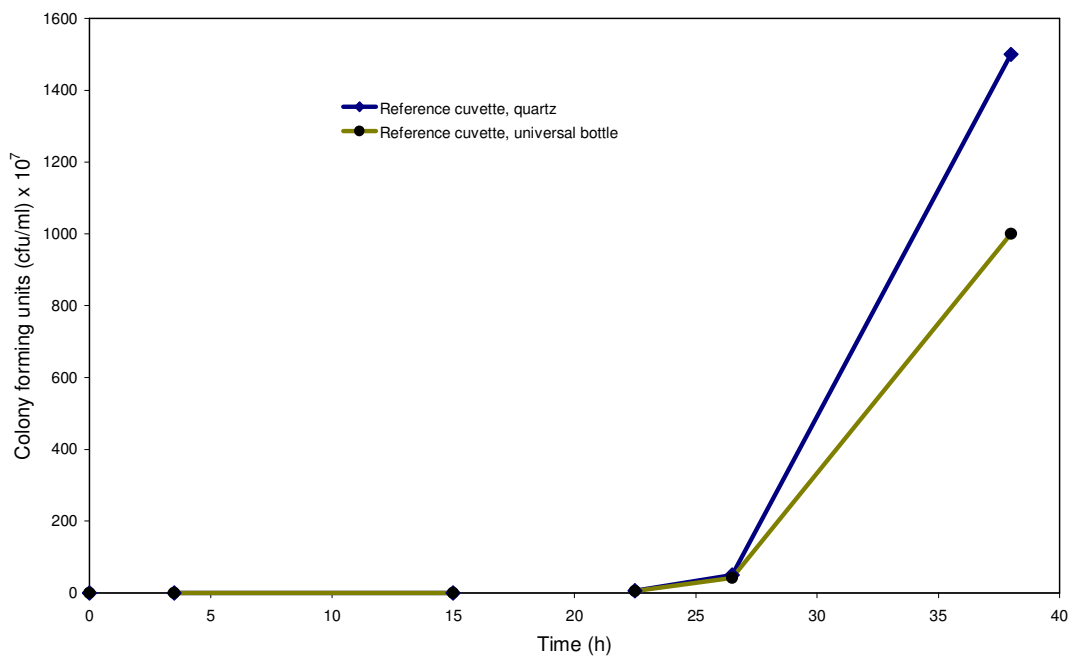


Figure 3.7 Effect of different cuvettes on growth of *E. coli* in the second experiment.

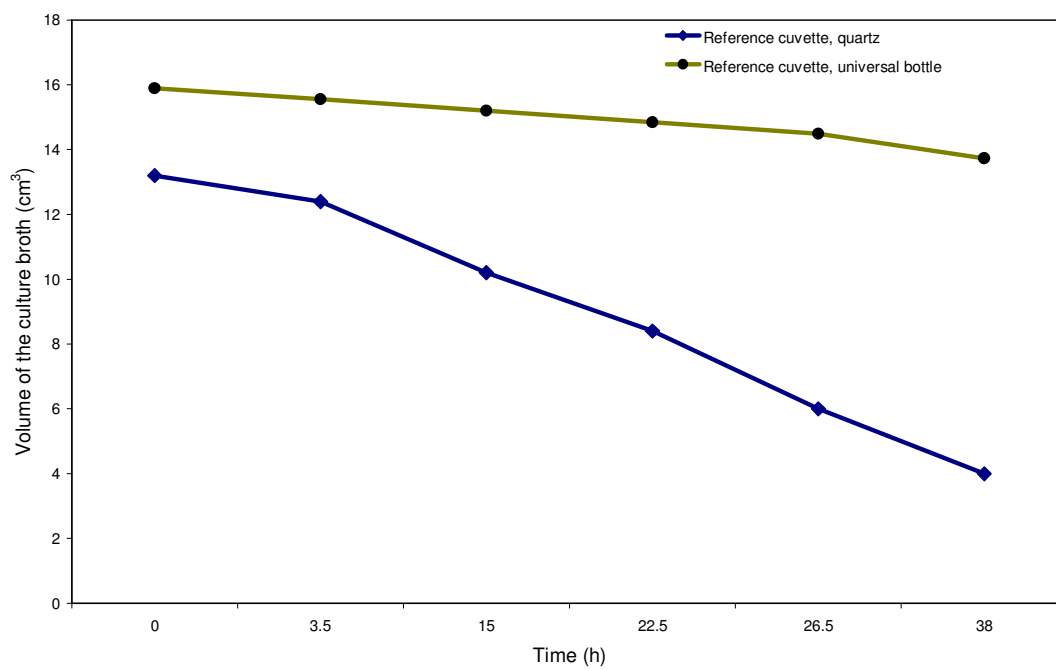


Figure 3.8 Volume drop in LB broth in the second experiment, for different cuvettes.

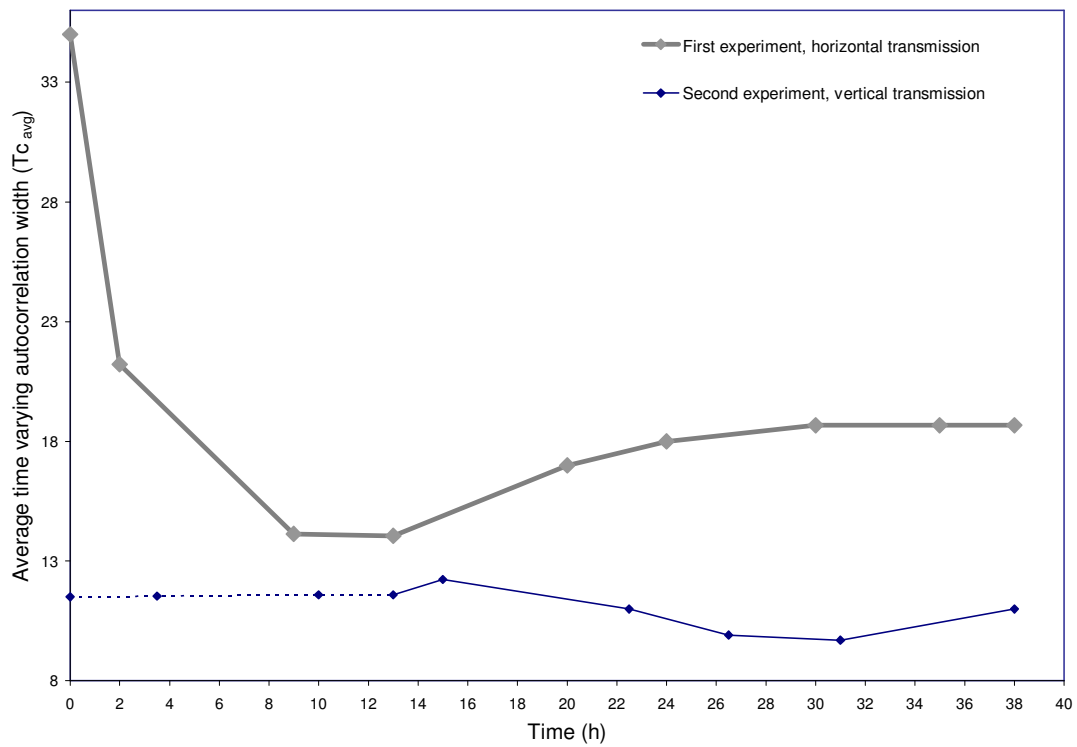


Figure 3.9 Variation of $T_{c_{avg}}$ for the first experiment (horizontal transmission) and the second experiment (vertical transmission). The dotted line indicates the broth prewarming phase of the second experiment.

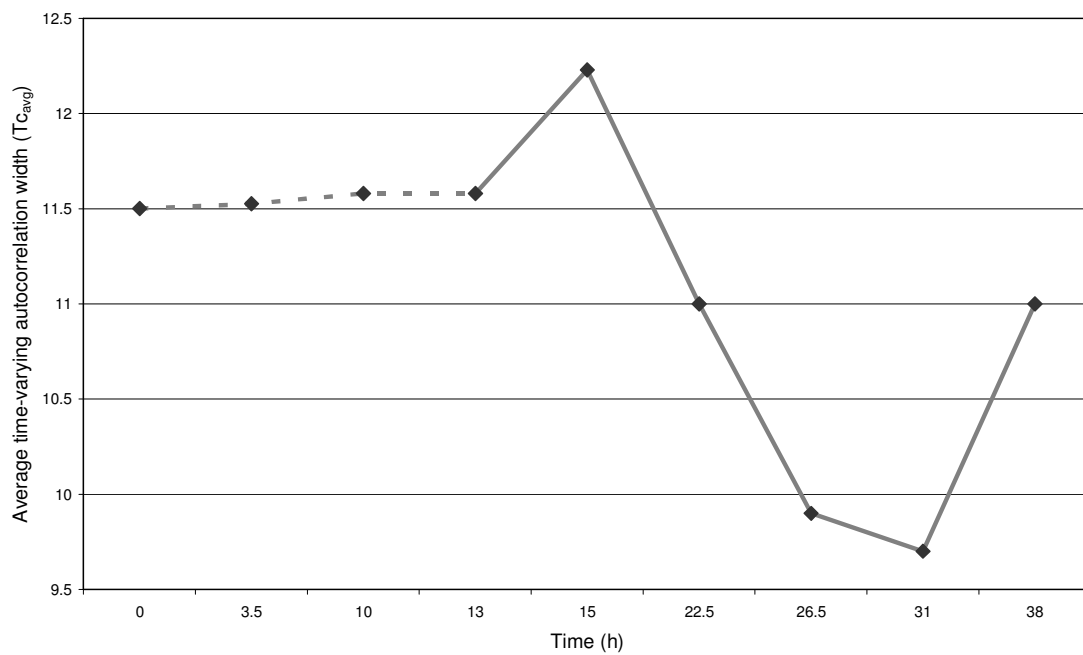


Figure 3.10 Variation of $T_{c_{avg}}$ for the second experiment (vertical transmission). The dotted line indicates the broth prewarming phase. This Figure is an exploded view of the experiment as shown in Figure 3.9.

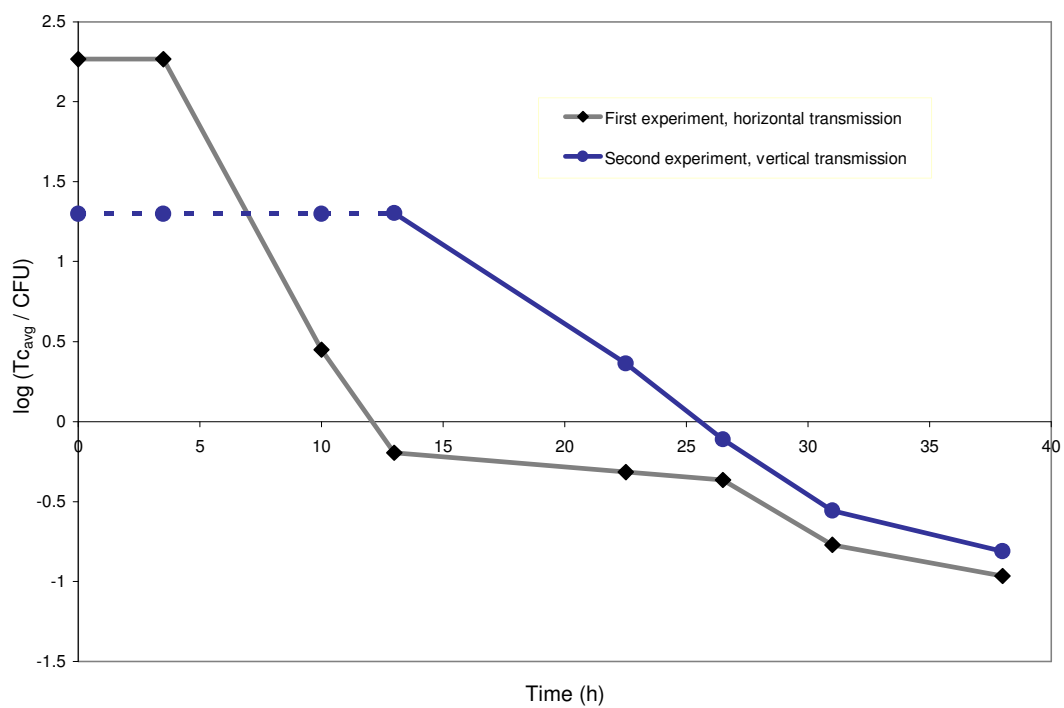


Figure 3.11 Change in $\frac{Tc_{avg}}{CFU}$ (log scale) in the *E. coli* culture for both the first and second experiments. The dotted line indicates the broth prewarming phase, before inoculation.

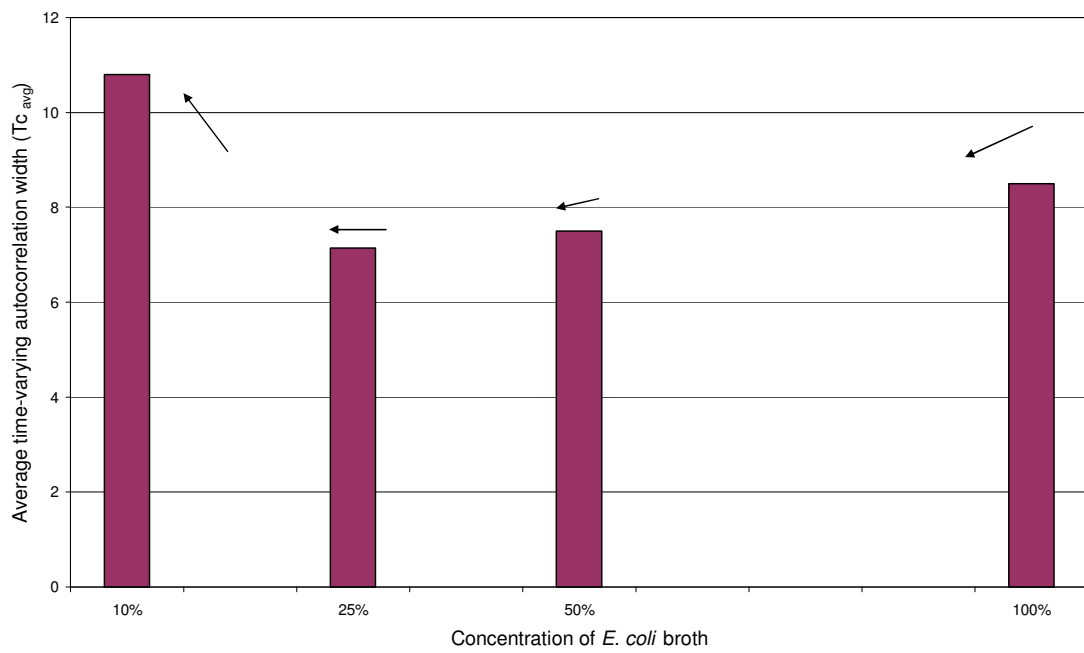


Figure 3.12 Variation of $T_{c_{avg}}$ through serial dilution for the third experiment (where 100% was 1.5×10^{10} CFU/ml).

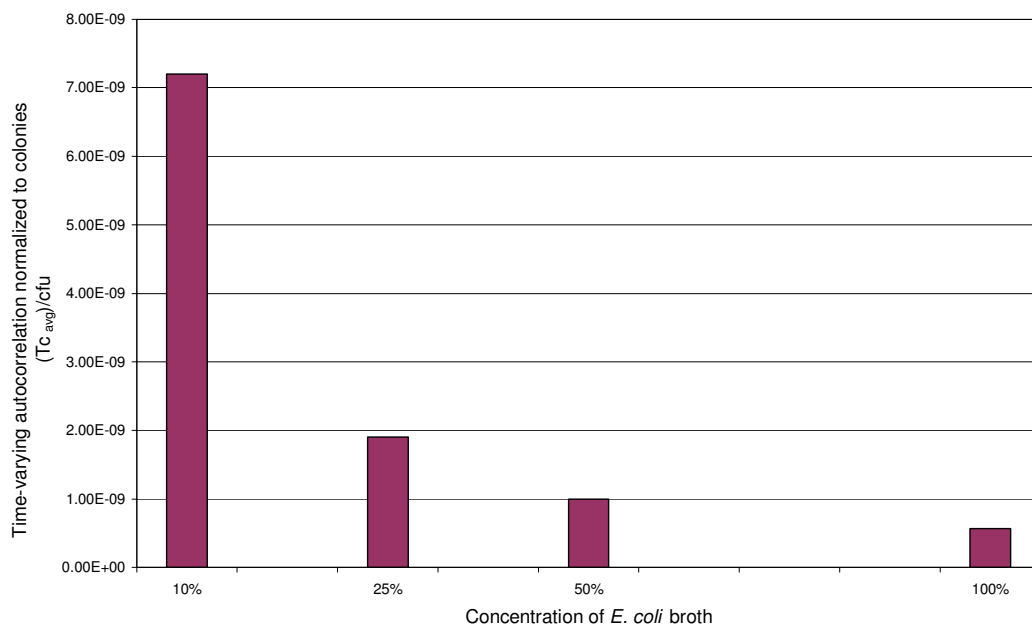


Figure 3.13 Variation of the normalized Tc_{avg} through different serial dilutions for the third experiment (vertical transmission), using *E. coli* in broth.

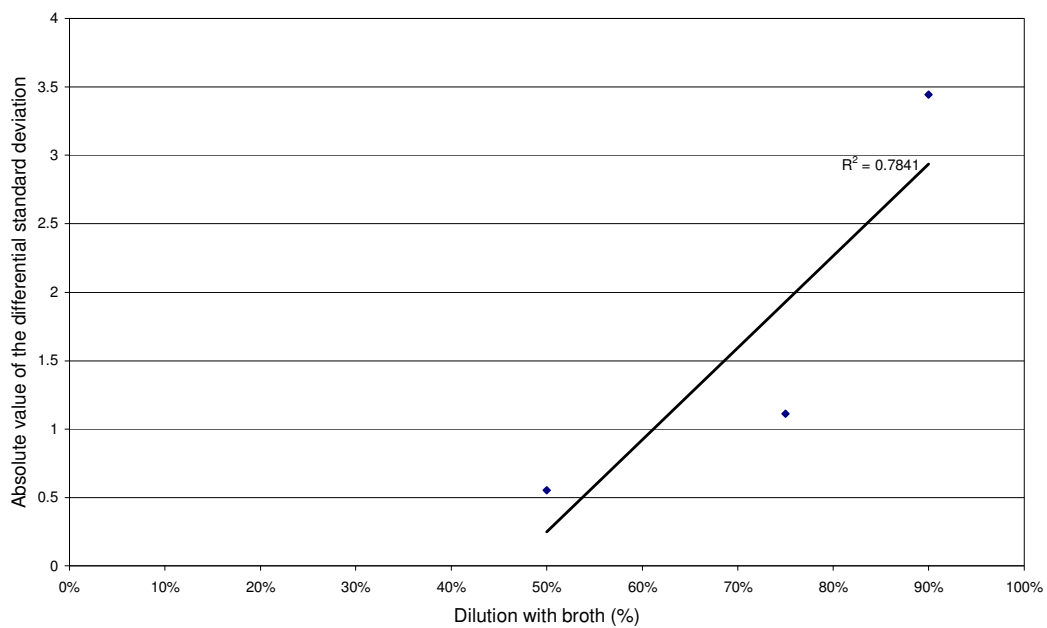


Figure 3.14 Absolute value of the differential between the standard deviations of the $T_{C_{avg}}$ for back dilutions shown in Figure 3.12.

Note that there exists a difference in the representation of the X-axis between this Figure and Figure 3.12. This Figure expresses the values in the X-axis as a percentage of the dilution. Here 10% represents 90% dilution (whereas in Figure 3.12 it means 90% neat).

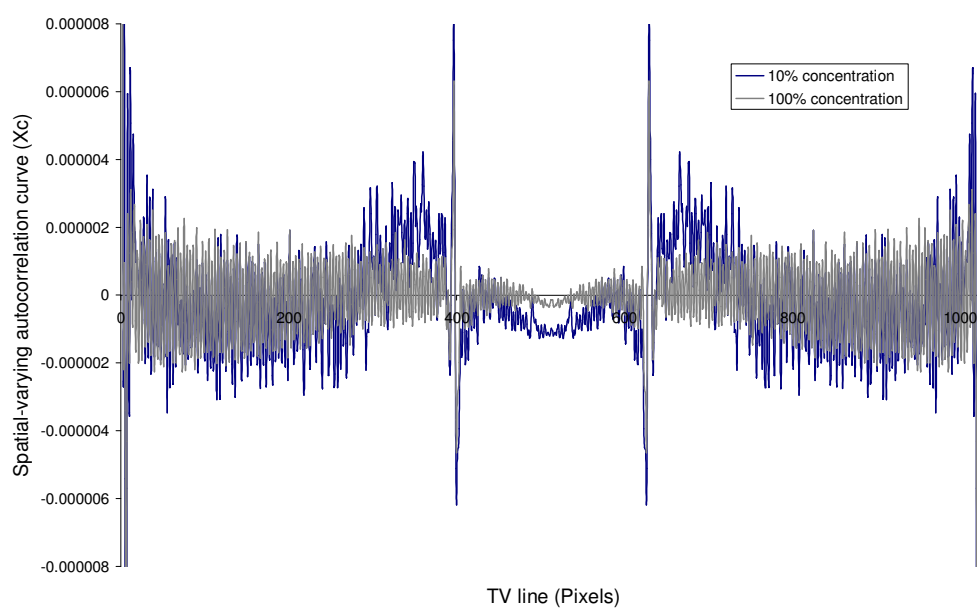


Figure 3.15 Variation of spatial autocorrelation for different concentration of the *E. coli* culture for the third experiment.

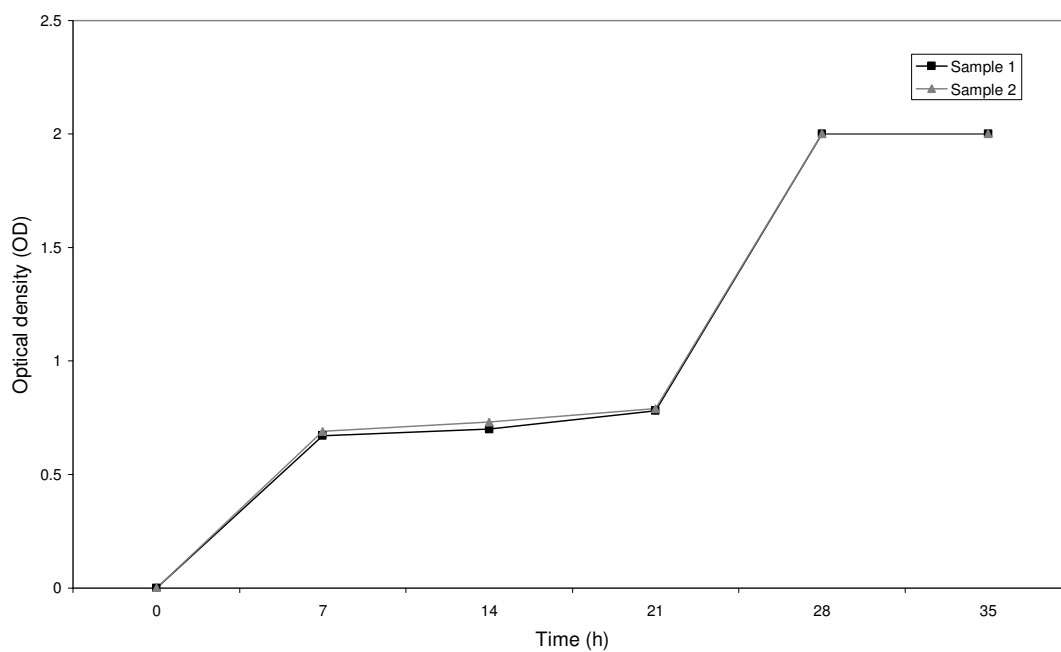


Figure 3.16 Changes in the optical density of the *E. coli* culture over period of 36 hours of sampling for two different samples.

CHAPTER 4 QUANTIFYING MORPHOLOGY DYNAMICS OF *EUGLENA GRACILIS*

4.1. INTRODUCTION

Significant research has been undertaken on assessing methods of tracking and identifying the motility of microorganisms. The photo-tactic movements of microorganisms have been predicted by reconstructing the spatiotemporal tracks by obtaining the cell movement parameters (Gualtieri *et al.*, 1988). The measurement of *Euglena gracilis* motion parameters such as the distributions of the cell rotation, flagella beating frequency and swimming speed were quantified via the spectral analysis of scattered laser light with the samples orientated by a radiofrequency field (Ascoli *et al.*, 1978).

In this work, *Euglena gracilis* was chosen as it provided an ideal, well known model to investigate transient analysis imaging methods of live cells. Additionally, *Euglena* is used in mutation research, pharmaceuticals studies (Brain *et al.*, 2004), as models for the study of trypanosomes and other parasitological diseases (Martin and Borst, 2003) and space biology (Hader *et al.*, 1998) where experiments were conducted under terrestrial and microgravity conditions to study gravitaxis and phototaxis.

Euglena gracilis is just one of many species of *Euglena* belonging to the protist kingdom. *Euglena gracilis* are typically 35-55 μm long, 6-25 μm wide (Lee *et al.*, 2000) and with a long hair-like flagellum that is used for translocation, moves at velocities of the order of micro-meter per second. The cell's morphology varies between cylindrical to elongate and ovate (Alexander and McNeill, 1979). Its morphological structure is dependent on internal microtubule arrangements within the cytoskeleton (Lonergan and Lachney, 1985). The effects of the biological clock, respiration and photosynthesis on the cell shape have been investigated. Various microscopy methods have been used to study *Euglena gracilis* including indirect immunofluorescence microscopy (Pablo *et al.*, 2003). Here the fluorescence image of the *Euglena* cells were analysed at low temperatures and at elevated Ca^{2+} levels. The fluorescence image stability was assessed in relation to the cell's microtubule arrangement (Mermelstein *et al.*, 1998). Often, simple bright field microscopy is used for cell analysis; if there is insufficient contrast in the subject matter, artificial

staining techniques are employed. Although *Euglena* is clearly seen under bright field microscopy, it is not easy to see cilia or most organelles.

The role of respiratory and photosynthetic pathways in the cell shape changes were investigated with energy pathway inhibitors. By growing cells with different inhibitors under the synchronizing effect of a daily light-dark cycle, the mean cell length of the population was monitored (Lonergan, 1983, 1984). In the present case, the performance of a bright field microscopy system was assessed. A video camera was used to capture images of *Euglena gracilis* and these images were processed and analyzed to quantify the morphological structure and temporal characteristics. The performance of image processing methods before and after filtering was compared with visual assessment and measurement methods.

4.2. MATERIALS AND METHODS

4.2.1. *Euglena* and sample preparation

A stock culture of *Euglena gracilis* on a slope of fresh *Euglena gracilis*: Jaworski's medium (Oxoid L11) was kindly provided by Mrs. Dorothy Armstrong, IBLS, Division of Infection and Immunity, GBRC, University of Glasgow. A loopful of this culture was inoculated into a fresh EG : JM (Oxoid L11) and the culture was incubated at 15 °C, under a 12:12 hour (light: dark) regime to create a primary culture. The illumination was provided by non-thermal white fluorescent lamps with a photon flux density of 50 $\mu\text{mol m}^{-2} \text{s}^{-1}$ at the surface of the culture flask. Cultures were maintained in 100 ml conical flasks containing 50 ml of the medium and are normally named as secondary cultures and were used for all the microbiological experiments. 10 μL samples of these cultures were pipetted onto plain microscope slides and viewed under the microscope system as described below.

4.2.2. Microscopy and image capturing system

Experiments were done with a bright-field microscopy system (**Figure 4.1**) optimized for high contrast and kept under ambient environmental conditions. The image capturing system comprised a ToUcam PRO II camera (Philips, UK) with a pixel resolution of 640 x 480, connected to the microscope and a PC. Video (25 frames per second) was collected for off-line processing and analysis. Images (BMP format) from the video (AVI format) were extracted using Arcsoft Video Impression (Version 1.6, ArcSoft, Inc., California) and

converted to FITS (Flexible Image Transport System) which is a standard data format designed by NOST (NASA/Science Office of Standards and Technology).

In order to assess the morphological changes of the microorganism it is necessary to relate the structural changes of the *Euglena* to corresponding changes in the images either in the space or spatial frequency domain. This was achieved by selecting and arranging a series of images from the video stream that were representative of the *Euglena* in different morphological states - from circular (broadest) to elongated. This was achieved by three different means: visual assessment, simple measurements in the spatial domain and image analysis methods.

4.2.3. Visual assessment method

The performance of the algorithms at ranking or quantifying images was compared to human visual assessment. 6 images were given to 12 different volunteers (see **Figure 4.2** for numbering) and they were requested to visually assess the shape of the *Euglena* cell and arrange the pictures in the order of changing shape from the broadest and bulkiest to the narrowest and most elongated.

4.2.4. Measurement method

Measurement methods included were:

- 1) direct measurement of the cellular eccentricity (a / b);
- 2) the major axis (a) divided by the sum of the widths at 3 different positions (equally spaced through out the cells length i.e. $a / (b_1+b_2+b_3)$);
- 3) the average eccentricity i.e. $(a / ((b_1+b_2+b_3)/3))$;
- 4) the area ;
- 5) the eccentricity normalized to the cell's area;
- 6) summed eccentricity normalized to the cell's area;
- 7) the average eccentricity, normalized to the cell's area.

4.2.5. Image analysis methods

In this method, the images were either converted immediately into the frequency domain or passed through a high-pass filter, edge-detected and the background noise removed before converting to the frequency domain, where the Power Spectral Density (PSD) was found.

Astroart was used for this purpose. The PSD images, with or without prefiltering, were analysed with various algorithms in an attempt to quantify the morphological state of the cell. Astroart was used to calculate the average pixel intensity and intensity standard deviation (see section 4.2.6.1 and 4.2.6.2). A program in MAPLE (Version 8.00, Waterloo Maple Inc., and USA) was written for calculating Gaussian standard deviation (see section 4.2.6.3) and Proprietary software written in MATLAB (Version 6.5, The MathWorks, Inc., and USA) was written for processing and analysis using correlation techniques (see section 4.2.6.4).

4.2.5.1 Image conversion to bitmap formats and RGB coding

As mentioned in section (4.2.2), the series of images selected from the video stream are converted into the bitmap file format (*.bmp). Bmps are the basic way of representing any coloured image in a computer's memory. A Bitmap is constituted of rows of pixels. Each pixel has a particular value that determined its appearing colour. This value is qualified by three numbers giving the decomposition of the colour in the three primary colours red, green and blue. The decomposition of a colour is quantified by a number between 0 and 255. Thus a white colour will be coded as $R = 255, G = 255, B = 255$; black will be coded as $R = 0, G = 0, B = 0$; and say bright pink will be coded as $(255,0,255)$. An image is an enormous two-dimensional array of colour values, pixels, each of them coded as 3 bytes, representing the three primary colours. Thus an image can contain $256 \times 256 \times 256 = 16.8$ million different colours.

By principle of vectors, colours can be interpreted as vectors in a three dimension space where each axis stands for one of the primary colours. Therefore the geometric mathematical concepts can be applied to deal with the colours, such as norms, scalar product, projection, rotation or distance.

4.2.5.2 Image-adaptive high-pass filtering

The images were high-pass filtered which removed the lower frequency components of the image. This filter is often used to increase sharpness, but can also increase noise. By using a full scale adaptive high-pass filter, the generation of dark areas around bright components of the images was prevented (Nascimento and Sayed, 2000). High-pass spatial filters often have large kernel centres (e.g. 20, centre of the matrix), so that the images with high

frequency changes are amplified and multiplied many times over. The negative coefficients are used to negate the large kernel centres, the chosen values can be seen in (4.1). Therefore, areas of the image that have large intensity changes are intensified, while areas of the image that have little or no change are not intensified. **Figure 4.3** shows the intensity distribution of the high pass filtering that was used on images of *Euglena gracilis*.

$$\begin{bmatrix} 0 & -1 & 0 \\ -1 & 20 & -1 \\ 0 & -1 & 0 \end{bmatrix} \quad (4.1)$$

Each number in the matrix is called a convolution coefficient and all the values in the 3x3 square of pixels are added up in order to make the normalization constant (0-1+0-1+20-1+0-1+0 = 16). The process of digital filtering is to multiply each of the surrounding pixels by the corresponding convolution coefficient and divided by the normalization constant.

4.2.5.3 Image edge-detection filtering

Edge-detection, or contour, filters are used in a variety of applications from counting blood cells (Barber *et al.*, 2000) to identifying fossils and geographical applications (Lyberis and Mering, 2004). There are variety of edge detection filters, such as Sobel, Prewitt, Freeman and Kirsch (Argialas and Mavrantza, 2004). In the present case, a two dimensional Sobel filter was used (Gonzalez *et al.*, 2004).

Typical horizontally Sobel filters was defined as

$$\begin{bmatrix} 1 & 2 & 1 \\ 0 & 0 & 0 \\ -1 & -2 & -1 \end{bmatrix} \quad (4.2)$$

$$\begin{bmatrix} 2 & 1 & 0 \\ 1 & 0 & -1 \\ 0 & -1 & -2 \end{bmatrix} \quad (4.3)$$

and typical vertical Sobel filters was defined as

$$\begin{bmatrix} 1 & 0 & -1 \\ 2 & 0 & -2 \\ 1 & 0 & -1 \end{bmatrix} \quad (4.4)$$

$$\begin{bmatrix} 0 & -1 & -2 \\ 1 & 0 & -2 \\ 2 & 0 & -1 \end{bmatrix} \quad (4.5)$$

The robustness of the parameters derived from the PSD images were compared in determining the shape characteristics of the *Euglena* cells. **Figure 4.4** shows images at each stage of the analysis, in this case for a spherical morphology. The original image was high-pass filtered and then edge-enhanced. Additionally, the background image was processed identically and subtracted from the edge-enhanced original image. As a comparison, images are shown of the original image *minus* the background image and the original image high pass filtered *minus* the high pass filtered background image. It is seen visually that the edge enhancement improves the image before the PSD is taken, resulting in an improved PSD image.

4.2.6 Algorithm development

In this study, unfiltered and filtered images derived from the video stream of the *Euglena* cells in motion were analyzed both in the time and frequency domain. It was then necessary to define a parameter that provides a measure of the characteristics of the image i.e. the real time spatial frequency behaviour of the protist. Ideally, the parameter should allow the state of the microorganism to be identified with adequate variation or sensitivity in that parameter to account for the changes in the cell shape. The variation in this parameter can then be assessed over time to quantify the dynamic behaviour of the cell. From the power spectral density (PSD) images, the average pixel value and standard deviation (defined below) were determined and compared for different cell shapes. Additionally, as the cell shape changed as a function of time the rate of change was investigated until cell death or complete lack of motility. In addition to these parameters, a correlation analysis was done on these images where a time 0 reference image was taken with the cell approximately spherical.

4.2.6.1 Average pixel intensity

The average pixel value of the image is defined as the ratio of the sum of all pixel values ($X_{(r,c)}$) where r is the r^{th} row and c is the c^{th} column to the number of pixels in the image (N), and given by

$$\bar{X} = \frac{\sum_{r=0}^{255} \sum_{c=0}^{255} X_{(r,c)}}{N} \quad \text{where } r = 0 \dots 480; c = 0 \dots 640 \quad (4.6)$$

4.2.6.2 Standard deviation of the pixel intensity

The standard deviation of the pixel intensity is defined by

$$\sigma = \left(\frac{1}{N} \sum_{i=1}^N (X_i - \bar{X})^2 \right)^{1/2} \quad \text{where } N = 1 \dots 307200 \quad (4.7)$$

Where X_i is the intensity for the i^{th} value, where $i = 1$ to N .

4.2.6.3 Gaussian standard deviation

As the PSD image resembled a Gaussian function, a parameter was identified to give a measure of the best Gaussian fit to the data. By converting the PSD image to a graph of irradiance vs spatial frequency, the Gaussian fit of this image was ascertained as

$$\sigma_g = \pm \frac{r_g^2}{\sqrt{\text{Lambert}(4w)}} \quad (4.8)$$

Where r_g is the radius of the assumed cylindrical portion of the 3D Gaussian curve, and

$$w = \frac{\pi^2 m^2 r^4}{S^2}, \quad (4.9)$$

Where S is the total sum of all the pixels of the PSD image and m is the peak intensity value obtained from the PSD image. The denominator contains an explicit expression based on the Lambert function. The *Lambert* $W(z)$ is defined as the root of

$$W(z)e^{W(z)} \quad (4.10)$$

where z is a complex number. For a given z , equation (4.10) has an infinite number of solutions and thus $W(z)$ is a multivalued function. The mathematical properties of the Lambert function have been explored only quite recently after its implementation in the mathematical library of MAPLE (Caillol, 2003). Equation (4.8) was derived through MAPLE.

4.2.6.4 Correlation analysis

Arbitrarily, the broadest cell shape as favoured by the majority of volunteers and measurement methods was taken and this image was cross-correlated with all other images in the series. In this way, the temporal shape changes are monitored from the value of the correlation function with respect to the reference image, which was taken as the broadest image of the cell.

4.3. RESULTS AND DISCUSSION

Figure 4.5 shows the visual assessment sequence from the 12 volunteers and the tabulated version, for ease of comparison and calculation is shown in **Table 4.1**. It was found that the sequence 4-1-2-3-5-6 was most common with 41.67% of the volunteers agreeing with this order. Whereas the sequence 4-1-3-2-5-6 was only agreed with by 16.67% of the population, all other sequences were agreed with by 8.33% of the population.

Table 4.2 shows the number of volunteers that agreed in placing the pictures at a particular position (i.e. 1 through 6). It was seen that the majority of the volunteers agreed for picture (1) to be in position 2, picture (2) in 3rd position, picture (3) in 4th position, picture (4) in 1st position, picture (5) in 5th position and picture (6) in 6th position. Thus the sequence 4-1-2-3-5-6 was the most common sequence. It should be noted that the volunteers were unaware of the numbers given to the pictures. This was only for convenience in identifying the pictures for analysis. This data was compared to the order that was produced from other methods of analysis. **Table 4.3** shows the area calculated from the *Euglena* cell by transferring them onto a piece of graph paper.

Figure 4.6 represents the sequences of the images as arranged by this measurement method. The score on the right represents the ratio between the methods agreeing to the total number of methods used.

Table 4.4 shows the results obtained by comparing the measurement and visual assessment methods. Scoring was done by matching the image number in a particular position to the maximum numbers of volunteers who agreed the same selection for the image to that particular position. The maximum number of volunteers agreed for the same selection was taken from Table 4.2. From Table 4.4, it was found that the sequence (4-1-2-3-5-6) calculated by the measurement method ($a / (b_1+b_2+b_3)$) produced overall the highest score of 49/72. The area calculation (first) method gave only 10/72. This suggests that the sequence (4-1-2-3-5-6) was the most agreed sequence both by visual assessment and this measurement method.

Figure 4.7 shows representative images (as in Figure 4.2) taken from a video stream of the *Euglena* motion under the bright-field microscopy system and the corresponding PSD (power spectral density) of these images without any prefiltering. There is a line running through the PSD images which is probably noise due to the camera. The PSD images were then analyzed as previously described. The average pixel intensity (Equation 4.6) was plotted as a histogram against the corresponding “shape” (sequence 4-1-2-3-5-6) to identify the discrimination capability of this analysis method, see **Figure 4.8**.

Figure 4.9 shows the intensity standard deviation of the unfiltered PSD image (Equation 4.7) plotted for the various cell shapes. It is seen that the methods employed in Figure 4.8

do not show any shape discrimination coincident with morphology whereas the intensity standard deviation of the PSD image (Figure 4.9) showed a higher value for the second broadest classification of the cell which reduced as the cell became narrower; indicating that this parameter could possibly be used to identify the morphological state of the *Euglena* cells. This could be done if the gradient of the intensity standard deviation is recorded as well.

Figure 4.10 shows the similar characteristics of Gaussian standard deviation as Figure 4.8 and in both cases the parameter value increased for the elongated shape of the *Euglena*. The error bars show the standard deviation of the parameters, as calculated from the value of four successive frames of the PSD images.

Figure 4.11 shows the crosscorrelation of every *Euglena* image with respect to the broadest shape of the *Euglena* cell. Therefore the graph will show a maximum correlation as the first value of the graph was due to the effect of autocorrelation. **Figure 4.12** shows the exploded details of Figure 4.11 relating to the lower crosscorrelation coefficients.

Figure 4.13 shows the crosscorrelation of every PSD *Euglena* image with respect to the broadest shape of the cell and **Figure 4.14** shows the exploded details of Figure 4.13. It was found that the crosscorrelation coefficients of the actual images (Figure 4.12) are more effective in shape discrimination than the PSD converted images. Though the crosscorrelation coefficient of the PSD image was sensitive enough to discriminate between the broadest and the elongated cells, it was not effective in discriminating between the intermediate shapes.

Figure 4.15 shows the effect of all the imaging parameters on the sequence arrangement of various shapes of *Euglena*. It was found that the sequence (4-1-2-6-3-5) was preferred by two different methods: average pixel intensity and Gaussian standard deviation. Interestingly the sequence (4-1-2-3-5-6) as arranged by crosscorrelation of the actual image (Figure 4.12) was also the favoured sequence by the majority of the volunteers in the visual assessment method.

An attempt was made to compare the results between the image processing parameters

before filtering and the visual assessment methods. **Table 4.5** shows the various imaging parameters, the corresponding sequences and the equivalent scores secured by those sequences in the visual assessment method (refer Table 4.2). It was found the crosscorrelation function of the actual image achieved the maximum score of 49/72 for the sequence (4-1-2-3-5-6). From Table 4.4, it was interesting that the ratio ($a / (b1+b2+b3)$) also achieved this score for arranging the pictures in the same sequence (4-1-2-3-5-6).

Another attempt was made to compare the results between the image processing parameters before filtering and the measurement methods. From Table 4.4 and Table 4.5 it was found that the sequence (4-1-2-3-5-6) gave an overall score of 49/72 for both the imaging and the measurement methods. Therefore it would be interesting to compare the relationship between the image processing parameters and ratio of major axis to summation of minor axes. **Figure 4.16** shows the variation of the average pixel intensity of the PSD converted images over the ratio ($a / (b1+b2+b3)$). It was found that the relationship was linear until picture (5) in the sequence 4-1-2-3-5-6 but increased suddenly for the elongated shape of the *Euglena*. **Figure 4.17** shows the variation of the intensity standard deviation of the PSD converted images over the same ratio and it was found that the relationship was relatively linear after picture (1) in the sequence 4-1-2-3-5-6 but started with a low value for the broadest shape of the *Euglena*. Interestingly, **Figure 4.18** shows the variation of the Gaussian standard deviation of the PSD images over the ratio ($a / (b1+b2+b3)$) and it was found that there was a perfect linear relationship between the Gaussian standard deviation and the ratio with the value of $R^2 = 1$. **Figure 4.19** shows the variation of the crosscorrelation coefficient of the *Euglena* images over the ratio ($a / (b1+b2+b3)$). It was found that there was a linear and inverse relationship with $R^2 = 0.9077$. **Figure 4.20** shows the crosscorrelation coefficient of the PSD converted images and it was found that a similar linear and inverse relationship applied with the ratio ($R^2 = 0.9484$).

Figure 4.21 shows the filtered and edge-enhanced images and the corresponding PSD for different cell morphologies including that of a dead cell (G1 and G2). **Figure 4.22** shows the average pixel intensity values from the PSD images in Figure 4.21 and **Figure 4.23** shows the intensity standard deviation values from the corresponding PSD images. The error bars show the statistical standard deviation, as calculated from the value of four successive frames of the PSD images. From this analysis it is clear that the edge

enhancement offers an improved image for discerning the cellular morphology. It was found that Figures 4.22 and 4.23 showed favourable shape discrimination coincident with that of the most preferred sequence (4-1-2-3-5-6) as determined by the previous methods. **Figure 4.24** shows the Gaussian standard deviation of the PSD images over different morphologies and this parameter was not found to give any shape discrimination.

It is seen from Figure 4.21 that the nucleus or the central core of the PSD image for the dead cell (G1 and G2) was different compared to the rest of the image and thus an attempt was made to plot the peak intensity values from the intensity standard deviation over a time period. **Figure 4.25** shows the temporal changes of the intensity standard deviation over 35 seconds and the values at death or near death, which occurred approximately 420 seconds later. As the data captured over 35 s at 25 fps would produce 875 images, the images were sampled from the video stream every 1 second to reduce computational analysis time. It is seen that the standard deviation analysis of the power spectral density images captures the shape changes as a function of time, allowing the cell activity to be quantified in real-time. Interestingly, at cell death (values to the right of the histogram in Figure 4.25) the intensity increased by about 25% of the values when the cells were alive, allowing a possible method of identifying viability. It was also found that the shape changed frequently between broadest to elongated approximately 9 times over a period of 35s.

Figure 4.26 shows representative results from the correlation analysis of the filtered, edge-enhanced images and the PSD. The filtered, edge enhanced images for different cell shape is shown in column A; column B shows the corresponding cross-correlation with the image denoted A1 (hence B1 is an autocorrelation). C and D show the PSD of A and the cross-correlation with respect to C1 (hence D1 is an autocorrelation). Peak correlation intensity values (from B) were taken from a range of data showing the cells in different morphological states (spherical to elongate) and plotted in **Figure 4.27**. As a comparison (**Figure 4.28**) the correlation peaks (from D) were identified from the PSD of the same images. **Figure 4.29** was plotted to explode the details of the low crosscorrelation coefficients in Figure 4.28. It is seen that the cross-correlation of these images show some discriminating ability as the cell shape deviated from the reference image. Interestingly, this behaviour was not observed for the correlation analysis with the PSD images. It has to be noted that B1 and D1 values indicates autocorrelation and are expected to produce a

sharp peak for the first values while plotting cross-correlation curves in Figures 4.27 and 4.28. It was found that the crosscorrelation coefficients of the actual images (Figure 4.28) are more effective than the PSD converted images (Figure 4.27). Although the crosscorrelation coefficient of the *Euglena* image was sensitive and linear, and able to discriminate the broadest and the elongated cells, it was not effective in discriminating the initial broad shape of the cell.

Figure 4.30 shows the results of all the imaging parameters on the sequence arrangement of various cell shapes. It was found that each method discriminated the morphology sequence in its own different order. Interestingly the sequence (4-1-2-3-5-6) as arranged by crosscorrelation of the PSD converted image (Figure 4.29) was also the favoured sequence by the majority of the volunteers and the measurement methods.

Table 4.6 shows the various imaging parameters, the corresponding sequences and the equivalent scores secured by those sequences from the visual assessment method (refer to Table 4.2). It was found that the crosscorrelation function of the PSD image achieved the maximum score of 49/72 for the sequence (4-1-2-3-5-6).

An attempt was made to compare the relationship between the image processing parameters and ratio of major axis to summation of minor axes. **Figures 4.31 and 4.32** show the variation of the average pixel intensity and the intensity standard deviation of the PSD converted images over the ratio ($a / (b_1+b_2+b_3)$) respectively. It was found in both cases the relationship was linear after picture (1) in the sequence 4-1-2-3-5-6 but started with a low value for the broadest shape of the *Euglena*. **Figure 4.33** shows the variation of Gaussian standard deviation of the PSD images over the same sequence and it was not possible to provide discrimination between the shapes. **Figure 4.34** shows the variation of crosscorrelation coefficient of the *Euglena* images over the ratio ($a / (b_1+b_2+b_3)$). It was found that there was a linear and inverse relationship with $R^2 = 0.8846$. **Figure 4.35** shows the crosscorrelation coefficient of the PSD converted images and it was found that a similar linear and inverse relationship existed with the ratio ($R^2 = 0.8507$).

4.4. CONCLUSION AND FUTURE SCOPE

This chapter addressed single cell analysis. *Euglena gracilis* was chosen as the model organism partly because of its large size, and hence suitability for investigation with light based microscopy systems, but also because of its changing morphology. A number of different methodologies were developed to characterise the cell shape and dynamic activity. These included visual assessment from 12 volunteers, measurements taken from the spatial domain relating to the cell's eccentricity, and image processing in the spatial and frequency domain.

Table 4.7 shows the results from the different methods of analysis as compared to those achieved with the visual assessment from the volunteers. It was found that 68.05% of the population favoured the sequence (4-1-2-3-5-6). The same sequence was preferred by four different methods of analysis namely: the summed eccentricity, the summed eccentricity normalized to the area, crosscorrelation of the actual image before filtering and crosscorrelation of the PSD image after filtering. A slight variation in the above sequence (4-1-3-2-5-6) was favoured by 59.72% population and was ranked 2. This sequence was preferred by the method using the crosscorrelation of the PSD image before filtering. Both intensity standard deviation methods before and after filtering favoured the sequence (1-2-3-4-5-6) which was favoured by 38.88% of the population. The sequence (2-5-6-4-3-1) was the lowest ranked at 4.16% and this sequence was obtained with the Gaussian standard deviation method after filtering.

Table 4.8 ranks the different methods of analysis from the different image processing methods. It was found that the Gaussian standard deviation before filtering gave the best fit plotted against the the ratio of major to summed minor axes values ($R^2 = 1$). Interestingly all four of the crosscorrelation parameters were ranked quite highly, from 2 to 5. Although the plots in Figures 4.19, 4.20, 4.34 and 3.35 are relatively linear, the crosscorrelation of the PSD image before filtering showed the best fit ($R^2 = 0.9484$). From Table 4.7, the crosscorrelation of the actual image before filtering and PSD image after filtering was the most preferred sequence and was favoured by two other measurement methods. These two parameters were ranked 3 and 5 respectively in Table 4.8 indicating that crosscorrelation may be the best image processing parameter that describes the sequence agreeable to the largest number of the population from the visual assessment. Interestingly, both Tables 4.7 and 4.8 indicate the least ranked values ($R^2 = 0.024$) for the parameter Gaussian standard

deviation after filtering. Although, it is probably less relevant to use a linear fit in this case. Thus the sequence (2-5-6-4-3-1) was the most unfavourable sequence overall.

The sensitivity of the results need to be investigated over a wider range of operating conditions, providing robust algorithms that work for a range of environmental and illuminating conditions. Consequently, there is likely to be merit in researching the effect of more parameters and understanding the errors in the system. In the analysis herein, the results from the image processing methods were compared with the visual assessment and eccentricity based measurements in the spatial domain. Possible errors in the system may be due to blurring of the images or variation in the He-Ne output power. The intensity fluctuation of the low power laser beam may induce significant contrast variations that in turn affect the power spectral density of the image. The image processing may inadvertently remove useful intensity information while filtering.

The system provides real time capability to quantify the cell shape. Furthermore, it may be possible to distinguish between a live cell and dead cell, as shown in Figure 4.25. It follows that compared to the intensity standard deviation values from a live cell, the dead cell values had increased by 25 % but still showed some variation, indicating some internal motion of the cell was evident or possible effects of Brownian motion or movement of organelles were being detected. Thus the intensity standard deviation analyzed over a time period provides an insight into the dynamic activity of the sample.

Image processing within the MATLAB environment provided a useful test bed for assessing the performance of the algorithms. Matlab allows individual pixel analysis and this would enhance the results and the ability to quantify the rapid changes induced in the cell.

It could be said that for membrane and unicellular analysis, a high objective lens could be used as it magnifies the specimen and the results of these studies where viability was detected would be very helpful in monitoring the real time effects of any decontamination treatments for individual organisms. A low objective lens with monochromatic illumination would provide a system to investigate large populations of cells, providing high contrast. Again, by detecting viability the effect of real time decontamination treatments on the organisms could be investigated.

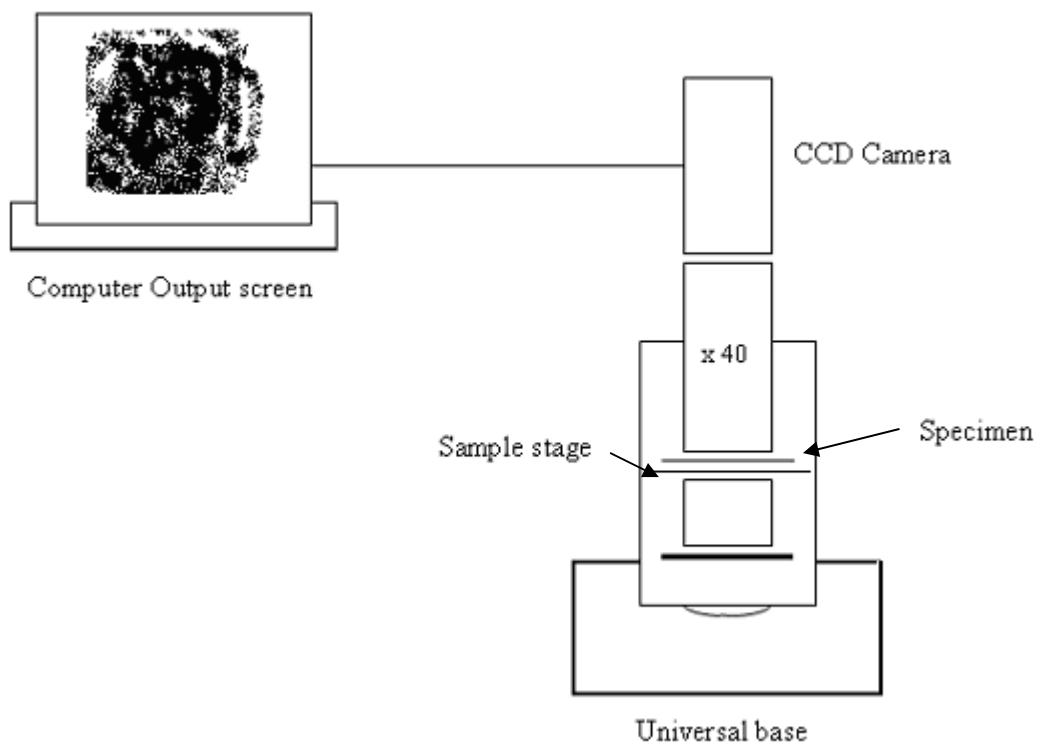


Figure 4.1 Bright-field microscopy and image capture system optimized for high contrast to capture the movements of a single *Euglena gracilis* cell.


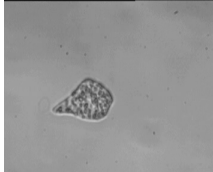

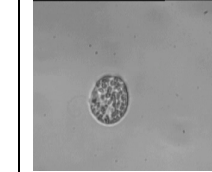

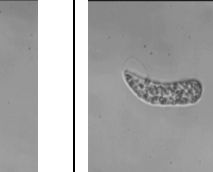
The random order considered for assessment						
Identifiers	1	2	3	4	5	6

Figure 4.2 The random sequences of the images given to volunteers and the corresponding identification numbers.

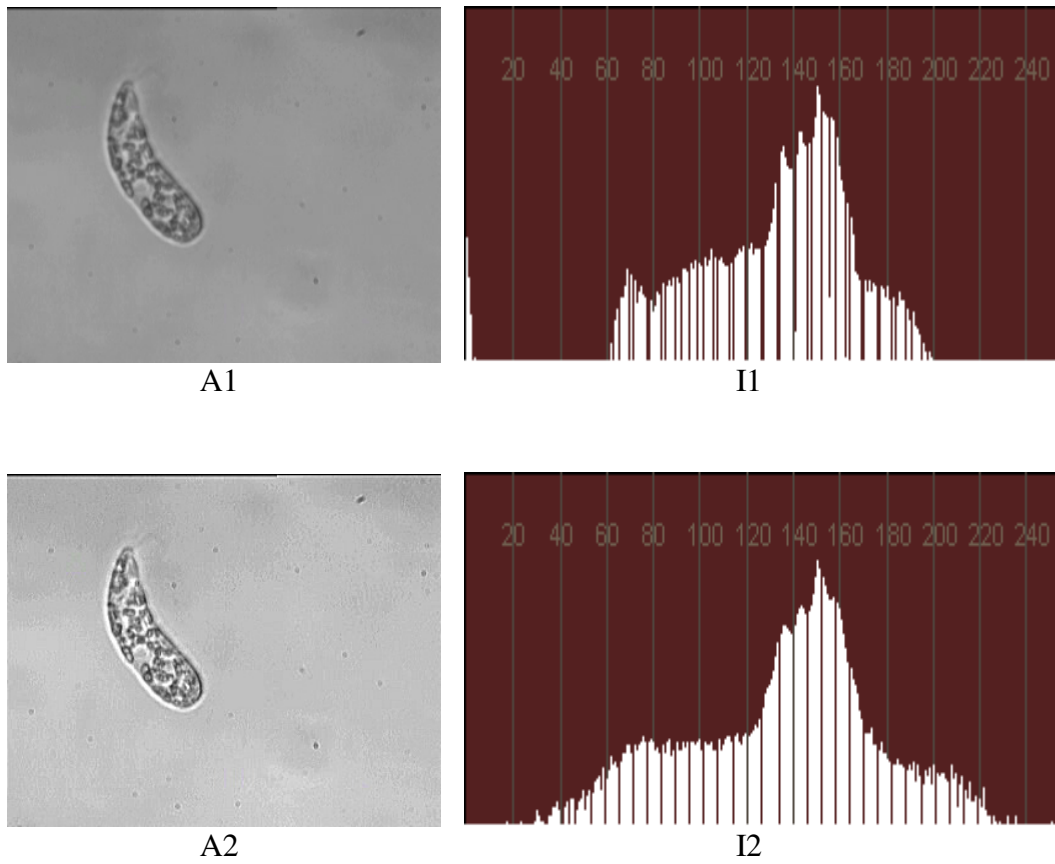


Figure 4.3 *Euglena gracilis* and its intensity distribution before (A1, I1) and after high pass filtering (A2, I2).

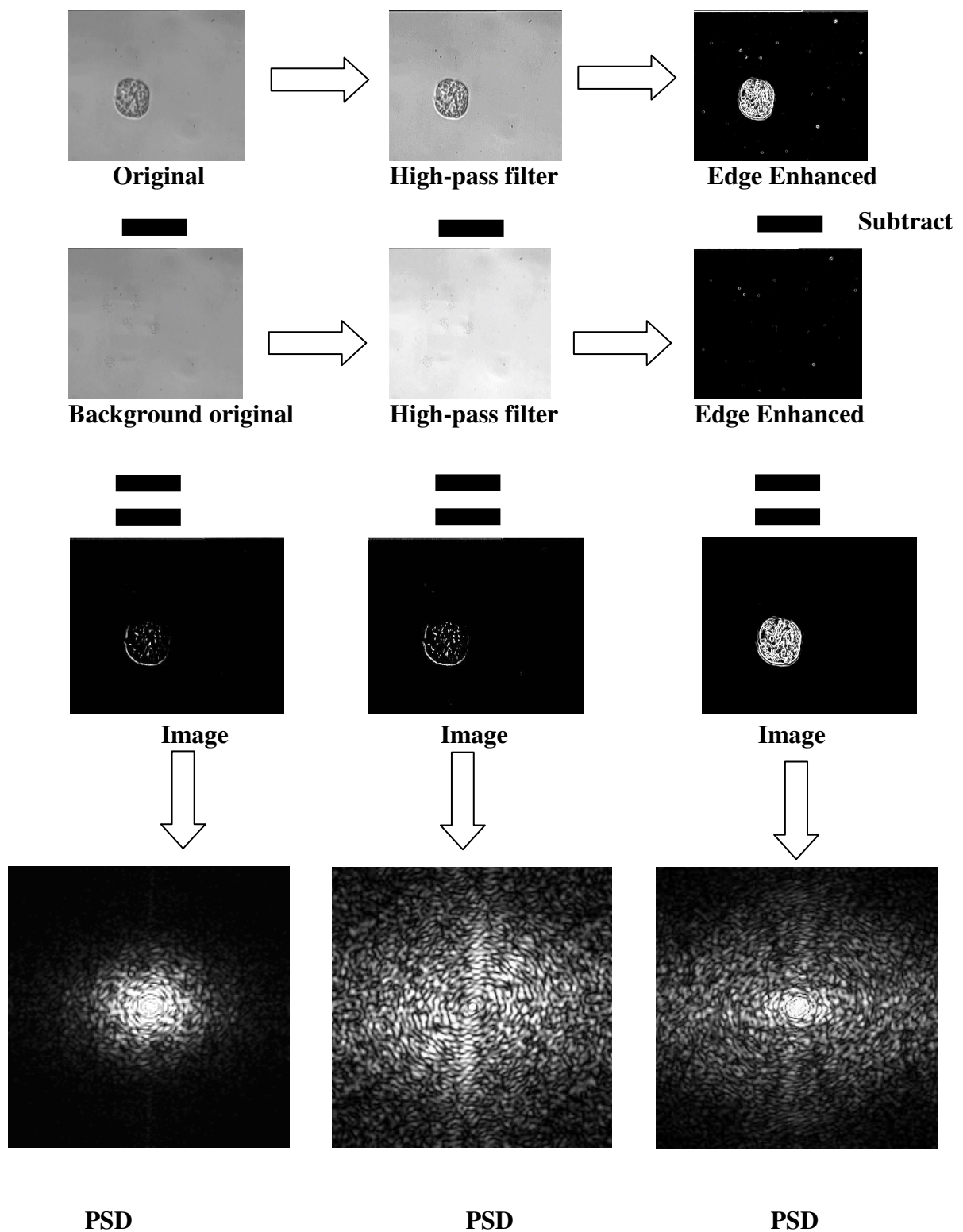

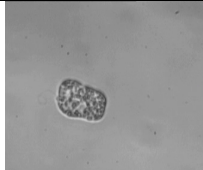
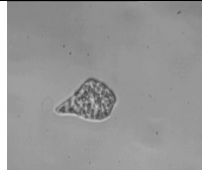
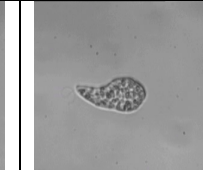
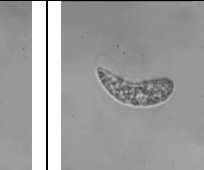
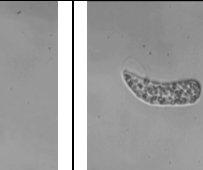
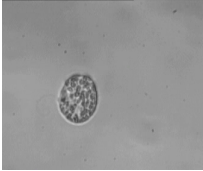
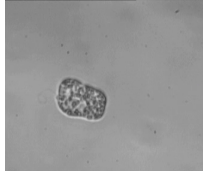

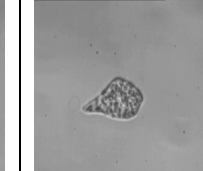
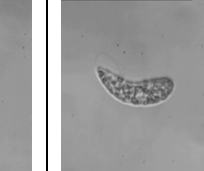
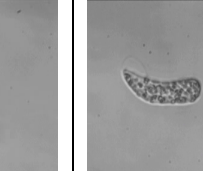
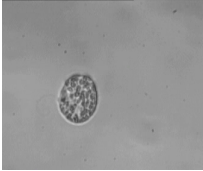
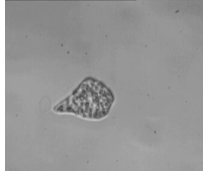
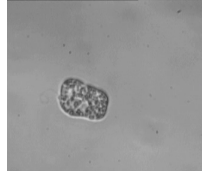

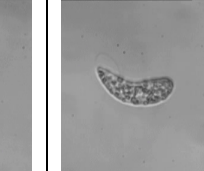
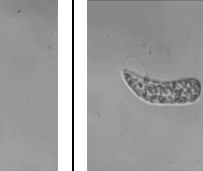
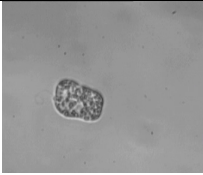
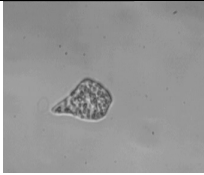




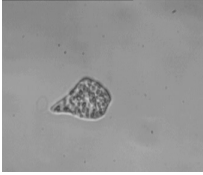

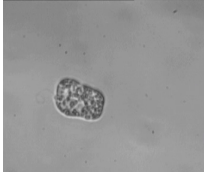





Figure 4.4 Schematic of the image processing workflow. Comparison of background subtracted and PSD images for unfiltered, filtered and edge-enhanced images of a *Euglena* cell.

<i>Visual assessment</i>							5/12
Sequence	4	1	2	3	5	6	
<i>Visual assessment</i>							2/12
Sequence	4	1	3	2	5	6	
<i>Visual assessment</i>							SCORE
Sequence	4	2	1	3	5	6	1/12

(PTO)

<i>Visual assessment</i>							SCORE
Sequence	1	2	3	4	5	6	1/12
<i>Visual assessment</i>							SCORE
Sequence	2	4	1	3	5	6	1/12

(PTO)

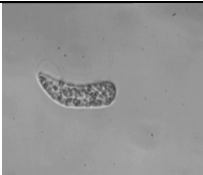


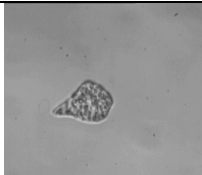
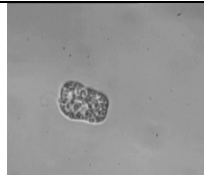
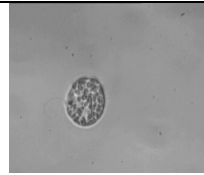

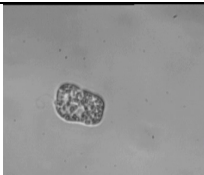
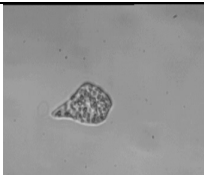
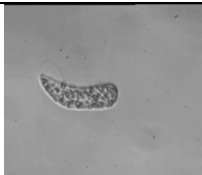
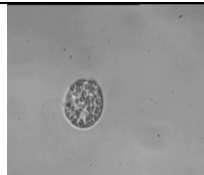

<i>Visual assessment</i>							SCORE
Sequence	6	5	3	2	1	4	1/12
<i>Visual assessment</i>							SCORE
Sequence	3	1	2	6	4	5	1/12

Figure 4.5 The sequences of the images as arranged by volunteers. The score on the right represents the ratio between the methods agreeing to the total number of volunteers.

Method	Picture numbers arranged in the sequence						No. of people agreed
	(1)	(2)	(3)	(4)	(5)	(6)	
Visual assessment sequence from 12 volunteers	1	2	3	4	5	6	1
	4	1	2	3	5	6	5
	4	1	3	2	5	6	2
	4	2	1	3	5	6	1
	2	4	1	3	5	6	1
	6	5	3	2	1	4	1
	3	1	2	6	4	5	1
						Total	12


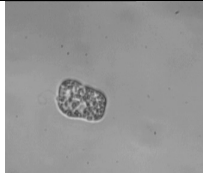
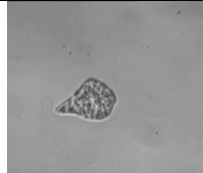

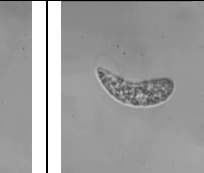
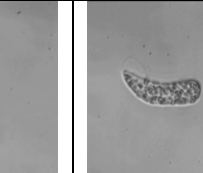




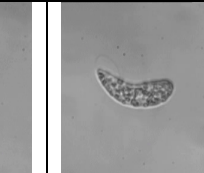
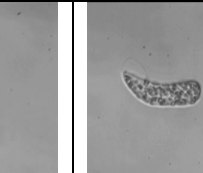
Table 4.1 Visual assessment sequence from volunteers.

Picture No.	Position					
	1 st	2 nd	3 rd	4 th	5 th	6 th
(1)	1	8	2	0	1	0
(2)	1	2	6	3	0	0
(3)	1	0	4	7	0	0
(4)	8	1	0	1	1	1
(5)	0	1	0	0	10	1
(6)	1	0	0	1	0	10
Total	12	12	12	12	12	12

Table 4.2 Number of volunteers agreed to place the particular picture at the particular position.

Picture Number	Area unit²
(1)	724
(2)	830
(3)	774
(4)	771
(5)	857
(6)	841

Table 4.3 Area calculated for different shapes of *Euglena*.

$(a/b_1+b_2+b_3)$ $(a/b_1+b_2+b_3)^*$ $(1/Area)$							SCORE
Sequence	4	1	2	3	5	6	2/7
(a/b_{avg}) $(a/b_{avg})^*$ $(1/Area)$							SCORE
Sequence	2	4	1	3	5	6	2/7

(PTO)

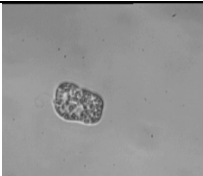
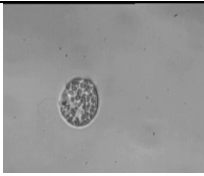

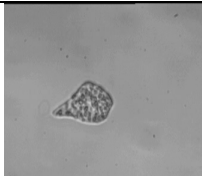
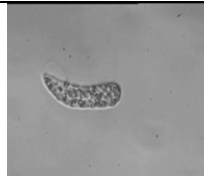

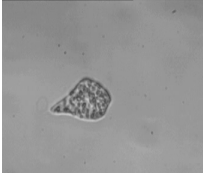
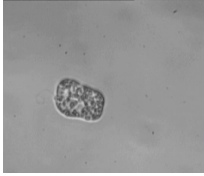




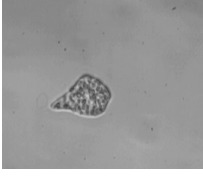
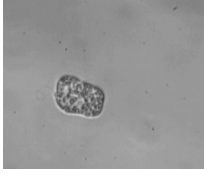
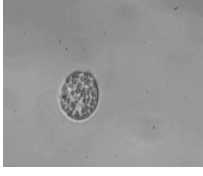



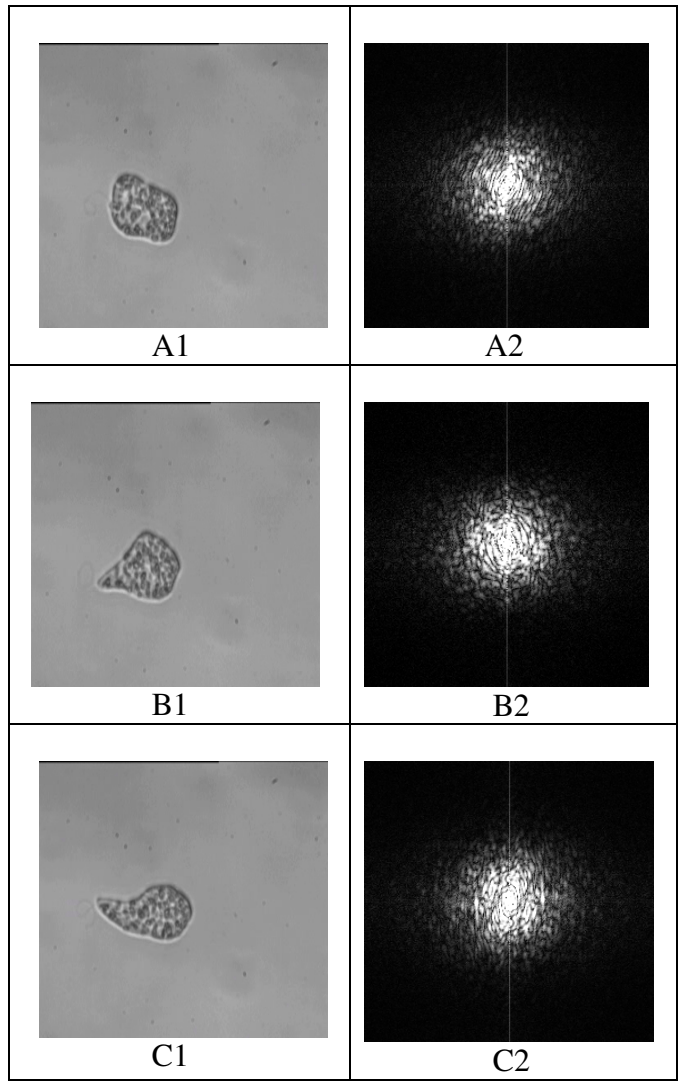
<i>Area</i>							SCORE
Sequence	1	4	3	2	6	5	1/7
<i>(a/b)</i>							SCORE
Sequence	2	1	3	4	5	6	1/7
<i>(a/b)*(1/Area)</i>							SCORE
Sequence	2	1	4	3	5	6	1/7

Figure 4.6 The sequences of the images as arranged by the measurement methods. The score on the right represents the ratio between the methods agreeing to the total number of methods.

Measurement method	Sequence	Overall score	%
Area	1-4-3-2-6-5	10/72	13.88
a/b_{avg}	2-1-3-4-5-6	34/72	47.22
$(a/b)/area$	2-1-4-3-5-6	36/72	50
$a/(b_1+b_2+b_3)$ and $a/(b_1+b_2+b_3)/area$	4-1-2-3-5-6	49/72	68.05
a/b_{avg} and $(a/b_{avg})/Area$	2-4-1-3-5-6	31/72	43.05

Table 4.4 Comparison of the results between the measurement method and the visual assessment method



(PTO)

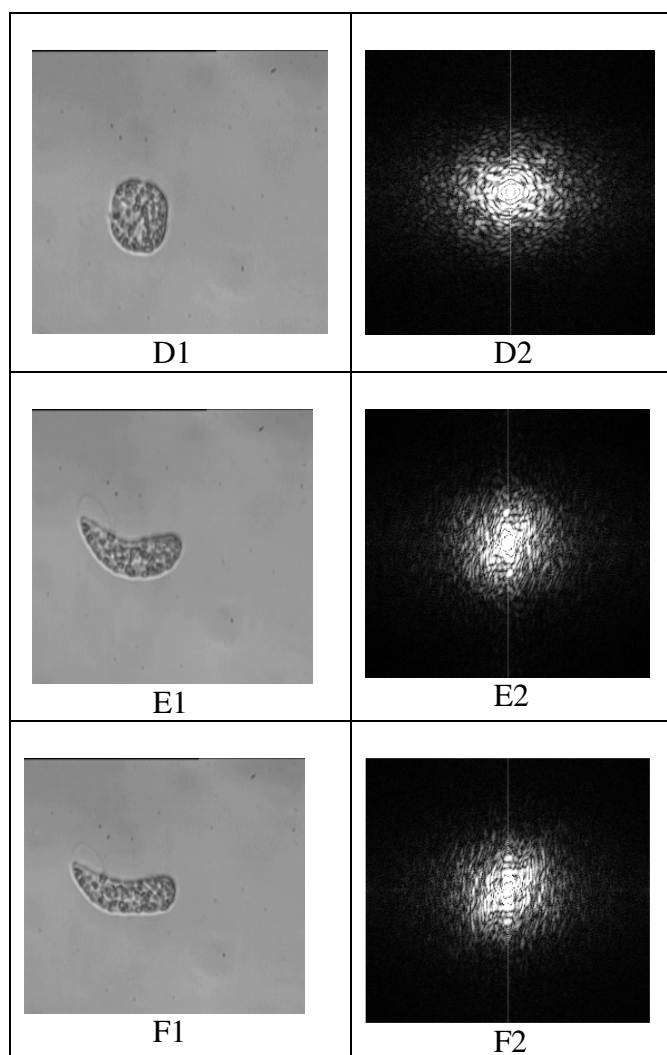


Figure 4.7 Images of *Euglena* from bright field microscopy (on left) and corresponding in PSD (right) for different cell morphologies and no filtering.

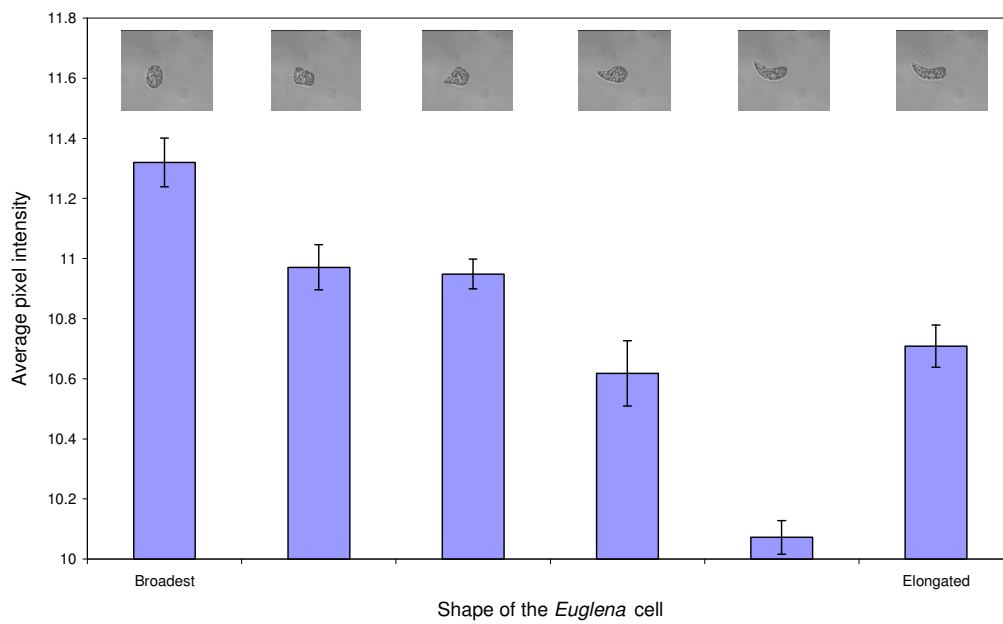


Figure 4.8 Variation of average pixel intensity of the PSD converted images over different shapes of the *Euglena* taken from bright-field microscopy

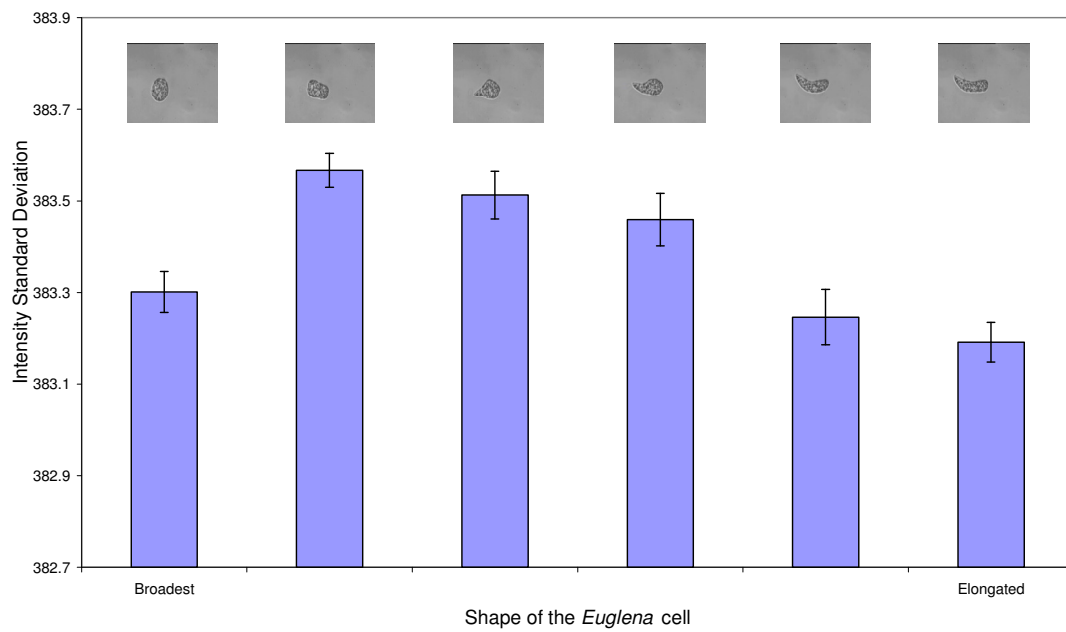


Figure 4.9 Variation of intensity standard deviation of a PSD image over different shapes of the *Euglena* taken from bright field microscopy

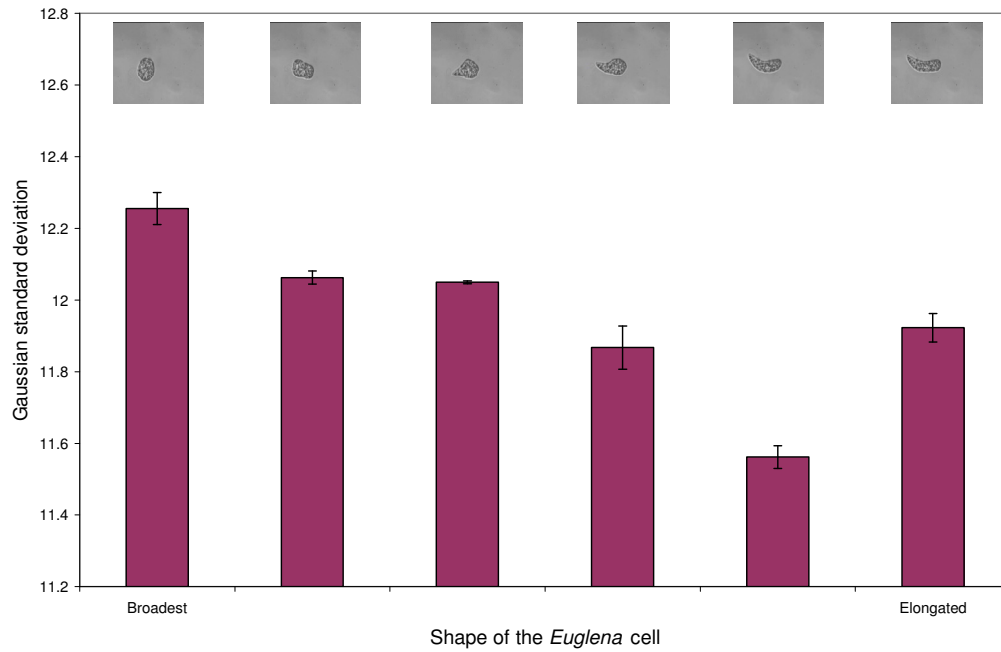


Figure 4.10 Variation of Gaussian standard deviation of a PSD image over different shapes of the *Euglena* taken from bright field microscopy

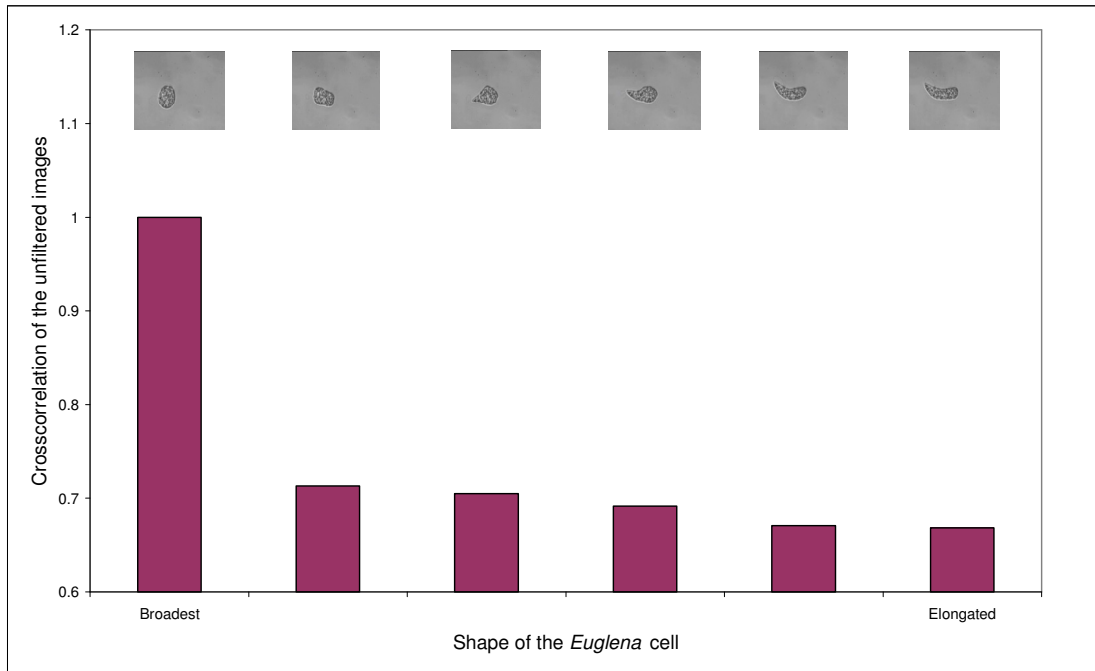


Figure 4.11 Crosscorrelation coefficient of every *Euglena* (unfiltered) image with respect to the broadest shape of the *Euglena* cell.

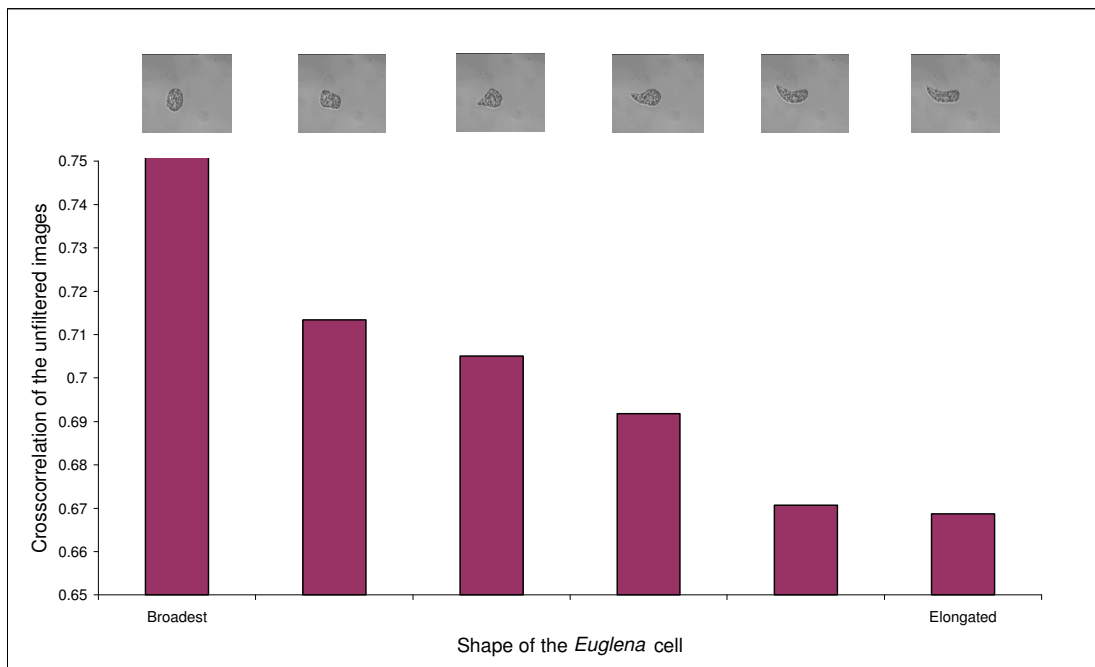


Figure 4.12 Exploded view of Figure 4.11 to unfold details within low crosscorrelation coefficients.

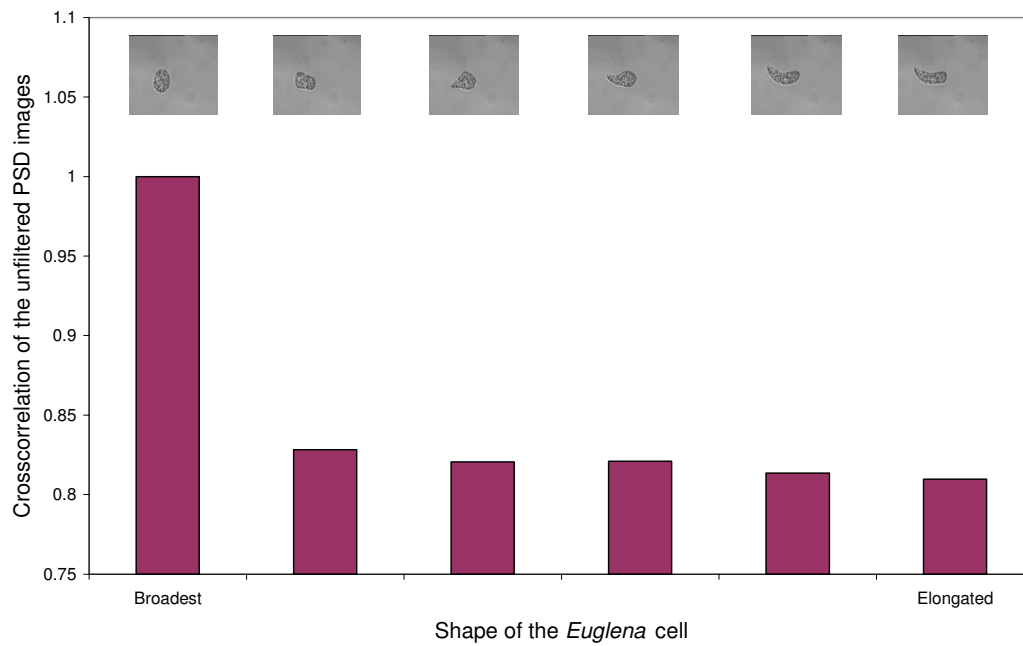


Figure 4.13 Crosscorrelation coefficient of every unfiltered PSD image of *Euglena* with respect to the broadest shape of the *Euglena* cell.

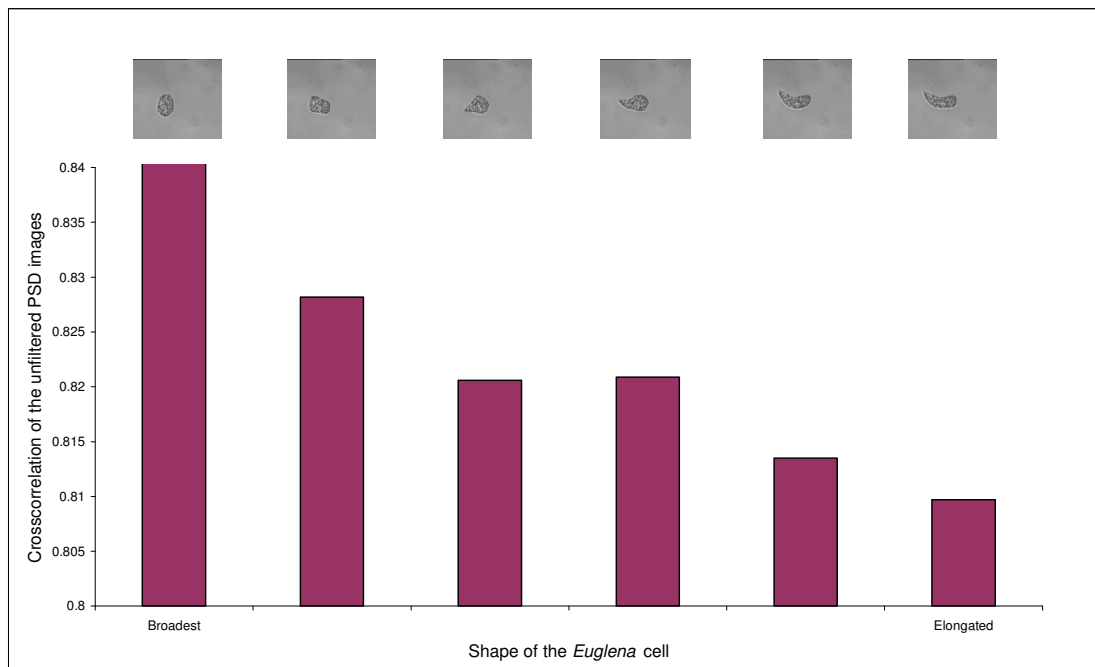
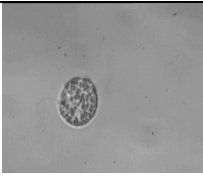
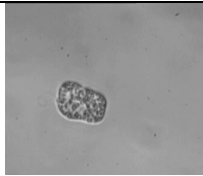
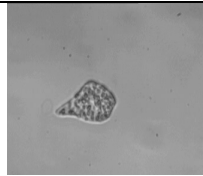
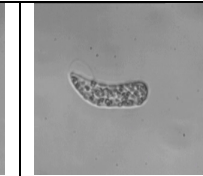
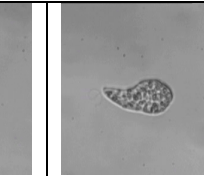
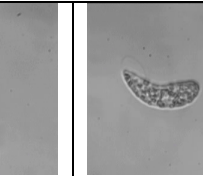
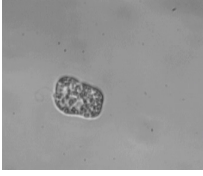
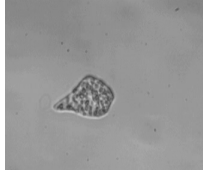

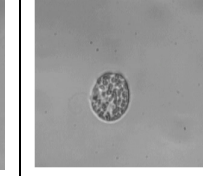
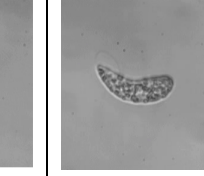
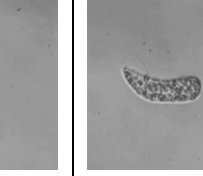


Figure 4.14 Exploded view of Figure 4.13 to unfold details within low crosscorrelation coefficients.

<i>Average and Gaussian standard deviation</i>							SCORE
Sequence	4	1	2	6	3	5	2/5
<i>Intensity standard deviation</i>							1/5
Sequence	1	2	3	4	5	6	

(PTO)


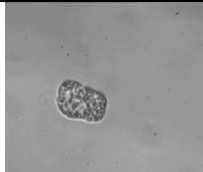


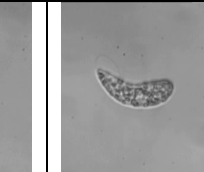
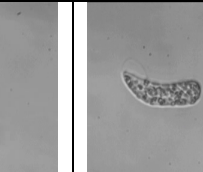

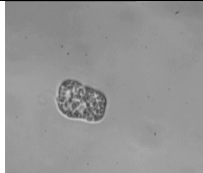

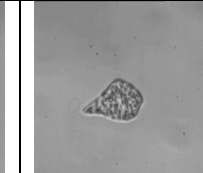
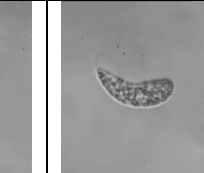
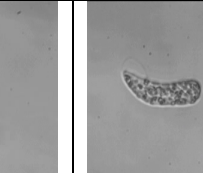
<i>Crosscorrelation function of the actual image</i>							1/5
Sequence	4	1	2	3	5	6	
<i>Crosscorrelation function of the actual image</i>							1/5
Sequence	4	1	3	2	5	6	

Figure 4.15 The sequences of the images as arranged by the image processing parameters before filtering. The score on the right represents the ratio between the numbers of parameters agreeing to the total number of parameters.

Image processing methods	Sequence	Overall score	%
Average pixel intensity and Gaussian standard deviation	4-1-2-6-3-5	24/72	33.33
Intensity standard deviation	1-2-3-4-5-6	28/72	38.88
Crosscorrelation function of the actual image	4-1-2-3-5-6	49/72	68.05
Crosscorrelation function of the PSD converted image	4-1-3-2-5-6	43/72	59.72

Table 4.5 Comparison of the results between the image processing before filtering and the visual assessment methods.

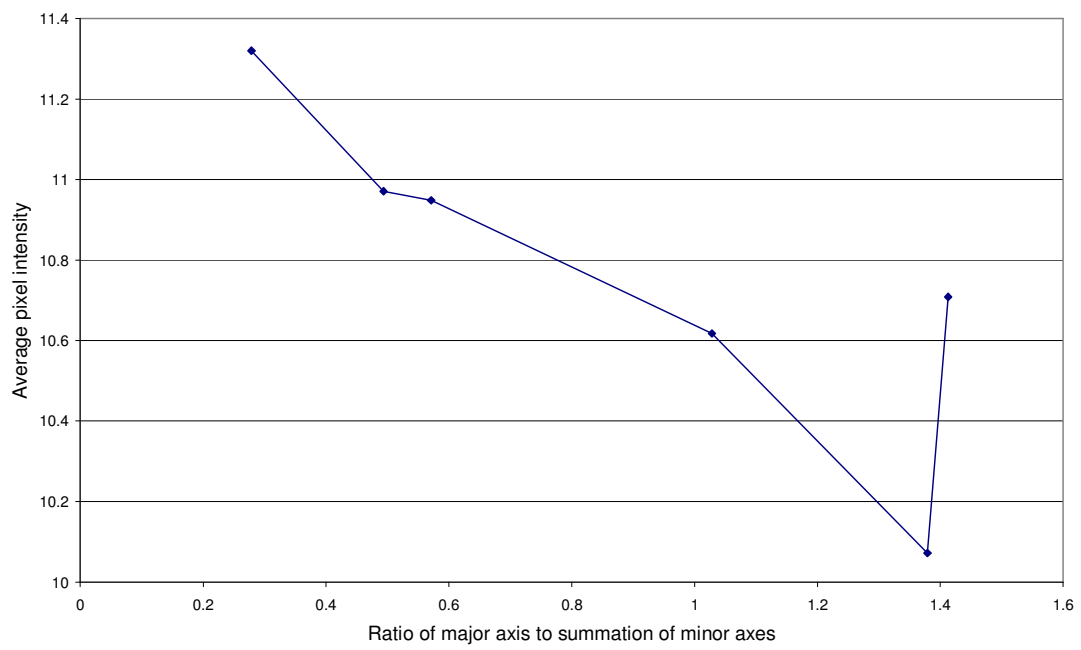


Figure 4.16 Variation of average pixel intensity of PSD images before filtering over the ratio of major axis to summation of minor axes.

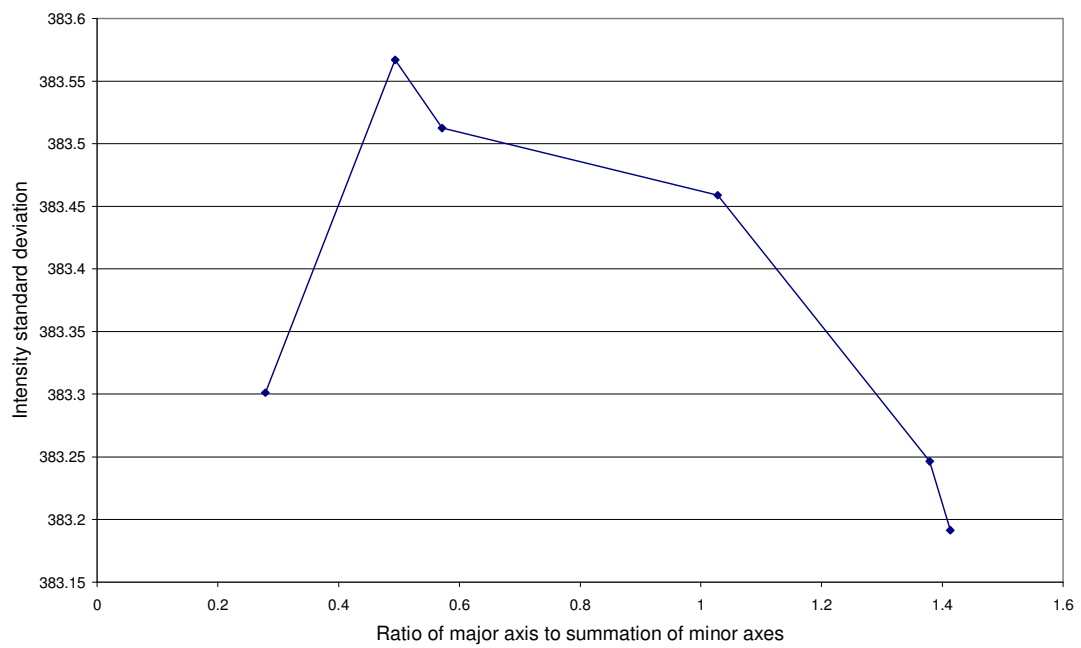


Figure 4.17 Variation of intensity standard deviation of PSD images before filtering over the ratio of major axis to summation of minor axes.

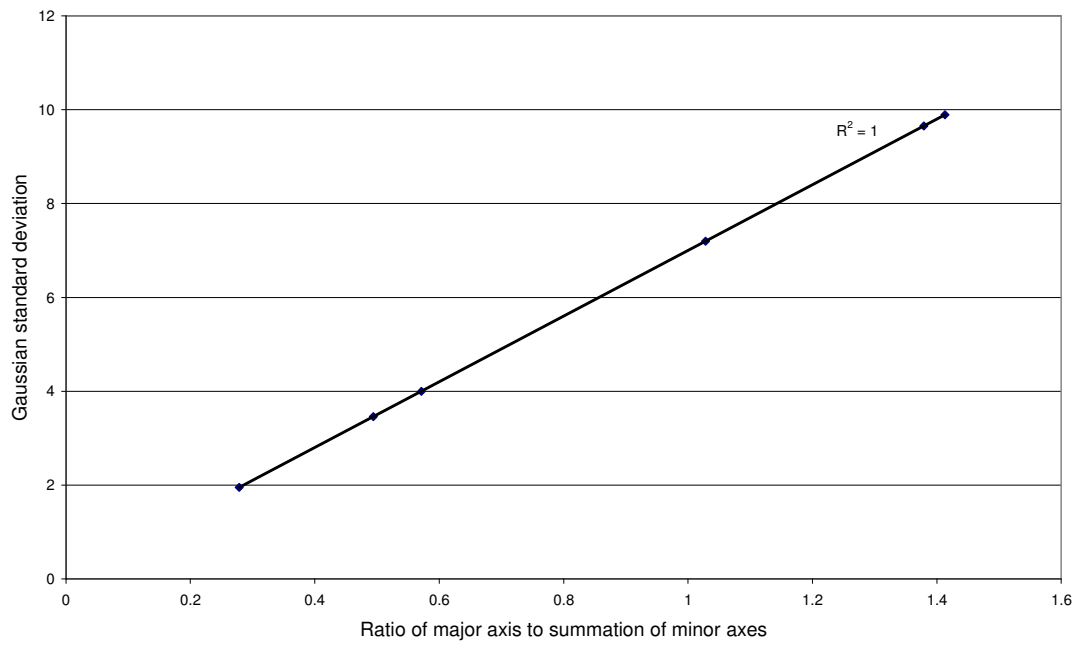


Figure 4.18 Variation of Gaussian standard deviation of PSD images before filtering over the ratio of major axis to summation of minor axes.

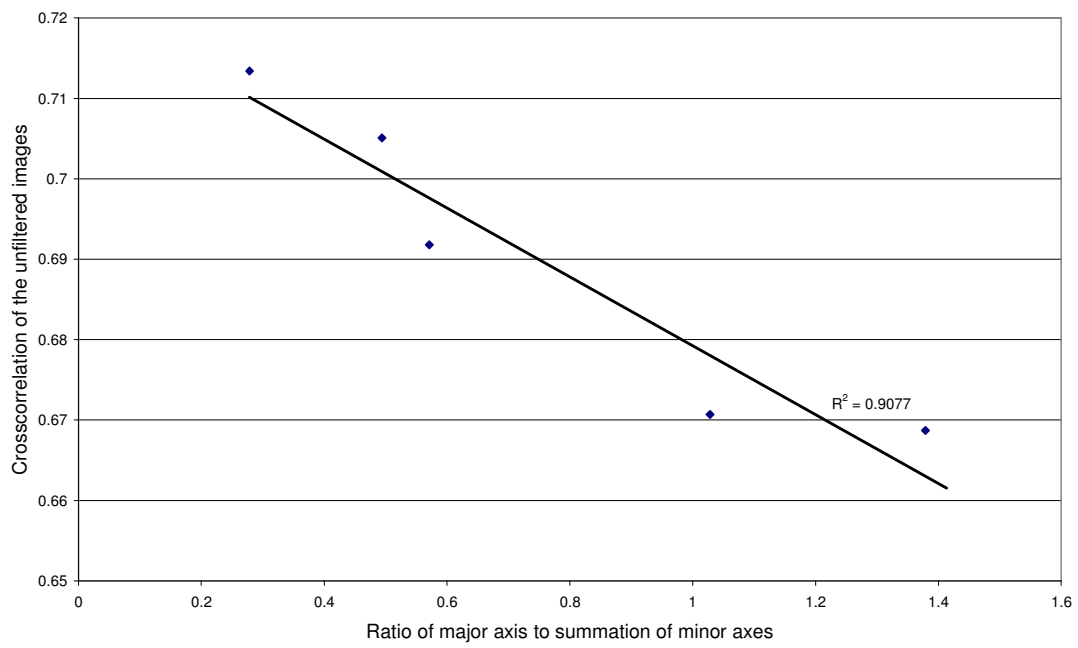


Figure 4.19 Variation of crosscorrelation coefficient of the *Euglena* images before filtering over the ratio of major axis to summation of minor axes.

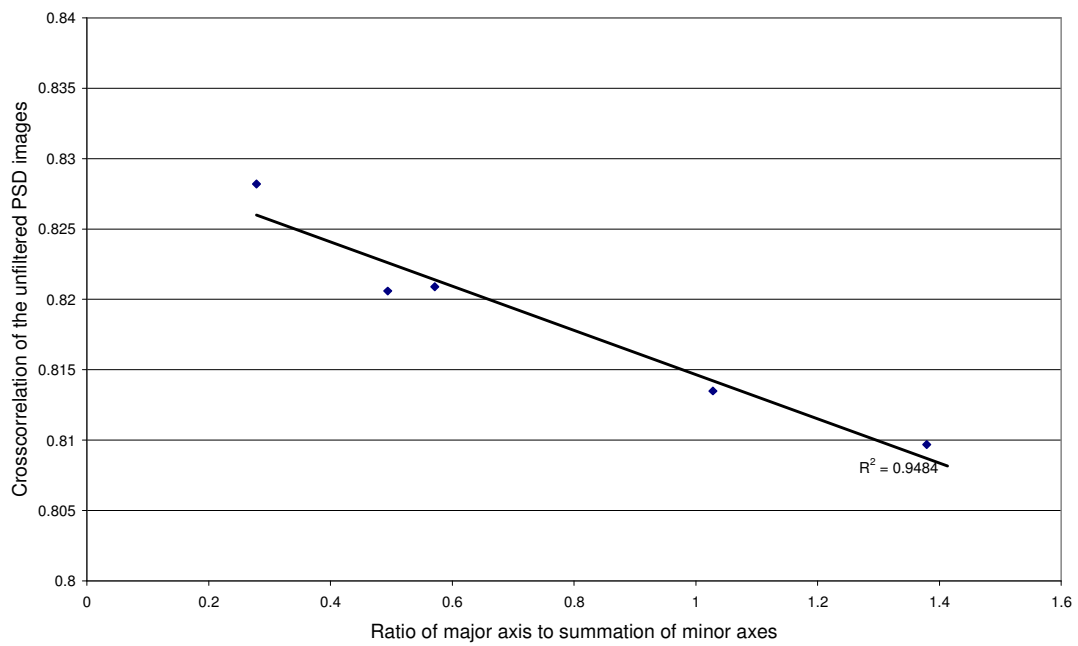
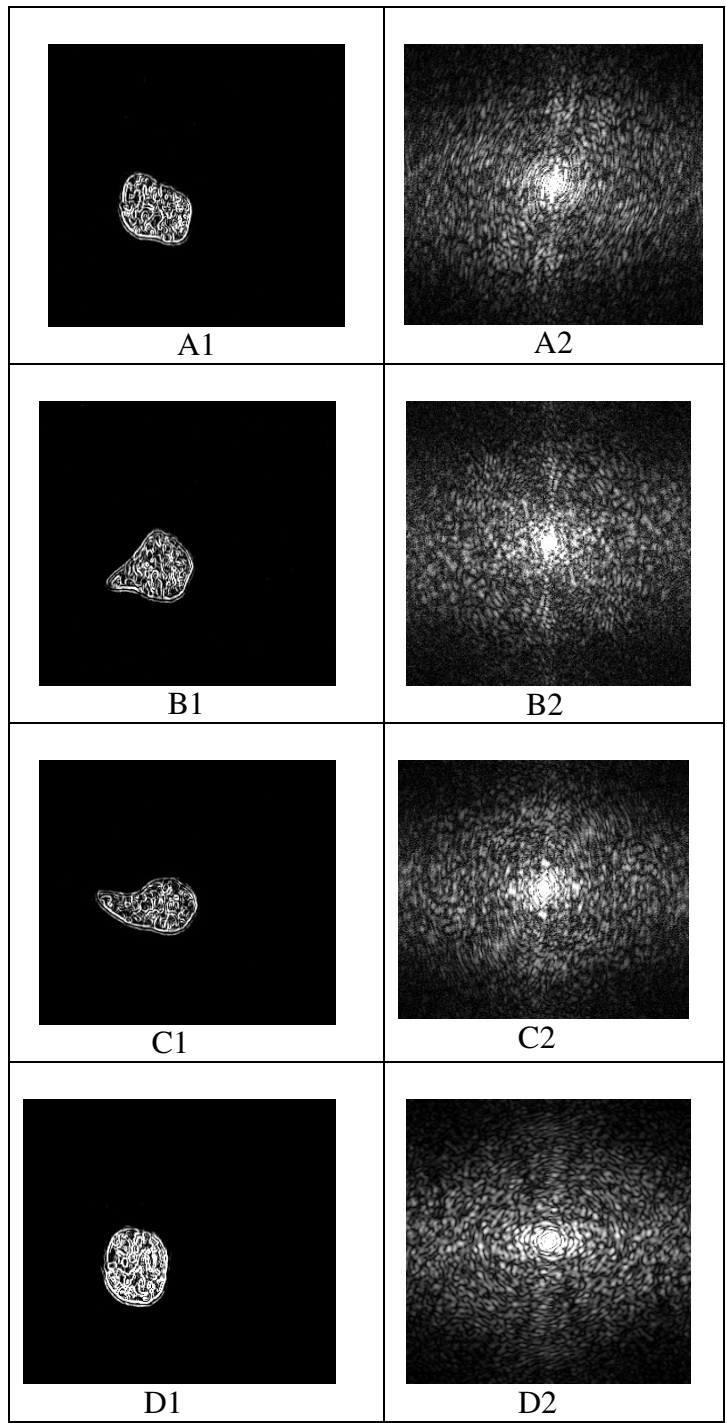


Figure 4.20 Variation of crosscorrelation coefficient of the PSD converted *Euglena* images before filtering over the ratio of major axis to summation of minor axes.



(PTO)

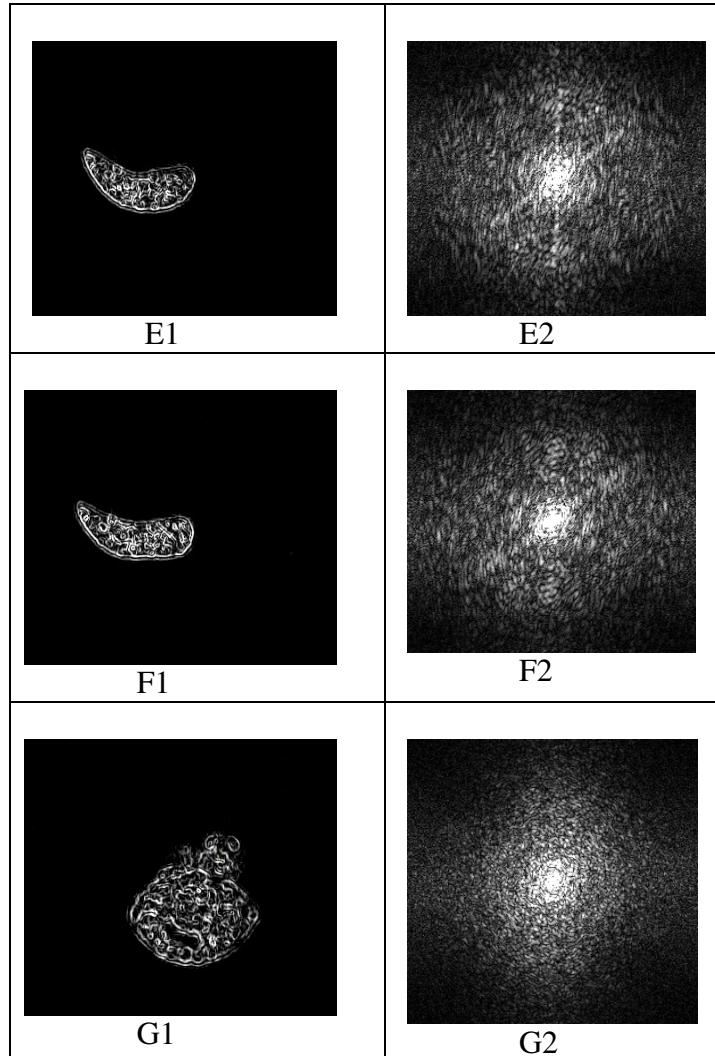


Figure 4.21 Actual (1) and PSD (2) image of the noise-filtered edge-enhanced image with A-F showing live cells and G showing the images derived from a dead cell.

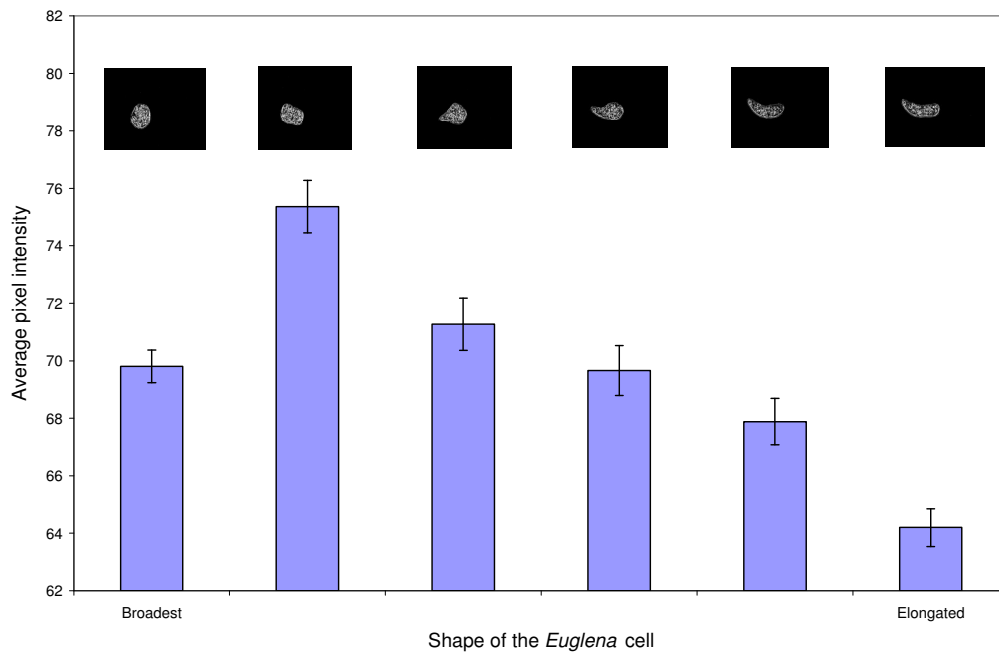


Figure 4.22 Variation of average pixel intensity of the PSD image after noise filtering

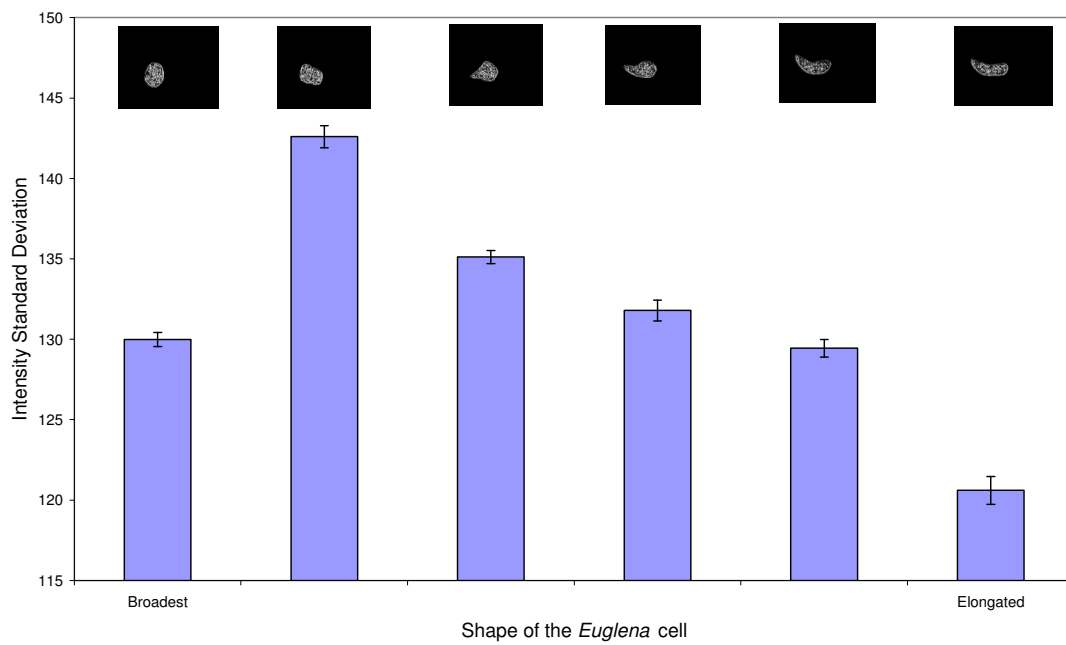


Figure 4.23 Variation of intensity standard deviation of the PSD image after noise filtering

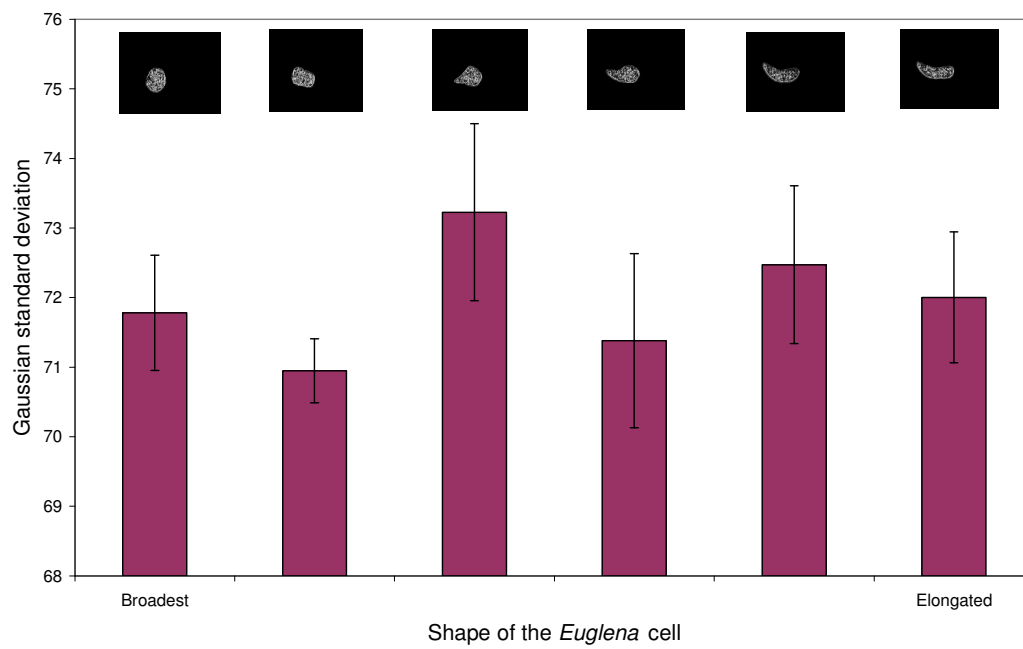


Figure 4.24 Variation of Gaussian standard deviation of the PSD image after noise filtering

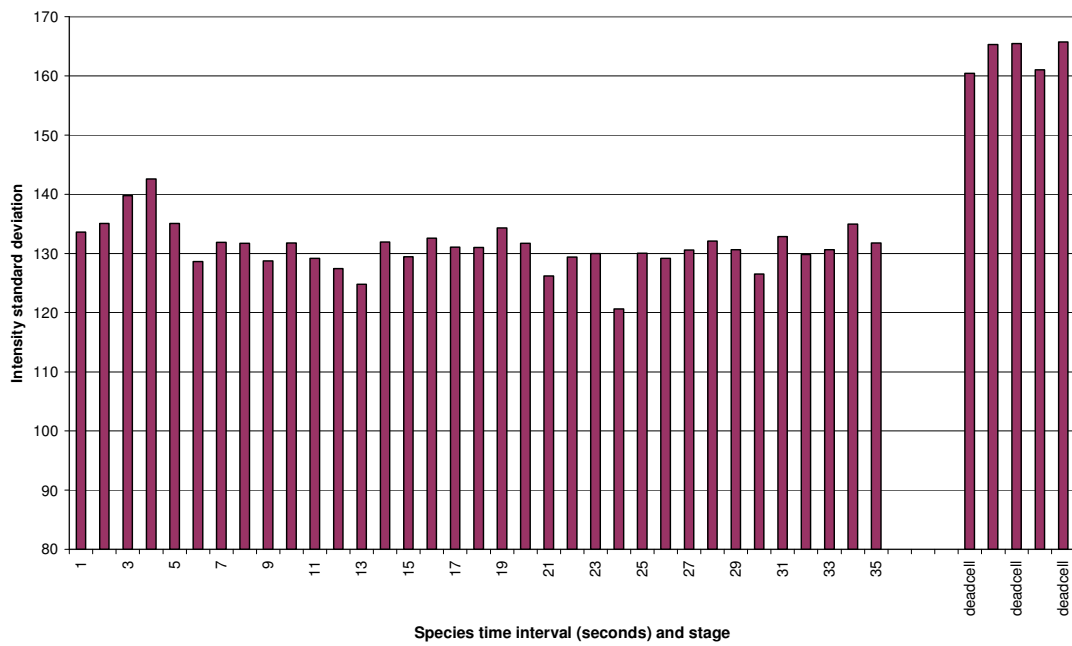
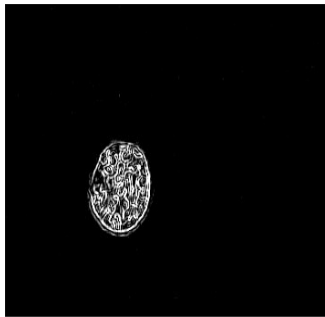
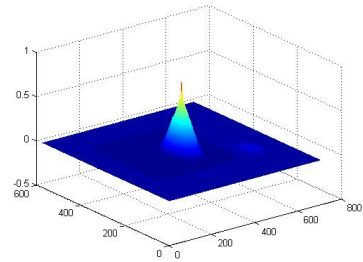


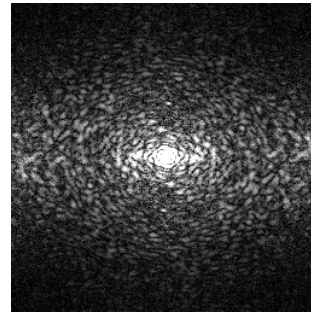
Figure 4.25 Temporal variation of Intensity standard deviation from the PSD image and comparison of values in live and dead *Euglena* cells



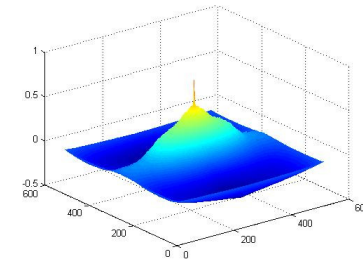
A1)



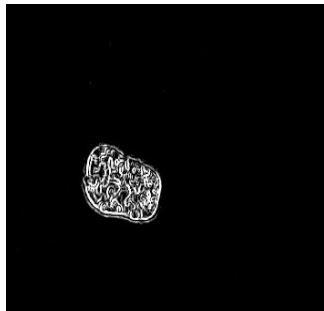
B1)



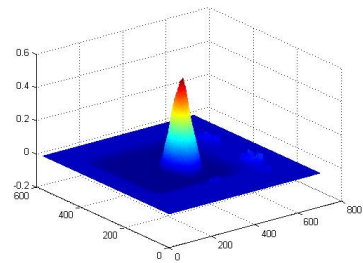
C1)



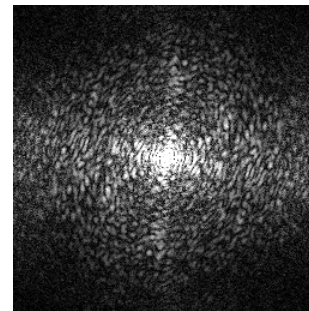
D1)



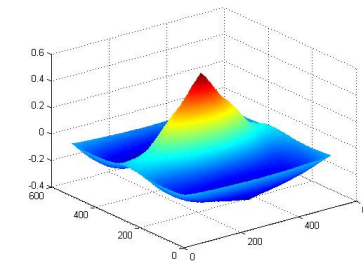
A2)



B2)

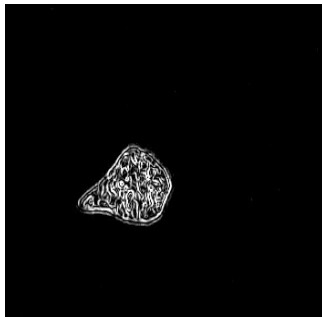


C2)

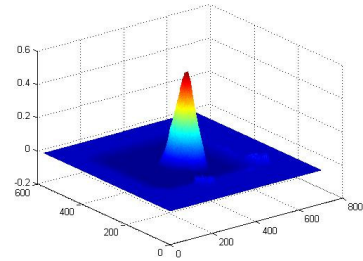


D2)

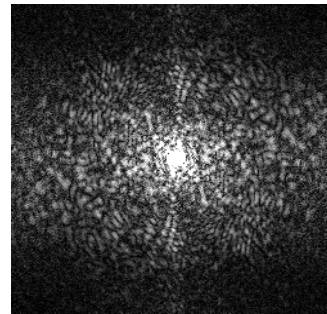
(PTO)



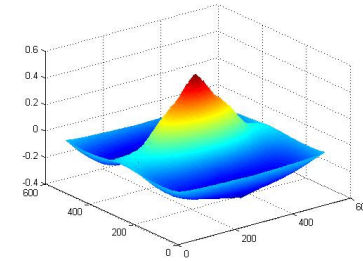
A3)



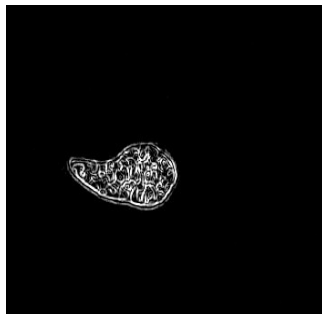
B3)



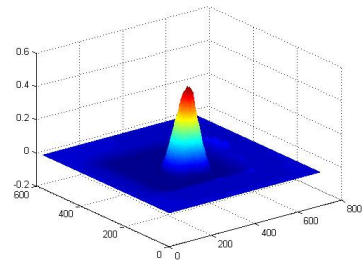
C3)



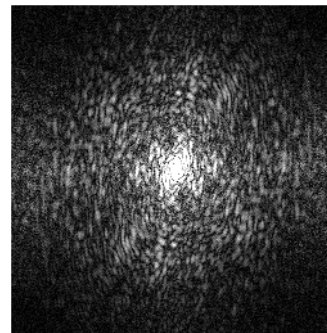
D3)



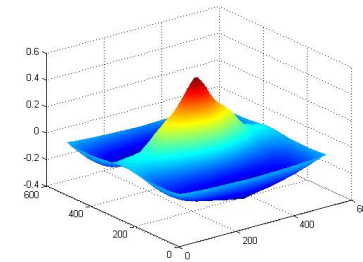
A4)



B4)

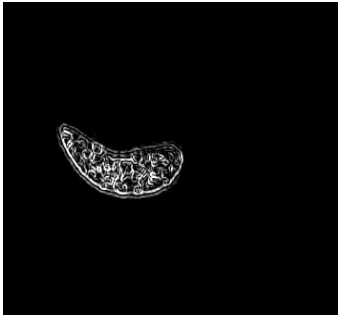


C4)

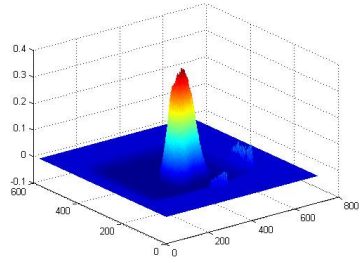


D4)

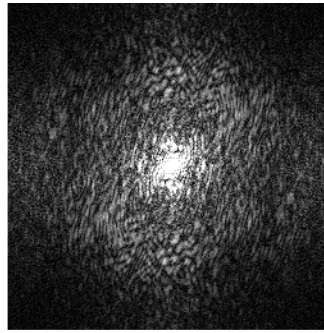
(PTO)



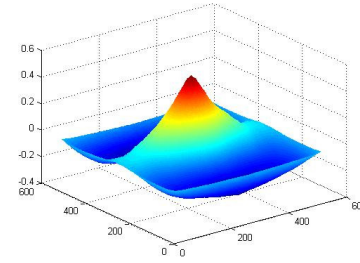
A5)



B5)

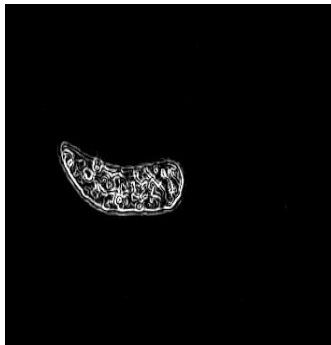


C5)

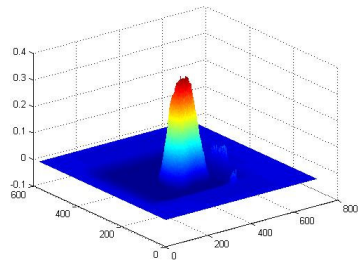


D5)

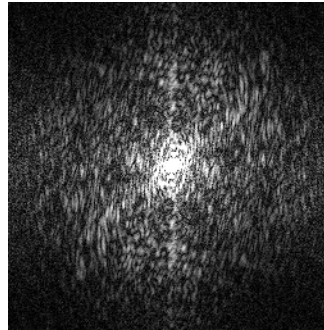
(PTO)



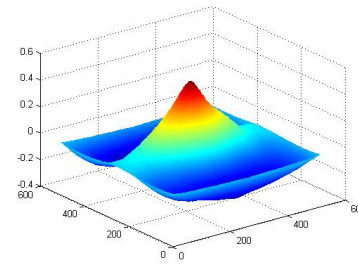
A6)



B6)



C6)



D6)

Figure 4.26 COLUMNS: A) Filtered image, B) Cross-correlation of filtered image, C) PSD of the filtered image, D) Cross-correlation of the PSD of filtered image. Figures arranged from broadest to elongated shape (A1, B1, C1, D1A6, B6, C6, D6)

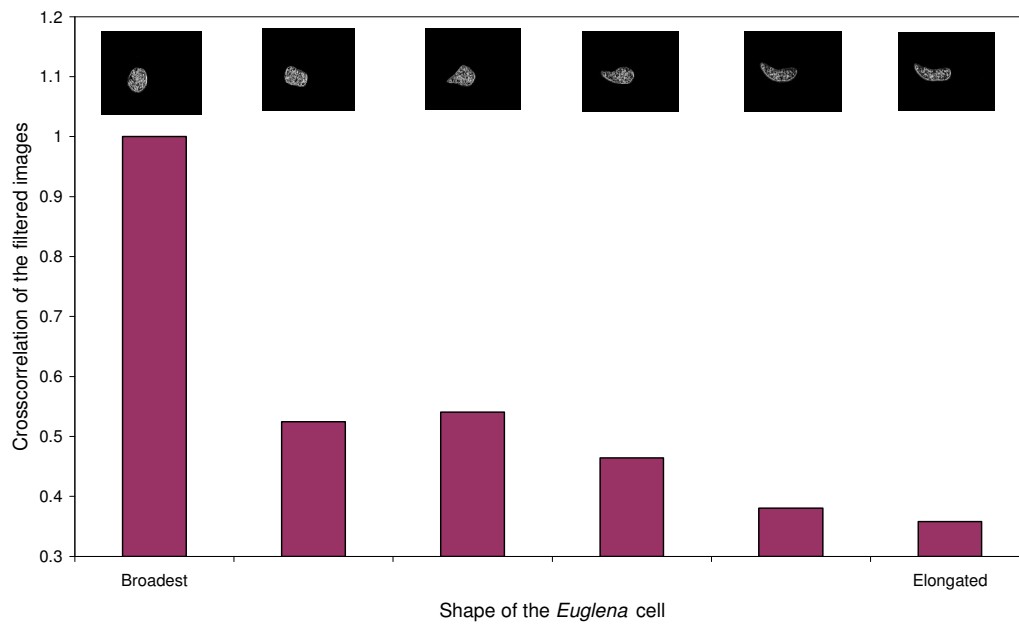


Figure 4.27 Crosscorrelation coefficient of every *Euglena* (filtered) image with respect to the broadest shape of the *Euglena* cell.

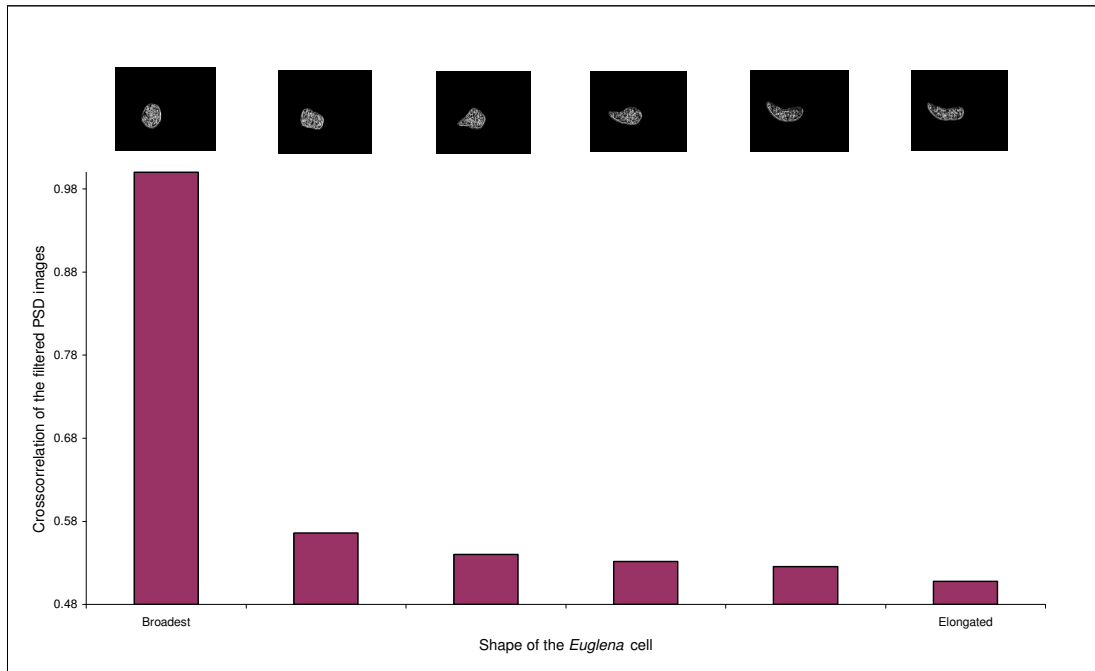


Figure 4.28 Crosscorrelation coefficient of every PSD *Euglena* (filtered) images with respect to the broadest shape of the *Euglena* cell.

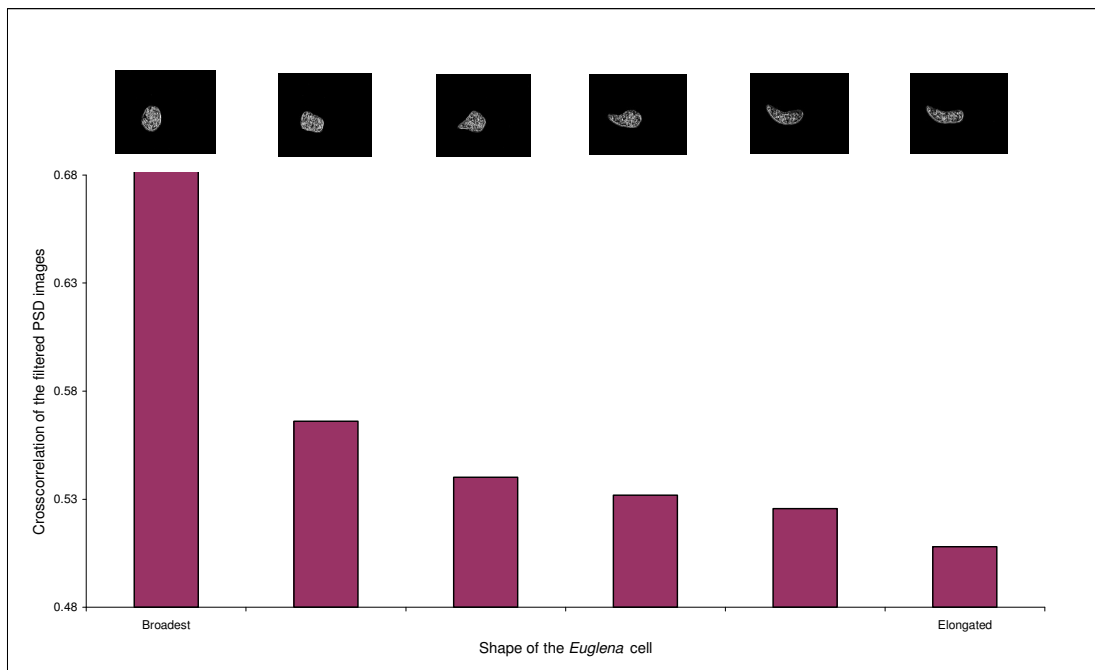

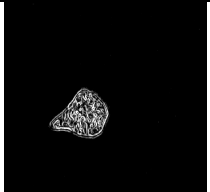



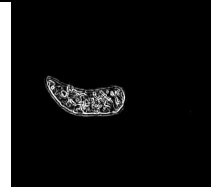

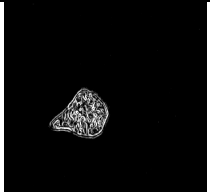

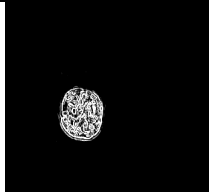

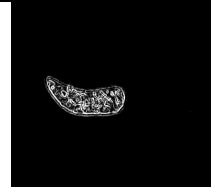
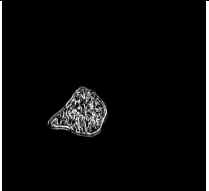

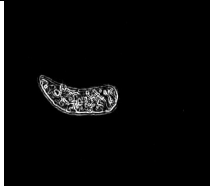


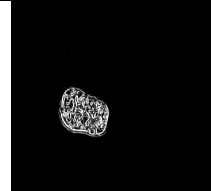


Figure 4.29 Exploded view of Figure 4.23 to unfold details within low crosscorrelation coefficients.

<i>Average pixel intensity</i>							SCORE
Sequence	1	2	4	3	5	6	1/5
<i>Intensity standard deviation</i>							SCORE
Sequence	1	2	3	4	5	6	1/5
<i>Gaussian standard deviation</i>							SCORE

(PTO)




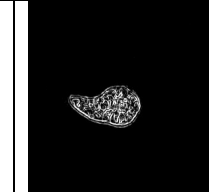
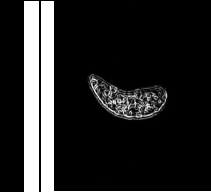
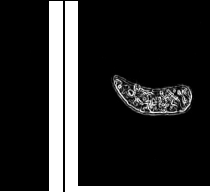

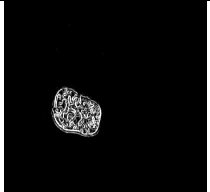

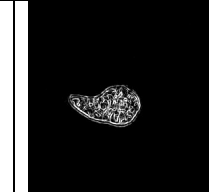
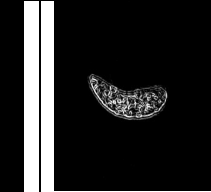
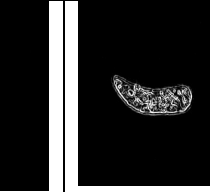
Sequence	2	5	6	4	3	1	1/5
<i>Crosscorrelation function of the actual image</i>							SCORE
Sequence	4	2	1	3	5	6	1/5
Crosscorrelation function of the PSD converted image							SCORE
Sequence	4	1	2	3	5	6	1/5

Figure 4.30 The sequences of the images as arranged by the image processing parameters after filtering. The score on the right represents the ratio between the numbers of parameters agreeing to the total number of parameters.

Image processing methods	Sequence	Overall score	%
Average pixel intensity	1-2-4-3-5-6	30/72	41.66
Intensity standard deviation	1-2-3-4-5-6	27/72	37.50
Gaussian standard deviation	2-5-6-4-3-1	3/72	4.16
Crosscorrelation function of the actual image	4-2-1-3-5-6	33/72	45.83
Crosscorrelation function of the PSD converted image	4-1-2-3-5-6	49/72	68.05

Table 4.6 Comparison of the results between the image processing after filtering and the visual assessment methods

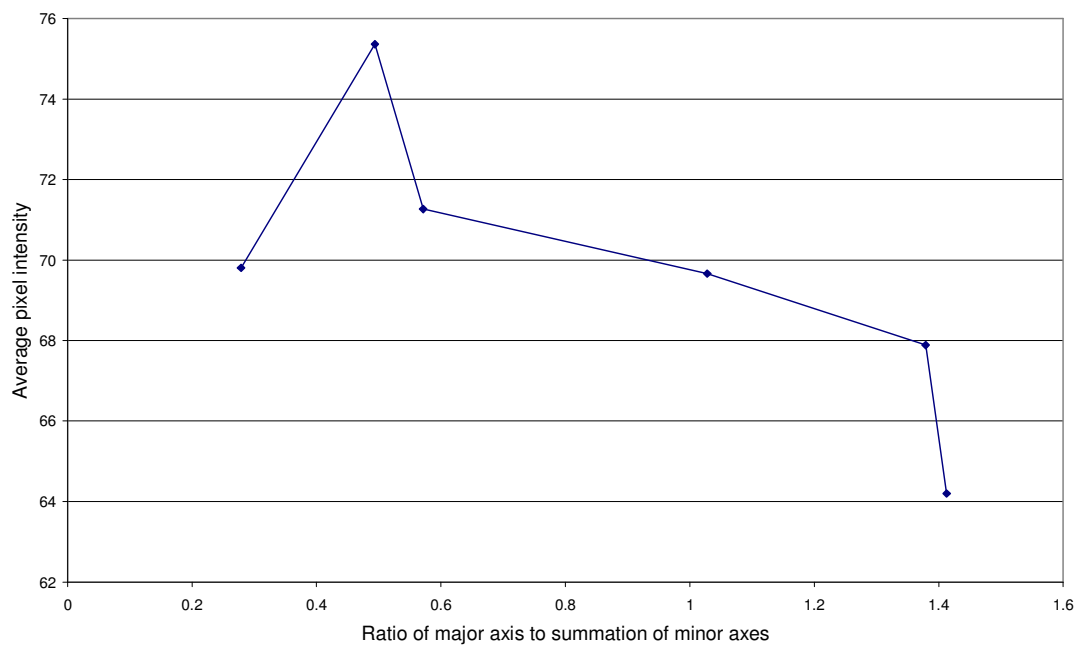


Figure 4.31 Variation of average pixel intensity of PSD images after filtering over the ratio of major axis to summation of minor axes.

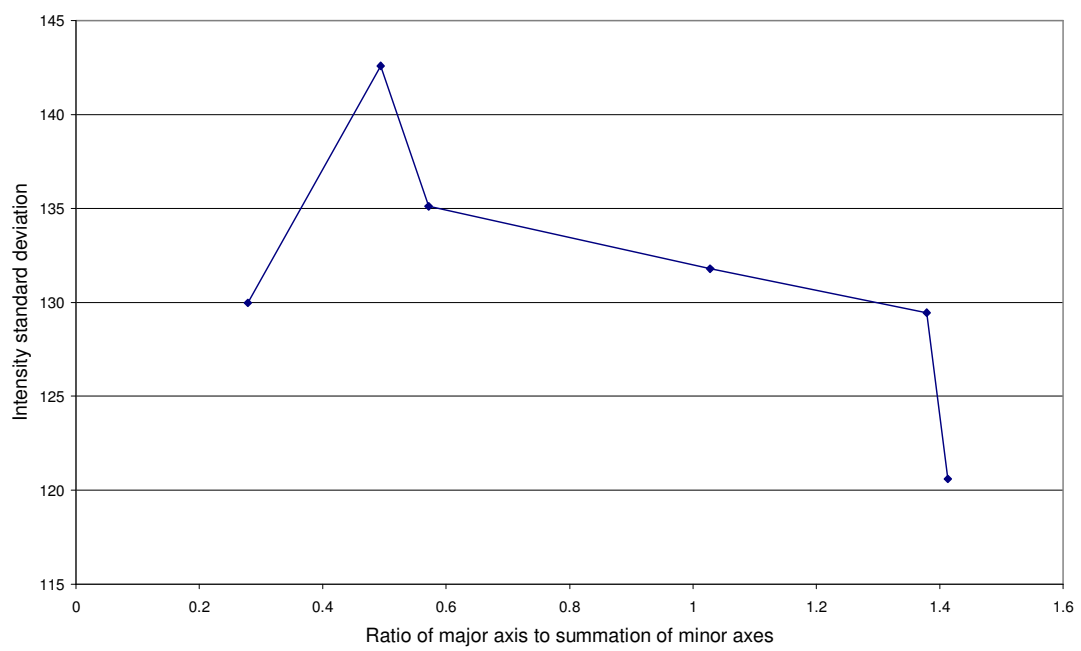


Figure 4.32 Variation of intensity standard deviation of a PSD images after filtering over the ratio of major axis to summation of minor axes.

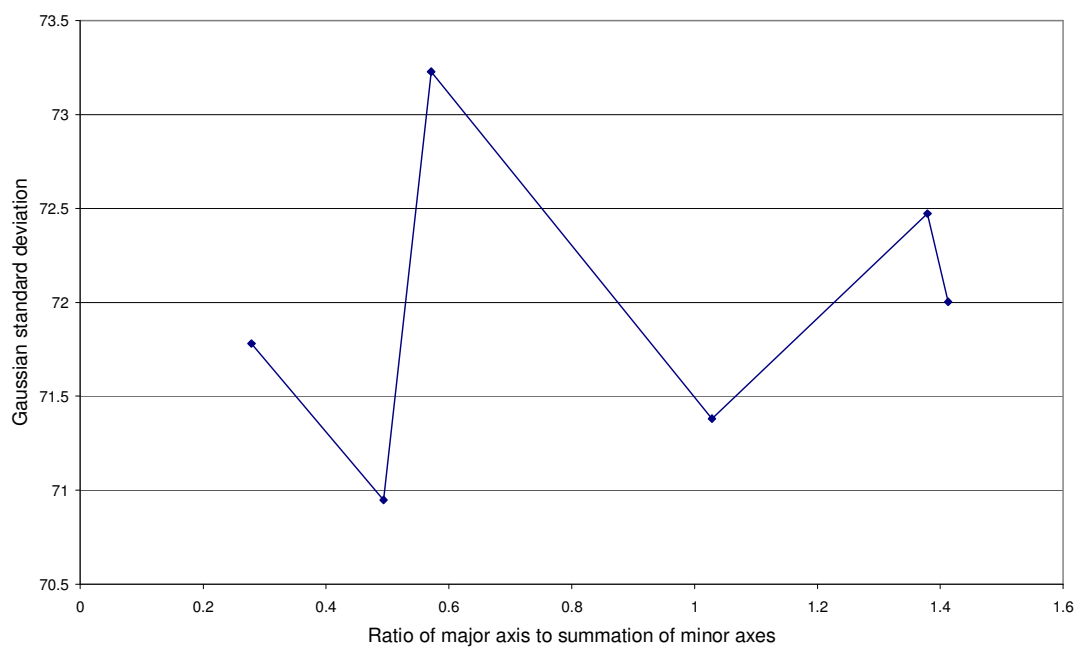


Figure 4.33 Variation of Gaussian standard deviation of a PSD images after filtering over the ratio of major axis to summation of minor axes.

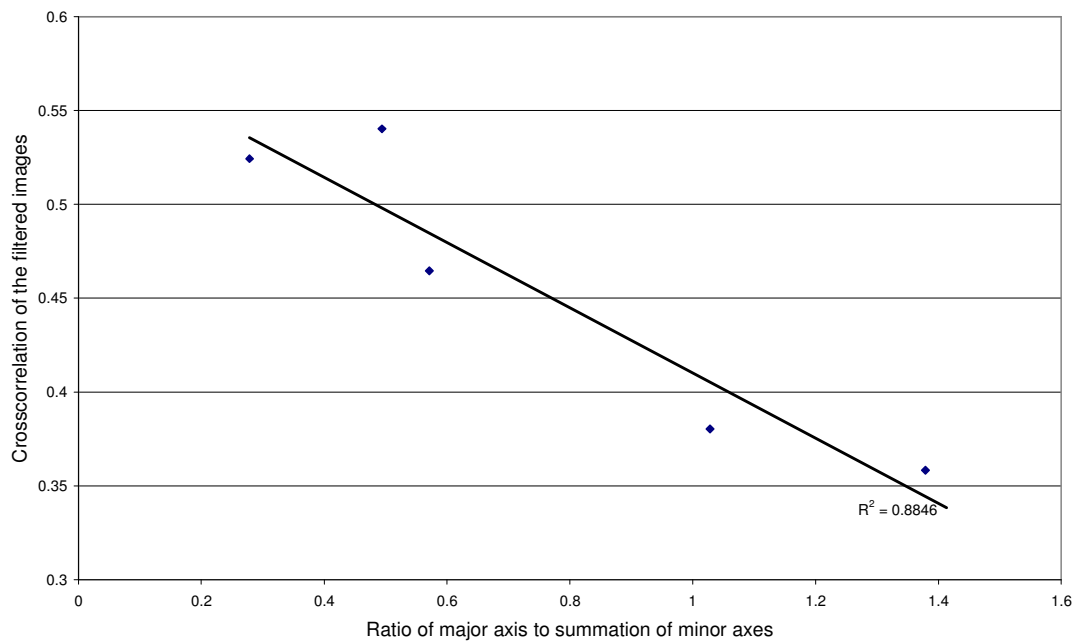


Figure 4.34 Variation of crosscorrelation coefficient of the *Euglena* images after filtering over the ratio of major axis to summation of minor axes.

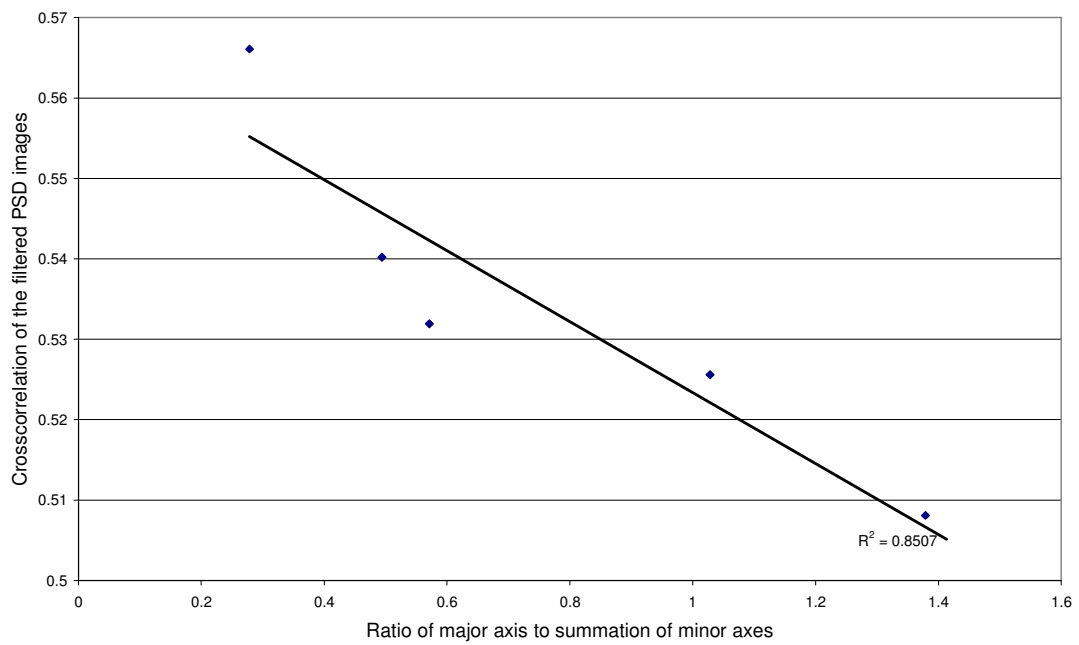


Figure 4.35 Variation of crosscorrelation coefficient of the PSD converted *Euglena* images after filtering over the ratio of major axis to summation of minor axes.

Rank	Method of analysis	Sequence	Overall score	%
1	<ul style="list-style-type: none"> • $(a/(b1+b2+b3))$ • $(a/(b1+b2+b3))^* (1/Area)$ • Crosscorrelation of the actual image before filtering • Crosscorrelation of the PSD image after filtering. 	4-1-2-3-5-6	49/72	68.05
2	<ul style="list-style-type: none"> • Crosscorrelation of the PSD image before filtering 	4-1-3-2-5-6	43/72	59.72
3	<ul style="list-style-type: none"> • $(a/b)^*(1/Area)$ 	2-1-4-3-5-6	36/72	50.00
4	<ul style="list-style-type: none"> • (a/b) 	2-1-3-4-5-6	34/72	47.22
5	<ul style="list-style-type: none"> • Crosscorrelation function of the actual image after filtering 	4-2-1-3-5-6	33/72	45.83
6	<ul style="list-style-type: none"> • (a/b_{avg}) • $(a/b_{avg})^* (1/Area)$ 	2-4-1-3-5-6	31/72	43.05
7	<ul style="list-style-type: none"> • Average pixel intensity after filtering 	1-2-4-3-5-6	30/72	41.66
8	<ul style="list-style-type: none"> • Intensity standard deviation before filtering • Intensity standard deviation after filtering 	1-2-3-4-5-6	28/72	38.88
9	<ul style="list-style-type: none"> • Average pixel intensity before filtering • Gaussian standard deviation before filtering 	4-1-2-6-3-5	24/72	33.33
10	<ul style="list-style-type: none"> • Crosscorrelation before filtering 	1-3-2-5-4-6	18/72	25.00
11	<ul style="list-style-type: none"> • $Area$ 	1-4-3-2-6-5	10/72	13.88
12	<ul style="list-style-type: none"> • Gaussian standard deviation after filtering 	2-5-6-4-3-1	3/72	4.16

Table 4.7 Comparison of the results from different analysis methods and the scores from visual assessment methods.

Image processing Parameter	R²	Rank
Gaussian standard deviation before filtering	1	1
Crosscorrelation of PSD image before filtering	0.9484	2
Crosscorrelation of actual image before filtering	0.9077	3
Crosscorrelation of actual image after filtering	0.8846	4
Crosscorrelation of PSD image after filtering	0.8507	5
Average pixel intensity before filtering	0.7295	6
Average pixel intensity after filtering	0.5485	7
Intensity standard deviation after filtering	0.4189	8
Intensity standard deviation before filtering	0.3571	9
Gaussian standard filtering after filtering	0.024	10

Table 4.8 Comparison of the results from image processing method with the ratio of major axis to summation of minor axes.

CHAPTER 5 POPULATION STATISTICS OF *EUGLENA GRACILIS*

5.1 INTRODUCTION

Euglena gracilis is a unicellular organism belonging to the protist kingdom and is typically 35-55 μm long, 6-25 μm wide (Lee *et al* 2000). It is noted that *Euglena gracilis* forms a green scum on the bottom of ponds and drainage ditches and reproduces by the process of mitosis that takes about five hours (Lee *et al* 2000). This microorganism grows in photoautotrophic conditions but it is also able to develop in heterotrophic or photoheterotrophic conditions (Rocchetta *et al.*, 2006).

Euglena gracilis possesses interesting morphological and motility characteristics. The cell's morphology varies between cylindrical to elongate ovate over time periods of a few seconds. Its morphological structure is dependent on internal microtubule arrangements within the cytoskeleton (Lonergon and Lachney, 1985). Lonergan(1983, 1985) did considerable work on the regulation of cell shape by monitoring the effect of altered intracellular and extracellular Ca^{2+} ions, the cell's biological clock, respiration and photosynthesis on the cell shape.

Gravity, light, chemicals and magnetic fields are some of the environmental stimuli for which the organism would react. The microorganism thus tends to position itself in regions that are best suited for optimal physiology and survival. Studies of microbial motility and sensory behaviour are thus important for understanding the role of motile microorganisms in microbial ecosystems and give important clues to the structure and ecology of microenvironments (Thar *et al* 2000). *Euglena* have been demonstrated to possess an internal store of Mg^{2+} , which is involved in the control of the flagellar motility (Nichols and Rikmenspoel, 1977). Basic evolutionary principles that explain the photoreception and locomotion of *Euglena* were investigated (Simanonok, 2006). The gravitaxis and phototaxis nature of *Euglena* was studied on the TEXUS 23 mission under μg conditions and the first experiment showed that Earth's gravitational field affects the orientation of *Euglena* in the absence of light (Hader, 1997). It is understood that this unicellular alga swims toward sunlight using the longer of its two flagella. The shorter one must be involved in photoreception as a 'comparator device' with the rhodopsin containing the

photoreceptor called paraflagellar swelling (Simanonok, 2006). Physical characterization of gravitactic orientation was explained as a phenomenon on the basis of a specific density difference between the cell body and surrounding medium. (Hader *et al.*, 1999).

It was found that there was an internal Mg^{2+} store present in the *Euglena* was localized in the area of paraflagellar swelling and when this area was irradiated with an infrared laser beam at a low dose it caused permanent loss of motility, it was found that the laser irradiation only caused a decrease in the flagella frequency and did not destroy the photoreceptor. It was concluded that the laser irradiation eliminates only the Mg^{2+} store in the photoreceptor but it did not destroy the ability of the stigma-paraflagella to control the flagellar activity (Nichols and Rikmenspoel, 1982).

Changes in cell mobility after exposure to continuous wave radiation from a red laser pointer were studied in *Euglena gracilis* cultures. It was found that the cell velocities increased by 10.3% and 14.1 % after exposure to 650nm and 830nm laser irradiation, respectively, as compared with control cells (Janisch, 2003).

The tedium of conventional methods (staining) of measuring the motile characteristics has been replaced with image analysis (Kreitz *et al.*, 1995) and optoelectronic techniques (Bahram *et al.*, 2005). For quantitative investigations of motility, cell tracking systems are advantageous. Some of the serious illnesses which can be better controlled by early diagnosis are tuberculosis and mycobacteriosis. To detect the bacilli in this process, the sputum images were analysed by a highly trained personnel and this is a time consuming process. Image processing in bacterial detection has been proven to be helpful with the detection of tuberculosis and other mycobacteriosis. The accuracy is dependent on the bacilli detection techniques and provides a good tool for improving the screening of sputum images (Forero *et al.*, 2004).

One of the conventional imaging methods in microbiology is to measure fluorescently stained bacteria directly. The tedium of making such measurements visually has prompted the use of image processing tools and techniques which can be done automatically in real-time. Reliable methods to eliminate background particles and select an appropriate threshold for automated counts and measurements are needed (Kreitz *et al.*, 1995). The

advances in imaging devices, optics, computer technology, light sources, and spatial and temporal light moderators has made implementing optoelectronics techniques for 3D image sensing, visualization and processing a reality (Bahram *et al.*, 2005).

A video-based 2D-tracking system for protist organisms with a diameter of 35-55 μm was developed for this study. The tracking system provides the possibility of tracking many cells simultaneously. The system resolution was improved with a high power objective (x50, x100) at the expense of a limited depth of field. Consequently, the cells can be tracked only during the time they spend in the focal plane. To increase the contrast, dark-field illumination was applied to the low resolution system, which was optimized for high illumination efficiency for minimizing any influence on the sample. A non-actinic monochromatic laser illumination was used to further increase the contrast, which allowed studies of the effect of irradiance on the specimen. The images captured using these microscopy systems were then processed by filtering with a convolution or deconvolution filter. The filtered images were analysed in the spatial and frequency domain to obtain meaningful information of the population statistics over time. Chapter 4 refers to the experiments done on the changing shape of a single *Euglena* cell. The spatial analysis allows the number of *Euglena* cells to be determined; whereas the frequency domain analysis allows extraction of the intensity information from the field of view. Thus by combining these two datasets, population statistics can be ascertained to understand and quantify the *Euglena* activity.

5.2 MATERIALS AND METHODS

The sample preparation involves the growing the *Euglena* sample on the Jaworski medium and preparing the optical slide for the specimen.

5.2.1 *Euglena* culture preparation

A sample looped from a slope culture of *Euglena gracilis* was added to a fresh EG: JM (*Euglena gracilis*: Jaworski's medium) nutrient broth (20 ml) prepared with doubly distilled deionized water. The culture was incubated at 15 °C, under a 12:12 hour (light: dark) regime to create a primary culture. The illumination was provided by non-thermal white fluorescent lamps with a photon flux density of 50 $\mu\text{mol m}^{-2} \text{s}^{-1}$ at the surface of the culture flask. An inoculum of 1 ml from the primary culture was transferred from a late

log/stationary phase culture into fresh, sterilised medium every 2 weeks. Cultures were maintained in 100 ml conical flasks containing 50 ml of the medium, stoppered with foam bungs. These cultures are normally named as secondary cultures and were used for all the microbiological experiments.

5.2.2 Specimen slide preparation

Figure 5.1 shows the ringing table used to add *Euglena* cultures uniformly to the microscope slide. The table consists of spring operated slide holders at both ends. The specimen slide is placed on the table so that the centre of the slide is inline with the axis of rotation of the table. The slide is rotated at uniform speed and the protist culture is added to the middle of the slide and moved radially outwards, ensuring that the volume distribution of the culture is uniform.

5.2.3 Microscopy and image capturing system

A preliminary experiment was done with a phase contrast microscopy system (**Figure 5.2**) with x40 magnification objective to identify the behaviour of a countable number of *Euglena* cells in detail. This was followed by experiments done with a custom built dark field microscopy system (**Figure 5.3**) optimized for high contrast and kept under ambient environmental conditions and relatively low magnification. The application involves monitoring a culture of *Euglena* on the slide and not specific to a single cell and its constituents (as described in Chapter 4).

A monochromatic source (10mW He-Ne laser, 633nm) was preferred as the means of illumination as the spatial frequency noise in the images under these conditions was reduced more than for bright field illumination. It was also observed that the contrast of images was enhanced compared with conventional dark field system (Goesele *et al.*, 2001).

In order to utilize the high intensity laser beam for illumination, it is important to increase the beam diameter, so that the far field divergence would be decreased by the inverse portion. To achieve this laser beam expander (Keplerian type) was employed thereby distributing the beam's power over a larger circular area. To further reduce the high frequency noise from the system, a spatial filter was used for uniform illumination of the condenser. The spatial filter comprised a pin hole (10 μ m, 25 μ m or 50 μ m). The beam

expander consisted of a microscope objective (x40) that expanded the Gaussian beam over a larger area. The laser beam was centered using the sliding micrometer studs, bolts and Allen screws. A flat mirror directed the incoming beam onto the dark field condenser to illuminate the specimen. The specimen was viewed under an x10 objective. A low NA objective was fitted into the assembly. It was possible to view a large number of cells rather than just single cells. Figure 5.4 shows the setup of the laser illuminated dark field microscopy system.

The image capturing system comprised a ToUcam PRO II camera (Philips, UK) with a pixel resolution of 640 x 480, connected to the microscope and output screen. Video (25 frames per second) was collected for off-line processing and analysis. Images (BMP format) from the video (AVI format) were extracted using Arcsoft Video impression (Version 1.6, ArcSoft, Inc., California) and converted to FITS (Flexible Image Transport System) which is a standard data format designed by NOST (NASA/Science Office of Standards and Technology). The images were imported into ASTROART (Version 3.0, MSB Software, Italy) astronomical software used by NASA for image analyse using non-correlation techniques. Proprietary software written in MATLAB (Version 6.5, MathWorks, Inc., MI) was written for performing noise removal, image filtering operations and for image analyse using correlation techniques.

Analysis of the *Euglena* images during dehydration conveniently allowed comparison of the performance of different algorithms at quantifying the activity and density of the population. Once parameters were identified to determine the activity, transient analysis was done during the cells' lifetime.

5.2.4 Image analysis methods

In order to assess the population statistics of the protists it is necessary to relate the decrease in cellular activity of the *Euglena* over time to corresponding changes in the images, either in the space or spatial frequency domain. The dehydration experiment allows a natural degradation of the viable cell numbers. An understanding of the captured data was achieved by selecting and arranging a series of images from the video stream that were representative of the *Euglena* from high to low activity during this dehydration period.

Figure 5.5 shows the flowchart of how the raw images were treated and analyzed using different tools and techniques. The images were either converted immediately into the frequency domain or passed through a series of noise reduction filters before performing analysis in the frequency or spatial domain. In the spatial analysis, the number of connected objects was determined and in the frequency analysis the power spectral density (PSD) was found. The PSD images both with or without pre-filtering were analysed with various algorithms and converted to polar images in an attempt to quantify the population dynamics of the cell.

5.2.5 Image convolution Filtering

The raw image as taken from the microscopy system was then filtered such that the redundant details from the images were removed before analysis. Convolution filters were applied by converting the image in the frequency domain and deconvolution filters were applied on the spatial domain. All these filters were applied on the raw image and the best output image was considered for image analysis.

Convolution is a simple mathematical operation which is fundamental to many common image processing operators. It provides a method of multiplying two images or arrays of numbers, generally of different sizes, but of the same dimensions, to produce a third image or array of the same dimensionality. In order to find the output image of a filter, the input image is convolved with the impulse response of the image filter. The impulse response is often called the point spread function (PSF).

The output image y of an entering bitmap x , through a filter system of bitmap impulse response h is given by the formula:

$$y[r, c] = \frac{1}{\sum_{i,j} h[i, j]} \sum_{j=0}^{M-1} \sum_{i=0}^{M-1} h[j, i] * x[r - j, c - i] \quad (5.1)$$

Where r and c stand for r^{th} row and c^{th} column of the image respectively, M is the width and height of the square image. In the case of convolution filters, the raw image is transformed to a Fourier transform with the output in the Fourier or frequency domain. This Fourier image is then convolved with one of those standard, special function filters or

custom made filters. Some of the standard filters are Gaussian and Laplacian. Special filters are low pass, high pass or band pass filters created using MATLAB special functions such as: *fsamp2*, *fwind1*, *fwind2*. Custom made filters are those which are application specific, designed accordingly to suit the needs based on the quality of the image captured.

One of the difficulties when convolution is applied to the border pixels is that the convolution kernel would extend beyond the borders of the image. There are three methods identified. One is to simply ignore the problematic pixel and to perform convolution only on pixels considerable distance from borders. This is known as zero boundary superposition. The second is to pad the missing pixels with zeroes known as zero padded superposition. The third is known as reflected boundary superposition and is quite effective because it regards the image as a single element in a tiled array of identical images and the kernel will overlap the missing pixels from the opposite side of the image (Spring *et al.*, 2006). This technique would result in an output image the same size as the input image whereas the other two techniques may result in output images that are smaller than the input image.

5.2.5.1 Standard convolution filters

Laplacian filter

Laplacian filters are often termed as operators, and resultant is found from the second derivative of intensity with respect to spatial position (Spring *et al.*, 2006).

The Laplacian filter returns a 3-by-3 filter which is an approximation of the shape of a two-dimensional Laplacian operator. In the MATLAB Laplacian function, the parameter alpha controls the shape of the Laplacian and must be in the range 0.0 to 1.0. The default value for alpha is 0.2 (Mathworks, Inc., 2002). One of the Laplacian matrix used in this application is

$$L = \begin{pmatrix} 0.1667 & 0.6667 & 0.1667 \\ 0.6667 & -3.3333 & 0.6667 \\ 0.1667 & 0.6667 & 0.1667 \end{pmatrix} \quad (5.2)$$

Figure 5.6 shows the image in the logarithmic magnitude and phase equivalent of the Laplacian filter (5.2) employed in the image filter application. Each pixel in the real image (640 x 480) corresponds to gray scale value '0' to '255'. Each pixel in the phase image shows the angles between $-\pi$ to $+\pi$, where $-\pi$ corresponds to gray scale value '0' and $+\pi$ corresponds to '255'. This representation remains consistent for all the magnitude and phase images mentioned in this chapter.

Gaussian filter

The MATLAB function for the Gaussian filter (*G*, see equation 5.3) returns a rotationally symmetric Gaussian lowpass filter of size *hsize* with standard deviation *sigma* (positive). *hsize* can be a vector specifying the number of rows and columns in *h*, or it can be a scalar, in which case *h* is a square matrix (Mathworks, Inc., 2002). The default value for *hsize* is [3 3]; the default value for *sigma* is 0.5.

$$G = \begin{pmatrix} 0.0000 & 0.0000 & 0.0000 & 0.0000 & 0.0000 & 0.0001 & 0.0000 & 0.0000 & 0.0000 & 0.0000 & 0.0000 \\ 0.0000 & 0.0000 & 0.0001 & 0.0003 & 0.0006 & 0.0008 & 0.0006 & 0.0003 & 0.0001 & 0.0000 & 0.0000 \\ 0.0000 & 0.0001 & 0.0005 & 0.0020 & 0.0049 & 0.0066 & 0.0049 & 0.0020 & 0.0005 & 0.0001 & 0.0000 \\ 0.0000 & 0.0003 & 0.0020 & 0.0088 & 0.0215 & 0.0288 & 0.0215 & 0.0088 & 0.0020 & 0.0003 & 0.0000 \\ 0.0000 & 0.0006 & 0.0049 & 0.0215 & 0.0521 & 0.0701 & 0.0521 & 0.0215 & 0.0049 & 0.0006 & 0.0000 \\ 0.0001 & 0.0008 & 0.0066 & 0.0288 & 0.0701 & 0.0942 & 0.0701 & 0.0288 & 0.0066 & 0.0008 & 0.0001 \\ 0.0000 & 0.0006 & 0.0049 & 0.0215 & 0.0521 & 0.0701 & 0.0521 & 0.0215 & 0.0049 & 0.0006 & 0.0000 \\ 0.0000 & 0.0003 & 0.0020 & 0.0088 & 0.0215 & 0.0288 & 0.0215 & 0.0088 & 0.0020 & 0.0003 & 0.0000 \\ 0.0000 & 0.0001 & 0.0005 & 0.0020 & 0.0049 & 0.0066 & 0.0049 & 0.0020 & 0.0005 & 0.0001 & 0.0000 \\ 0.0000 & 0.0000 & 0.0001 & 0.0003 & 0.0006 & 0.0008 & 0.0006 & 0.0003 & 0.0001 & 0.0000 & 0.0000 \\ 0.0000 & 0.0000 & 0.0000 & 0.0000 & 0.0000 & 0.0001 & 0.0000 & 0.0000 & 0.0000 & 0.0000 & 0.0000 \end{pmatrix} \quad (5.3)$$

Figure 5.7 shows the logarithmic magnitude and phase equivalent of the Gaussian image filter (5.3) employed in the image filter application

5.2.5.2 Tailored convolution filters

The tailored convolution filters are those which use special functions of MATLAB such as: *fsamp2*, *fwind1*, *fwind2*. These are two-dimensional finite impulse response filters using either sampling or windowing methods. *fsamp2* as the name indicates is a function that is used to design two-dimensional finite impulse response (FIR) filters using sampling methods and *fwind1*, *fwind2* are used to design the same using one-dimensional or two-dimensional windowing methods.

Low pass filter

The low pass filter used in image processing is mainly intended to generate a blurred image. Weighted difference of the blurred image and the original image results in an amplification of high frequency components and overall enhancement of the image (Reza *et al.*, 1998). The MATLAB code written in this application uses the threshold value 0.6 and any component less than this value is accepted. **Figure 5.8** shows the logarithmic magnitude and phase equivalent of the low pass image filter using *fsamp2*. **Figures 5.9 and 5.10** shows the equivalent filter obtained through *fwind1* and *fwind2* functions respectively.

High pass filter

The high pass filter as mentioned in section 4.2.3.2, is used in digital image processing to remove or suppress the low frequency components, resulting in a sharpened image (Nascimento and Sayed, 2000). The MATLAB code written in this application again uses the threshold value of 0.6 and any component more than 0.6 are accepted. **Figure 5.11** shows the logarithmic magnitude and phase equivalent of the high pass image filter using *fsamp2*. **Figures 5.12 and 5.13** show the equivalent filter obtained through *fwind1* and *fwind2* functions.

Band pass filter

The MATLAB code written in this application uses a band pass filter which allows the components within the intensity range of 0.1 to 0.6 and suppresses all other values. **Figure 5.14** shows the logarithmic magnitude and phase equivalent of the band pass image filter using *fsamp2*. **Figures 5.15 and 5.16** show the equivalent filter obtained through *fwind1* and *fwind2* functions, respectively.

5.2.5.3 Deconvolution filters

Normalize background intensity

This operation is performed between two images and it sets a background value of the active image equal to the background value of the other, multiplying it by a coefficient. This method is important because though the images were captured under the same hardware and optical devices, it is possible to correct the imaging and intensity errors through software algorithms. By normalizing the background intensity through this

algorithm, the light intensity of both the images from the control sample and the image under study will have uniform illumination in the background.

Background subtraction

Background subtraction is performed on the image so the unwanted components contributed to the image by the broth would be eliminated. This would only enhance the contrast of the image of the necessary field or object of interest.

Choosing the point spread function

The images captured under these microscopy systems are the product of the convolution of frequency responses from the dark field condenser, the specimen slide and objective lens. The frequency response from the specimen slide also includes the responses corresponding to the broth and the culture. It is important to deconvolve the redundant information provided by the broth. Thus images of broth were randomly chosen and deconvolved from the rest of the image. The PSF of the selected portion is calculated through the special functions available in ASTROART. **Figure 5.17** shows the point spread function from an image of only broth (in AstroArt) and **Figure 5.18** shows the same on a 3-d plot.

Deconvolution filtering

Deconvolution algorithms are basically iterative algorithms that can correct almost any blurring defects over the whole image. There are normally three different types of algorithms that could be performed on the images (Li *et al.*, 2006). The algorithms such as: Richardson-Lucy, Van Cittert or maximum entropy can be used as deconvolution filters. During the iterations, logarithms are calculated and thus the filter is not linear and the restored image cannot be used for photometry. Richardson-Lucy is a linear algorithm that maintains the photometric characteristics of the image, but degrades the images. Van Cittert is a linear filter sometimes useful on images of planets, but it can be used only with Gaussian kernels. Maximum entropy restoration is one of the powerful algorithms for deconvolution (Bassnett, 2005). The maximum entropy restoration has been used for this application (Figure 5.17).

Full scale adaptive low pass filter

One of the important objectives of this filter design is to enable the software to count the number of connected objects in the densely populated images containing a high number of cells. The deconvolution removes the unwanted information from the picture. But there is a chance that the low frequency component values would reduce considerably as a side effect. Therefore a low pass filter was used to minimize such effects. A full scale adaptive filter can reduce noise without blurring (Nascimento and Sayed, 2000). Thus a full scale adaptive filter from ASTROART was used in this application.

5.2.6 Algorithm development

Significant research has been undertaken on assessing methods of tracking and identifying the motility of microorganisms. The photo-tactic movements of microorganism have been predicted by reconstructing the spatiotemporal tracks by obtaining the cell movement parameters (Gualtieri *et al.*, 1988). While other research has enabled measurement of *Euglena gracilis*' motion parameters such as the distribution of the cell rotation, flagella beating frequency and swimming speed distributions. These were determined by the spectral analysis of scattered laser light with the samples orientated by a radiofrequency field (Ascoli *et al.*, 1978). In this study, the unfiltered and filtered images derived from the *Euglena* motion were analyzed both in the time and frequency domain.

5.2.6.1. Frequency domain analysis

There is a need then to define a mathematical parameter which provides a measure of the image's characteristics i.e. the real time spatial frequency behaviour of the *Euglena*. Ideally the parameter should follow the motility and population state of the microorganism to be identified with adequate variation or sensitivity in that parameter. Then the variation in this parameter can be assessed over time to quantify the population's dynamic behaviour. From the power spectral density (PSD) images, the pixel statistics allow important parameters to be found namely: average pixel value, the standard deviation of these values and a parameter termed the Gaussian standard deviation derived from the best Gaussian fit to the data, defined below. These parameters were found and compared for different cell populations. Additionally, polar images were derived from the PSD images and the standard deviations of these values were also found. The most effective of these four parameters that tracked the changes in the population characteristics was chosen for further

analysis. In addition to these four parameters, a spatial domain analysis was done on these images where the number of connected objects was found and related to the cellular activity.

Average pixel intensity

Intensity standard deviation

Gaussian standard deviation

Detailed descriptions of these three parameters are as mentioned in Chapter 4 Section 4.2.6.

Polar Standard deviation

The power spectral density image and standard deviation are in Cartesian coordinates. By converting them to angular coordinates, characteristics are revealed that are not readily visible in the rectangular coordinate representation (Hanbury and Serra, 2002).

5.2.6.2 Spatial domain analysis

Erosion and dilation filters were applied to the image as a morphology opening operation. Contrast enhancement and software counting operations were performed. The objective was to count the number of connected objects by removing the unwanted information from the raw image. The entire spatial analysis was done using MATLAB image processing tools.

Morphological opening operation

In this step, a morphological opening operation is performed to estimate the background illumination. Morphological opening comprised erosion followed by dilation, using the same structuring element for both operations. The opening operation has the effect of removing objects that cannot completely contain the structuring element. The MATLAB code calls the *imopen* function to perform the morphological opening operation and the *strel* function to create a disk-shaped structuring element with a radius of 15 pixels. To recognise the individual *Euglena* cells from the image. The structuring element must be large enough so that it cannot fit entirely inside a single cell of euglena.

Contrast enhancement operation

While performing the erosion and dilation, the intensity values of the useful information may reduce. The background information would not be completely revealed in the

morphology opened image. It is always a good practice to enhance the contrast of the meaningful information available on the image. Thus a contrast enhancement operation improves the overall contrast of the image.

Counting the number of connected objects

The contrast enhanced images are first converted into a binary image as an input image to the software that counts connected objects of *Euglena*. The *bwlabel* function from the MATLAB image processing tool labels all the individual components in the binary image and returns the number of components it finds in the image as the output value.

5.3 RESULTS AND DISCUSSIONS

5.3.1 Microscopy Images

Figure 5.19 shows the images from a phase contrast microscopy system. As a preliminary work these images were captured to identify the events happening during dehydration. The time scale shown was from $t = 40$ to 65 seconds. Interestingly it was noticed that the intensity information in the slide appeared brighter with time. This experiment marked a useful way to understand the dehydration of the specimen and to investigate ways to quantify the process.

Figure 5.20 shows the images from a laser illuminated dark field microscopy system. These are the raw images taken at times $t = 0, 1, 3, 6, 8$ and 11 seconds. These images display the population from a large number of *Euglena* cells. As can be seen the individual cells are not clear. It is important to analyse any meaningful information from these images and to quantify such a sensitive transition through some mathematical parameters.

5.3.2 Image Analysis without filtering

As previously mentioned, analysis was done over the spatial frequency and time domains. The analysis in the frequency domain monitored the intensity variation as a means to define the activity and the analysis in the time domain monitored the number of objects involved in that particular activity. The results from both the analysis provide an indication of the activity and enabled quantification of the population dynamics over time.

5.3.2.1 Frequency domain analysis

Figure 5.21 shows the power spectral densities of the filtered images in **Figure 5.20** over the period $t = 1$ to 7 s. It is seen that there are differences in the images during dehydration. It is useful to identify parameters which quantify the changes due to dehydration in the images. The images in the Cartesian form are converted into their polar coordinate form. The 1-D and 2-D conversion of PSD images into polar coordinates are given in **Figures 5.22** and **5.23** respectively.

Four possible parameters that could be used to describe dehydration of the protozoa *Euglena* samples were identified (section 5.2.6.1). The results are shown in **Figure 5.24** and all of these parameters were calculated from the images in the frequency domain without filtering. The average pixel intensity from the PSD X-Y coordinate image shows significant changes with dehydration. The intensity standard deviation again changes value in accordance with dehydration. It follows a $1/e$ curve for the number of pixels vs intensity values plotted from the PSD image in Cartesian coordinates upto complete dehydration. It was found that the standard deviation of the Gaussian parameter did not show significant changes with dehydration. The reason was it involves a direct assumption that the distribution followed by PSD images (**Figure 5.21**) was a Gaussian fit. However, the parameter “Polar standard deviation” calculated from the statistics of the polar form image from the PSD X-Y coordinates image, gave the greatest sensitivity to the dehydration process. The parameters follow a wide range of value and therefore appear to show small changes in the intensity values. The polar standard deviation parameter was identified as the best parameter to define changes in the population statistics of the sample. The parameters: average, standard deviation and Gaussian values were multiplied by 10 to fit on the same graph.

5.3.2.2 Spatial domain analysis

For the spatial domain analysis the number of connected objects was counted which should be proportional to the number of *Euglena* cells. **Figure 5.25** depicts the morphological opening operation. As mentioned previously, morphological opening is image erosion followed by dilation, using the same structuring element for both operations. **Figure 5.25a** indicates the structuring element used in this process. **Figure 5.25b** shows the intensity graph of the same element in a 3D chart. The opening operation has the effect of removing

objects that cannot completely contain the structuring element. The proprietary software calls the *strel* function to create a disk-shaped structuring element with a radius 'k'. To remove the *Euglena* cells from the image, the structuring element must be large enough so that it cannot fit entirely inside a single cell of *Euglena*. **Figure 5.25c** shows the image after background subtraction, i.e. subtracting the image after morphological operation from the original image. **Figure 5.25d** indicates the contrast enhanced image which is the final image, on which the counting of the connected objects was performed. **Figure 5.26** shows the results from the software counting without filtering as the suspension evaporates over time. The graph follows a similar shape as the polar standard deviation (Figure 5.24). It is obvious that the program is quite efficient in counting the connected objects but the values vary drastically, dipping at 4s because of the broth substance and other background noise which contributed to the number of objects connected to *Euglena cells*. Thus it is important to do filtering of the broth and background noise before performing the same analysis in the frequency or spatial domain.

5.3.3 Image filtering

5.3.3.1 Convolution filters

Figure 5.27 shows the results from the standard Laplacian and Gaussian filters available with MATLAB image processing tool functions. The magnitude and phase information are the product of convolution performed between the original image and the Laplacian or Gaussian filters. The Laplacian filter creates the same effect as a high pass filter and the Gaussian filter the same as a low pass filter (MathWorks Inc., 2002). The image processing was also done with the special function filters such as *fsamp2*, *fwind1* and *fwind2*. Each of these functions is utilized to design high pass, low pass and band pass filters. **Figure 5.28** shows the results from the convolution of high pass filter designed using special functions. **Figure 5.29** shows the results from convolution of low pass filters and **Figure 5.30** shows the results from the convolution of band pass filters. The magnitude and phase information are the product of convolution performed between the special function filters and the original image.

Figure 5.31 shows the effect of filtering on a surface chart. It is clear that the Laplace high pass filter cuts off more information during the process. There are possibilities that it may neglect useful information from the background (See **Figure 5.31 b**). The Gaussian low

pass filter on the other hand eliminated only information from the background. Thus Low pass filtering therefore should provide good contrast for the background.

Figure 5.32 shows the comparison chart for all the spatial frequency domain filters. These are the inverse Fourier transform of all the convolution images. It is found that the convolution with any of the high pass filters did not provide sufficiently high quality images to determine the connected objects. After low pass filtering the background of the images was optimized. The bandpass filtering produced images that enhanced the background but some of the information was lost. The broth and *Euglena* cells information could not be separated, Figure 5.32. Also it is to be noted that the culture of *Euglena gracilis* exists at different planes in the broth and the messy structure does not really allow the cells to be counted properly. The requirement here is a filter that counts the approximate number of connected objects between the cells after filtering the redundant portions of the images.

5.3.3.2 Deconvolution filters

Figure 5.33 shows the results from the deconvolution filters for different times from the original data ($t = 1$ to 11s). As mentioned above, the original image after background correction (when it is deconvolved from the point spread function of an unwanted image) yields the filtered image. The image clearly shows the connecting objects between *Euglena* cells and if the connected objects are counted it shows proportionality to the number of *Euglena* cells.

Figure 5.34 shows the results from the deconvolution filtered image of the PSD image at different times ($t = 1$ to 11s). The spectrum covered by this image is broader and clearer than the unfiltered image (Figure 5.21). This is mainly due to removal of noise that exists due to the broth and the camera noise. **Figure 5.35** shows the PSD image before and after filtering and the corresponding polar images. There is more detail apparent in the polar PSD image after filtering.

5.3.4 Image analysis after filtering

5.3.4.1 Frequency & Spatial domain analysis

Figure 5.36 shows a comparison of all the parameters after filtering. The parameters: average, standard deviation and Gaussian values were multiplied by 10 to fit on the same graph. The polar standard deviation of the PSD image was found to provide more meaningful information, as with image analysis before filtering (if Figure 5.24).

5.3.4.2 Spatial domain analysis

Figure 5.37 shows the graph of the connected objects over the time period of the same dehydration experiment. The results show that there is a decrease in the connected objects as the time increases. The image filtering process has eliminated the unwanted information from the image in the specimen and provided a measure of the cell population. Thus there exists a notable difference in the numbers counted before and after filtering (See Figure 5.26).

5.3.5 Selection of parameters

Figure 5.38 shows two selected parameters: polar standard deviation and the number of connected objects chosen from the frequency (Figure 5.36) and spatial analysis (Figure 5.37) respectively. They represent the dehydration process of the *Euglena* population happening within a period of 11 seconds and it is seen that they essentially give the same information.

5.3.6 Inference

Figure 5.39 shows the magnified view of Figure 5.38 over a period of $t = 4$ to 11 s. Initially the number of connected objects and polar standard deviation values reduces with time as dehydration progresses. However, after $t = 4$ s the polar standard deviation begins to increase but the number of connected objects decreases, showing that there is reductive of liquid. The decrease in the value of connected objects is directly related to the dehydrated conditions prevailing, whereas the increase in polar PSD value was due to the easier transmission of the light through the specimen because of the reduction in broth. The increase in intensity as indicated by the polar values and the decrease in the number of connected objects indicates that the *Euglena* cells are dying or becoming less motile due to dehydration.

5.4 CONCLUSIONS

The aim of these experiments was to develop and test the robustness of algorithms that could be used to show temporal variations in population statistics, this was conveniently taken over a dehydration period. The events occurring during normal dehydration were first investigated under a phase contrast microscopy system. The same experiment was repeated and viewed under a dark field microscopy system. The images obtained from the dark field microscopy system were processed in the frequency domain to determine four different parameters and in the spatial domain to determine the number of connected objects both with and without filtering. The performance of a series of standard convolution filters and special function convolution filters available in MATLAB were assessed and finally a custom made filter was applied to the raw images. The results were quantified in both the frequency and spatial domain. The five parameters were: average pixel intensity, intensity standard deviation, Gaussian standard deviation, polar standard deviation and number of connected objects. The polar standard deviation and the number of connected objects gave the best results and it may prove useful to monitor both these values simultaneously. The application of these findings will be particularly useful during fast changing environments, where the motility of a population or culture of cells could be continuously monitored by determining the polar standard deviation changes and number of connected objects with respect to time.

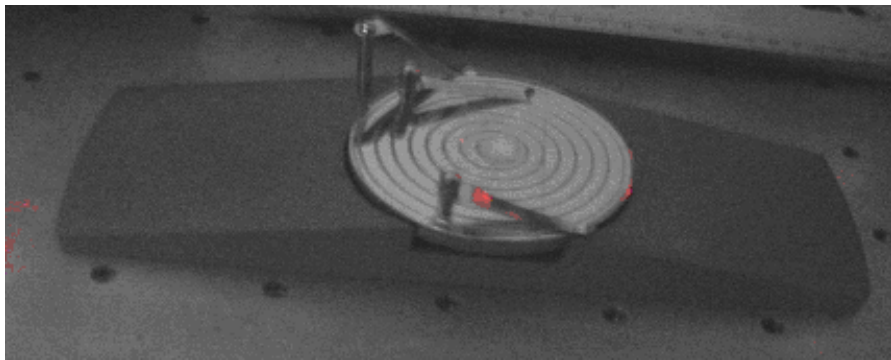


Figure 5.1 Ringing table for specimen preparation

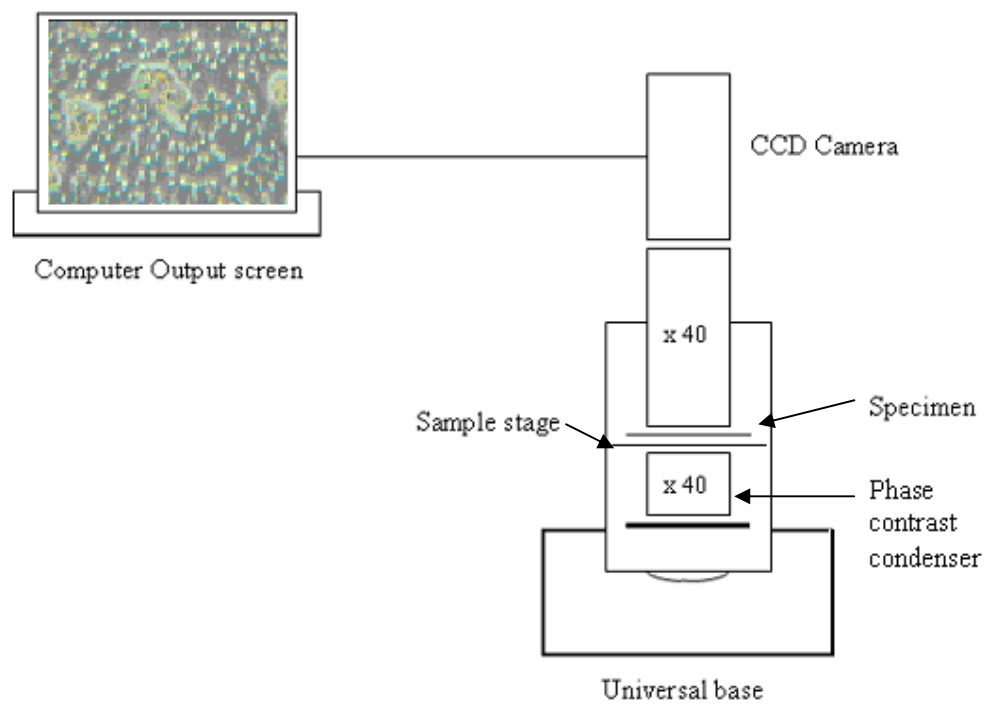


Figure 5.2 Preliminary experiment under phase contrast microscopy system

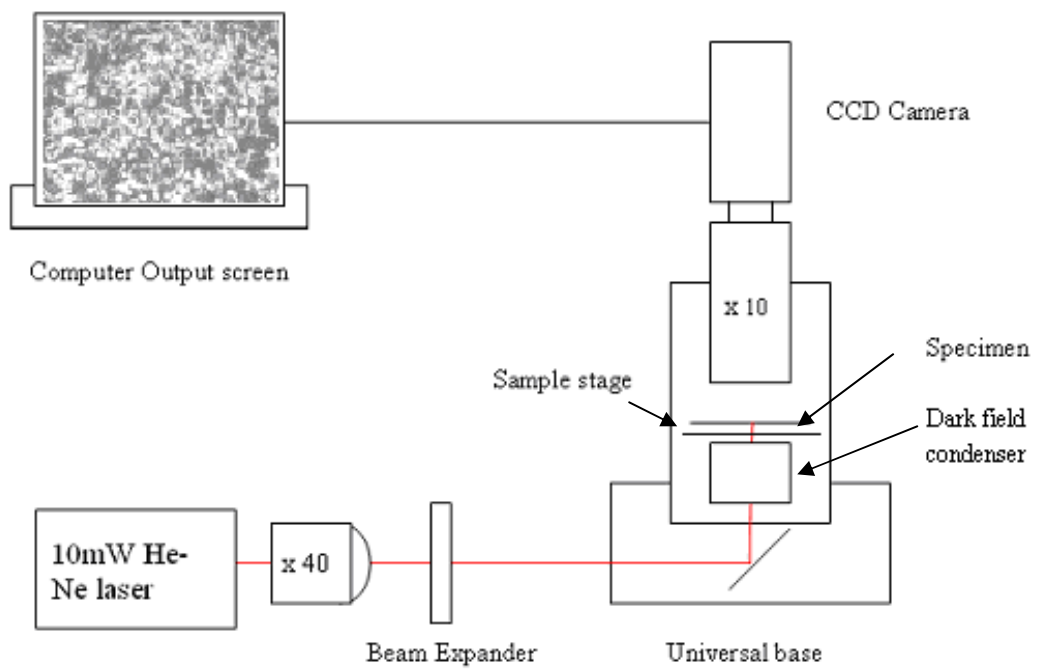


Figure 5.3 Schematic of the laser illuminated dark field microscopy system

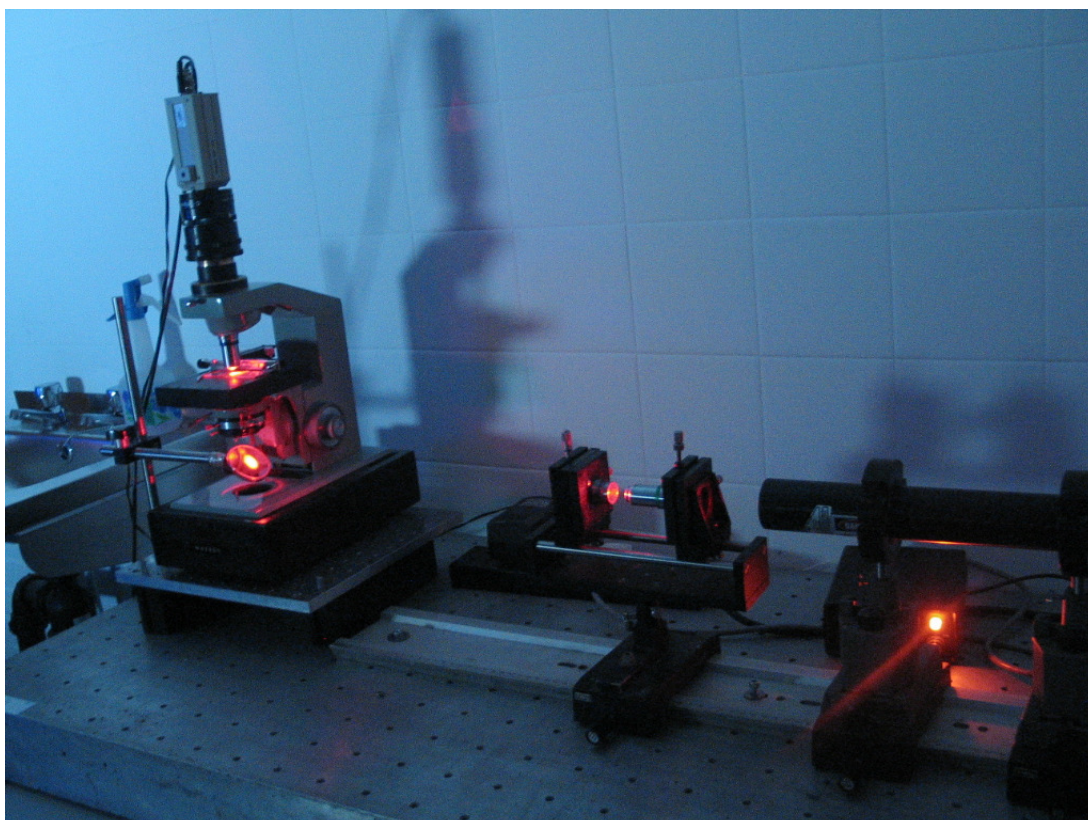


Figure 5.4 Custom built laser illuminated dark field microscopy system with beam expanders (middle).

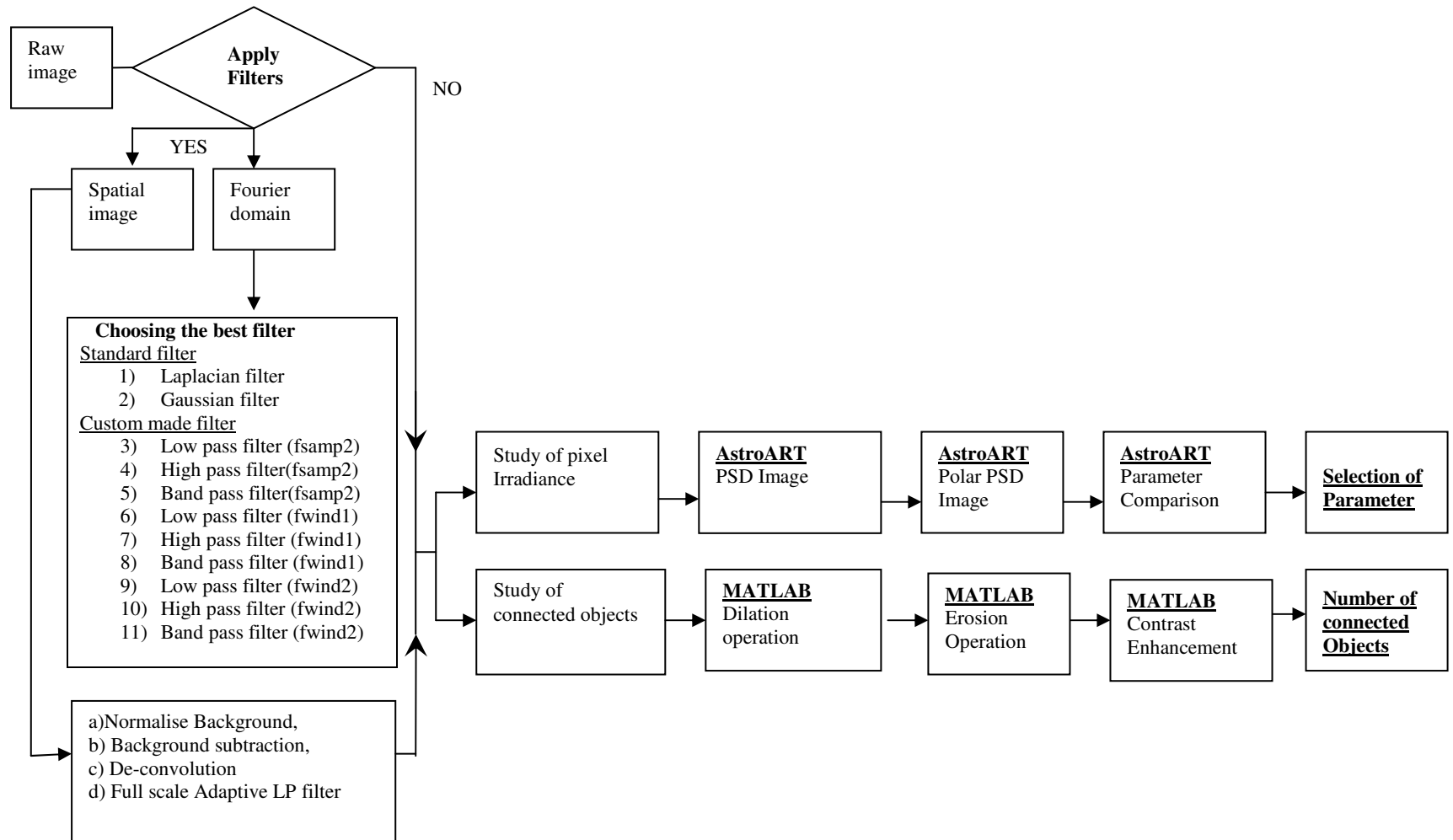


Figure 5.5 Image processing flowchart

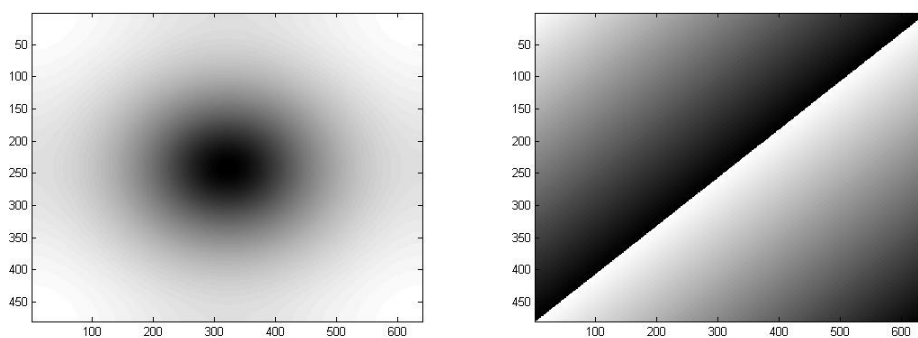


Figure 5.6 Log. magnitude and phase of the Laplacian image filter

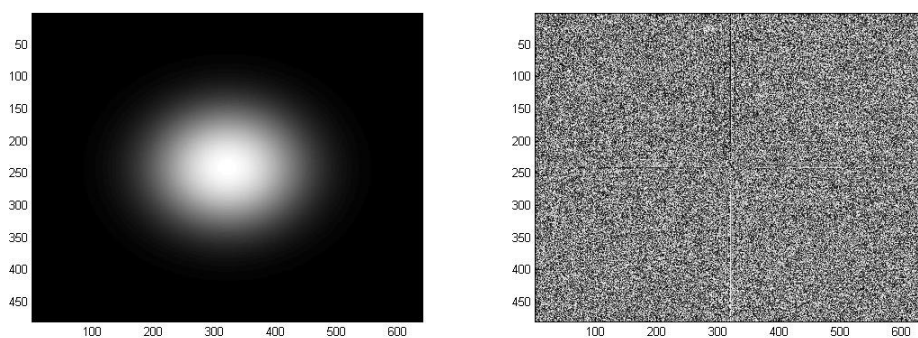


Figure 5.7 Log. magnitude and phase of the Gaussian image filter

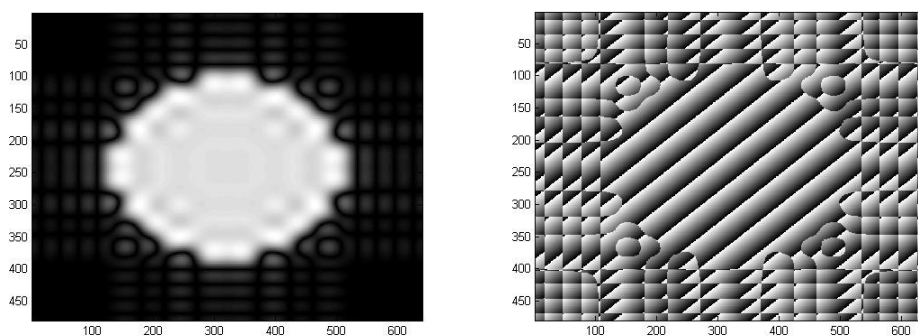


Figure 5.8 Log. magnitude and phase of the low pass image filter using *fsamp2*

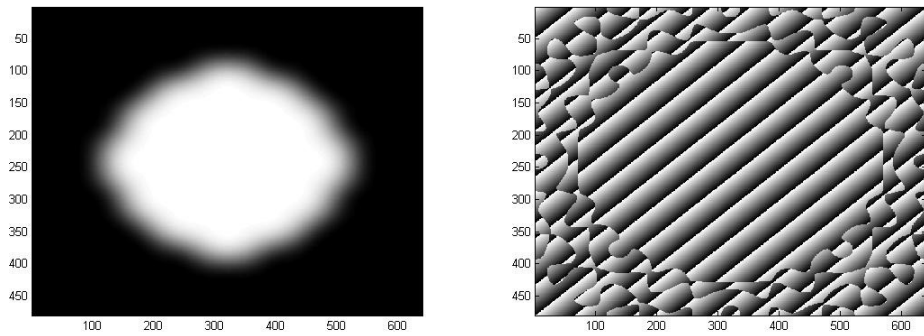


Figure 5.9 Log. magnitude and phase of the low pass image filter using *fwind1*

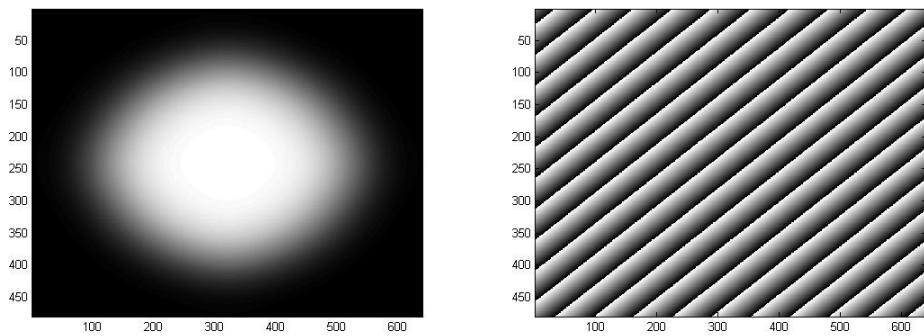


Figure 5.10 Log. magnitude and phase of the low pass image filter using *fwind2*

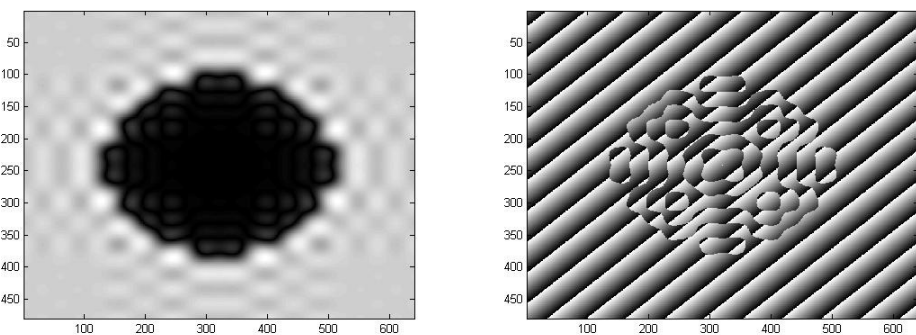


Figure 5.11 Log. magnitude and phase of the high pass image filter using *fsamp2*

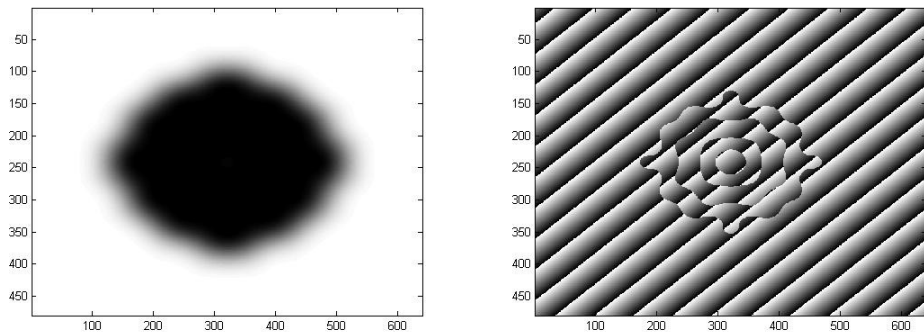


Figure 5.12 Log. magnitude and phase of the high pass image filter using *fwind1*

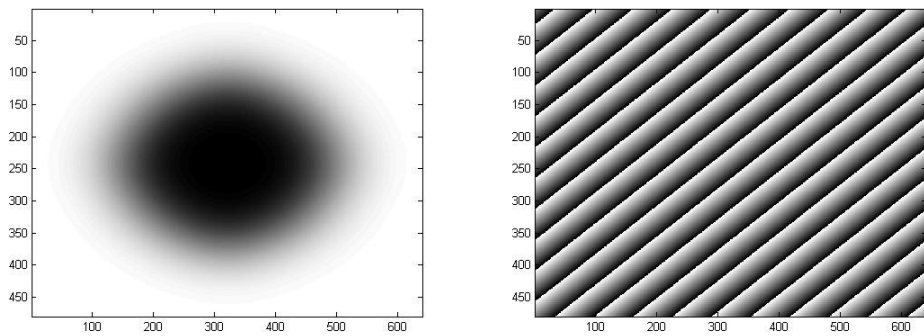


Figure 5.13 Log. magnitude and phase of the high pass image filter using *fwind2*

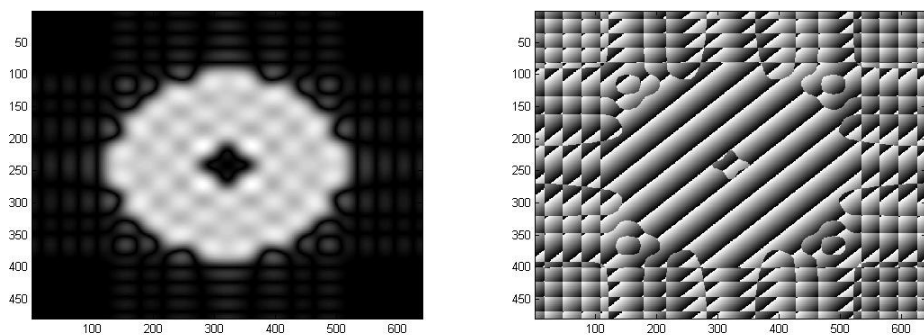


Figure 5.14 Log. magnitude and phase of the band pass image filter using *fsamp2*

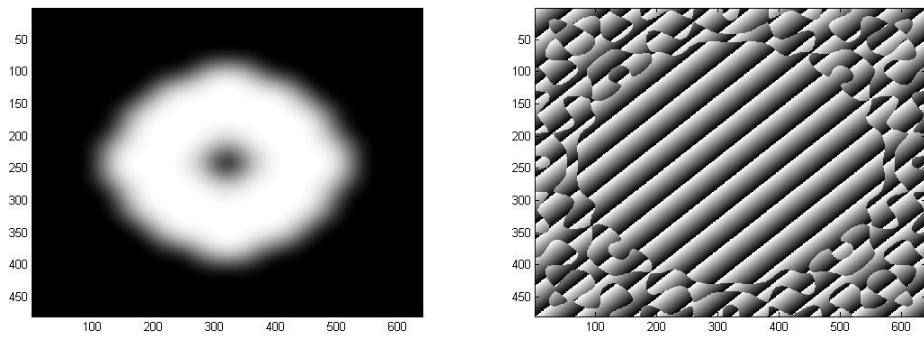


Figure 5.15 Log. magnitude and phase of the band pass image filter using *fwind1*

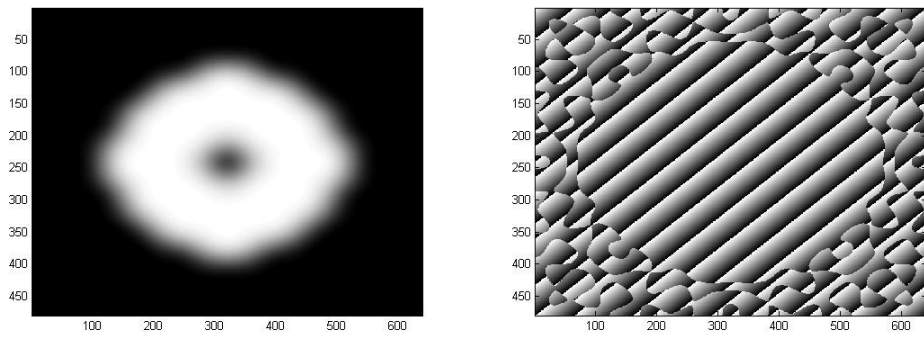


Figure 5.16 Log. magnitude and phase of the band pass image filter using *fwind2*

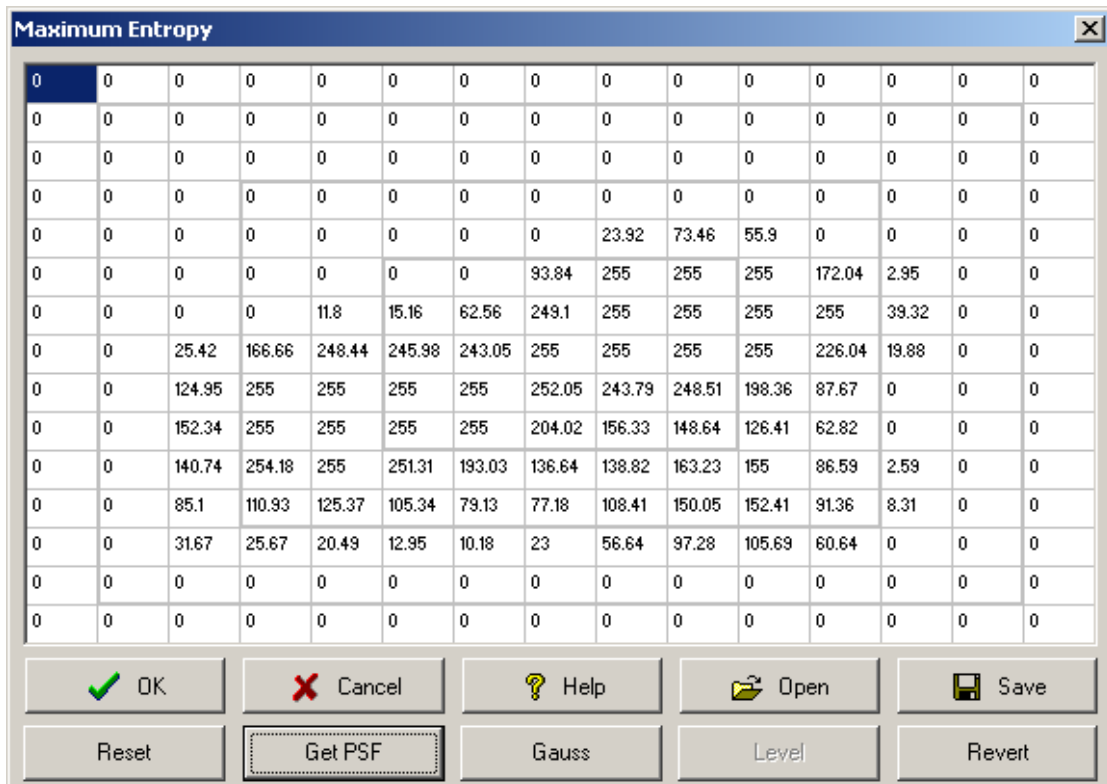


Figure 5.17 Point spread function intensity values of the portion to be deconvolved.

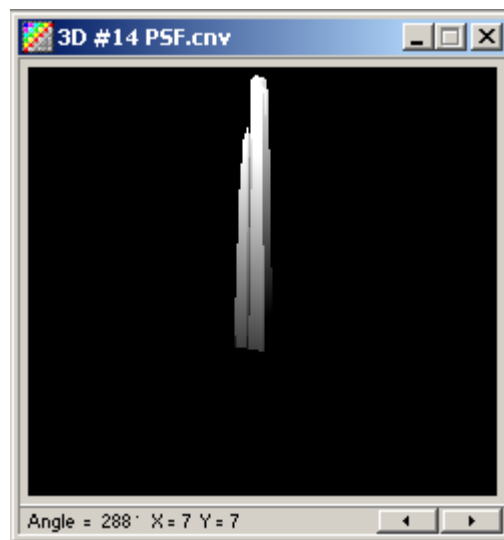


Figure 5.18 3-d plot of the point spread function intensity values of the portion (Figure 5.17) to be deconvolved.

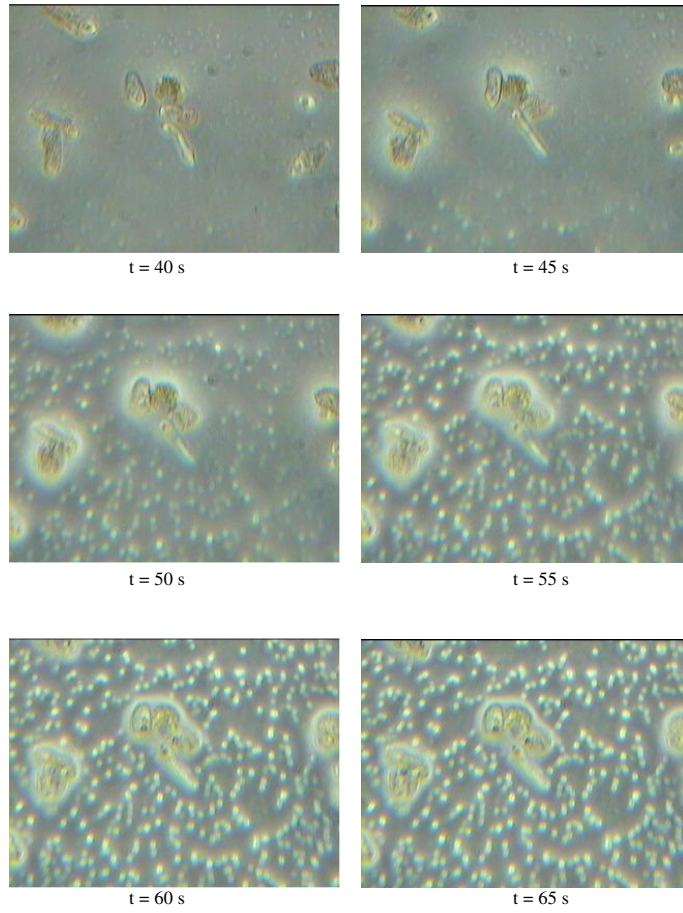


Figure 5.19 Images of *Euglena gracilis* from a phase contrast microscopy system at different times (t= 40 to 65s).

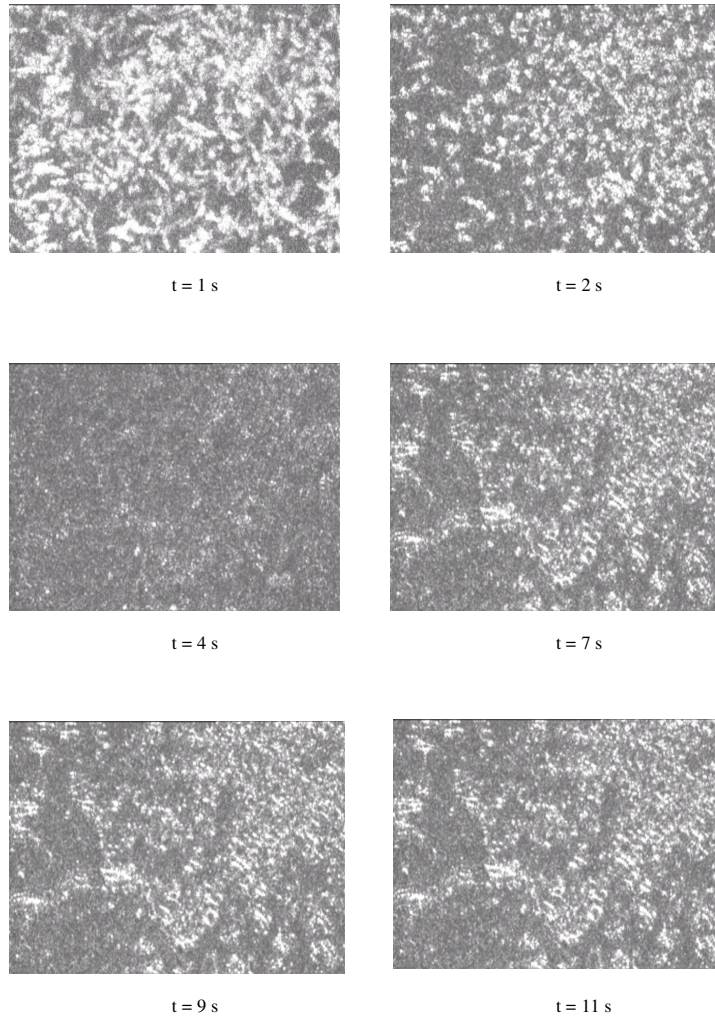


Figure 5.20 Images of *Euglena gracilis* under laser dark field microscopy system before filtering (t= 1 to 11s).

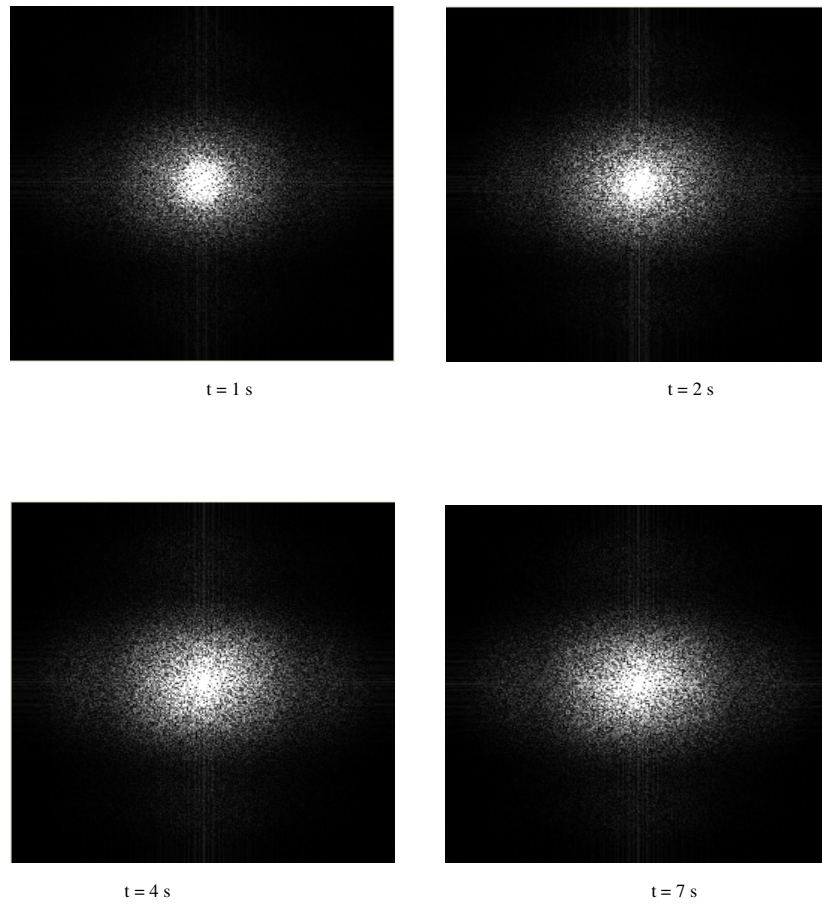


Figure 5.21 Power spectral densities of the *Euglena gracilis* images (Figure 5.20) under laser dark field microscopy over time ($t = 1$ to 7s) before filtering

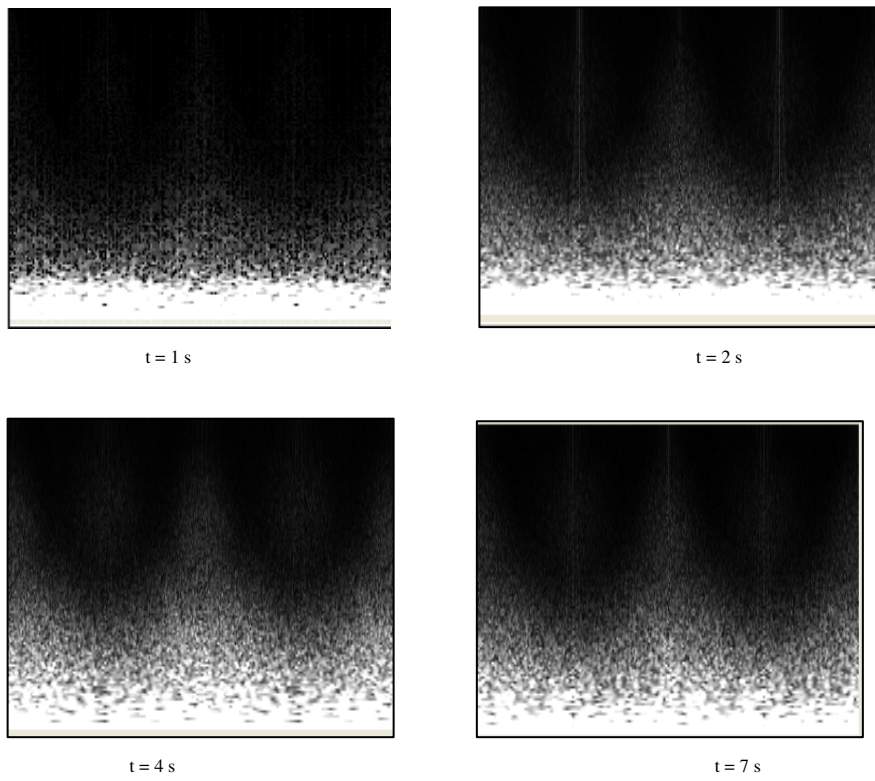


Figure 5.22 Polar PSD of the *Euglena gracilis* images under laser dark field microscopy over time ($t = 1$ to 7s) before filtering

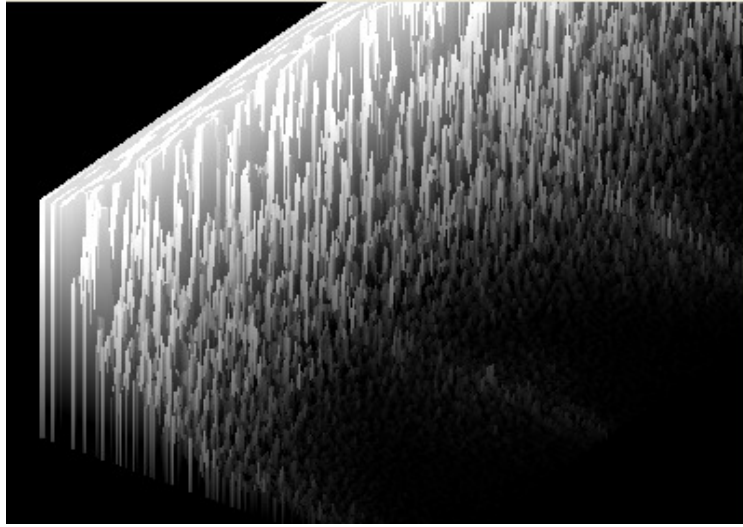


Figure 5.23 2-D representation of the polar PSD image of the *Euglena gracilis* under laser dark field microscopy (image at $t = 1$ s).

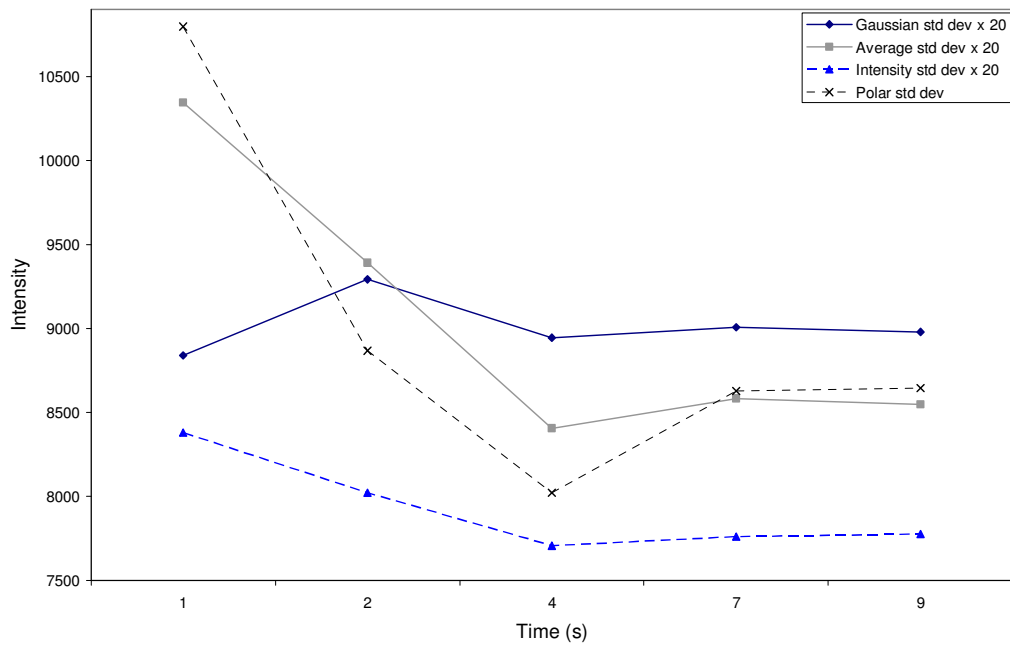
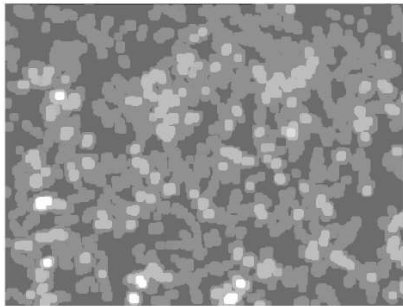
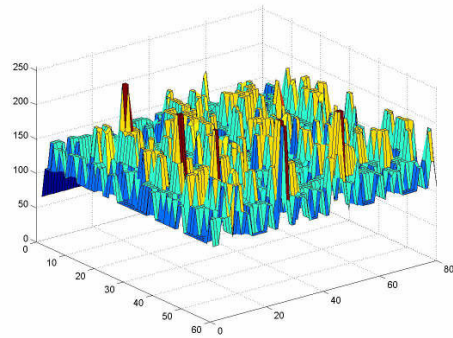


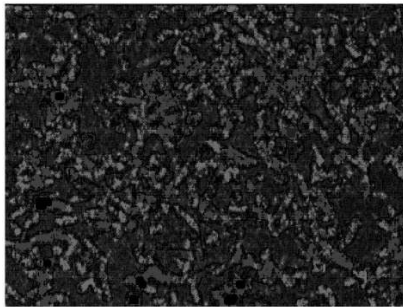
Figure 5.24 Comparison of all the parameters of the PSD images before filtering



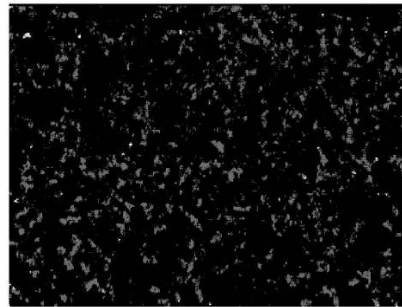
a) Morphological opening operation



b) 3-D representation of the operation



c) Background subtraction



d) Contrast enhancement

Figure 5.25 Spatial domain analysis to perform counting without filtering

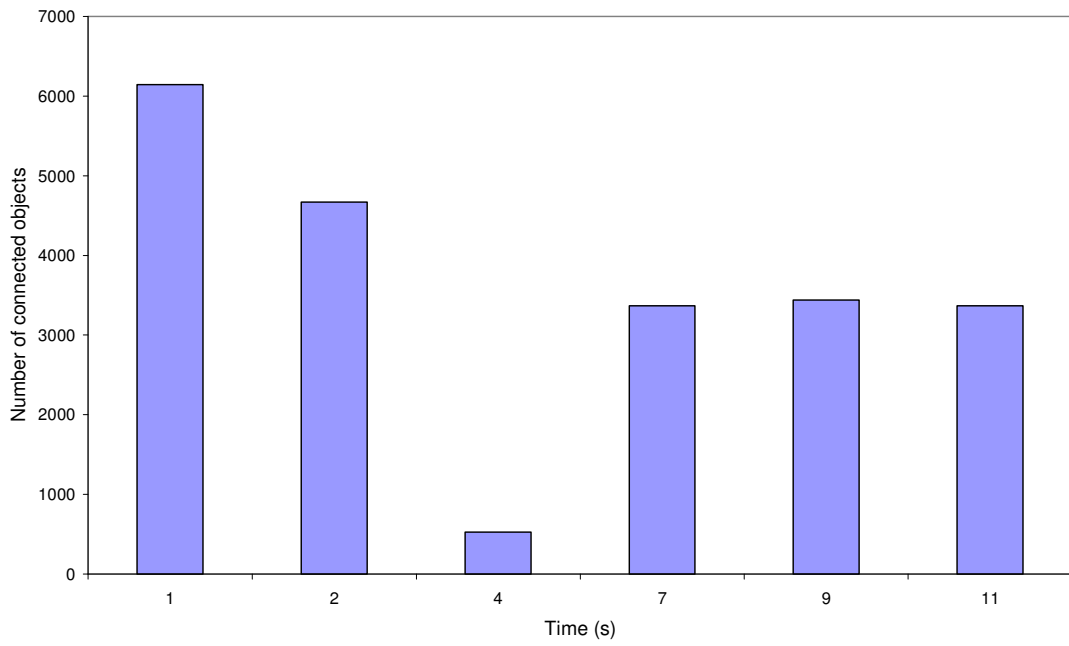
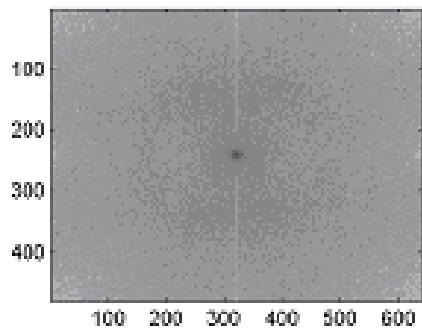
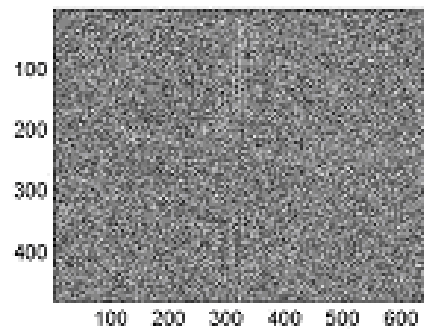


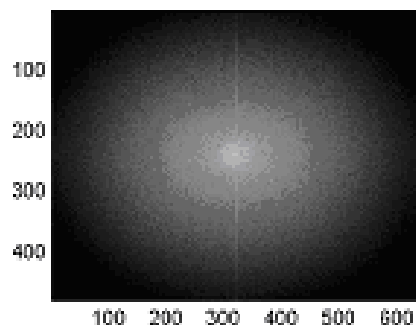
Figure 5.26 The number of connected objects performed before any filtering



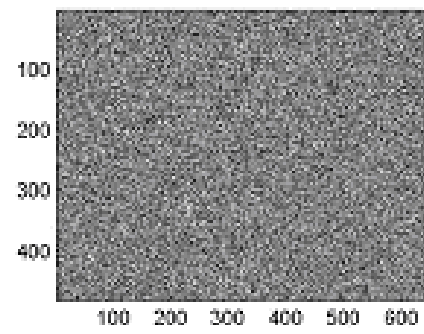
Magnitude of Laplacian filter convolution



Phase of Laplacian filter convolution

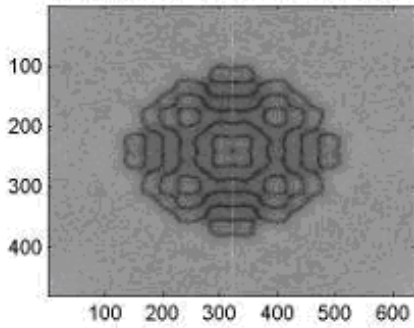


Magnitude of Gaussian filter convolution

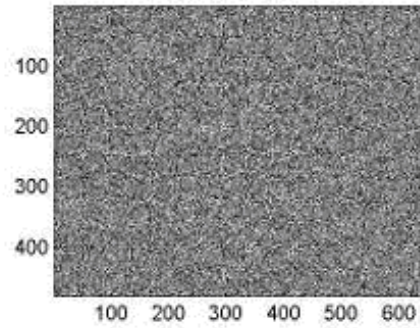


Phase of Gaussian filter convolution

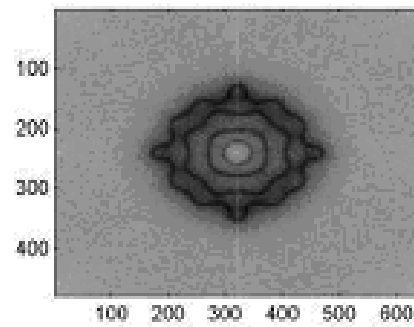
Figure 5.27 Image convolution using standard Laplacian and Gaussian filters



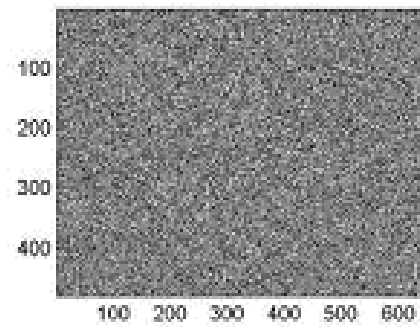
Magnitude of HP convolved using fsamp2



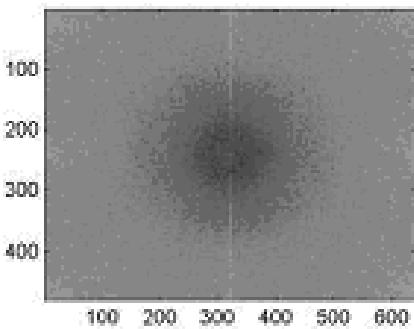
Phase of HP convolved using fsamp2



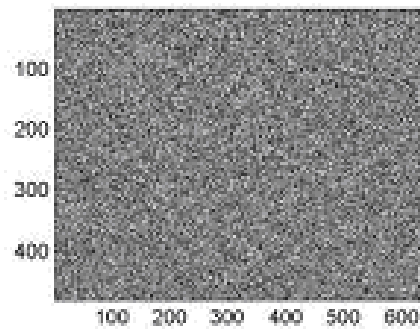
Magnitude of HP convolved using fwind1



Phase of HP convolved using fwind1

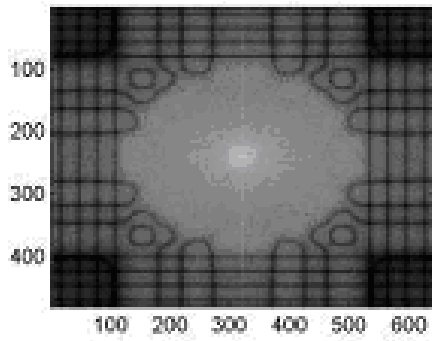


Magnitude of HP convolved using fwind2

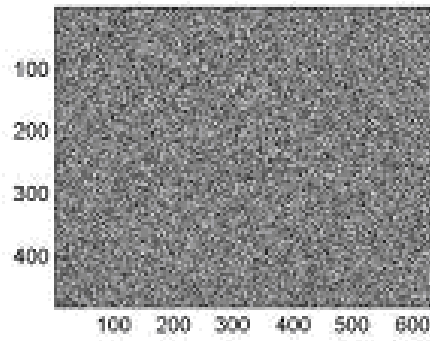


Phase of HP convolved using fwind2

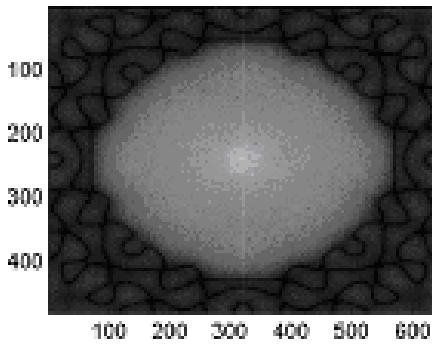
Figure 5.28 Image convolution for high pass filtering using MATLAB's special functions



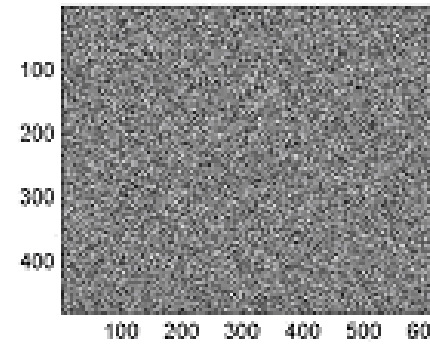
Magnitude image of LP convolved using fsamp2



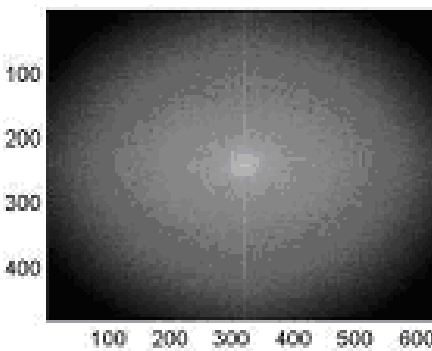
Phase of LP convolved using fsamp2



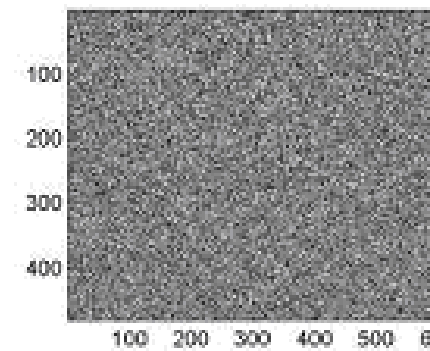
Magnitude image of LP convolved using fwind1



Phase of LP convolved using fwind1



Magnitude of LP convolved using fwind2



Phase of LP convolved using fwind2

Figure 5.29 Image convolutions for low pass filtering using MATLAB's special functions

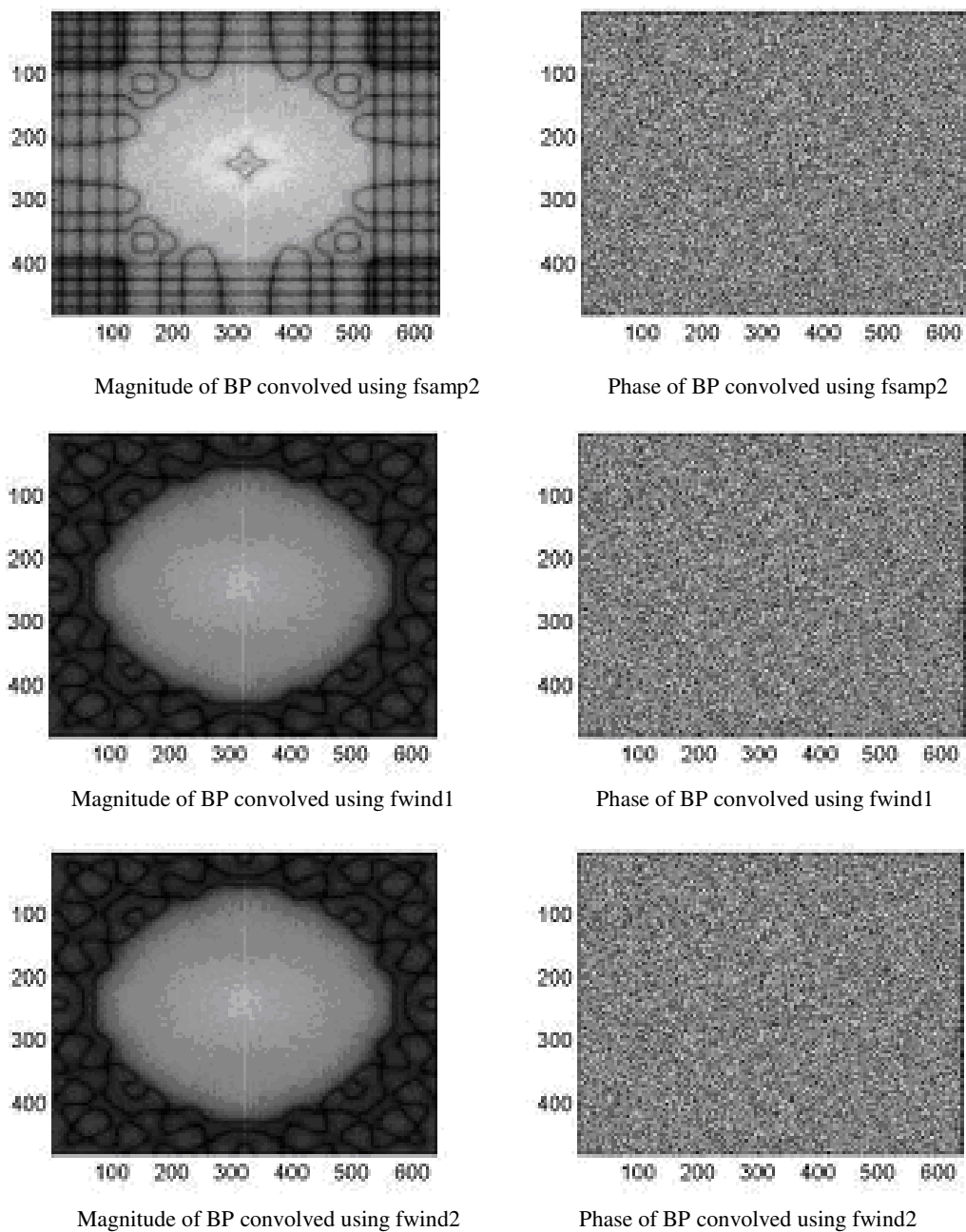
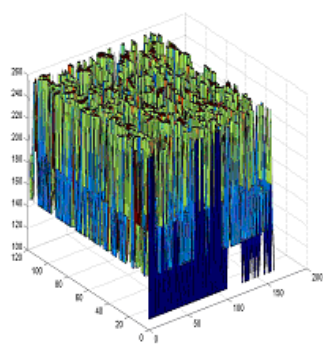
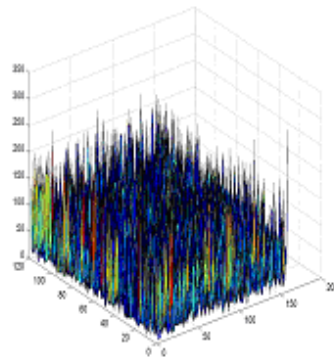


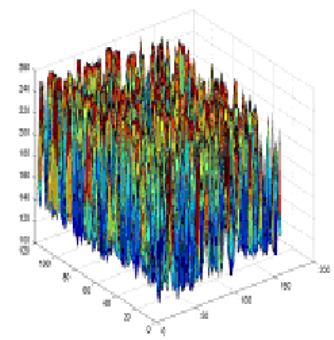
Figure 5.30 Image convolution for band pass filtering using MATLAB's special functions



a) Without filtering



b) After Laplacian filtering



c) After Gaussian filtering

Figure 5.31 Surface plots showing the effect of the standard filters

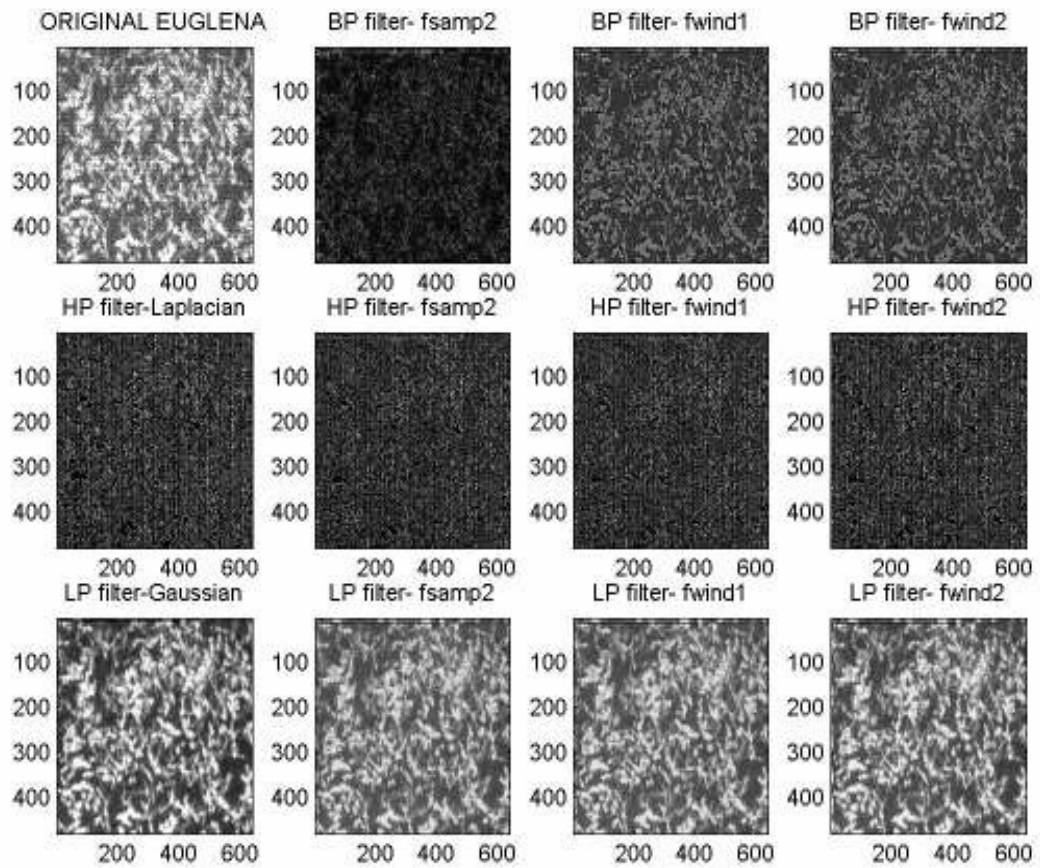


Figure 5.32 Comparison of the original image and the resultant images of convolution filters (from Figures 5.28, 5.29, 5.30, 5.31).

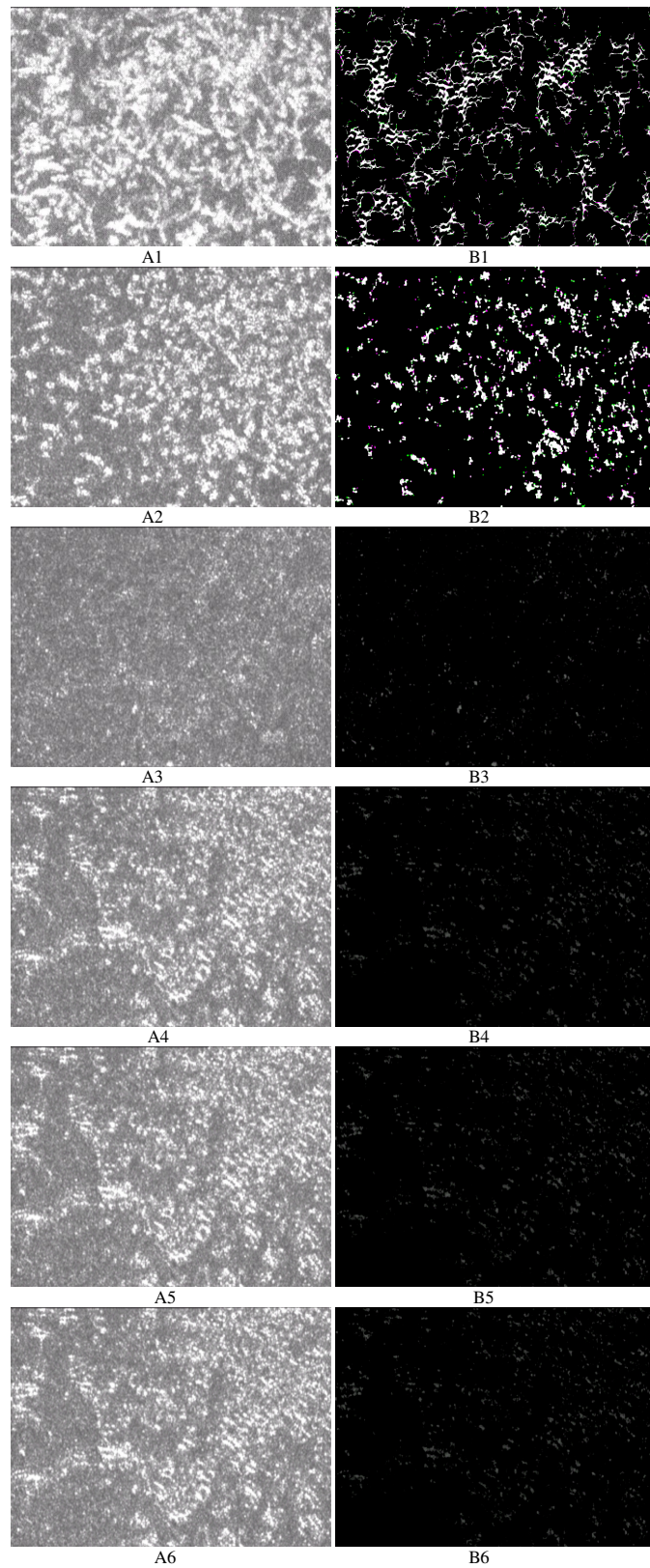


Figure 5.33 Comparison of the original (A series) and spatial domain filtered images (B series) over $t = 1, 2, 4, 7, 9, 11$ s respectively

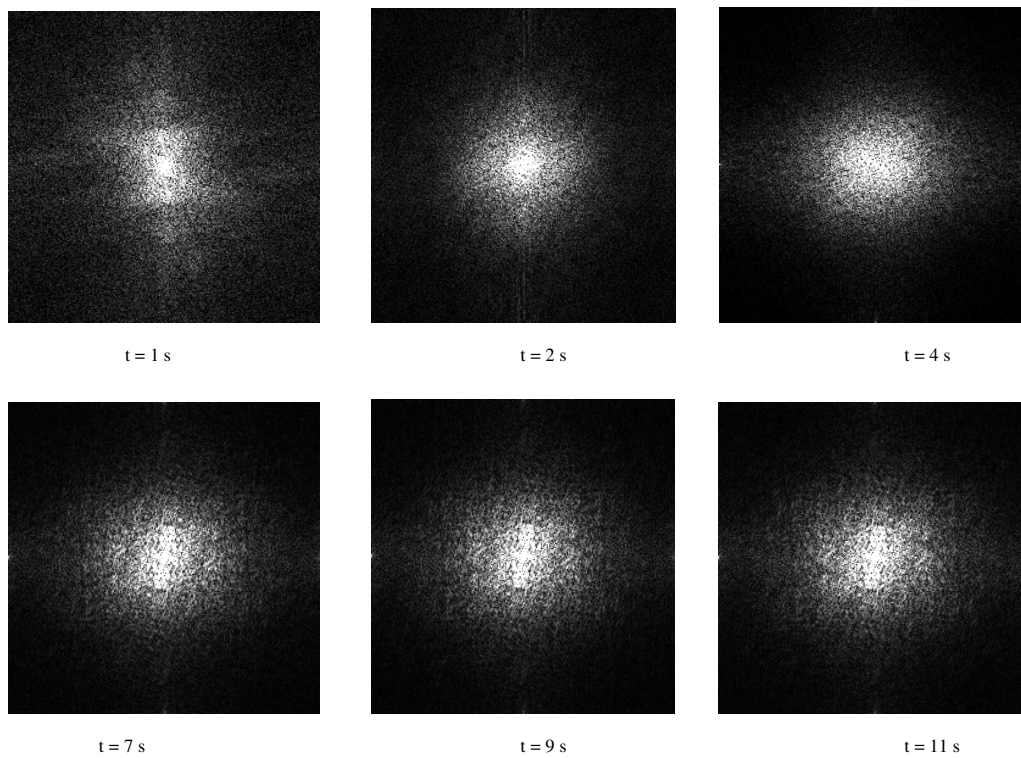
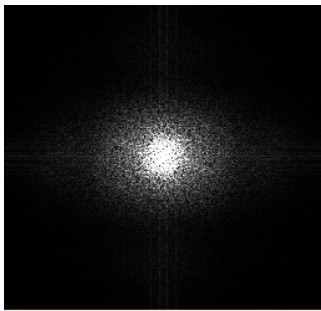
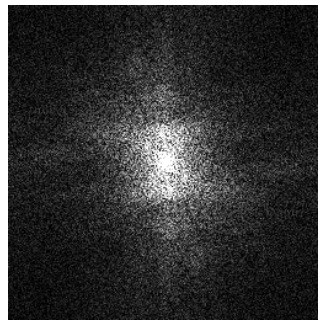


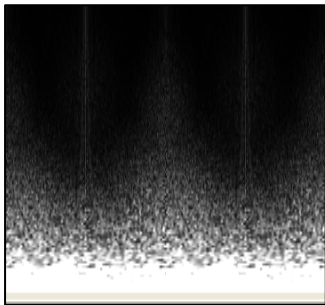
Figure 5.34 PSD images of *Euglena gracilis* after deconvolution filtering at different times ($t= 1$ to 11s).



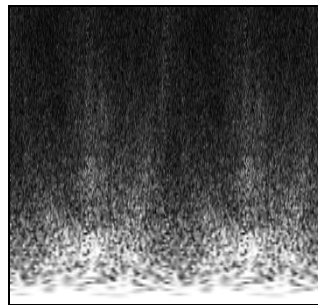
a) PSD image before filtering



b) PSD image after filtering



c) Polar PSD image before filtering



d) Polar PSD image after filtering

Figure 5.35 Comparison of polar PSD images before and after spatial filtering

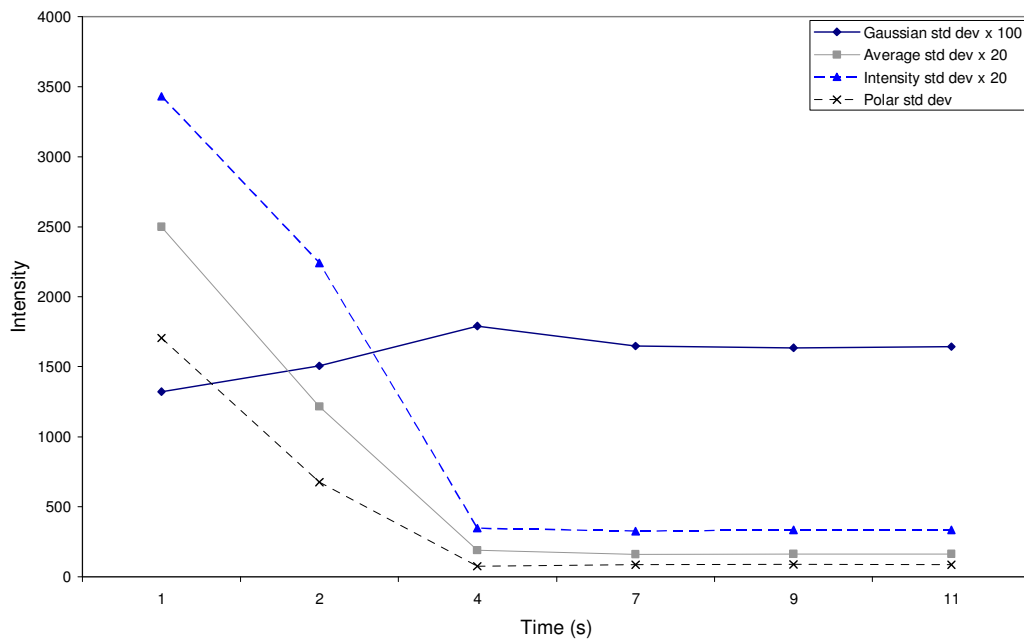


Figure 5.36 Comparison of all the parameters of the PSD images (Figure 5.24) after frequency domain filtering.

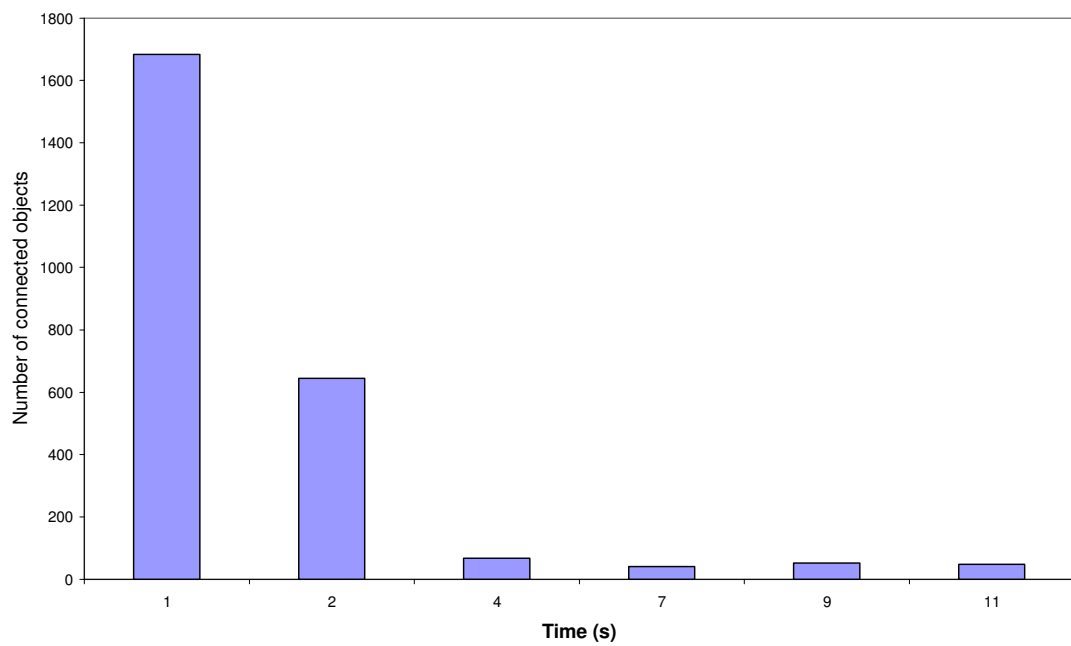


Figure 5.37 The number of connected objects (Figure 5.26) after spatial domain filtering

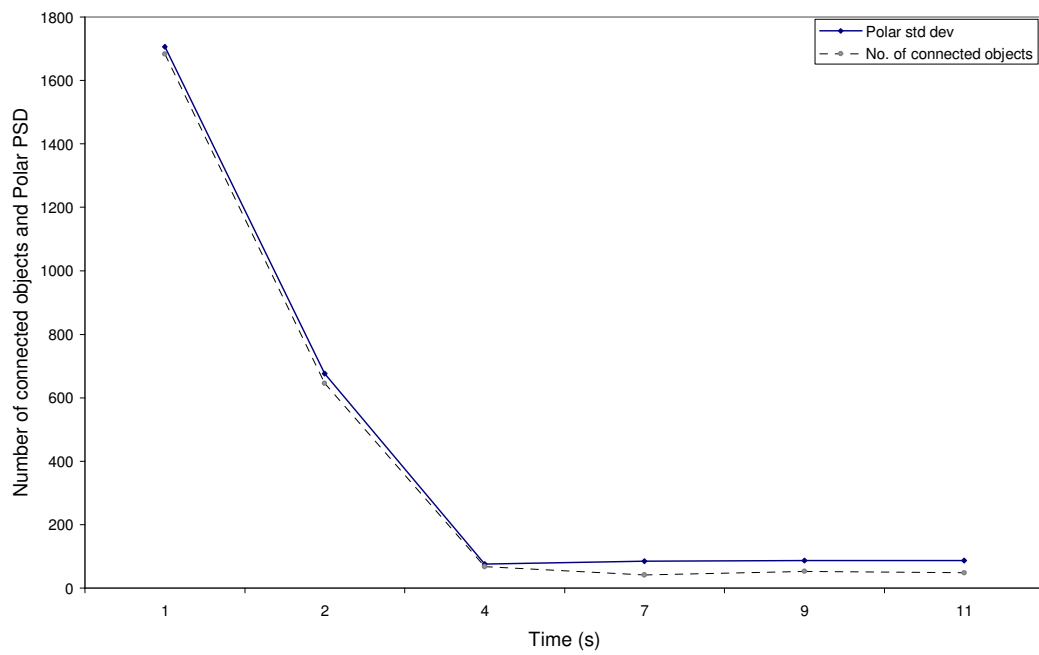


Figure 5.38 Comparison of number of connected objects (spatial domain) and polar standard deviation of the PSD images (frequency domain) after filtering.

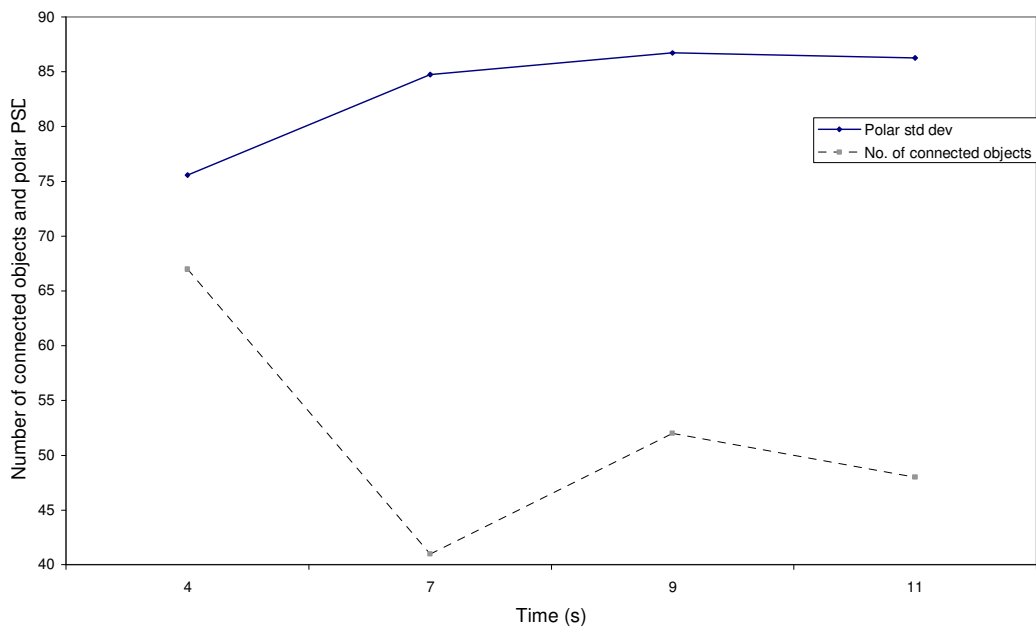


Figure 5.39 Magnified View of Figure 5.38 showing the comparison between number of connected objects and polar standard deviation of the PSD images.

CHAPTER 6 CONCLUSIONS AND FUTURE WORK

Chapter 1 introduced the need for the research work investigating real time detection systems for quantifying the behaviour and characteristics of microorganisms. Similar work done in this and related fields was described. An explanation of the space-time varying correlation function which is the fundamental equation for the experiments in Chapters 2 and 3 was also described.

Chapter 2 discusses control experiments that were designed for the speckle system discussed in the chapter 3. Inert polystyrene microspheres were chosen for studying dilutions (1.6×10^6 per ml to 1.6×10^8 microspheres per ml) and suspension made from less-motile organism like *Staphylococcus aureus* were chosen for higher order dilution studies (suspension containing 2.4×10^4 cfu per ml). In order to minimize the motility of the organism, pellets were made and diluted in water as a suspension. The same could have been achieved through microspheres (1 μm diameter spheres and 100 μm diameter spheres) but they are prohibitively expensive and they dehydrated quickly and cannot be used in large quantities. The optical density spectrophotometer is normally used in the laboratory to measure concentrations of suspensions. The main drawback with this system is it cannot detect suspensions which are more turbid or highly diluted. The experiments were aimed to test the sensitivity of the time-varying autocorrelation width (T_c) and spatial autocorrelation curves in detecting the motility and concentration of the various suspensions. The system was also helpful in comparing the sensitivity of speckle methods vs. OD photometers.

In Chapter 3, experiments showed that the laser speckle system employed in this application was useful in determining the presence of microorganisms, their growth and motility. In this system, it was found that the correlation parameter (T_c) derived from analysing the speckle-data in the spatial and Fourier domain provided details about the motility of the bacterial culture. Additionally the gradient of T_c plotted against time was at its highest value for low concentration, indicating that the system has a high sensitivity to low bacterial concentration.

The spectrophotometer was used to measure the optical density of the growing *E.coli* culture under the same conditions. It is interesting to note that the photometer was only efficient in detecting the concentration of the samples for a certain range of cell concentrations of the medium. When the sample was at its nascent stage of its growth, the optical density (OD) values were not measurable. The OD began to increase as the culture grew, detecting the changes in the concentration until a threshold was reached with an optical density of 2.0. When there was a peak population, it was not able to ascertain the optical density due to poor transmission and internal reflections inside the photometer. Thus it is evident that the proposed laser speckle system employed in this application may be utilized for detecting the motility of the organisms where there are high concentrations and the concentrations that cannot be ascertained using an optical density photometer. Chapter 3 also concluded with a proposed 3-D study of micro-organisms.

Instead of considering a single TV line, if all the lines were considered, this would provide better results from the analysis. This requires high end computers for capturing the images, storing and rapid analysis. An idea to determine the velocity of the scattering centres was derived from the equation described in Chapter 1 (equation 1.6), namely:

$$Tc = \frac{1}{|v|} \left(\frac{1}{w^2} + \frac{\sigma^2}{\Delta x^2} \right)^{-\frac{1}{2}} \quad (6.1)$$

From this equation, the velocity of the scattering centres can be ascertained. This is achieved by convolution by capturing a signal frame from the speckle image and calculating its point spread function (PSF). When this function is convolved with the velocity function, it gives the point spread function of a moving blurred image. By deconvolving the point spread function of the actual image from the point spread function of moving image, the velocity function or the motion function could be found. The motivation behind Chapters 4 and 5 was to consider all TV lines or the whole image for providing better results from the analysis.

Various image processing parameters were calculated in Chapter 4 including: average pixel intensity, intensity standard deviation, Gaussian standard deviation and the crosscorrelation analysis. These parameters were quantified in terms of how they recorded changes in the

morphology of a single *Euglena* cell. A visual assessment method was used where 12 volunteers were selected to place the images in order from broadest to most elongated. The most favoured sequence was selected by 68% of the population (4-1-2-3-5-6) using a scoring system for each image in a particular location. This same sequence was identified by four methods of analysis: the summed eccentricity, the summed eccentricity normalized to the area, crosscorrelation of the actual image before filtering and crosscorrelation of the PSD image after filtering. The sequence (4-1-3-2-5-6) was selected by 59.72% of the population and this method was ranked 2nd. Both the intensity standard deviation methods favoured the sequence (1-2-3-4-5-6) which was selected by 38.88% of the population. The sequence (2-5-6-4-3-1) was the lowest ranked with 4.16%.

Results were compared from different image processing methods with the summed eccentricity measurement method. Before filtering, the Gaussian standard deviation gave the maximum linear and increasing relationship with the ratio of major to summed minor axes values ($R^2 = 1$). The four crosscorrelation methods of assessment were ranked from 2nd to 5th. The crosscorrelation of the image before filtering and the PSD image after filtering were the most popular sequence and was favoured by two other measurement methods. These two parameters were ranked 3rd and 5th. This indicates that the crosscorrelation method may be the best image processing parameter that described the sequence most closely to the visual assessment method. The lowest ranked ($R^2 = 0.024$) parameter was the Gaussian standard deviation after filtering. The sequence (2-5-6-4-3-1) was the most unfavourable sequence overall.

It would be useful to identify more parameters and filtering processes that reduce the errors and sequence the images in accordance with the visual assessment method. One possible cause for the change in sequence could be the variation in the motion function of the *Euglena* cell while capturing the image. Secondly, the intensity fluctuation of the low power laser beam would induce significant contrast variations that in turn affect the power spectral density of the image. Other possible reason while image processing may be the removal of useful intensity information while filtering.

The system can be used as a method of determining cellular activity and to distinguish between a live cell and a dead cell. It follows that compared to the intensity standard deviation values from a live cell the dead cell showed values that were increased by 25 %

but still showed some variation, probably indicating internal motion of the cell possibly due to Brownian motion or movement of organelles. The intensity standard deviation analyzed over a time period would provide an insight into the dynamic activity of the specimen.

A high objective lens system was used to magnify the specimen to investigate the morphology characteristics of a single cell. Population statistics can be assessed with a low objective lens and with monochromatic illumination system which would provide high contrast.

Chapter 5 addressed the development of systems and processing algorithms to determine the population statistics of *Euglena gracilis* in solution. The robustness of the algorithms was investigated against temporal variations in the population. To achieve this, the sample was allowed to dehydrate for various time periods. Phase contrast microscopy was used to monitor events over this time. This was repeated under a dark field microscopy system. These images were analysed in the frequency domain via four different parameters and in the spatial domain via the number of connected objects both with and without filtering. A series of standard convolution filters and special function convolution filters available in MATLAB were assessed and finally a custom made filter was applied to the raw images. The results were quantified in both the frequency and spatial domain. Five parameters that were determined included: average intensity, intensity standard deviation, Gaussian standard deviation, polar standard deviation and number of connected objects. The best result was achieved with the polar standard deviation and the number of connected objects. It was considered that improved results may be achieved by monitoring both of these parameters simultaneously. These findings are particularly useful if the environment is changing rapidly, here the motility of the population could be continuously measured by determining the polar standard deviation changes and number of connected objects with respect to time.

One of the drawbacks while sampling with this system is the multiple plane of focus. Although the microscope was optimised for a high contrast, it was found that there was more than one plane of focus. This meant that when the *Euglena* sample was pipetted onto the microslide groups of *Euglena* cells could be found according to the planes of focus. More image processing algorithms filters need to be designed to enhance the low contrast images that exists in the background of the plane of focus. The system can also be improved

by changing the sample mounting mechanism where only one plane of focus exists at any time.

It would be useful to investigate more filtering process and parameters to neglect the noise due to the rapidly changing motion function. It was suggested in the shape study (Chapter 4) that the variation in the motion function of the single *Euglena* cell may have an effect on the sequence arrangement using image analysis. It is expected that the rapidly changing motion function from the large number of *Euglena* cells can also have an impact on the parameters. Filtering additionally may remove useful intensity information. As suggested in the shape study (Chapter 4), the intensity fluctuations of the low power laser beam may induce significant contrast variations that would affect the power spectral density of the image.

Other potential application of the systems developed here may include analysis of cancer cells, saliva spit carries and stem cells. Monitoring rainfall or drought conditions is an important area in an increasing number of areas around the world. Here an optical system could be developed to transmit the information wirelessly. The images recorded by a system on chip (SOC) could be analysed offline to monitor drought conditions and its effect on cells ascertained. By continuously monitoring of the behaviour of the cells or organisms in suspension under different environmental conditions, the technique could be used as a drought monitoring system. A further application of significant benefit would be the real time behavioral studies of the microorganisms as they undergo various decontamination treatments. For example, investigating single or population statistics as the organisms are exposed to UV, laser, microwave or chemical treatments.

REFERENCES

Alaluusua.S, Kujala.K.E, Nystrom.M, Evalahti.M, Gronroos.L (1987). Caries in the primary teeth and salivary *Streptococcus mutans* and *lactobacillus* levels as indicators of caries in permanent teeth. *Pediatric Dentistry*. **9**: 126-130.

Alaluusua.S, Savolainen.J, Tuompo.H, Gronroos.L (1984). Slidescoring method for estimation of *Streptococcus mutans* levels in saliva. *Scandinavian Journal of Dental Research*. **92**: 127-133.

Alexander.R, McNeill. The Invertebrates. London: Cambridge University Press, (1979).

Argialas.D.P, Mavrantza.O.D (2004). Comparison of edge detection and hough transform techniques for the extraction of geologic features. *The international archives of the photogrammetry, remote sensing and spatial information sciences*. **34**: Part XXX.

Arizaga.R, Lucia.C.N, Rabal.H, Trivi.M (2002). Display of local activity using dynamical speckle patterns, Society of photo-optical instrumentation engineers. *Opt. Eng.* **41**(2): 287-294.

Asakura.T, Takai.N, (1981). Dynamic laser speckles and their application to velocity measurements of the diffuse object, *Appl. Phys.* **25**: 179-194.

Ascoli.C, Barbi.M, Frediani.C, Mure.A (1978). Measurements of euglena motion parameters by laser light scattering. *Biophys J.* **24**: 585-599.

Ascoli.C, Barbi.M, Frediani.C, Petracchi.D (1978). Effects of electromagnetic fields on the motion of *Euglena gracilis*: *Biophys J.* **24**(3): 601-612.

Bahceci.K.S, Acar.J (2007). Determination of Guaiacol produced by Alicyclobacillus acidoterrestris in Apple Juice by Using HPLC and Spectrophotometric Methods, and Mathematical Modeling of Guaiacol Production. *Eur Food Res Technol.* 225:873-878.

Bahram.J, Inkyu.M, Seokwon.Y, Edward.C (2005). Three-dimensional imaging and recognition of microorganism using single-exposure on-line (SEOL) digital holography, *Optics Express.* **13**(12): 4492-4506.

Barber.P.R, Vojnovic.B, Kelly.J, Mayes.C.R, Boulton.P, Woodcock.M, Joiner.M.C (2000). Automated counting of mammalian cell colonies, *Institute of physics publishing- Nanotechnology.* **46**: 63-76.

Bassnett.S (2005). Three-dimensional reconstruction of cells in the living lens: The relationship between cell length and volume, *Experimental eye research.* **81**(6): 716-723.

Boozer.C, Kim.G, Cong.S, Guan.H.W, Londergan.T, (2006). Looking towards label-free biomolecular interaction analysis in a highthroughput format: A review of new surface plasmon resonance technologies. *Current Opinion in Biotechnology.* **17**(4): 400–4005.

Bowen.W.H (1996). Salivary influences on the oral microflora. In: Saliva and oral health. Edgar.W.M, O'Mullane.D.M, eds. 2nd ed. *British Dental Journal*: London. pp. 95-103.

Braga.R.A, Borem.F.M, Rabelo.G, Dal.F.I, Arizaga.R, Rabal.H.J, Trivi.M (2001). Seeds analysis using bio-speckle. *Proc SPIE.* **4419**:34–7.

Brain.R.A, Johnson.D.J, Richards.S.M, Sanderson.H, Sibley.P.K, Solomon.K.R (2004). Effects of 25 pharmaceutical compounds to lemna gibba using a seven-day static-renewal test: *Environmental Toxicology And Chemistry.* **23**: 371-382.

Briers.J.D (1975). Wavelength dependence of intensity fluctuations in laser speckle patterns from biological specimens *Opt. Commun.* **13**: 324–326.

Briers.J.D (1993). Speckle fluctuations and biomedical optics: implications and applications. *Opt. Eng.* **32**: 277–283.

Briers J.D (1996). Laser Doppler and time-varying speckle: a reconciliation, *J. Opt. Soc. Am.* **13**: 345–350.

Briers.J.D, Webster.S (1996). Laser speckle contrast analysis (LASCA): a non-scanning, full field technique for monitoring capillary blood flow. *J Biomed Opt* **2**: 174–9.

Briers.J.D (2001). Laser Doppler, speckle and related techniques for blood perfusion mapping and imaging, *Physiol. Meas.* **22**: R35-R66.

Caillol.J.M, (2003). Some applications of the Lambert W function to classical statistical mechanics, *J. Phys. A: Math. Gen.* **36**: 10431-10442.

Chan.J.W, Esposito.A.P, Talley.C.E, Hollars.C.W, Lane.S.M, Huser.T, (2004). Reagentless Identification of single bacterial spores in aqueous solution by confocal laser tweezers Raman spectroscopy. *Anal Chem.* **76**: 599–603.

Chan.W.J, Winhold.H, Corzett.M.H, Ulloa.J.M, Cosman.M, Balhorn.R, Huser.T (2007). Monitoring dynamic protein expression in living *E. Coli* bacterial cells by laser tweezers Raman spectroscopy: *Cytometry A.* **71**(7): 468-74.

Cheng.P, Sutton.M.A, Schreier.H.W, McNeill.S.R (2002). Full-field speckle pattern image correlation with B-spline deformation function, *Exp. Mech.* **42**: 344-352.

Cheng.H.Y, Zhu.D, Luo.Q.M, Zeng.S.Q, Wang.Z, Ul'yanov.S.S (2003). Optical monitoring of the dynamic change of blood perfusion. *Chin. J. Lasers.* **30**: 668–705.

Choi.J.W, Pu.A, Psaltis.D (2006). Optical detection of asymmetric bacteria utilizing electro orientation. *Optics Express.* **14**(21): 9780-9785.

Clay.R, Court.T (1975). The history of the microscope. *Holland Press.*

- Deisingh.A (2003). Biosensors for microbial detection. *Microbiologist*. 30–33.
- Deisingh, A.K., Thompson, M., (2002). Detection of infectious and toxigenic bacteria. *Analyst*. **127**: 567–581.
- Duchin.S, Van Houte.J (1978). Colonization of teeth in humans by *Streptococcus mutans* as related to its concentrations in saliva and host age. *Infect. Immun.* **20**: 120–125.
- Dudak.F.C, Boyacl.I.H (2007). Development of an immunosensor based on surface plasmon resonance for enumeration of *Escherichia coli* in water samples: *Food Research International*. **40**(7): 803-807.
- Feng.P, Weagant.S, Grant.M (2002). Enumeration of *Escherichia coli* and the Coliform bacteria. Bacteriological Analytical Manual (8th ed.). *FDA/Center for Food Safety & Applied Nutrition*.
- Fesenko.D.O, Nasedkina.T.V, Prokopenko.D.V, Mirzabekov.A.D (2005). Biosensing and monitoring of cell populations using the hydrogel bacterial microchip. *Biosensors and Bioelectronics*. **20**: 1860–1865.
- Fitzgerald.P.J, Keyes.P.H (1960). Demonstration of the etiologic role of streptococci in experimental caries in the hamster. *Journal of American Dental Association*. **61**: 9-19.
- Forero.M.G, Sroubek.F, Cristóbal.G (2004). Identification of tuberculosis bacteria based on shape and color. *Special issue on imaging in bioinformatics: Part III*. **10**(4): 251-262.
- Fouchet.P, Manin.C, Richard.H, Frelat.G, Barbotin.J.N (1994). Flow cytometry studies of recombinant *Escherichia coli* in batch and continuous cultures: DNA and RNA contents; light-scatter parameters. *Appl Microbiol Biotechnol J*. **41**(5): 584-590.

Francis.D, James.S.W, Tatam.R.P (2007). Surface strain measurement using multi-component shearography with coherent fibre-optic imaging bundles. *Meas. Sci. Technol.* **18**: 3583–3591

Galajda.P, Keymer.J, Chaikin.P, Austin.R (2007). A Wall of Funnels Concentrates Swimming Bacteria, American Society for Microbiology. *J Bacteriol.* **89**(23): 8704–8707.

Gale.M.F.R, Landau.M.R, Hogert.E.N, Gaggioli.N.G (2004). Changing surfaces - A theoretical and experimental approach, *Journal of Optics A. Pure and Applied Optics.* **6**(2): 187-192.

Goesele.M, Heidrich.W, Seidel.H-P, (2001). Entropy-based dark frame subtraction, *The Society for Imaging Science and Technology (IS&T)*, ISBN / ISSN: 0-89208-232-1: 293-298.

Gonzalez.R.C, Woods.R.E, Eddins.S.L (2004). Digital image processing using Matlab, *Pearson Education, Inc.*, Newjersey 07458.

Gronroos.L, (2000). Quantitative and qualitative characterization of *mutans Streptococcus* in saliva and in dentition, *Academic dissertation*. University of Helsinki, Finland.

Gualtieri.P, Ghetti.F, Passarelli.V, Barsanti.L (1988). Microorganism track reconstruction: an image processing approach. *Comput Biol Med.* **18**: 57-63.

Hader.D.P, Lebert.M, Richter.P (1998). Gravitaxis and Graviperception in *Euglena gracilis*. *Advances In Space Research.* **21**(8-9): 1277-1284.

Hader, D.P, Porst.M, Tahedl.H, Richter.P, Lebert.M. (1997). Gravitactic Orientation in the Flagellate *Euglena gracilis*. *Microgravity Science and Technology.* **10**:53.

Hanbury.A, Serra.J, (2002). A 3D-polar coordinate colour representation suitable for image analysis, *Pattern Recognition and Image Processing Group.* **77**: 1-35.

Hobson, N.S., Tothill, I., Turner, A.P.F., (1997). Microbial detection. *Biosens. Bioelectron.* **61**: 279–286.

Hoffman.L.R, Deziel.E, D'Argenio.D.A, Lepine.F, Emerson.J, McNamara.S, Gibson.R.L, Ramsey.B.W, Miller.S.I (2006). Selection for *Staphylococcus aureus* small-colony variants due to growth in the presence of *Pseudomonas aeruginos.*, PNAS. *The National Academy of Sciences of the USA.* **103**(52): 19890-19895.

Homola.J, Sinclair.S.Y, Gauglitz.G (1999). Surface plasmon resonance sensors. Review. *Sensors and Actuators B: Chemical.* **54**(1–2): 3–15.

Howe.E, Harding.G (2000). A comparison of protocols for the optimisation of detection of bacteria using a surface acoustic wave (SAW) biosensor. *Biosens. Bioelectron.***15**: 641

Hudault.S, Guignot.J, Servin.A.L (2001). *Escherichia coli* strains colonizing the gastrointestinal tract protect germ free mice against *Salmonella Typhimurium* infection. *Gut* **49**: 47-55.

Ivnitski D, Hamid A.I, Atanasov P, Wilkins E (1999). Biosensors for detection of pathogenic bacteria. *Biosens.Bioelectron.* **14**: 599

Janisch.R (2003). Therapeutic laser effects on model cell systems, *Journal of Applied Biomedicine*, ISSN 1214-021X: S12-S14.

John.M.S, Radhakrishnan.P, Nampoore.V.P.N, Vallabhan.C.P.G, (1999). A fiber optic evanescent wave sensor for monitoring the rate of pulsed lased deposition of metal thin films. *Measurement Science and Technology.* **10**: 17-20.

Johnson.P.E, Deromedi.A.J, Lebaron.P, Catala.P, Cash.J (2006). Fountain flow cytometry, a new technique for the rapid detection and enumeration of microorganisms in aqueous samples. *Cytometry A.* **69**(12): 1212-21.

Kalchenko.V, Preise.D, Bayewitch.M, Fine.I, Burd.K, Harmelin.A (2007). In vivo dynamic light scattering microscopy of tumour blood vessels. *Journal of Microscopy*. **228**(2): 118-122.

Kalele.S.A, Kundu.A.A, Gosavi.S.W, Deobagkar.D.N, Deobagkar.D.D, Kulkarni.S.K (2006). Rapid detection of *Escherichia coli* by using antibody-conjugated silver nanoshells: *Small J*. **2**(3): 335-338.

Kishen.A, John.M.S, Lim.C.S, Asundi.A (2003). Development and application of a fiber Optic Biosensor (FOBS) to monitor *mutans streptococci* activity in human saliva. *Biosensors & Bioelectronics*. **18** (11): 1371-1378.

Kohler.B, Andreen.I, Jonsson.B, (1984). The effect of caries preventive measures in mothers on dental caries and the oral presence of the bacteria *Streptococcus mutans* and *lactobacilli* in their children. *Archives of Oral Biology*. **29**: 879-883.

Kohler.B, Andreen.I, Jonsson.B, (1988). The earlier colonization by *mutans streptococci*, the higher the caries prevalence at 4 years of age. *Oral Microbiology Immunology*. **3**: 14-17.

Kreitz.S, Hess.A, Anderson.T.H, (1995). Direct enumeration and size classification of soil bacteria using confocal laser scanning microscopy and image analysis. *International Conference on Image Processing (ICIP'95)*. **1**: 454.

Lee.J.J, Leedale.G.F, Bradbury.P (Eds.) (2000). An Illustrated Guide To The Protozoa, Second Ed., *Society Of Protozoologists*.

Lequin.R.M (2005). Enzyme Immunoassay (EIA)/Enzyme-Linked Immunosorbent Assay (ELISA). *Clinical Chemistry*. **51**(12): 2415–2418.

Li.J.H, Mark J. Gultinan.M.J, Donald B. Thompson.D.B, (2006). The use of laser differential interference contrast microscopy for the characterization of starch granule ring structure. *Starch Journal*. **58**(1): 1-5.

Lonergan.T.A (1983). Regulation of cell-shape in *Euglena gracilis* .1. Involvement of the biological clock, respiration, photosynthesis, and cytoskeleton. *Plant physiology*. **71**(44): 719-730

Lonergan.T.A (1984). Regulation Of Cell-Shape In *Euglena gracilis* .2. The effects of altered extracellular and intracellular Ca-2+ concentrations and the effect of calmodulin antagonists, *Journal Of Cell Science*. **71**: 37-50.

Lonergan.T.A (1985). Regulation of cell-shape in *Euglena-gracilis* .4. Localization of actin, myosin and calmodulin. *Journal Of Cell Science*. **77**: 197-208.

Lonergan.T.A, Lachney.C.I (1985). Regulation of cell shape in *Euglena gracilis*. I. Involvement of stable microtubules. *Journal of cell science*. **74**(1): 219-237.

Lebert.M, Porst.M, Richter.P, Hader.D.P (1999). Physical characterization of gravitaxis in *Euglena gracilis*. *Journal of plant physiology*. **155**(3): 338-343.

Lewis.I.R, Griffiths.P.R (1996). Raman spectrometry with fiber optic sampling. *Applied Spectroscopy*. **50**(10): 12-30.

Lyberis.N, Mering.C (2004). Evolution of the hydrographic network of the Karakum desert and environmental implications for the aral sea. *European Space Agency Article List*. **219**: 1-8.

Malins.M, Fielden.P.R, Goddard.N.J (2004). Imaging of unlabelled bacteria at a sensor surface using aluminium-clad integrated waveguide chips. *Measurement Science and Technology*. **15**(5): 948-954.

Martin.W, Borst.P (2003). Secondary loss of chloroplasts in *Trypanosomes*. *Proc Natl Acad Sci*. **100**(3): 765-767.

MathWorks, Inc (2002). Using MATLAB, Version 6.5.

Mathew.F, Alocilja.E.C (2005). Porous Silicon-Based Biosensor for Pathogen Detection. *Biosensors and Bioelectronics Journal*. **20**(8): 1656-1661.

Mavrodineanu.R, Lazar.J.W (1973). Standard reference materials: Standard quartz cuvettes for high-accuracy spectrophotometry. *Clinical Chemistry*. **19**(9): 1053-1057.

McMaster.C, Roch.E.A, Willshaw.G.A, Doherty.A, Kinnear.W, Cheasty.T (2001). Verocytotoxin-producing *E. coli* serotype O26:H11 outbreak in an Irish creche. *Eur. J. Clin. Microbiol. Infect. Dis*. **20**: 430–432.

Mermelstein.C.S, Rodrigues.A.P, Einicker-Lamas.M, Navarrete.R.E, Farina.M, Costa.M.L (1998). Distribution of F-Actin, Alpha-Actinin, Tropomyosin, Tubulin and organelles in *Euglena gracilis* by Immunofluorescence microscopy. *Tissue & Cell*. **30**: 545-553.

Miles.A.A, Misra.S.S (1938). *J. Hyg.* (London), 38: 732.

Moll.N, Pascal.E, Dinh.D.H, Pillot.J.P, Bennetau.B, Rebiere.D, Moynet.D, Mas.Y, Mossalayi.D, Pistre.J, Dejous.C, (2007). A Love wave immunosensor for whole *E. coli* bacteria detection using an innovative two-step immobilisation approach. *Biosens Bioelectron*. **22**(9-10): 2145-2150.

Mountain.R.D (1966). Spectral distribution of scattered light in a simple fluid, *Rev. Mod. Phys*. **38**: 205-214.

Murphy.M, Carroll.A, Walsh.C, Whyte.P, O'Mahony.M, Anderson.W, McNamara.E, Fanning.S, (2007). Development and assessment of a rapid method to detect *E. coli* O26, O111 and O157 in retail minced beef. *Int J Hyg Environ Health*. **210**(2):155-61.

Nascimento.V.H, Sayed.A.H (2000). On the learning mechanism of adaptive filters. *IEEE transactions on signal processing*. **48**: 1609-1625.

Nichols.K.M, Rikmenspoel.R, (1977). Mg^{2+} Dependent electrical control of flagellar activity in *Euglena*. *J Cell Sci*. **23**: 211-225.

Nichols.K.M, Rikmenspoel.R, (1982). Effects of infrared laser damage to the *Euglena* Photoreceptor on the control of flagellar motility. *Journal of Cell Motility*. **2**(6): 573-582.

Oulamara.A, Tribillon.G, Duvernoy.J, (1989). Biological activity measurement on botanical specimen surfaces using a temporal decorrelation effect of laser speckle. *J. Mod. Opt.* **36**: 165-179.

Pablo.P.J, Schaap.I.A.T, Schmidt.C.F (2003). Observation of microtubules with scanning force microscopy in liquid. *Institute of physics publishing- Nanotechnology*. **14**, 143-146.

Pajuelo.M, Baldwin.G, Arizaga.R, Cap.N, Rabal.H, Trivi.M (2003). Bio-speckle assessment of bruising in fruits. *Opt. Lasers Eng.* **40**: 13-24.

Piederrière.Y, Le Meur.J, Cariou.J, Abgrall.J, Blouch.M.T (2004). Particle aggregation monitoring by speckle size measurement; application to blood platelets aggregation. *Opt. Express*. **12**: 4596-4601.

Popov.P, Pulov.S, Pulov.V (2004). A laser speckle pattern technique for designing an optical computer mouse, *Optics and Lasers in Engineering*, **42**(1): 21-26.

Powledge.T.M (2004). The Polymerase chain reaction. *Adv Physiol Educ.* **28**: 44–50.

Reza.M.A, Delva.G.R, Justin.S.R, Turney.D.R (1998). Issues on medical image enhancement. *Xilinx* **6**.

Riley.L.W, Remis.R.S, Helgerson.S.D, McGee.H.B, Wells.J.G, Davis.B.R, Hebert.R.J, Olcott.E.S, Johnson.L.M, Hargrett.N.T, Blake.P.A, Cohen.M.L, (1983). Hemorrhagic colitis associated with a rare *E. coli* serotype. *N. Engl. J. Med.* **308**: 681–685.

Rocchetta.I, Mazzuca.M, Confortia.V, Ruiz.L, Balzaretic.V, Maria Carmen del.R (2006). Effect of chromium on the fatty acid composition of two strains of *Euglena gracilis*. *Environmental Pollution*. **141**(2): 353-358.

Ross.D.A, Dhadwal.S, Foulkes.J.A, (1983). Laser measurement of the motility of bull spermatozoa in an egg-yolk diluent. *J. Reprod. Fertil.* **67**: 263–268.

Schaap.A.P, DeSilva.R, Akhavan-Tafti.H, Handley.R.S (1991). Chemical and enzymatic triggering of 1,2-dioxetanes: Structural effects on chemiluminescence efficiency. In: Stanley.P.E, Kricka.L.J. (Eds.), *Bioluminescence and Chemiluminescence Current Status*. Wiley, Chichester. pp. 103–106.

Sezonov.G, Petit.D.J, D'Ari.R (2007). *Escherichia coli* Physiology in Luria-Bertani Broth. *Journal of Bacteriology*. **189**(23): 8746-8749.

Simanonok.K (2006). Endogenous light nexus theory of consciousness. *Journal of Consciousness Studies*. **8**(5): 1-16.

Spring.R.K, Russ.C.J, Davidson.W, Michael.W (2006).
<http://micro.magnet.fsu.edu/primer/digitalimaging/imageprocessingintro.html>.

Kneist.S, Heinrich-Wetzien.R, Tietze.W, Fischer.T, Stosser.L (1998). Salivary microbiology and dentist's ability in the prediction of caries activity. *J. Dental Res.* **75**: 1251–1251.

Subramanian.A, Irudayaraj.J, Ryanc.T (2006). A mixed self-assembled monolayer-based surface plasmon immunosensor for detection of *E. coli* O157:H7. *Biosens. Bioelectron.* **21**: 998–1006.

Suehiro J, Hamada R, Noutomi D, Shutou M and Hara M, (2003). Selective detection of viable bacteria using dielectrophoretic impedance measurement method. *J. Electrostat.* **57**: 157

Tamarin.O, Déjous.C, Rebière.D, Pistré.J, Comeau.S, Moynet.D, Bezian.J (2003). Study of acoustic Love wave devices for real time bacteriophage detection. *Sens. Actuators B* **91**: 275–284.

Tanzer.J.M (1992). Microbiology of dental caries; in Slots J, Taubman MA (eds): *Contemporary Oral Microbiology and Immunology*. 377-424

Tarr.P.I, Neill.M.A, (1996). Perspective: the problem of non- O157 Shiga toxin (verocytotoxin)-producing *E. coli*. *J.Infect. Dis.* **174**: 1136–1139.

Taylor.A.D, Yu.Q, Chen.S, Homola.J, Jiang.S (2005). Comparison of *E. coli* O157:H7 preparation methods used for detection with surface plasmon resonance sensor. *Sens. Actuators B.* **107**: 202–208.

Thar.R, Blackburn.N, Kuhl.M, (2000). A new system for three-dimensional tracking of motile microorganisms. *Applied and environmental microbiology.* **66**(5): 2238-2242.

Vogt.R.L, Dippold.L (2005). *Escherichia coli* O157:H7 outbreak associated with consumption of ground beef. *Public health reports* **2**: 174-178.

Xu.Z, Joenathan.C, Khorana.B.M (1995). Temporal and spatial properties of the time-varying speckles of botanical specimens. *Opt. Eng.* **34**:1487–502.

Zhao.Y, Schmidt.R.J, Wang.J, Williams.F.W, Xiaoping.W (1997). Point-wise and whole-field laser speckle intensity fluctuation measurements applied to botanical specimens. *Optics and Lasers in Engineering.* **28**: 443-456.

Zheng.B, Pleass.C.M, Charles.S (1994). Feature information extraction from dynamic biospeckle. *Applied Optics.* **33**(2): 231-237.

Zimmermann.C, Rebière.D, Déjous.C, Pistré.J, Chastaing.E, Planade.R (2001). A love-wave gas sensor coated with functionalized polysiloxane for sensing organophosphorus compounds. *Sens. Actuators B.* **76**: 86–94.

Zourob.M, Mohr.S, Treves Brown.B.J, Fielden.P.R, McDonnell.M.B, Goddard.N.J
(2005). Bacteria detection using disposable optical leaky waveguide sensors. *Biosens.
Bioelectron.* **21**(2): 293-302.

APPENDICES

APPENDIX A

Preparation methods for LB Broth (Luria Bertani) Medium to grow *E. coli*

Ingredients

800 ml sterile distilled water

10g Bacto-tryptone.

5g yeast extract.

10g NaCl.

Method

Add constituents above adjust pH to 7.5 with NaOH (not really necessary) and make up the volume to 1 litre by adding sterile distilled water. Sterilize by autoclaving immediately after making.

APPENDIX B

Preparation methods for Jaworski medium to grow *Euglena gracilis*

Ingredients

Sodium acetate trihydrate 1.0 g

Lab-Lemco" powder (Oxoid L29) 1.0 g

Tryptone (Oxoid L42) 2.0 g

Yeast extract (Oxoid L21) 2.0 g

CaCl₂ stock solution (1) 10.0 ml

Method

Add constituents above and make up to 1 litre with deionized water. For agar preparation, add 15 g per litre of Bacteriological Agar (Oxoid L11). Autoclave at 15 psi for a period of 15 minutes.

APPENDIX C

Program to perform crosscorrelation between images using convolution filtering

```
% USE THIS PROGRAM FOR CROSSCORRELATION OF IMAGES
% Use it for filtered images - frrr*.,
%     unfiltered images - rrr*
%     filtered PSD images - pfrrr*
%     unfiltered PSD images - prrr*

close all;
clear all;
    eug1 = imread('pfrrr01.bmp');

    figure;
    [sub_eug1, rect_pos1] = imcrop(eug1); % Choose a big rectangle of the area you need to see
    figure, imshow(sub_eug1)
    c1 = normxcorr2(sub_eug1(:,1),eug1(:,1));
    figure, surf(c1), shading flat
k=dir('pfrrr*.bmp')
for i=1:length(k)
    FileName=k(i).name %% list of each file name

    ARR(i) = CROSSCORR(i,FileName,sub_eug1);
end
figure, plot(ARR);
end

function D= CROSSCORR(i,char,sub_eug1)

% TAKE ONE IMAGES, Crop two images,, let the first cropped image represents the portion you like to analyse with
other images
% Let the second cropped Image represents live cell ---Now do cross correlation to cropped images

% Read the IMAGES

eug2 = imread(char);
figure,imshow(eug2);

% Choose Subregions of Each image interactively
%[sub_eug2, rect_pos2] = imcrop(eug1); % Choose a small rectangle of a live cell for instance

% Display subimages

%figure, imshow(sub_eug2)

% Do normalised Cross-correlation and Find Coordinates of peak

c2 = normxcorr2(sub_eug1(:,1),eug2(:,1));
D = max(abs(c2(:)))
figure, surf(c2), shading flat

% offset found by correlation

% The total offset or translation between images depends on the location of the peak in the
% cross-correlation matrix, and on the size and position of the sub images.
```

APPENDIX D

Program to perform convolution filtering with standard and special function filters

```
% Laser optics System Engineering Center
% 12 Jan 2006

A = imread('pop_15_29_1.bmp','bmp');

% Finding out the 2D fft

% CALCULATION OF FOURIER FUNCTIONS
eug_fft = fftshift(fft2(A));           % Performs the 2D fft of an Image
eug_ang = angle(eug_fft);             % Performs the Phase of the FFT image
eug_logM = log10(1 + abs(eug_fft));    % Performs the log magnitude of the FFT image
eug_ifft = abs(iff2(eug_fft));        % Performs the inverse FFT of the FFT image

% DISPLAY OF FOURIER FUNCTIONS
colormap(gray);
subplot(2,2,1), imagesc(A); title('ORIGINAL EUGLENA');
subplot(2,2,2), imagesc(eug_ang); title('Phase of FFT EUGLENA');
subplot(2,2,3), imagesc(eug_logM); title('MAGNITUDE of FFT EUGLENA');
subplot(2,2,4), imagesc(eug_ifft); title('Inverse of FFT EUGLENA');

% CREATING A LOW PASS FILTER

H = fspecial('gaussian',[11 11],1.3); % fspecial uses one of the special functions to create a 2d filter,
                                     % The whole line returns a rotationally symmetrical gaussian filter with size
                                     % [11 11] and Std dev 1.3
[rows columns] = size(A);           % Copy the same number of columns of what u have in the original image

gauss_fft = fftshift(fft2(H, rows, columns)); % pads matrix H, with 0's to size rows and columns, all before
                                     transforming

gauss_log = log10(1 + abs(gauss_fft)); % Performs the log magnitude of the fft converted gaussian filter

gauss_phase = angle(gauss_fft); % Performs the Phase of FFT converted gaussian filter

Figure(2);                          % Creates a new Figure 8.with handle 2

colormap(gray);

subplot(2,1,1), imagesc(gauss_log); title('MAGNITUDE of FFT of Gaussian filter');
subplot(2,1,2), imagesc(eug_ang); title('Phase of FFT of Gaussian filter');

G = gauss_fft .* eug_fft; % Convolution of two ffts (fft of original image and filter)
LogG = log10(1 + abs(G));
PhaseG = angle(G);
InvG = abs(iff2(G));
Figure(3);

colormap(gray);
subplot(2,2,1), imagesc(LogG); title('Log Magnitude of Convolution');
subplot(2,2,2), imagesc(PhaseG); title('Phase of Convolution');
subplot(2,2,3), imagesc(InvG); title('Low pass Filtered Image');
subplot(2,2,4), imagesc(A); title('Original unfiltered Image');

% CREATING A HIGH PASS FILTER

H = fspecial('laplacian');
[rows columns] = size(A);
laplace_fft = fftshift(fft2(H,rows,columns));
laplace_log = log10(1 + abs(laplace_fft));
```

```

laplace_phase = angle(laplace_fft);
Figure(4);
colormap(gray);
subplot(2,1,1), imagesc(laplace_log); title('MAGNITUDE of FFT of Laplacian HP filter');
subplot(2,1,2), imagesc(laplace_phase); title('PHASE of FFT of Laplacian HP filter');

```

```

L = laplace_fft .* eug_fft; % Convolution of two ffts (fft of original image and filter)
LogL = log10(1 + abs(L));
PhaseL = angle(L);
InvL = abs(iff2(L));

```

```
Figure(5);
```

```

colormap(gray);
subplot(2,2,1), imagesc(LogL); title('Log Magnitude of Convolution');
subplot(2,2,2), imagesc(PhaseL); title('Phase of Convolution');
subplot(2,2,3), imagesc(InvL); title('HIGH pass Filtered Image');
subplot(2,2,4), imagesc(A); title('Original unfiltered Image');

```

```
% TWO DIMENSTIONAL FILTER DESIGN
```

```
    % Setting up for the filters
```

```

[f1,f2] = freqspace(21,'meshgrid'); % Creates a 2-d freq vectors f1,f2 for 21 x 21 matrix and performs 3d plot
r = sqrt(f1.^2 + f2.^2); % Sq root of f1 and f2

```

```

BandPass = ones(size(f1)); % BandPass is a matrix of size f1 and make all elements as ONES
BandPass((r<.1) | (r >.6)) = 0; % Wherever we find values outside range of 0.1 to 0.6, make it ZERO

```

```

HighPass = ones(size(f1)); % Highpass is a matrix of size f1 and make all elements as ONES
HighPass(r<.6)=0; % Wherever we find values less than 0.6, make it ZERO

```

```

LowPass = ones(size(f1)); % Highpass is a matrix of size f1 and make all elements as ONES
LowPass(r>.6)=0; % Wherever we find values more than 0.6, make it ZERO

```

```
    % Filter design using fsamp2
```

```
    % Band pass
```

```

HBP = fsamp2(BandPass);
HBP_fft = fftshift(fft2(HBP,rows,columns));

```

```

logHBP_fft = log10(1 + abs(HBP_fft));
PhaseHBP_fft = angle(HBP_fft);

```

```
Figure(6);
```

```

colormap(gray);
subplot(2,1,1), imagesc(logHBP_fft); title('Log Magnitude of BANDPASS using fsamp2');
subplot(2,1,2), imagesc(PhaseHBP_fft); title('Phase of BandPass');

```

```
    %Convolution Bandpass
```

```

BPconv = HBP_fft .* eug_fft;
logBPconv = log10(1 + abs(BPconv));
PhaseBPconv = angle(BPconv);
invBPconv = abs(iff2(BPconv));
invBPConv = circshift(invBPconv,[-10 10]);

```

```
Figure(7);
```

```

colormap(gray);

subplot(2,2,1), imagesc(logBPconv); title('Log Magnitude of CONV BP using fsamp2');

```

```

subplot(2,2,2),imagesc(PhaseBPconv); title('Phase of CONVBP');
subplot(2,2,3),imagesc(invBPconv); title('Inverse of Conv BP filter');
subplot(2,2,4), imagesc(A); title('Original unfiltered Image');

% Low pass

HLP = fsamp2(LowPass);
HLP_fft = fftshift(fft2(HLP,rows,columns));
logHLP_fft = log10( 1 + abs(HLP_fft));
PhaseHLP_fft = angle(HLP_fft);

Figure(8);

colormap(gray);

subplot(2,1,1),imagesc(logHLP_fft); title('Log Magnitude of LOWPASS using fsamp2');
subplot(2,1,2),imagesc(PhaseHLP_fft); title('Phase of LOWPASS');

%Convolution LOWpass

LPconv = HLP_fft .* eug_fft;
logLPconv = log10( 1 + abs(LPconv));
PhaseLPconv = angle(LPconv);
invLPconv = abs(iff2(LPconv));
invLPConv = circshift(invLPconv,[-10 10]);

Figure(9);

colormap(gray);

subplot(2,2,1),imagesc(logLPconv); title('Log Magnitude of CONV LP using fsamp2');
subplot(2,2,2),imagesc(PhaseLPconv); title('Phase of CONVLP');
subplot(2,2,3),imagesc(invLPconv); title('Inverse of Conv LP filter');
subplot(2,2,4), imagesc(A); title('Original unfiltered Image');

% High pass

HHP = fsamp2(HighPass);
HHP_fft = fftshift(fft2(HHP,rows,columns));
logHHP_fft = log10( 1 + abs(HHP_fft));
PhaseHHP_fft = angle(HHP_fft);

Figure(10);

colormap(gray);

subplot(2,1,1),imagesc(logHHP_fft); title('Log Magnitude of HIGHPASS using fsamp2');
subplot(2,1,2),imagesc(PhaseHHP_fft); title('Phase of HIGHPASS');

%Convolution Highpass

HPconv = HHP_fft .* eug_fft;
logHPconv = log10( 1 + abs(HPconv));
PhaseHPconv = angle(HPconv);
invHPconv = abs(iff2(HPconv));
invHPConv = circshift(invHPconv,[-10 10]);

Figure(11);

colormap(gray);

subplot(2,2,1),imagesc(logHPconv); title('Log Magnitude of CONV HP using fsamp2');
subplot(2,2,2),imagesc(PhaseHPconv); title('Phase of CONVHP');
subplot(2,2,3),imagesc(invHPconv); title('Inverse of Conv HP filter');
subplot(2,2,4), imagesc(A); title('Original unfiltered Image');

```



```

% filter design using fwind1

% BandPass

HBP1 = fwind1(BandPass,hamming(21));
HBP1_fft = fftshift(fft2(HBP1,rows,columns));
logHBP1_fft = log10( 1 + abs(HBP1_fft));
PhaseHBP1_fft = angle(HBP1_fft);

Figure(12);

colormap(gray);

subplot(2,1,1),imagesc(logHBP1_fft); title('Log Magnitude of BANDPASS using fwind1');
subplot(2,1,2),imagesc(PhaseHBP1_fft); title('Phase of BAND-PASS');

%Convolution Bandpass-fwind1

BP1conv = HBP1_fft .* eug_fft;
logBP1conv = log10( 1 + abs(BP1conv));
PhaseBP1conv = angle(BP1conv);
invBP1conv = abs(iff2(BP1conv));
invBP1Conv = circshift(invBP1conv,[-10 10]);

Figure(13);

colormap(gray);

subplot(2,2,1),imagesc(logBP1conv); title('Log Magnitude of CONV BP using fwind1');
subplot(2,2,2),imagesc(PhaseBP1conv); title('Phase of CONVBP');
subplot(2,2,3),imagesc(invBP1conv); title('Inverse of Conv BP filter');
subplot(2,2,4), imagesc(A); title('Original unfiltered Image');

% *****

% Low pass

HLP1 = fwind1(LowPass,hamming(21));
HLP1_fft = fftshift(fft2(HLP1,rows,columns));
logHLP1_fft = log10( 1 + abs(HLP1_fft));
PhaseHLP1_fft = angle(HLP1_fft);

Figure(14);

colormap(gray);

subplot(2,1,1),imagesc(logHLP1_fft); title('Log Magnitude of LOWPASS using fwind1');
subplot(2,1,2),imagesc(PhaseHLP1_fft); title('Phase of LOWPASS');

%Convolution LOWpass

LP1conv = HLP1_fft .* eug_fft;
logLP1conv = log10( 1 + abs(LP1conv));
PhaseLP1conv = angle(LP1conv);
invLP1conv = abs(iff2(LP1conv));
invLP1Conv = circshift(invLP1conv,[-10 10]);

Figure(15);

colormap(gray);

subplot(2,2,1),imagesc(logLP1conv); title('Log Magnitude of CONV LP using fwind1');
subplot(2,2,2),imagesc(PhaseLP1conv); title('Phase of CONVLP');
subplot(2,2,3),imagesc(invLP1conv); title('Inverse of Conv LP filter');
subplot(2,2,4), imagesc(A); title('Original unfiltered Image');

```

```

% High pass

HHP1 = fwind1(HighPass,hamming(21));
HHP1_fft = fftshift(fft2(HHP1,rows,columns));
logHHP1_fft = log10( 1 + abs(HHP1_fft));
PhaseHHP1_fft = angle(HHP1_fft);

Figure(16);

colormap(gray);

subplot(2,1,1),imagesc(logHHP1_fft); title('Log Magnitude of HIGHPASS using fwind1');
subplot(2,1,2),imagesc(PhaseHHP1_fft); title('Phase of HIGHPASS');

%Convolution Highpass

HP1conv = HHP1_fft .* eug_fft;
logHP1conv = log10( 1 + abs(HP1conv));
PhaseHP1conv = angle(HP1conv);
invHP1conv = abs(iff2(HP1conv));
invHP1Conv = circshift(invHP1conv,[-10 10]);

Figure(17);

colormap(gray);

subplot(2,2,1),imagesc(logHP1conv); title('Log Magnitude of CONV HP using fwind1');
subplot(2,2,2),imagesc(PhaseHP1conv); title('Phase of CONVHP');
subplot(2,2,3),imagesc(invHP1conv); title('Inverse of Conv HP filter');
subplot(2,2,4), imagesc(A); title('Original unfiltered Image');

% FOR FILTERS USING FWIND2

win = fspecial('gaussian',21,2);
win = win ./ max(win(:));

%*****

% Low pass

HLP2 = fwind2(LowPass,win);
HLP2_fft = fftshift(fft2(HLP2,rows,columns));
logHLP2_fft = log10( 1 + abs(HLP2_fft));
PhaseHLP2_fft = angle(HLP2_fft);

Figure(18);

colormap(gray);

subplot(2,1,1),imagesc(logHLP2_fft); title('Log Magnitude of LOWPASS using fwind2');
subplot(2,1,2),imagesc(PhaseHLP2_fft); title('Phase of LOWPASS');

%Convolution LOWpass

LP2conv = HLP2_fft .* eug_fft;
logLP2conv = log10( 1 + abs(LP2conv));
PhaseLP2conv = angle(LP2conv);
invLP2conv = abs(iff2(LP2conv));
invLP2Conv = circshift(invLP2conv,[-10 10]);

Figure(19);

colormap(gray);

subplot(2,2,1),imagesc(logLP2conv); title('Log Magnitude of CONV LP using fwind2');

```

```

subplot(2,2,2),imagesc(PhaseLP2conv); title('Phase of CONVLP');
subplot(2,2,3),imagesc(invLP2conv); title('Inverse of Conv LP filter');
subplot(2,2,4), imagesc(A); title('Original unfiltered Image');

% High pass

HHP2 = fwind2(HighPass,win);
HHP2_fft = fftshift(fft2(HHP2,rows,columns));
logHHP2_fft = log10( 1 + abs(HHP2_fft));
PhaseHHP2_fft = angle(HHP2_fft);

Figure(20);

colormap(gray);

subplot(2,1,1),imagesc(logHHP2_fft); title('Log Magnitude of HIGHPASS using fwind2');
subplot(2,1,2),imagesc(PhaseHHP2_fft); title('Phase of HIGHPASS');

%Convolution Highpass

HP2conv = HHP2_fft .* eug_fft;
logHP2conv = log10( 1 + abs(HP2conv));
PhaseHP2conv = angle(HP2conv);
invHP2conv = abs(iff2(HP2conv));
invHP2Conv = circshift(invHP2conv,[-10 10]);

Figure(21);

colormap(gray);

subplot(2,2,1),imagesc(logHP2conv); title('Log Magnitude of CONV HP using fwind2');
subplot(2,2,2),imagesc(PhaseHP2conv); title('Phase of CONVHP');
subplot(2,2,3),imagesc(invHP2conv); title('Inverse of Conv HP filter');
subplot(2,2,4), imagesc(A); title('Original unfiltered Image');

% Band pass

HBP2 = fwind1(BandPass,hamming(21));
HBP2_fft = fftshift(fft2(HBP2,rows,columns));
logHBP2_fft = log10( 1 + abs(HBP2_fft));
PhaseHBP2_fft = angle(HBP2_fft);

Figure(22);

colormap(gray);

subplot(2,1,1),imagesc(logHBP2_fft); title('Log Magnitude of BANDPASS using fwind2');
subplot(2,1,2),imagesc(PhaseHBP2_fft); title('Phase of BAND-PASS');

%Convolution Bandpass-fwind2

BP2conv = HBP2_fft .* eug_fft;
logBP2conv = log10( 1 + abs(BP2conv));
PhaseBP2conv = angle(BP2conv);
invBP2conv = abs(iff2(BP2conv));
invBP2Conv = circshift(invBP2conv,[-10 10]);

Figure(23);

colormap(gray);

subplot(2,2,1),imagesc(logBP2conv); title('Log Magnitude of CONV BP using fwind2');
subplot(2,2,2),imagesc(PhaseBP2conv); title('Phase of CONVBP');
subplot(2,2,3),imagesc(invBP2conv); title('Inverse of Conv BP filter');
subplot(2,2,4), imagesc(A); title('Original unfiltered Image');

```

```
% COMPLETE FILTER RESULTS
% COLOR
```

```
Figure(24);
```

```
subplot(3,4,9), imagesc(InvG); title('LP filter-Gaussian');
subplot(3,4,5), imagesc(InvL); title('HP filter-Laplacian');

subplot(3,4,2), imagesc(invBPconv); title('BP filter- fsamp2');
subplot(3,4,10), imagesc(invLPconv); title('LP filter- fsamp2');
subplot(3,4,6), imagesc(invHPconv); title('HP filter- fsamp2');

subplot(3,4,3), imagesc(invBP1conv); title('BP filter- fwind1');
subplot(3,4,11), imagesc(invLP1conv); title('LP filter- fwind1');
subplot(3,4,7), imagesc(invHP1conv); title('HP filter- fwind1');

subplot(3,4,4), imagesc(invBP2conv); title('BP filter- fwind2');
subplot(3,4,12), imagesc(invLP2conv); title('LP filter- fwind2');
subplot(3,4,8), imagesc(invHP2conv); title('HP filter- fwind2');
subplot(3,4,1), imagesc(A); title('ORIGINAL EUGLENA');
```

```
% GRAY SCALE
```

```
Figure(25);
```

```
subplot(3,4,9), imagesc(InvG); title('LP filter-Gaussian');
subplot(3,4,5), imagesc(InvL); title('HP filter-Laplacian');

subplot(3,4,2), imagesc(invBPconv); title('BP filter- fsamp2');
subplot(3,4,10), imagesc(invLPconv); title('LP filter- fsamp2');
subplot(3,4,6), imagesc(invHPconv); title('HP filter- fsamp2');

subplot(3,4,3), imagesc(invBP1conv); title('BP filter- fwind1');
subplot(3,4,11), imagesc(invLP1conv); title('LP filter- fwind1');
subplot(3,4,7), imagesc(invHP1conv); title('HP filter- fwind1');

subplot(3,4,4), imagesc(invBP2conv); title('BP filter- fwind2');
subplot(3,4,12), imagesc(invLP2conv); title('LP filter- fwind2');
subplot(3,4,8), imagesc(invHP2conv); title('HP filter- fwind2');
subplot(3,4,1), imagesc(A); title('ORIGINAL EUGLENA');
colormap(gray);
```

APPENDIX E

Program to perform morphology opening operation, contrast enhancement and counting the number of connected objects.

```
clear
close all

k=dir('pop_15*.bmp')
for i=1:length(k)
    FileName=k(i).name %% list of each file name
    I = imread(FileName);
    %I = imread('euglena.gif','gif');
    imshow(I);

    background = imopen(I,strel('disk',7));
    Figure 8., imshow(background);

    Figure 8.,surf(double(background(1:8:end, 1:8:end))),zlim([0 255]);
    set(gca,'ydir','reverse');

    I2 = imsubtract(I,background);
    Figure 8.,imshow(I2);

    I3 = imadjust(I2,[0.3 0.7],[,]);
    Figure 8.,imshow(I3);

    level = graythresh(I3);
    bw = im2bw(I3,level);
    Figure 8.,imshow(bw);

    [labeled,numObjects(i)] = bwlabel(bw,4);

end
plot(numObjects);
```